UNIVERSIDADE ESTADUAL PAULISTA
"JÚLIO DE MESQUITA FILHO"

Programa de Pós-Graduação em
Engenharia Elétrica

THIAGO GLISSOI LOPES

MONITORING THE ADDITIVE MANUFACTURING TECHNIQUE OF FUSED DEPOSITION MODELLING: A NEW APPROACH USING ELECTRET MICRO-PHONE AND SIGNAL PROCESSING

Bauru
2024

THIAGO GLISSOI LOPES

MONITORING THE ADDITIVE MANUFACTURING TECHNIQUE OF FUSED DEPOSITION MODELLING: A NEW APPROACH USING ELECTRET MICROPHONE AND SIGNAL PROCESSING

Thesis presented to the Faculty of Engineering of Bauru/ FEB of the São Paulo State University "Júlio de Mesquita Filho" / UNESP, for obtaining the title of Doctor in Electrical Engineering.

Area of concentration: Automation

Research line: Mechatronics

Advisor: Professor Dr. Paulo Roberto de Aguiar
Co-advisor: Professor Dr. Thiago Valle França
Co-advisor: Professor Dr. Pedro de Oliveira Conceição Junior

Bauru
2024

Lopes, Thiago Glissoi
L864d Monitoring the Additive Manufacturing Technique of Fused Deposition Modelling: A New Approach using Electret Microphone and Signal Processing: Thiago Glissoi Lopes, 2024
130 p. :il.,tabs.,fotos

Tese (doutorado) – Universidade Estadual Paulista (Unesp), Faculdade de Engenharia, Bauru, 2024
Orientador: Paulo Roberto de Aguiar
Coorientador: Thiago Valle França
Coorientador: Pedro de Oliveira Conceição Junior

1.Manufatura por fusão e deposição. 2. Monitoramento. 3.Detecção de anomalias. I. Universidade Estadual Paulista. Faculdade de Engenharia de Bauru. II. Título.

UNIVERSIDADE ESTADUAL PAULISTA

Câmpus de Bauru

ATA DA DEFESA PÚBLICA DA TESE DE DOUTORADO DE THIAGO GLISSOI LOPES, DISCENTE DO PROGRAMA DE PÓS-GRADUAÇÃO EM ENGENHARIA ELÉTRICA, DA FACULDADE DE ENGENHARIA - CÂMPUS DE BAURU.

Aos 25 dias do mês de outubro do ano de 2024, às 09:00 horas, por meio de Videoconferência, realizou-se a defesa de TESE DE DOUTORADO de THIAGO GLISSOI LOPES, intitulada **MONITORING THE ADDITIVE MANUFACTURING TECHNIQUE OF FUSED DEPOSITION MODELLING: A NEW APPROACH USING ELECTRET MICROPHONE AND SIGNAL PROCESSING**. A Comissão Examinadora foi constituida pelos seguintes membros: Prof. Dr. PAULO ROBERTO DE AGUIAR (Orientador(a) - Participação Virtual) do(a) Departamento de Engenharia Elétrica / Universidade Estadual Paulista UNESP Faculdade de Engenharia de Bauru, Prof. Dr. ALESSANDRO ROGER RODRIGUES (Participação Virtual) do(a) Departamento de Engenharia Mecânica / Universidade de São Paulo / USP - São Carlos, Prof. Dr. WENDERSON NASCIMENTO LOPES (Participação Virtual) do(a) Departamento de Engenharia de Controle e Automação / Instituto Federal de Educação, Ciência e Tecnologia do Paraná (IFPR-Jacarezinho), Prof. Dr. FABRICIO GUIMARÃES BAPTISTA (Participação Virtual) do(a) Departamento de Engenharia Elétrica / Faculdade de Engenharia de Bauru UNESP, Prof. Dr. DANILO HERNANE SPATTI (Participação Virtual) do(a) Departamento de Sistemas de Computação / Instituto de Ciências Matemáticas e de Computação/USP. Após a exposição pelo doutorando e arguição pelos membros da Comissão Examinadora que participaram do ato, de forma presencial e/ou virtual, o discente recebeu o conceito final: Aprovado. Nada mais havendo, foi lavrada a presente ata, que após lida e aprovada, foi assinada pelo(a) Presidente(a) da Comissão Examinadora.

Prof. Dr. PAULO ROBERTO DE AGUIAR

gov.br Documento assinado digitalmente
PAULO ROBERTO DE AGUIAR
Data: 25/10/2024 12:22:42-0300
Verifique em https://validar.iti.gov.br

POTENTIAL IMPACT OF THIS RESEARCH

This research on the Fused Filament Fabrication (FFF) process offers significant contributions to society by advancing the quality and efficiency of additive manufacturing, an essential technology in modern industry. By developing a low-cost, open-source monitoring system using an electret microphone, advanced signal processing, and machine learning algorithms, the study addresses key challenges in ensuring the reliability of 3D printing processes. The immediate societal impact is evident in the ability to reduce waste and improve the quality of manufactured goods, which in turn supports industries that rely on rapid prototyping and customized production.

From a sustainable development perspective, this research promotes resource efficiency by enabling real-time monitoring and early detection of defects in the 3D printing process. The system can cancel faulty prints early, saving energy, materials, and production time, which directly contributes to reducing the environmental footprint of manufacturing operations. Furthermore, the use of Free and Open-Source Software (FOSS) ensures that this technology can be accessed and adapted by a wide range of users, promoting inclusivity and innovation, particularly in regions with limited resources for expensive proprietary systems.

The local and regional impact of this research is rooted in its potential to enhance manufacturing processes in Small and Medium-sized Enterprises (SMEs) that rely on 3D printing for product development. By offering a low-cost solution, these businesses can adopt more efficient practices, improving competitiveness and innovation capacity. Nationally and internationally, the open-source nature of the **`fff_segmenter`** script encourages global collaboration, fostering technological advancements in additive manufacturing that can be shared and further developed by the academic and industrial communities worldwide.

I dedicate this thesis to my family who support me in everything in their power to make me happy.

ACKNOWLODGMENTS

I would like to express my heartfelt gratitude to my mother, Marcia Glissoi, for always doing everything within her reach for me.

To my dear wife, Jessyka Sanches, for her unwavering support throughout the development of this thesis.

To my grandparents, Maria and Nilton (Cabrera), for always taking care of me.

To my uncle, Reinaldo Glissoi, for doing everything for me and being an inspiring role model as I grew up.

I also thank the rest of my family for their constant encouragement and support.

I extend my deepest thanks to Professor Paulo Roberto de Aguiar for the invaluable opportunity and guidance throughout this thesis. Under your mentorship, I have grown tremendously, both academically and personally. You taught me the importance of meticulous attention to detail and thoroughness in every task to allow for deeper analysis.

To Professor Thiago Valle França, for his dedication to teaching and mentoring. Thank you for your honesty, availability, and for always finding ways to contribute to the research.

To Professor Pedro Oliveira de Conceição Júnior, for his invaluable support, especially during my sandwich doctorate period in Naples. I am grateful for your honesty, availability, and wise counsel.

I hereby publicly acknowledge that Paulo Monteiro de Carvalho Monson had major importance in the development of study B, about monitoring FFF machine conditions with electret microphones, Support Vector Machines (SVM), and Neural Networks (NN). If it were not for Paulo Monson's expertise in NN and other Computational Intelligence tools, and his willingness to assist by conducting the processing in regard to the SVM and NN aspects of the study, study B could not have been developed in the manner displayed in this thesis. I also publicly acknowledge that Paulo Monson gave the initial idea for the journal that study A, in regard to the development of the **`fff_segmenter`** segmentation script, was conclusively published in.

I am deeply grateful to Reinaldo Götz, who played a crucial role in the development of Study A, particularly with the creation of the **`fff_segmenter`** segmentation script. Without his assistance in developing and installing the splitter boards used in this study, the completion of Study A would not have been possible. I am also sincerely thankful for his help with the development of the signal conditioning and amplification hardware used for the electret microphone signals in both Study A and Study B. Reinaldo, your support was invaluable, and I am truly grateful for everything.

I am also deeply grateful to the professors, staff, and colleagues at the Faculty of Engineering of Bauru and the Università degli Studi di Napoli "Federico II" (UniNA) for all the support and guidance provided during this PhD journey.

To my lab colleagues at UNESP and dearest friends – Cristiano Soares, Fábio Dotto, Gabriel David, Luanne Barbosa, Victoria Kennerly, and Zaqueu Antônio – your friendship has been invaluable. I would also like to acknowledge friends and colleagues from other UNESP research labs, especially Abdo Khoury and Matheus Carmo, for their fantastic support.

To Professor Doriana D'Donna, for all her guidance and assistance during my time at UniNA.

To my closest colleagues and friends at UniNA – Dario de Fazio, Ersilia Cozzolino, Giulio Mattera, and Martina Panico – thank you for making my time in Naples unforgettable. *Grazie mille per tutto*!

To my dear friend, Felipe Alexandre (*in memoriam*). I know that you were with me in spirit throughout this journey. You are deeply missed, my friend and brother∴.

To my friends Adriel Senna, Breno Ortega, Bruno Castro, Erick Ruas, Igor Bazan, José Vital, Leandro Campeiro, and Wenderson Nascimento, for your companionship and valuable advice.

Finally, I acknowledge everyone who contributed to and supported me throughout this period of my life. Thank you all for being a part of this journey.

“In life, unlike chess, the game continues after checkmate.”
Isaac Asimov

RESUMO

O processo de Modelagem por Deposição Fundida, também conhecido como Fabricação por Filamento Fundido (FFF), envolve a construção de objetos tridimensionais por meio da deposição sucessiva de filamentos plásticos derretidos. Apesar de seu uso extensivo, monitorar e diagnosticar esse processo continua complexo, exigindo métodos sofisticados para garantir alta qualidade e eficiência. A primeira camada no processo FFF é muito importante, pois serve como a base para todo o objeto impresso em 3D. Esta camada estabelece a fundação para as camadas subsequentes, influenciando a qualidade geral da impressão, a precisão dimensional e a integridade estrutural do produto final. Isso faz da primeira camada um foco para estudos de monitoramento do processo FFF, considerando que, se qualquer defeito puder ser detectado durante essa fase de fabricação, o processo pode ser cancelado, evitando perdas adicionais. A presente tese aborda lacunas significativas na literatura atual sobre monitoramento do processo FFF, integrando métodos avançados de processamento de sinais com ferramentas de inteligência computacional. Utilizando um microfone eletreto montado no extrusor, a pesquisa realiza um processamento abrangente de sinais e extração de características, incluindo análise espectral, valores de Root Mean Square (RMS), Ratio of Power (ROP), estatística de contagens, curtose e assimetria. O uso de algoritmos de aprendizado de máquina, particularmente a Máquina de Vetores de Suporte (SVM) e Redes Neurais, aprimora as capacidades de classificação e diagnóstico do sistema. A análise espectral foi fundamental na identificação de valores de frequência associados a defeitos e na extração de características que distinguiram efetivamente diferentes estados da máquina. A implementação de algoritmos de aprendizado de máquina, notavelmente o SVM, alcançou uma precisão excepcional de 100% na classificação de condições normais e irregulares da máquina com base nas características extraídas. A tese também detalha o desenvolvimento do script **`fff_segmenter`**. Esta ferramenta inovadora, de Software Livre e de Código Aberto (FOSS), automatiza a segmentação de sinais acústicos de monitoramento usando sinais de controle dos eixos dos motores de passo X e Y e a taxa de amostragem do sinal, reduzindo significativamente os erros e o tempo consumido pelos métodos de segmentação manual. Os resultados da segmentação do script podem ser facilmente integrados a outras aplicações do MATLAB ou Octave. Em conclusão, esta tese apresenta um quadro abrangente para aprimorar as capacidades de monitoramento e diagnóstico do processo FFF. Ao integrar sensores de baixo custo, como o microfone eletreto, processamento avançado de sinais, aprendizado de máquina e ferramentas de código aberto, ela fornece uma estrutura clara para o monitoramento do FFF, abrindo caminho para futuros avanços na manufatura aditiva.

Palvras-chave: Fabricação por Filamento Fundido, Monitoramento de Processos, Segmentação de Sinais

ABSTRACT

The Fused Deposition Modeling process, also known as Fused Filament Fabrication (FFF), involves building three-dimensional objects through the successive layering of molten plastic filaments. Despite its extensive use, monitoring and diagnosing this process remains complex, requiring sophisticated methods to ensure high quality and efficiency. The first layer in the FFF process is very important, as it serves as the foundation for the entire 3D printed object. This layer sets the base for subsequent layers, influencing the overall print quality, dimensional accuracy, and structural integrity of the final product. This makes the first layer a focus for FFF process monitoring studies, given that if any defect could be detected during this fabrication, the fabrication process can be canceled avoiding further losses. The present thesis addresses significant gaps in the current body of research on FFF process monitoring by integrating advanced signal processing methods with computational intelligence tools. By utilizing an electret microphone mounted on the extruder, the research performs comprehensive signal processing and feature extraction, including spectral analysis, Root Mean Square (RMS) values, Ratio of Power (ROP), Counts statistic, Kurtosis, and Skewness. The use of machine learning algorithms, particularly Support Vector Machine (SVM) and Neural Networks, enhances the system's classification and diagnostic capabilities. Spectral analysis was pivotal in identifying frequency values linked to defects and in extracting features that effectively distinguished between different machine states. The implementation of machine learning algorithms, notably SVM, achieved an outstanding 100% accuracy in classifying normal and irregular machine conditions based on the extracted features. The thesis also details the development of the **`fff_segmenter`** script. This innovative and Free and Open Source Software (FOSS) tool automates the segmentation of monitoring acoustic signals using control signals from the X and Y stepper motor axes and the signal's sampling rate, significantly reducing errors and time consumption associated with manual segmentation methods. The script’s segmentation results can be easily into other MATLAB or Octave applications. In conclusion, this thesis presents a comprehensive framework for enhancing the monitoring and diagnostic capabilities of the FFF process. By integrating low-cost sensors such as the electret microphone, advanced signal processing, machine learning, and open-source tools, it provides a clear framework for FFF monitoring, paving the way for future advancements in additive manufacturing.

Keywords: Fused Filament Fabrication, Process monitoring, Signal segmentation

SUMMARY

Potential impact of this research ..... **v**

ACKNOWLODGMENTS ..... **vii**

RESUMO ..... **x**

ABSTRACT ..... **xi**

SUMMARY ..... **xii**

FIGURES ..... **xv**

TABLES ..... **xix**

SYMBOLS AND ABBREVIATIONS ..... **xx**

1 – INTRODUCTION **22**

1.1 BRIEF EXPOSITION ABOUT FUSED DEPOSITION MODELLING AND ITS MONITORING 22

1.2 OBJECTIVE 26

1.3 PUBLICATIONS 27

2 – LITERATURE REVIEW **31**

2.1 MONITORING OF AM MACHINE CONDITIONS 31

2.2 ACOUSTIC SIGNALS IN FFF 3D PRINTING AND APPLICATION OF ELECTRET MICROPHONES 34

2.3 SIGNAL ANALYSIS STATISTICS IN THE TIME-DOMAIN AND FREQUENCY-DOMAIN AND THEIR USE IN STUDIES REGARDING THE MONITORING OF MANUFACTURING PROCESSES 36

2.3.1 COUNTS 36

2.3.2 ROOT MEAN SQUARE (RMS) 37

2.3.3 RATIO OF POWER (ROP) 38

2.3.4 SKEWNESS 38

2.3.5 KURTOSIS 39

2.4 KNOWLEDGE FRONTIER AND OUR PRIMARY CONTRIBUTIONS 40

3 – MATERIAL AND METHODS **43**

3.1 STUDY A: MATERIAL AND METHODS REGARDING THE DEVELOPMENT OF THE `FFF_SEGMENTER` SEGMENTATION SCRIPT 43

3.1.1 STUDY A: EXPERIMENTAL SETUP 45

3.1.2 STUDY A: ACESSING AND USING THE `FFF_SEGMENTER` SCRIPT 50

3.1.2.1 STUDY A: OBTAIN THE FFF-LINE-SEGMENTATION GITHUB REPOSITORY FILES 50

3.1.2.2 STUDY A: DEPENDENCIES 51

3.1.2.3 STUDY A: MATLAB EXAMPLE 51

3.1.2.4 STUDY A: OCTAVE EXAMPLE 53

3.2 STUDY B: MATERIAL AND METHODS REGARDING THE STUDY ABOUT MONITORING FFF MACHINE CONDITIONS WITH ELECTRET MICROPHONES, SVM, AND NEURAL NETWORKS 56

3.2.1 STUDY B: EXPERIMENTAL SETUP 56
3.2.2 STUDY B: 3D PRINTING TESTS OF SINGLE-LAYER PARTS FOR THREE MACHINE CONDITIONS....57
3.2.3 STUDY B: THE PROPOSED METHOD OF SIGNAL PROCESSING AND FEATURES EXTRACTION – INCLUDING THE SIGNAL SEGMENTATION ALGORITHM; 58
3.2.4 STUDY B: NEURAL NETWORK MODELS AND SVM FOR CLASSIFYING THE CONDITIONS 60
4 – RESULTS AND DISCUSSION 63
4.1 STUDY A: RESULTS AND DISCUSSION REGARDING THE DEVELOPMENT OF THE `FFF_SEGMENTER` SEGMENTATION SCRIPT 63
4.1.1 STUDY A: CONSIDERATIONS REGARDING THE WORKPIECE 63
4.1.1.1 STUDY A: SEGMENTATION OF THE EXTERNAL AND INTERNAL PATTERNS 64
4.1.2 STUDY A: CONSIDERATIONS BASED ON FABRICATION MOVEMENTS 66
4.1.3 STUDY A: SCRIPT SEGMENTATION OPERATION....67
4.1.3.1 STUDY A: USER INPUT 67
4.1.3.1.1 STUDY A: MATLAB INPUT APP....67
4.1.3.1.2 STUDY A: OCTAVE INPUT USER INTERFACE....69
4.1.3.2 STUDY A: ATRIBUTING SPECIFIC VARIABLES 69
4.1.3.2.1 STUDY A: WORKPIECE SPECIFIC VARIABLES 70
4.1.3.2.2 STUDY A: SEGMENTATION LOGIC VARIABLES 71
4.1.3.3 STUDY A: PRE-PROCESSING 73
4.1.3.4 STUDY A: EXTERNAL PATTERN SEGMENTATION....78
4.1.3.5 STUDY A: INTERNAL PATTERN SEGMENTATION 81
4.1.4 STUDY A: SEGMENTATION RESULTS....88
4.2 STUDY B: RESULTS AND DISCUSSION REGARDING THE STUDY ABOUT MONITORING FFF MACHINE CONDITIONS WITH ELECTRET MICROPHONES, SVM, AND NEURAL NETWORKS 92
4.2.1 STUDY B: EVALUATION AND EXTRACTION OF THE RAW SIGNALS 92
4.2.2 STUDY B: RAW SIGNALS FOR THE EXTERNAL AND INTERNAL INFILL PATTERNS 93
4.2.3 STUDY B: SPECTRAL ANALYSIS AND FREQUENCY BAND DETERMINATION 95
4.2.4 STUDY B: ROOT MEAN SQUARE VALUE ANALYSIS....96
4.2.5 STUDY B: ANALYSIS OF KURTOSIS AND SKEWNESS 97
4.2.6 STUDY B: COUNTS STATISTIC RESULTS AND DISCUSSION 98
4.2.7 STUDY B: ANALYSIS OF THE RATIO OF POWER....99
4.2.8 STUDY B: PERFORMANCE ANALYSIS FOR THE COUNTS FEATURE OBTAINED FROM THE RAW SIGNAL100
4.2.9 STUDY B: PERFORMANCE ANALYSIS FOR THE COUNTS FEATURE OBTAINED FROM THE FILTERED RAW SIGNAL 101
4.2.10 STUDY B: PERFORMANCE ANALYSIS FOR THE RMS, ROP, SKEWNESS AND KURTOSIS....103
5 – CONCLUSION 105
5.1 SUGGESTIONS FOR FUTURE WORKS.....105

6 – REFERENCES..... 107

7 – APPENDIX I 122

FIGURES

Figure 1.1 - Representation of the movement of the workpiece or of the extruder, necessary for the filament deposition in the FDM process....22
Figure 1.2 - Representation of the workpiece elements of fabrication, constituted of raster lines infill, contour lines infill, and combination infill of both raster and contour lines 25
Figure 2.1 - Counts statistic representation on a raw signal acquired from a Pencil Lead Break test, whereas a threshold is visible, and the counts number is observed in a specific period of interest 36
Figure 2.2 - Graphical representation of the Positive and Negative Skewness profiles....39
Figure 2.3 - Graphical representation of the Lepticurtic and Platicurtic Kurtosis profiles 39
Figure 2.4 - Normalized raw signal acquired from a sensor attached to the printer table during a monolayer workpiece FDM fabrication....41
Figure 3.1 – Geometrical elements of a FFF printed layer, with representation of the contour width, raster width and angle, the GAP between raster lines, and the VOID between raster and contour type infills.....43
Figure 3.2 - RepRap Arduino Mega Pololu Shield (RAMPS) 1.4 schematic with indications of the stepper motors direction signals 45
Figure 3.3 – Splitter board and connection to the A4988 Carrier, with indications of the cables related to the Dir and Step pins 46
Figure 3.4 – Splitter boards placement on the A1V2 3D priter RAMPS board, with the identification of the which splitter board is related to the X and Y axis 46
Figure 3.5 – Signal acquisition process visualization on the DAQ, with the representation of the Sensor signal, X-axis and Y-axis direction signals, X-axis and Y-axis step signals....47
Figure 3.6 – *Test1.mat* dataset sensors placement in a glass appendix attached to right side of the printer table....48
Figure 3.7 – *Test2.mat* dataset sensors placement in a glass appendix attached to the printer table and on the right side of the printer extruder block....49
Figure 3.8 – *Test3.mat* dataset sensors placement on the printer extruder block, where an electret microphone was placed on the left side of the block, and a piezoelectric diaphram was placed on the right side of the block.....49
Figure 3.9 – Instructional representation on how to perform a manual download of the FFF-Line-Segmentation repository on Github 50
Figure 3.10 – MATLAB Input Graphical User Interface (GUI). (a) Unfilled GUI, with comments certain elements of the interface; (b) Filled GUI, with default options and values regarding the *Test1.mat* dataset 51
Figure 3.11 – Octave file navigation, running inside an Ubuntu machine, with the Xcfe desktop enviroment and Thunar file manager....53
Figure 3.12 – Octave input User Interface (UI). (a) Unfilled UI, with comments certain elements of the interface; (b) Filled UI, with default options and values regarding the *Test1.mat* dataset 54
Figure 3.13 - Experimental setup regarding the study about monitoring FFF machine conditions with electret microphones, SVM, and neural networks....56

Figure 3.14 - Single-layer part used in the study B, with a zoom visualization on upper corner of the workpiece with identification of the Raster and Contour lines 57
Figure 3.15 – Schematic representation regarding the steps taken in the study B methodology, with visualization of the general analysis sequence, and detailed sequence in regard to the segment extraction process 59
Figure 3.16 – Schematic with a deeper representation regarding the steps taken in the study B methodology, with specific visualization of the signal process analysis sequence 62
Figure 4.1 – Representation of the elements of fabrication in regard to the monolayer workpiece utilized in the study A 63
Figure 4.2 – Study A workpiece with identifications of each contour line, raster line, and transition between raster lines (transistion raster) 64
Figure 4.3 – Study A workpiece internal pattern fabrication behaviour, with the visualization of the first, second and third raster and transtion raster lines 65
Figure 4.4 – Study A workpiece fabrication Movement Without Deposition (MWD) `Test1` detailing, with visualization of the positions regarding the MWD G-code lines 68
Figure 4.5 – Schematic representing the workpiece specific variables values, and the necessary variables values for the segmentation logic utilized in the study A 70
Figure 4.6 - DEBUG Point of Interest 1 (POI-1) for `Test1`, where the raw direction signals of both X and Y axis are visible, and an aproximation on the timeframe between 50s and 55s is displayed for each signal 74
Figure 4.7 - DEBUG Point of Interest 1 (POI-1) for `Test2`, where the raw direction signals of both X and Y axis are visible, and an aproximation on the timeframe between 50s and 55s is displayed for each signal 74
Figure 4.8 - DEBUG Point of Interest 2 (POI-2) for `Test1`, where the raw adjusted direction signals of both X and Y axis are visible, and an aproximation on the timeframe between 50s and 55s is displayed for each signal 75
Figure 4.9 - DEBUG Point of Interest 2 (POI-2) for `Test2`, where the raw adjusted direction signals of both X and Y axis are visible, and an aproximation on the timeframe between 50s and 55s is displayed for each signal 75
Figure 4.10 - DEBUG POI-3 for `Test1` 76
Figure 4.11 - DEBUG Point of Interest 3 (POI-3) for `Test1`, where the normalized direction signals of both X and Y axis are visible, and an aproximation on the timeframe between 50s and 55s is displayed for each signal 76
Figure 4.12 - DEBUG Point of Interest 4 (POI-4) for `Test1`, where the normalized direction X signal is visible, alongside an aproximation of the signal on the timeframe between 50.11s and 50.16s, and on the timeframe between 50.133s and 50.135s 77
Figure 4.13 - DEBUG Point of Interest 5 (POI-5) for `Test1`, where the duration value for each obtained segment is displayed 77
Figure 4.14 - DEBUG Point of Interest 5 (POI-5) for `Test2`, where the normalized direction X signal is visible, alongside an aproximation of the signal on the timeframe between 50.11s and 50.16s, and on the timeframe between 50.133s and 50.135s 78
Figure 4.15 - DEBUG Point of Interest 5 (POI-5) for `Test2`, where the duration value for each obtained segment is displayed 79

Figure 4.16 - *Test1* Debug Point of Interest 6 (POI-6) MWD's detailing, where the duration value for each obtained segment is displayed alongside an approximation on the segments related to the external pattern 80
Figure 4.17 – Debug Point of Interest 7 (POI-7) for *Test1*, where the duration value for each obtained segment is displayed 82
Figure 4.18 – Debug Point of Interest 8 (POI-8) for *Test1*, where the duration value for each obtained segment is displayed alongside an approximation on the first third of the internal printing pattern, where multiple abnormal behaviour regions are present 83
Figure 4.19 - Debug Point of Interest 9 (POI-9) for *Test1*, where the duration value for each obtained segment in regard to the first half of the internal printing pattern is displayed, alongside one raster and two transition rasters segments in regard to the second half of the internal printing pattern 85
Figure 4.20 - Debug Point of Interest 10 (POI-10) for *Test1* where the duration value for each obtained segment in regard to the first half of the internal printing pattern is displayed 86
Figure 4.21 - DEBUG Point of Interest 11 (POI-11) for *Test1*, where the duration value for each obtained segment in regard to the almost complete internal printing pattern is displayed, alongside an approximation on the first segments of the internal printing pattern 86
Figure 4.22 - DEBUG Point of Interest 12 (POI-12) for *Test1*, where the duration value for each obtained segment in regard to the complete internal printing pattern is displayed, alongside an approximation on the first segments of the internal printing pattern 87
Figure 4.23 – MATLAB workspace with the segmentation results tables 89
Figure 4.24 – MATLAB segmentation results tables, with a representation of each result table content 89
Figure 4.25 – Octave workspace with the segmentation results structs 90
Figure 4.26 – Octave segmentation results structs, with a representation of each result struct content 90
Figure 4.27 – Graphical representation of the segmentation results upon the *Test1.mat* dataset acoustic signal, with specific visualization of the segmentation results in the transition period between external and internal infill patterns 91
Figure 4.28 - Raw Signal and RMS Values for Normal Printing Condition 92
Figure 4.29 - Decimated Raw Signal, RMS Values, and Counts Statistic 93
Figure 4.30 - Raw Signals for the Normal Printing, Clogging and Lack of Filament machine conditions 93
Figure 4.31 – Obtained workpieces. (a), (b), and (c): Under clogging condition; (d), (e), and (f): Under filament lack condition 94
Figure 4.32 - Magnified Raw Signals for Normal Printing, Clogging and Lack of Filament machine conditions 95
Figure 4.33 - Spectral Analysis of Raw Signals for Normal Printing, Clogging and Interrupted (Lack of Filament) machine conditions and Selected Frequency Band 95
Figure 4.34 - RMS Values from Unfiltered Raw Signals for Normal Printing, Clogging and Interrupted (Lack of Filament) machine conditions 96
Figure 4.35 - RMS Values from Filtered Raw Signals for Normal Printing, Clogging and Lack of Filament machine conditions 97

Figure 4.36 - Kurtosis (a) and Skewness (b) from Unfiltered Raw Signals, and Kurtosis (c) and Skewness (d) from Filtered Raw Signals for Normal Printing, Clogging and Lack of Filament machine conditions 98
Figure 4.37 - Counts from Unfiltered (a) and Filtered (b) Raw Signals for Normal Printing, Clogging and Filament Lack machine conditions 98
Figure 4.38 - Ratio of Power for Normal Printing, Clogging and Filament Lack machine conditions 99
Figure 4.39 - Neural network and SVM analysis workflow 100
Figure 4.40 - Confusion matrix for (a) validation and (b) Test data 100
Figure 4.41 - Area Under the Curve for (a) Validation and (b) Test Data 101
Figure 4.42 - Feature space for Counts statistic for (a) raw unfiltered signal and (b) filtered signal for Normal Printing, Clogging and Filament Lack machine conditions 102
Figure 7.1 - `numofContourLoops` value found in the workpiece G-code 122
Figure 7.2 - Outer perimeter G-code in regard to contour lines furthest from the center 122
Figure 7.3 - Internal printing pattern G-code in regard to the middle raster lines and transition between raster lines 122
Figure 7.4 - Code for normalize the X and Y step motor control signals between 0V and 5V 122
Figure 7.5 - Code to test for the occurrence of the variation problem 123
Figure 7.6 - Code to obtain the `Duration` matrix 123
Figure 7.7 - Code to find the separation point 123
Figure 7.8 - Code to obtain the temporary contour lines matrix 123
Figure 7.9 - Code to obtain the correct contour lines matrix and MWD matrix 124
Figure 7.10 - Code to obtain the first duration matrix for the internal pattern 124
Figure 7.11 - Code to obtain the second duration matrix for the internal pattern 125
Figure 7.12 - Code to obtain the third duration matrix for the internal pattern 126
Figure 7.13 - Code to obtain the fourth duration matrix for the internal pattern 126
Figure 7.14 - Code to obtain the fifth duration matrix for the internal pattern 127
Figure 7.15 - Code to obtain the sixth duration matrix for the internal pattern 127
Figure 7.16 - Code to obtain the index values from the last duration matrix 128
Figure 7.17 - Code to obtain the segmentation results 129
Figure 7.18 - Code to save the results and generate the graphs 130

TABLES

Table 3.1 - Training matrix for each test 61
Table 4.1 - External printing pattern movements for *Test1* 67
Table 4.2 - Results for RMS, ROP, and Skewness 103

SYMBOLS AND ABBREVIATIONS

ºC	**Celsius degree**
3DP	**3D Printing**
ABS	**Acrylonitrile Butadiene Styrene**
AE	**Acoustic Emission**
AI	**Artificial Intelligence**
Aka	**Also known as**
AM	**Additive Manufacturing**
ANN	**Artificial Neural Network**
App	**Application**
AUC	**Area Under the Curve**
CAD	**Computer Aided Design**
CNN	**Convolutional Neural Network**
DAQ	**Data Acquisition device**
Dir	**Direction**
DFT	**Discrete Fourier Transform**
EIP	**External Infill Pattern**
FDM	**Fused Deposition Modeling | Fused Deposition Modelling**
FFF	**Fused Filament Fabrication**
FFT	**Fast Fourier Transform**
FIR	**Finite Impulse Response**
FOSS	**Free and Open-Source Software**
Fs	**Sampling frequency**
GNU	**GNU's Not Unix!**
GPL	**General Public License**
GUI	**Graphical User Interface**
Hz	**Hertz**
IIP	**Internal Infill Pattern**
IIR	**Infinite Impulse Response**
JOSS	**Journal of Open-Source Software**
LADAPS	**Laboratory of Data Acquisition and Signal Processing**
LPBF	**Laser Powder Bed Fusion**
MIT	**Massachusetts Institute of Technology**
ML	**Machine Learning**
MLP	**Multilayer Perceptron**
MWD	**Movements Without Deposition**
ND	**Non-Destructive**
NN	**Neural Network**
OSD	**Open-Source Definition**
OSI	**Open-Source Initiative**
PETG	**Polyethylene Terephthalate Glycol**
PC	**Personal Computer**

PCA	**Principal Component Analysis**
PLA	**Polylactic Acid**
POI-n	**Point of Interest “n”**
PSD	**Power Spectral Density**
PVDF	**Piezoelectric Polyvinylidene DiFluoride**
PZT	**Piezoelectric diaphragm**
RAMPS	**RepRap Arduino Mega Pololu Shield**
RepRap	**Replicating Rapid-prototyper**
RMS	**Root Mean Square**
ROC	**Receiver Operating Characteristic**
ROP	**Ratio of Power**
SLM	**Selective Laser Melting**
S/s	**Samples per second**
Struct	**Structure**
STL	**Stereolithography**
SVM	**Support Vector Machine**
TIM	**Three-phase Induction Motor**
TR	**Termination Return**
UI	**User Interface**
UNESP	**São Paulo State University**
WAAM	**Wire Arc Additive Manufacturing**
ZIP	**Zipped archive**

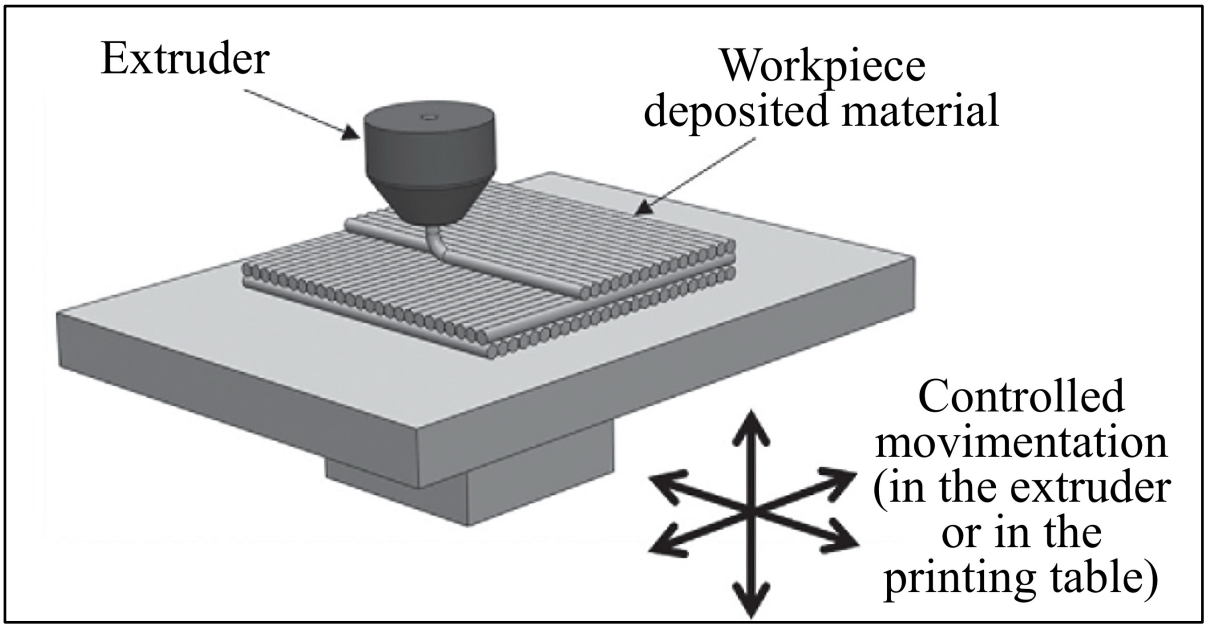
1 – INTRODUCTION

1.1 BRIEF EXPOSITION ABOUT FUSED DEPOSITION MODELLING AND ITS MONITORING

The Additive Manufacturing (AM) technologies have revolutionized the manufacturing industry by enabling small batch and cost-effective fabrication of complex geometry products [1]. Among these technologies, Fused Deposition Modeling (FDM) is one of the most extensively employed [2], and that also grown in research interest [3], [4].

The process of AM known as FDM was developed in the 1980s by S. Scott Crump, the co-founder of Stratasys®. FDM technology employs a thermoplastic filament that is extruded through a heated nozzle and deposited layer by layer to create a three-dimensional object [5]. Initially, the FDM process was patented by Stratasys, which restricted its commercial use to products and systems developed by the company. During the patent's validity, FDM established itself as one of the most recognized 3D printing technologies, particularly in industrial applications and rapid prototyping [5], [6]. With the expiration of the FDM patent in 2009, the 3D printing community began adopting the term Fused Filament Fabrication (FFF) to describe the same process [7]. In the FDM process, the travel required for filament deposition is achieved through the movement of the extruder or the printing table as represented in Figure 1.1.

Figure 1.1 - Representation of the movement of the workpiece or of the extruder, necessary for the filament deposition in the FDM process



Source: Altered from Volpato (2017) [8]

Objects obtained through the FFF process can be applied in a wide range of applications [9]. Specific application examples, as provided in the work by Schniederjans (2017) [10], are found in: aviation and air defense, such as in the construction of lightweight fuselages; civil construction, such as topographic models; and the automotive industry, such as in the construction of aerodynamic car bodies. There is also significant utilization of objects produced by the process in the orthopedic [11], orthodontic [12], and medical diagnostic sectors [13].

The adoption of the FFF process as an alternative to other industrial and rapid prototyping processes has been extensively studied [4], [10], [14], [15], [16]. Among the criteria identified as focuses for this adoption, are performance improvement, compatibility with other processes, and facilitated processing conditions [10]. Regarding the percentage of FFF process utilization in the five largest manufacturing industries, the percentages are as follows: 35% for automotive and aerospace, 28% for consumer services, 17% in biomedicine, 12% for education, and 8% for other uses [9].

The term FFF was popularized by the Replicating Rapid Prototyper (RepRap) project [17]. The adoption of the term FFF was intended to avoid legal issues associated with using a trademarked term and to promote the concept of an accessible and modifiable technology by the community [18], [19]. However, even with the broad adoption of the term FFF, there are still a lot of recent published articles and other scientific productions that use the term FDM to refer to the process [2], [20], [21], [22], [23], [24], [25], [26], [27].

The RepRap project is a pioneering initiative in the field of FFF 3D printing, established by Dr. Adrian Bowyer in 2005 [17]. The primary goal of RepRap is to develop 3D printers that can replicate most of their own components, thereby enabling a self-replicating manufacturing system. This innovative concept is grounded in the open-source philosophy, with all designs and specifications released under the GNU General Public License (GPL), allowing individuals worldwide to build, modify, and enhance their own 3D printers [17], [28].

The success of the RepRap project has also influenced the development of numerous other open-source FFF 3D printers, further promoting innovation in the field. As a result, various models inspired by the RepRap concept and form factor have emerged. These models inspired by the RepRap concept and form factor are known as “RepRap-based printers”, each offering unique features and enhancements. These derivatives have expanded the capabilities of 3D printing, enabling more precise and diverse applications, from intricate prototyping to functional end-use products [19], [29].

The process of manufacturing a part by FFF involves several crucial steps to ensure the quality and precision of the final piece. [30] define eight sequential steps that must be followed for the production and application of an object using the FFF process: Obtention of the part digital 3D model, conversion to stereolithography (STL) file, transfer and manipulation of the STL file in the slicing software, printer setup and print parameterization, object fabrication, removal of the printed object and cleaning of the print bed, finishing of the printed object, and application.

In the first step the digital 3D model of the part is acquired using Computer-Aided Design (CAD) software or through digitization techniques, such as scanning existing physical models [31]. With the 3D model of the part, the digital file is converted to a format compatible with the 3D printer, usually the STL format. This file is then processed by slicer software, which divides the model into layers and generates the G-code necessary to guide the printer during fabrication [31], [32].

The next step involves preparing the 3D printer and the printing material. The most commonly used material in the FFF process is thermoplastic, which is fed in filament form. The printer heats the filament to the melting temperature, which varies depending on the type of material used (such as Polylactic Acid (PLA), Acrylonitrile Butadiene Styrene (ABS), Polyethylene Terephthalate Glycol (PETG), among others). The temperature of the extrusion nozzle

and the print bed are adjusted in accordance with the material specifications to ensure proper adhesion between layers and minimize defects in the part [33]. Additionally, parameters such as printing speed, layer height, and infill density are configured in the slicer software, directly influencing the final quality of the part [6], [34].

During the printing process, the heated filament is extruded through a nozzle and deposited layer by layer, according to the instructions of the G-code. Precise control of the temperature, material flow rate, and movement of the extrusion nozzle is essential to avoid issues such as delamination, warping, and porosity in the final part [35], [36]. After printing is complete, the part is removed from the print bed and, if necessary, undergoes post-processing, such as sanding, heat treatment or painting, to improve its mechanical and aesthetic properties [31], [37].

The FFF process is controlled by a combination of parameters, including extrusion temperature, printing bed temperature, layer height, and infill pattern. However, the complex process parameters are considered to be a major limitation of the FFF process [2]. This, combined with the fact that different postprocessing software provides the option to modify distinctive process parameters [34], makes the monitoring of the FFF process a particularly difficult task.

As stated by Fu *et al.* (2021) [38], there are in general two forms of quality monitoring for the FFF process: (1) monitoring of printer health state; and (2) detecting product defects during the printing process. In both cases, monitoring of the FFF process require real-time measurement and analysis of various process variables. Sensors play a crucial role in capturing data related to temperature, pressure, position, and other relevant process parameters. Acoustic sensors, in particular, have shown promise in providing valuable information about the printer's health state and performance [38].

The printing time and final quality of an object produced by the FFF process are difficult to predict [34]. This is due to the numerous stages of the process where manufacturing changes are defined. Initially, the STL file undergoes a preparation process in a program known as a post-processor, where initial process parameterization occurs. In this parameterization, which takes place during the slicing process, the printing parameters are defined. Another factor that introduces uncertainties in the printing time and final quality of an object produced by the FFF process is the choice of post-processor for the initial process parameterization. Each chosen post-processor has intrinsic parameters that establish, among other factors, which printing parameters can be defined during slicing [34], [39], adding a degree of uncertainty to the predictability of the final characteristics of an object produced by the FFF process [40]. However, these changes in the final characteristics of an object can be so small that they become difficult for a human operator to perceive [41].

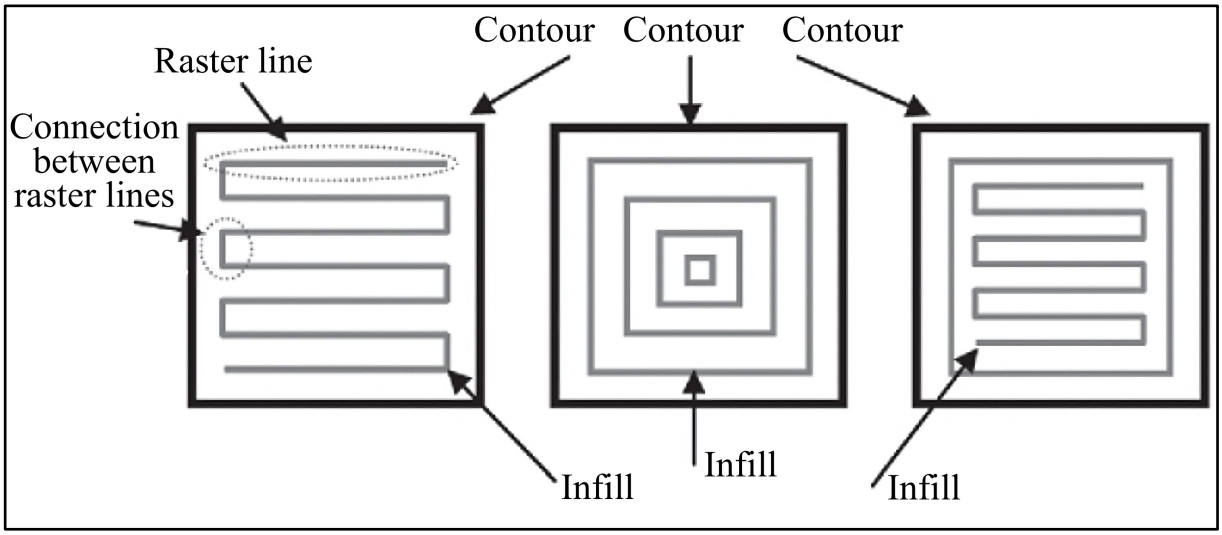
Undesired variations in the final characteristics of a part can be depicted as printing anomalies in fundamental layer parameters [8] or in geometric variations between the idealized object and the printed object [42].

Damage to parts during the FFF AM process incurs high costs and losses due to the high added value they possess. The most common damages in the FFF process include layer debonding or peeling off from the print bed, surface scratching by the extruder, shrinkage of the deposited filament, geometric variation between the idealized model and the fabricated part,

warping at the edges of the part, clogging or partial clogging of the extruder, and filament runout in the extruder [35], [43], [44], [45].

The fabrication of each layer by the FFF process is achieved through the deposition of molten filament using different manufacturing or infill strategies [46]. Each layer of the part fabricated by the FFF process displays a combination of different workpiece elements of fabrication, such as the contour, raster, void, gap, and others [6], [8], as represented in Figure 1.2. The combination of different manufacturing strategies, such as raster and contour strategies, or the variation of parameters within the same strategy, such as raster angle, results in the existence of multiple infill patterns within the same layer [47].

Figure 1.2 - Representation of the workpiece elements of fabrication, constituted of raster lines infill, contour lines infill, and combination infill of both raster and contour lines



Source: Altered from Volpato (2017) [8]

Throughout the entire FFF process, the printing of the first layer is the most critical for detecting abnormalities that may indicate failures [48]. This is because, in the FFF process, the first layer provides the foundation for the object being fabricated [49]. In all of the layers, the different elements of fabrication of the workpiece are present in a signal acquired *in-situ* from the FFF process, alongside with periods without deposition; therefore, the monitoring of the FFF process must take in consideration the segmentation of different periods of signal, related to the elements of fabrication and other fabrication phenomena, in order to allow for accurate evaluation [50], [51].

There is a growing trend in research focused on monitoring manufacturing processes, which involves the exploration of low-cost transducers as alternatives to conventional and more expensive transducers. This trend is evident in studies that assess the feasibility of employing low-cost piezoelectric transducers as substitutes for Acoustic Emission (AE) sensors [52], [53], [54], [55], [56] and ultrasound transducers [57], as well as in studies evaluating the potential of electret microphones as alternatives to AE sensors [58].

Electret microphones, initially introduced by [59], [60], are commonplace in many electronic devices that operate on the electrostatic principle, which exhibits nonlinear behavior and requires biasing to operate in a linear region. Electret microphones utilize the permanent

polarization induced during manufacturing in a plastic polymer film, which serves as the electret material. This polarization attracts free charge on the metallic electrodes of the device, necessary for proper electrostatic transduction. It is a cost-effective microphone, but this does not indicate low quality [61].

The acquired sensor signals need to be processed and analyzed to extract meaningful information regarding the machine conditions. Signal processing techniques enable the characterization and interpretation of the signals in the time, frequency, and time-frequency domains [62]. By applying appropriate statistics, valuable insights can be gained, such as detecting anomalies, identifying patterns, and assessing the overall performance of the FFF system [63].

Among the multitude of signal processing techniques, the Support Vector Machine (SVM) is a powerful machine learning algorithm that has been widely used for classification and regression tasks. SVM utilizes a training dataset to build a model that can predict the class or value of unseen data [64]. In the context of FFF process monitoring, a modified version of the SVM algorithm has been employed to predict the dimensional accuracy of FFF fabricated parts for different layer thicknesses, nozzle temperatures, and infill densities [65], and a classic version of the SVM algorithm to classify between a healthy and faulty printed part [66].

Neural Networks (NN) have demonstrated remarkable capabilities in several applications, including pattern recognition, damage classification, and features prediction. They are particularly well-suited for complex and non-linear problems [67]. In the context of FFF process monitoring, neural networks can be trained to learn the intricate relationships between the sensor signals and the corresponding machine conditions, enabling accurate estimation and classification [68].

1.2 OBJECTIVE

The primary objective of this thesis is to develop a comprehensive monitoring and diagnostic system for the FFF process, delivering practical tools and methodologies that directly benefit engineers, technicians, manufacturers, and researchers in the additive manufacturing industry. Specifically, this research aims to bridge significant gaps in the current literature on monitoring the FFF process by integrating advanced signal processing techniques with computational intelligence tools.

The main product includes the development of a multifaceted approach that utilizes an electret microphone attached to the extruder, coupled with extensive signal processing and feature extraction methods—such as spectral analysis, RMS, Ratio of Power, Counts, Kurtosis, Skewness, and a signal segmentation algorithm. This comprehensive analysis is further enhanced by the application of both SVM and NN to estimate and classify machine conditions, thereby providing robust and reliable diagnostics for the FFF process.

Additionally, the thesis introduces the **`fff_segmenter`** script, an innovative tool designed to automate the segmentation of acoustic signals. This script uses the direction control signals of the X and Y stepper motor axes and the signal's sampling frequency, enabling accurate segmentation of contour and raster printing lines. This automation reduces errors and time consumption associated with manual segmentation methods.

By presenting detailed development and usage instructions for the **`fff_segmenter`** script, this research offers a scalable framework applicable to various shapes and printing pa-

rameters, specifically tailored for cartesian RepRap-based FFF printers. Through these advancements, the thesis aims to significantly improve the monitoring, control, and diagnostic capabilities within the FFF process, thereby directly benefiting the clients in the additive manufacturing industry.

1.3 PUBLICATIONS

The following are the works developed at the Laboratory of Data Acquisition and Signal Processing (LADAPS) of the São Paulo State University (UNESP) – Bauru, which the author of this thesis published during his PhD period, and which are directly related to the monitoring of the Fused Filament Fabrication process, the central theme of this thesis.

- AGUIAR, PAULO ROBERTO.; **LOPES, THIAGO GLISSOI**.; D'ADDONA, DORIANA MARILENA.; OLIVEIRA JUNIOR, REINALDO GÖTZ.; FRANÇA, THIAGO VALLE. A Study on Acoustic Signals from an Electret Microphone in 3D Printing. Procedia CIRP, v. 126, p. 651–655, 2024. doi: 10.1016/j.procir.2024.08.282. [69]
- **LOPES, THIAGO GLISSOI**.; MONSON, PAULO MONTEIRO DE CARVALHO.; AGUIAR, PAULO ROBERTO.; OLIVEIRA JUNIOR, REINALDO GÖTZ.; CONCEIÇÃO JÚNIOR, PEDRO DE OLIVEIRA. "fff_segmenter: A signal segmentation script for acoustic FFF fabrication data in MATLAB," Journal of Open Source Software, vol. 9, no. 99, p. 6620, Jul. 2024, doi: 10.21105/joss.06620. [70]
- **GLISSOI LOPES, THIAGO**.; MONSON, PAULO MONTEIRO DE CARVALHO.; AGUIAR, PAULO ROBERTO.; OLIVEIRA JUNIOR, REINALDO GÖTZ.; CONCEIÇÃO JÚNIOR, PEDRO DE OLIVEIRA. "fff_segmenter: A signal segmentation script for acoustic FFF fabrication data in MATLAB.", Version v3.0.1, Zenodo, Online, Jul. 12, 2024. doi: 10.5281/zenodo.12733091. [71]
- **LOPES, THIAGO GLISSOI**.; KENNERLY, VICTORIA DUTRA.; AGUIAR, PAULO ROBERTO.; SOARES JUNIOR, CRISTIANO.; MONSON, PAULO MONTEIRO DE CARVALHO.; D'ADDONA, DORIANA MARILENA. "Detection and Classification of Defects in 3D Printing using a Novel Skewness and Kurtosis-based Parameter of Sound Signals and Machine Learning", in 2024 International Conference on Control, Automation and Diagnosis (ICCAD), IEEE, May 2024, pp. 1–5. doi: 10.1109/ICCAD60883.2024.10553900. [18]
- **LOPES, THIAGO GLISSOI**.; AGUIAR, PAULO ROBERTO.; Impacto da variação térmica na eficiência de microfones de baixo custo para monitoramento do processo de impressão 3D. In: BEZERRA, Adriano; PINTO, Sandro da Silva; SOUZA, Vinicius Roberto Prioli de. (Org). Avanços Tecnológicos, Gestão da Qualidade e Linguagem. Editora Dialética: São Paulo, 2023. ISBN 978-65-270-1474-4. doi: 10.48021/978-65-270-1474-4. [33]
- **LOPES, THIAGO GLISSOI**.; AGUIAR, PAULO ROBERTO.; MONSON, PAULO MONTEIRO DE CARVALHO.; D'ADDONA, DORIANA MARILENA.; CONCEIÇÃO JÚNIOR, PEDRO DE OLIVEIRA.; OLIVEIRA JUNIOR, REINALDO GÖTZ. "Machine condition monitoring in FDM based on electret microphone, SVM, and neural networks", The International Journal of Advanced Manufacturing Technology, Oct. 2023, doi: 10.1007/s00170-023-12375-0. [51]

- BARBOSA, LUANNE.; **LOPES. THIAGO GLISSOI**.; AGUIAR, PAULO ROBERTO.; MONSON, PAULO MONTEIRO DE CARVALHO.; OLIVEIRA JUNIOR, REINALDO GÖTZ.; CONCEIÇÃO JÚNIOR, PEDRO DE OLIVEIRA. "Electret Microphone and Counts Statistic in Monitoring 3D Printing", in 2023 15th IEEE International Conference on Industry Applications (INDUSCON), IEEE, Nov. 2023, pp. 802–806. doi: 10.1109/INDUSCON58041.2023.10374939. [72]
- **LOPES. THIAGO GLISSOI**.; AGUIAR, PAURO ROBERTO.; FRANÇA, THIAGO VALLE.; CONCEIÇÃO JÚNIOR, PEDRO DE OLIVEIRA.; SOARES JUNIOR, CRISTIANO.; ANTONIO, ZAQUEU RICARDO FERNANDO. Time-Domain Analysis of Acoustic Emission Signals during the First Layer Manufacturing in FFF Process. Engineering Proceedings, v. 27, n. 1, p. 83, jan. 2022. [50]
- **LOPES, THIAGO GLISSOI**.; ROCHA, ISABELA MÜLLER MARTINS.; AGUIAR, PAULO ROBERTO.; FRANÇA, THIAGO VALLE. Influence of Vibroacoustic Phenomena from FFF Process on Surface Characteristics of Printed Parts. Engineering Proceedings, v. 19, n. 1, p. 44, 17 maio 2022. [73]
- BARBOSA, LUANNE.; **LOPES, THIAGO GLISSOI**.; AGUIAR, PAULO ROBERTO.; OLIVEIRA JUNIOR, REINALDO GÖTZ.; FRANÇA, THIAGO VALLE. Evaluating Temperature Influence on Low-Cost Microphone Response for 3D Printing Process Monitoring. Engineering Proceedings, v. 10, n. 1, p. 67, 1 nov. 2021. [58]

The following are the works developed in the Laboratory of Data Acquisition and Signal Processing (LADAPS) of UNESP – Bauru, in which the author of this thesis participated during his PhD period, and have themes related to the development of this work.

- RUAS, ERICK LUIZ VIEIRA.; AGUIAR, PAULO ROBERTO.; LOPES, WENDERSON NASCIMENTO.; **LOPES, THIAGO GLISSOI**.; SOARES JUNIOR, CRISTIANO. Monitoramento da Operação de Dressagem por Meio de Emissão Acústica e Índice de Dano. Procceedings of the 11th Brazilian Congress on Manufacturing Engineering. Anais...Curitiba: ABCM, 2021. [74]
- **LOPES, THIAGO GLISSOI**.; FREIRE, LEONARDO DARRI.; DA CUNHA, PEDRO AUGUSTO.; AGUIAR, PAURO ROBERTO.; FRANÇA, THIAGO VALLE. Evaluating Liquid Influence on Low-Cost Piezoelectric Transducer Response for Elastic Emission Machining Monitoring. Engineering Proceedings, v. 24, n. 1, p. 7, 21 set. 2022. [75]
- RUAS, ERICK LUIZ VIEIRA.; LOPES, WENDERSON NASCIMENTO.; AGUIAR, PAURO ROBERTO.; **LOPES, THIAGO GLISSOI**.; JUNIOR, PEDRO OLIVEIRA CONCEIÇÃO. Monitoring the dressing operation of conventional aluminum oxide grinding wheels through damage index, power spectral density, and piezoelectric sensors. The International Journal of Advanced Manufacturing Technology. https://doi.org/10.1007/s00170-023-11682-w [76]

The following are the works developed in which the author of this thesis participated during his PhD period and have themes related to the development of this work, however, which were developed outside the Laboratory of Data Acquisition and Signal Processing (LADAPS) of UNESP – Bauru.

- **LOPES, THIAGO GLISSOI**.; OLIVEIRA CANDIDO, ADRIEL SENNA DE.; PUZIPE, IGOR BAZAN GIMENES. "A MANUFATURA ADITIVA EM PROJETOS

DE PESQUISA - PROGRESSO E DESENVOLVIMENTOS NOS ÚLTIMOS CINCO ANOS", in Avanços Tecnológicos, Gestão da Qualidade e Linguagem, Dialética., vol. 1, A. Bezerra, S. da S. Pinto, and V. R. P. de Souza, Eds., Dialética, 2024, pp. 147–171. Accessed: Apr. 02, 2024. [Online]. Available https://www.researchgate.net/publication/376713793_A_Manufatura_Aditiva_em_Projetos_de_Pesquisa_-_Progresso_e_Desenvolvimentos_nos_Ultimos_Cinco_Anos [3]

- **LOPES, THIAGO GLISSOI**. "O PROCESSO DE MANUFATURA ADITIVA POR IMPRESSÃO 3D COMO INSTRUMENTO EDUCACIONAL ATIVO", in Avanços Tecnológicos, Gestão da Qualidade e Linguagem, Dialética., vol. 1, A. Bezerra, S. da S. Pinto, and V. R. P. de Souza, Eds., Dialética, 2024, pp. 173–204. Accessed: Apr. 02, 2024. [Online]. Available: https://www.researchgate.net/publication/376713862_O_Processo_de_Manufatura_Aditiva_por_Impressao_3D_como_Instrumento_Educacional_Ativo [31]
- BORTOLI, ADRIANA DE.; BEZERRA, ADRIANO.; OLIVEIRA CANDIDO, ADRIEL SENNA DE.; SAVIAN DA SILVA, ALISON RIAN.; OLIVEIRA, ALEXANDRE PONCE DE.; STROPPA, ANDRÉ FELIPE DOMINGUES.; SANTOS, ANDRÉ RICARDO PONCE DOS.; PAZIN, ANDERSON.; CAVINA JUNIOR, ARIOVALDO APARECIDO.; FERNANDEZ, BRENO ORTEGA.; SANTOS MAIETTO, CRISTIANE ALINE.; MANFIO, EDIO ROBERTO.; SILVA, HAYSSA BARBOSA DA.; SANTOS, HENRIQUE FERNANDES.; PUZIPE, IGOR BAZAN GIMENES.; SANTOS JUNIOR, JAIRO GERALDO DOS.; DOURADO, JULIEL BRONZATI.; SOUZA, LUCIANO SOARES DE.; NITTA, MARIANA CARVALHO CHIECCO.; PARDO, MARIO HENRIQUE DE SOUZA.; AGUIAR, PAULO ROBERTO DE.; ANTUNES, PEDRO HENRIQUE FERNANDES.; NOCCHI, REINALDO DE OLIVEIRA.; BUCHALA, ROGÉRIO.; PINTO, SANDRO DA SILVA.; **LOPES, THIAGO GLISSOI**.; VALENTE, VÂNIA CRISTINA PIRES NOGUEIRA.; SOUZA, VINICIUS ROBERTO PRIOLI DE.; RODRIGUES, ZIONICE GARBELINE MARTOS.; LOPES, WENDERSON NASCIMENTO. Avanços Tecnológicos, Gestão da Qualidade e Linguagem, Dialética., vol. 1. Dialética, 2024. doi: 10.48021/978-65-270-1474-4. [77]
- PEREIRA, DANIEL.; ANDREOTI, ELIANE.; MARIN, GUSTAVO SCHIAVON.; GUILHERME, LUIS.; **LOPES, THIAGO GLISSOI**. A impressão 3D como ferramenta na obtenção de peças para projeto de cidade inteligente, in VI Congresso de Inovação e Tecnologia | VIII Workshop de Iniciação Científica e Tecnológica, Lins: Fatec Lins, Nov. 2023. [37]
- DAMASCENO, ANA BEATRIZ.; PANEQUE, TALITA NAKASHIMA.; TELES, VANILDA CATUABA FERREIRA.; MORAES, MARCO ANTÔNIO AVÁ TATAENDY FOGAÇA.; **LOPES, THIAGO GLISSOI**. O Efeito do Parâmetro Densidade de Preenchimento na Obtenção de Peças pelo Processo FFF. V Congresso de Inovação e Tecnologia | VII Workshop de Iniciação Científica e Tecnológica. Anais...Lins: Fatec Lins, nov. 2022. [32]
- TELES, VANILDA CATUABA FERREIRA.; DAMASCENO, ANA BEATRIZ.; PANEQUE, TALITA NAKASHIMA.; MORAES, MARCO ANTÔNIO AVÁ TATAENDY FOGAÇA.; **LOPES, THIAGO GLISSOI**. O efeito do Posicionamento do

Modelo Tridimensional para o Fatiamento na Obtenção de Peças pelo Processo FFF. V Congresso de Inovação e Tecnologia | VII Workshop de Iniciação Científica e Tecnológica. Anais...Lins: Fatec Lins, nov. 2022. [78]

The following are the works developed in which the author of this thesis participated during his PhD period, which were developed outside the Laboratory of Data Acquisition and Signal Processing (LADAPS) of UNESP – Bauru and have themes not directly related to the development of this work.

- MORAES, MARCO ANTÔNIO AVÁ TATAENDY FOGAÇA.; DAMASCENO, ANA BEATRIZ.; PANEQUE, TALITA NAKASHIMA.; TELES, VANILDA CATUABA FERREIRA.; **LOPES, THIAGO GLISSOI**. "UM ESTUDO DE CASO COMPARATIVO ENTRE VEÍCULOS A COMBUSTÍVEL FOSSIL E ELÉTRICOS NA CIDADE DE LINS-SP," in V Congresso de Inovação e Tecnologia | VII Workshop de Iniciação Científica e Tecnológica, Lins: FATEC Lins, Nov. 2022. Accessed: Jul. 17, 2024. [Online]. Available: https://www.researchgate.net/publication/365791866_UM_ESTUDO_DE_CASO_COMPARATIVO_ENTRE_VEICULOS_A_COMBUSTIVEL_FOSSIL_E_ELETRICOS_NA_CIDADE_DE_LINS-SP [79]

2 – LITERATURE REVIEW

This chapter reviews literature related to the present thesis, focusing on the monitoring of AM machine conditions and the application of acoustic signals in FFF 3D printing. It discusses various methods and techniques used for *in-situ* monitoring, particularly through Non-Destructive (ND) analysis, AE, and digital signal processing. The chapter highlights studies that utilize machine learning and artificial intelligence to diagnose machine failures and anomalies during the AM process. Additionally, it surveys the use of electret microphones in process monitoring and the methods of signal segmentation, offering a comprehensive overview of advancements in monitoring and diagnosing conditions in the FFF process. Finally, the chapter surveys the latest advancements in knowledge related to these themes, as identified in the literature review.

2.1 MONITORING OF AM MACHINE CONDITIONS

The monitoring of AM processes has been the focus of numerous academic studies. One such study, conducted by Hirsch *et al.* (2017) [80], evaluated the *in-situ* non-destructive analysis capability of two laser-based AM processes. Mattera (2024) [81] investigated the application of frequency domain analysis for defect monitoring in the Wire Arc Additive Manufacturing (WAAM) process, highlighting the importance of timely anomaly detection to reduce waste and ensure high-quality components. Furthermore, a time-frequency domain feature extraction approach, enhanced by computer vision, was utilized by G. Mattera *et al.* (2024) [82] for monitoring WAAM using Fourier and Wavelet transforms. This technique allowed for a more precise analysis of welding signals, contributing to the effective detection of defects such as arc instability and porosity.

In another study, Yuan *et al.* (2018) [83] investigated the monitoring of the Laser Powder Bed Fusion (LPBF) AM process using machine learning techniques applied to visual data acquired *in-situ*. The integration of Machine Learning (ML) and Artificial Intelligence (AI) in AM has also shown promising results. G. Mattera *et al.* (2024) [84], [85] developed an optimal data-driven control approach using reinforcement learning for the control of AM processes. This methodology not only improved process performance but also reduced defect occurrence, optimizing the production of high-quality components.

The detection of anomalies in WAAM parts via surface tension transfer through unsupervised machine learning techniques was explored by G. Mattera *et al.* (2023) [86]. This research demonstrated how advanced machine learning techniques could be applied to identify and mitigate defects during the manufacturing process, ensuring the integrity and quality of the produced parts. Additionally, Wang *et al.* (2020) [87] provided a comprehensive review of the application of machine learning techniques in the monitoring of AM processes.

AM has been a key technology for enhancing sustainability in metal fabrication. One study investigated how switching from a Gaussian laser profile to a ring laser profile can increase the productivity of the LPBF AM process of nickel alloy 718, reducing energy consumption without compromising mechanical properties [88].

Another study took an integrated approach to analyze energy consumption in the manufacturing and surface finishing of 3D-printed Inconel 718 parts, highlighting the importance of energy efficiency in AM processes [89]. Additionally, a review on laser polishing of AM

produced metal parts discussed various techniques to improve surface quality and reduce energy consumption, contributing to the sustainability of the processes [90].

The feasibility of utilizing acoustic signatures for monitoring AM processes was explored in the study by Koester *et al.* (2018) [91]. AE was also employed in the research by Strantza *et al.* (2017) [92], which aimed to detect cracks during the AM process. The integration of AI techniques with the processing of AE data collected during AM process monitoring was the focus of the work by Wasmer *et al.* (2017) [93].

In-situ monitoring during Fused Filament Fabrication (FFF) processes can also be achieved through the digital processing of data indirectly acquired from sensors. For instance, Tlegenov *et al.* (2018) [45] investigated the monitoring of the FFF process by processing vibration data acquired from the extruder. Similarly, Kim *et al.* (2018) [66] used acceleration data obtained from the extruder during FFF manufacturing. The study by Baumann *et al.* (2016) [94] focused on an approach employing various sensors to monitor the FFF process. In the research conducted by Bhavsar *et al.* (2020) [48], the fabrication of the first layer in the FFF process was monitored using vibro-acoustic data obtained from a Piezoelectric Polyvinylidene DiFluoride (PVDF) sensor.

Regarding extruder-focused monitoring, Greeff and Schilling (2017) [95] examined filament flow control. Another study by Heller *et al.* (2016) [96] aimed to investigate filament flow in the FFF process using the finite element method. The effects of extrusion rates on temperature profiles and extrusion forces were observed in ABS filament printed parts in the study by Luo *et al.* (2020) [97].

The identification and classification of anomalies in AM processes can be performed at two stages. Initially, through the combined use of indirect process monitoring and the digital processing of *in-situ* data, as demonstrated by Wu *et al.* (2016) [49] in their study of the FFF process and by Wasmer *et al.* (2017) [93] in their research on the Selective Laser Melting (SLM) AM process. Subsequently, upon the completion of manufacturing, the properties of the produced objects can be analyzed. This approach was taken by Dizon *et al.* (2018) [98] in their study of properties obtained from different AM techniques, by Torrado *et al.* (2015) [99] in their investigation of mechanical properties with additives in ABS filament used in the FFF process, and by Santana *et al.* (2018) [100] in a comparative study of the thermal, mechanical, and chemical properties of parts produced with PETG and PLA filament in the FFF process.

FFF has been a critical area of research due to its potential for enhancing sustainability in AM. One study investigated the influence of heated-bed material on the mechanical properties of PLA and energy consumption in the FFF process. The findings highlighted how different bed materials can significantly impact the overall energy efficiency and mechanical performance of printed parts [26].

In another study, researchers examined the role of the plate material in the sustainability of FFF. This study emphasized the importance of selecting appropriate materials for the printing plate to optimize energy usage and improve the environmental footprint of the FFF process [27].

An experimental integrated approach was used to optimize the mechanical characteristics of FFF-printed PLA, focusing on energy-saving perspectives. This study provided insights into how process parameters and material choices can be adjusted to achieve better energy efficiency while maintaining the desired mechanical properties of the printed parts [25].

The most critical period for detecting abnormalities that may indicate failures in the FFF process is during the printing of the first layer [48]. Due to the sequential nature of the FFF process, the fabrication of the initial layer holds significant importance in achieving successful 3D printing [101]. This is because the first layer provides the foundation for the object being fabricated [49]. Examples of single-layer part fabrication for the study of abnormalities can be found in the works of Carmo *et al.* (2020), Tlegenov *et al.* (2018), Lopes *et al.* (2022) and Wendt *et al.* (2017) [35], [45], [50], [102]. Furthermore, the first layer has been the subject of studies on how print parameterization affects the structural quality of the fabricated part [47], [102]. Recognizing the criticality of first layer fabrication, numerous studies have focused on monitoring the condition of the FFF machine during the construction of a monolayer part, which solely consists of the first layer [6], [18], [42], [50], [51].

The signal segmentation is a fundamental step in the process monitoring of FFF, as it allows the identification of printing lines and extraction of relevant information for process monitoring and control [51]. However, due to stochastic acoustic interferences arising from the FFF process, accurate manual segmentation may not be possible [50].

The study conducted by Wu *et al.* (2017) [63] aimed to investigate the categorization of four distinct printing states with a monolayer fabrication: State 1 as extrusion without material, State 2 as material loading/unloading, State 3 as idle, and State 4 as normal extrusion. This classification was accomplished by employing a hidden semi-Markov model, which analyzed data acquired from an acoustic signal affixed to the printer's extruder.

The authors of Tlegenov *et al.* (2018) [45] employed an accelerometer attached to a direct type and to a Bowden type extruder in order to investigate the detection of the nozzle clogging defect in the FFF process. The authors utilized spectral analysis of the vibration data acquired and compared the experimental acceleration amplitudes with theoretical values. It was determined that the proposed theoretical model, suggesting an increase in vibrations of the FFF extruder's bar mount when the nozzle becomes clogged, was confirmed through experiments using both Direct and Bowden extruder types.

In the article published by Zhu *et al.* (2022) [103], the authors sought out to investigate the monitoring of the layer detachment defect in the first layer printing period. The authors utilized two ultrasonic transducers attached to the printing table in order to analyze the energy leakage of the first layer deposition and correlate it to an occurrence of the layer detachment defect.

The work developed by Bhavsar *et al.* (2020) [48] employed a PVDF vibroacoustic sensor mounted into the printing table in order to investigate the possibility of evaluating the adhesion quality between the first layer and the printing table. To achieve this, the authors utilized a time-frequency analysis of the signals collected under the fabrication of the first layer with three adhesion qualities: Excellent as a near perfect bond, Good as a reasonable bond, and Bad as an imperfect bond.

With the goal of evaluating the influence of vibroacoustic phenomena from the FFF process on surface characteristics of printed parts, the authors of Lopes *et al.* (2022) [50] produced monolayer parts by varying the Z offset processing parameter. The authors utilized an optical profilometer to evaluate the surface roughness values and the printed line width of different regions of the part surface. As a result, the authors observed that the different movements

of the table or extruder throughout printing cause substantial variations of the surface roughness values.

2.2 ACOUSTIC SIGNALS IN FFF 3D PRINTING AND APPLICATION OF ELECTRET MICROPHONES

Acoustic Emission (AE) is defined as a phenomenon in which strain energy accumulated in a solid is released because of deformation or cracking, and thus emits or generates elastic waves, which are sonic or ultrasonic AEs [104], [105]. AE can also be defined as transient elastic waves generated in the structure by an external source, such as impacts and interaction between bodies [106].

Many works that used AE can be found in several areas of knowledge, such as in inspecting and monitoring pipelines [107], pressure vessels [108], storage tanks [109], bridges [110], aircraft [111], grinding process [56], AM [112]. However, a few works are found in machine condition monitoring of 3D printing using AE. The work of Wu *et al.* (2015) [113] presented a condition monitoring method for FFF machines based on AE sensing techniques, where time-domain features of AE hits were used to identify five different extruder operating conditions. In the work of Wu *et al.* (2017) [63], a FFF machine condition monitoring approach is proposed, where an AE sensor is used, where was possible to identify operation conditions of the machine's extruder, including both normal and abnormal states. The authors of Li *et al.* (2022) [68], a real-time monitoring of the flow state in the nozzle of FFF was proposed, where the authors claim that the method can effectively monitor the AE signal of the internal state to distinguish different extrusion shapes in real-time. Filament breakage in FFF was investigated by Yang *et al.* (2018) [114] through AE techniques. The results indicated that the instantaneous skewness could be used as a preliminary indicator for filament breakage. Finally, the work of Li *et al.* (2020) [115] aimed to identify distortion defects in FFF process and understand the condition of the distortion area through AE and digital signal processing techniques. The authors, however, reported that the accuracy of the technique for distortion monitoring needs to be further studied, as the accuracy may be influenced by the temperature and plasticity of the defect area, and the results suggest that AE is a promising technique for monitoring FFF processes.

On the other hand, since the introduction by Sessler and West (1962) and Sessler and West (1964) [59], [60], electret microphones have been widely used for various applications due to their cost-effectiveness and good performance in monitoring acoustic phenomena [116]. Examples of electret microphone applications include their use in medical applications, as demonstrated by Kraman *et al.* (1995) [117], which employed the microphone for respiratory system evaluation, and the work by Souza *et al.* (2020) [118], where the electret microphone was utilized to capture AEs for chemical composition evaluation using a portable spectrometer.

Among the applications for the electret microphone, literature review reveals various studies utilizing it for process monitoring. The electret microphone is employed in photoacoustic spectroscopy for detecting acoustic waves with the aim of identifying traces of vestigial gases [119], [120]. Another application is found in the monitoring of pharmaceutical tablet breakage during pneumatic transport, achieved through the capture of acoustic waves by the electret microphone [121]. The capture of acoustic waves by the electret microphone is also used to monitor the flow regime in upward inclined pneumatic transport [122] and horizontal

pneumatic transport [123]. The electret microphone was additionally employed to facilitate the evaluation of the response time of a thermal flow sensor [124].

Examples of the application of the electret microphone in studies aiming at the detection of anomalies in processes are also found in the literature. One such example is the work by Albion *et al.* (2009) [125], where the electret microphone was used to capture acoustic waves in the hydro transport process of materials, aiming to detect anomalies such as the transport of materials larger than planned. The optimal positioning of the electret microphone for anomaly detection was studied in the work by Albion *et al.* (2009) [126], where the capture of acoustic waves generated by the hydro transport of large solids enabled the modeling of the best position along the transport duct for the electret microphone.

Literature review also indicates the use of electret microphones for monitoring manufacturing processes. An example is found in the work by Briens *et al.* (2008) [127], which utilized an electret microphone to capture AEs in the rotary drying process. Another application of the electret microphone in monitoring manufacturing processes involving rotational machinery is presented in the study by Iyer *et al.* (2014) [128], where the microphone was used for bearing wear evaluation. The phenomenon of torque ripple, commonly observed in manufacturing processes that employ permanent magnet synchronous motors, was investigated by capturing acoustic waves using an electret microphone in the work by Hill *et al.* (2017) [129]. The monitoring of cutting tool wear in a horizontal sawing process was conducted using an electret microphone in the study by Nguyen *et al.* (2018) [130].

In regard to the FFF process monitoring, the literature review shows that there are a few studies that employed the electret microphone. In one of such studies, Barbosa *et al.* (2021) [58] sought out to investigate the influence of the table temperature of the FFF process in the response of an electret microphone. As a result, the authors found that the table temperature have major influence on the electret microphone response, affecting significant variation in the collected signals. In another of such studies, the authors of [131] employed an electret microphone to corroborate the findings of the clogging defect detection which had previously been documented and scrutinized in their article, using data from a smartphone microphone. They successfully confirmed the initial clogging detection results with the electret microphone through the printing of two different parts.

It is worth mentioning that AE signal collected from AE sensor and audio signal collected from microphone can be considered similar signals, as they are a result of elastic waves that travel through a medium. However, acoustic testing is the measurement of sound, noise and vibration, and generally it implies in frequencies inside the audio band of 20Hz to 20kHz, whereas AE testing is conducted above the audio band of 20kHz [132]. Elastic or acoustic waves are mechanical disturbances that reproduce in an elastic medium [133]. A partial case of acoustic waves is a sound, which is audible to man; thus, the term “acoustics” was given to this phenomenon. In the widest sense, acoustics involves the study of elastic waves, and in the narrowest, it is often used to define their sound range only.

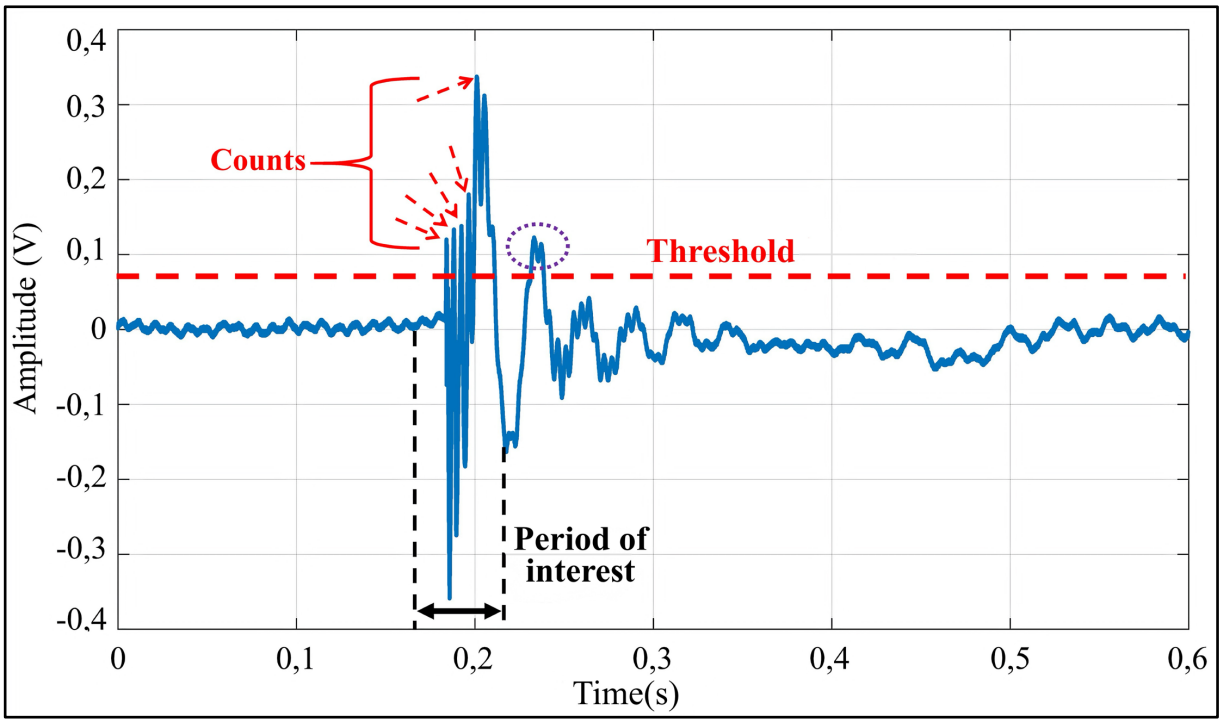
2.3 SIGNAL ANALYSIS STATISTICS IN THE TIME-DOMAIN AND FREQUENCY-DOMAIN AND THEIR USE IN STUDIES REGARDING THE MONITORING OF MANUFACTURING PROCESSES

2.3.1 COUNTS

One of the statistics that can be used for processing signals in regard to monitoring process in the time-domain is Counts, a statistic that measures the number of times a signal crosses a pre-determined amplitude threshold in a likewise pre-determined window of time [134]. This method was used by Alexandre *et al.* (2019) [57] for these types of signals, and the authors were able to show the efficacy of this method. Similar results were also reported by Lopes *et al.* (2017) [134]. Both of these studies used a band filter chosen from the power spectrum density (PSD) of each collected signal, obtained by the Welch method.

A representation of the Counts statistic can be observed in Figure 2.1. In the Counts statistic, a threshold is determined, and the number of times that this threshold is surpassed is added while in a specific period of interest.

Figure 2.1 - Counts statistic representation on a raw signal acquired from a Pencil Lead Break test, whereas a threshold is visible, and the counts number is observed in a specific period of interest



Counts has been applied in various studies, including the analysis of material removal in grinding processes [57], fault detection in the FDM process [135], and assessing the condition of the tool used in dressing processes [136]. It is important to note that, if a period of interest is defined for studying the signal, other points outside this period will not be considered when calculating the statistic. This is demonstrated in the purple circular region visible in Figure 2.10, which contains points that meet the criteria for the Counts statistic but are located outside the period of interest. As such, these Counts would not be included in the analysis, as the period of interest is delineated by dotted lines in Figure 2.10.

2.3.2 ROOT MEAN SQUARE (RMS)

Another statistic that can be used for processing signals in regard to monitoring process in the time-domain is the RMS. The RMS of a given signal can be utilized to study various phenomena. Analysis using the RMS of a signal filtered within a specific frequency band enabled an indirect assessment of the amount of material removed in a grinding process conducted at different cutting depths [57]. The application of various statistics in processing signals from grinding has demonstrated that RMS can be useful for monitoring and detecting burning in ABNT 1045 steel parts [137]. RMS was also applied in digital signal processing to validate the use of a PZT sensor for estimating the load in a three-phase induction motor (TIM) [138]. For determining different grooving modes in ceramic parts through indirect monitoring with signal processing statistics, RMS, along with Counts and other measures, has proven effective [139].

The RMS of a signal at any given time "t" can be expressed as per Equation 2.1:

$$x_{rms} = \sqrt{\frac{1}{N} \times \sum_{i=1}^{N} x^2(i)} \tag{2.1}$$

where x is the raw signal, and N represents the number of discrete samples (ii) considered in the calculation [57].

Using the RMS technique in time-domain analyses requires defining parameters like the integration time (Ti), which may vary according to the process under study [140], [141], [142]. An in-depth study on the Ti suitable for RMS calculation of signals from grinding processes showed that a 1 ms Ti is ideal for both internal and external grinding, as a longer Ti would compromise important signal characteristics for analysis [140].

The 1 ms Ti found to be optimal for RMS calculations of EA signals from grinding has also been widely used in monitoring grinding processes by calculating RMS in signals from PZT sensors [56], [57], [143]. For signals acquired by EA sensors during metal-cutting, Ti values above 0.1 ms were found unsuitable for analyses based on "bursts" of acoustic emission [141]. Another study identified a 10 ms Ti as short enough to permit analysis in the centerless grinding process [142].

In high-speed machining of 7050-T7451 aluminum alloy and Inconel 718 superalloy, the RMS statistic helped explore the relationship between EA sensor signals, chip formation, and cutting energy consumption, with a time constant of 12 ms justified by hardware limitations in the RMS converter used [144]. When monitoring the surface produced by a polishing robot, a 500 ms time constant was used, as a relative change in EA signal energy over time was sufficient to detect the polishing process endpoint, and minor data loss was not critical [145].

Similarly, RMS was employed to monitor laser rust removal using EA sensor signals, with a 500 ms Ti considered adequate [146].

For monitoring the FDM process, some studies have used Counts and RMS as input data in analyses aimed at detecting and classifying anomalies and failures. The RMS calculated from signals obtained by EA and vibration sensors during the FDM process was employed as input data for a machine learning algorithm designed to detect faults [66]. RMS was also used alongside Counts as two of the input data in a study where the CFSFDP clustering method enabled the detection and classification of different failure modes in the FDM process [135]. To identify and categorize various failure modes in the FDM process, Counts and RMS were

similarly employed as input data for a K-Means clustering algorithm [49]. The detection and classification of different failure modes in the FDM process was also the focus of a study where RMS and Counts were applied as input data in a hidden semi-Markov model (HSMM) [63].

2.3.3 RATIO OF POWER (ROP)

A statistic often used in the study of signals in the frequency domain is the power ratio (ROP) [147]. ROP is described by Martins *et al.* (2014) [148] and used by Alexandre *et al.* (2017) [149] according to Equation 2.2:

$$ROP = \frac{\sum_{k=n1}^{n2} |X_k|^2}{\sum_{k=0}^{N-1} |X_k|^2} \tag{2.2}$$

where N is the block size of the sampled signal during the process under analysis, $n1$ and $n2$ represent the frequency band to be analyzed, and $\mathbf{X_k}$ is the k_{th} DFT output.

ROP was employed in a study focused on monitoring for chatter detection in the grinding process of SAE 1045 steel parts [149]. Another study applied ROP in comparison with other time-domain and frequency-domain statistics to determine the most suitable metric for burn detection in grinding process monitoring [147]. Similarly, ROP was used in a comparative study to assess the most appropriate statistic for burn detection in the grinding process [154].

The ROP was found to be more effective in detecting burn in surface grinding machining than other statistics, such as the RMS [137]. In regarding to the dressing process, the ROP was used as input for a Multilayer perceptron (MLP) Neural Network (NN) in order to verify the classification ability of such a NN trained with ROP inputted data [150].

In regard to the FDM process, an example on the use of ROP is found in the work developed by Lopes (2021) [6]. In this study, an analysis in regard to the frequency content of FDM process signals were conducted, and the ROP evaluated from a frequency band of PZT signals was found to be related to the occurrence of different failures in monolayer printed parts.

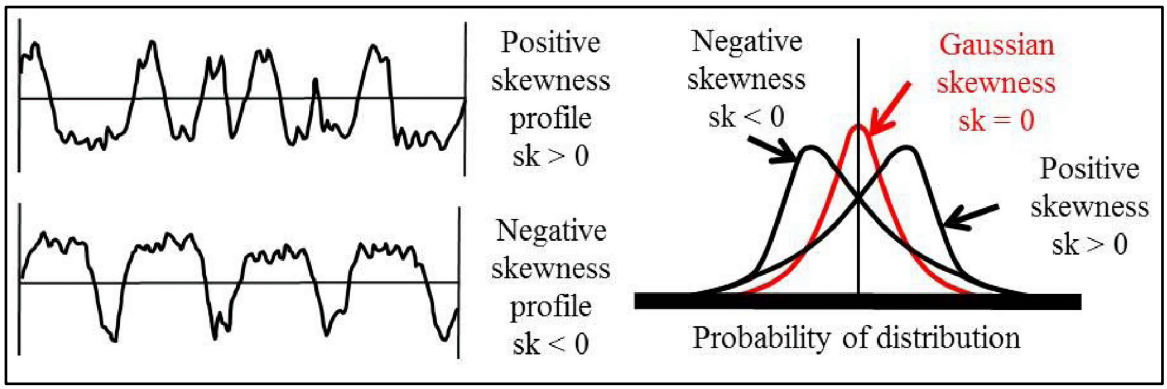
2.3.4 SKEWNESS

The skewness metric indicates the degree of asymmetry of a distribution. It can be applied to a signal, by analyzing the skewness profile along a period, as represented in Figure 2.2. A positive skewness suggests a distribution with a longer or fatter tail on the right side, while a negative skewness indicates a longer or fatter tail on the left side. Skewness near zero implies a symmetrical distribution [151]. The skewness is expressed as shown in Equation 2.3. [152].

$$Skewness = \frac{\frac{1}{N} * \sum_{k=1}^{N} (y_k - \bar{y})^3}{[\frac{1}{N} * \sum_{k=1}^{N} (y_k - \bar{y})^2]^{\frac{3}{2}}} \tag{2.3}$$

where N is the number of observations, y_k represents each observation, $\bar{y}$ is the mean, the numerator captures the asymmetry of the data through the third moment of the mean, and the denominator standardizes this asymmetry by the variance raised to the power of $\frac{3}{2}$.

Figure 2.2 - Graphical representation of the Positive and Negative Skewness profiles



Source: Adaptated from Talibouya Ba *et al.* (2021) [151]

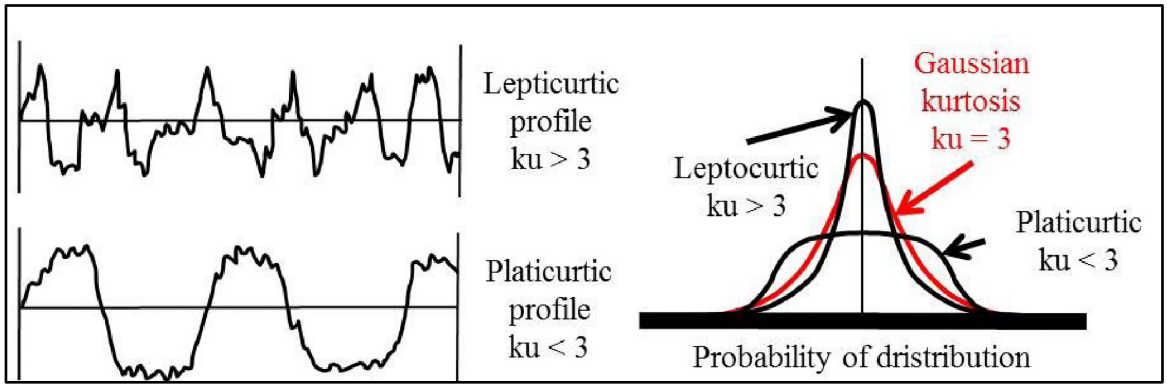
The use of skewness and kurtosis can be found in the works of [152], [153], [154], [155]. The Skewness was one of the time-domain features employed in the study by Mattera *et al.* (2024) [156], regarding the anomaly detection in WAAM. Another example in the use of the Skewness in WAAM is found in the work developed by Mattera *et al.* (2024) [157], where the skewness, alongside other statistical features, was extracted from the signals in order to be used as input for isolation forest algorithm.

In regard to the FDM process, an example on the use of a parameter derived from Skewness and Kurtosis can be found in the work developed by Lopes *et al.* (2024) [18]. In this work, the novel parameter was used to detect and classify different types of defects in 3D printing.

2.3.5 KURTOSIS

Kurtosis is the fourth-order standardized moment of a given signal, providing a measure of the significant peaks within that signal [158]. For signals containing Gaussian noise, the kurtosis value is approximately three, while signals with more pronounced and sharper peaks yield a higher kurtosis value [155]. The kurtosis is expressed as shown in Equation 2.4. [155].

Figure 2.3 - Graphical representation of the Lepticurtic and Platicurtic Kurtosis profiles



Source: Adaptated from Talibouya Ba *et al.* (2021) [151]

$$Kurtosis = \frac{N*\sum_{k=1}^{N}(y_k-\bar{y})^4}{[\sum_{k=1}^{N}(y_k-\bar{y})^2]^2} \quad (2.4)$$

where N is the number of observations, y_k represents each observation, $\bar{y}$ is the mean the numerator captures the peak and tail extremity through the fourth moment of the mean, and the denominator standardizes this by the square of the variance, highlighting the distribution's concentration around the mean.

The use of skewness and kurtosis can be found in the works of [152], [153], [154], [155]. The Kurtosis was found to be more effective in detecting burn in surface grinding machining than other statistics, such as the RMS [137]. The Kurtosis was another one of the time domain features employed in the study by Mattera *et al.* (2024) [156], regarding the anomaly detection in WAAM. Another example in the use of the Kurtosis in WAAM is found in the work developed by Mattera *et al.* (2024) [157], where the Kurtosis, alongside other statistical features, was extracted from the signals in order to be used as input for isolation forest algorithm.

As previously mentioned, in regard to the FDM process, an example on the use of a parameter derived from Skewness and Kurtosis can be found in the work developed by Lopes *et al.* (2024) [18].

2.4 KNOWLEDGE FRONTIER AND OUR PRIMARY CONTRIBUTIONS

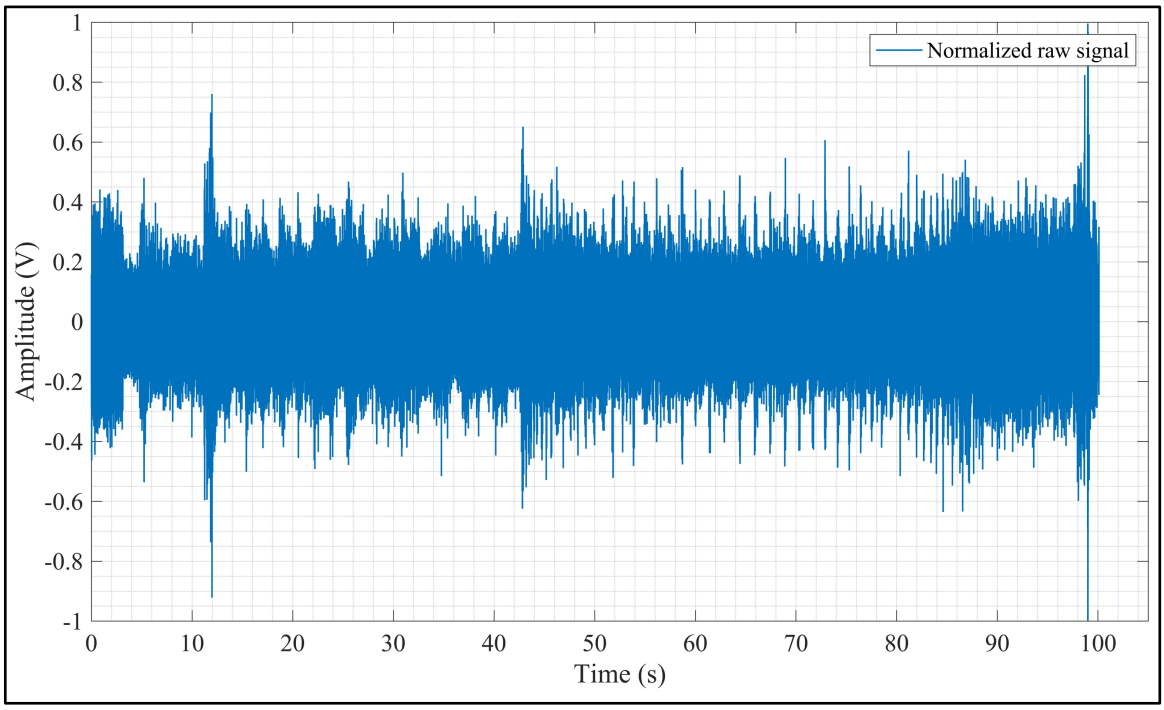
The literature review demonstrates significant developments in monitoring the FFF process through the use of sensors coupled with signal processing techniques and computational intelligence tools to diagnose machine failure conditions. For instance, Wu *et al.* (2015) [113] investigated diagnosing various machine conditions using SVM on data collected by an AE sensor attached to the extruder, employing signal processing and feature extraction techniques in both time and time-frequency domains. Another study by Wu *et al.* (2017) [63] applied similar techniques, using an AE sensor and computational intelligence tools. Both studies utilized traditional AE sensors, which are more expensive than alternative transducers like those explored in Lambos *et al.* (2020) [131]. The latter study used a smartphone microphone and validated results with an electret microphone but limited its analysis to the periodicity of vibration knocks, successfully identifying frequency values associated with clogging using Goertzel's algorithm. However, it did not incorporate computational intelligence.

A noticeable gap in the literature is the absence of studies integrating both SVM and Neural Networks with comprehensive signal processing and feature extraction for evaluating FFF printing conditions. The present thesis aims to bridge this gap by employing a multifaceted approach. We monitor the FFF process with an electret microphone attached to the extruder, coupled with extensive signal processing and feature extraction analysis (including raw data, spectra, RMS, ROP, Counts, kurtosis, skewness, and a signal segmentation algorithm).

Additionally, we examine the application of both SVM and Neural Networks in estimating and classifying machine conditions, delving into the characterization of the printing process through spectral analysis of the collected data. This synthesis of techniques and analysis represents a significant advancement in the field, offering comprehensive insights and tools for effectively monitoring and diagnosing conditions in the FFF process.

Current research on the FFF process often relies on manual methods to segment raw acoustic signals such as evaluating printing time through video recordings or manually selecting printing lines based on amplitude variations. These manual segmentation methods are time-consuming and prone to errors due to human mistakes [6], [50], [51], given that the raw signal for a monolayer workpiece fabrication, such as the one represented in Figure 2.4, does not display sufficient characteristics for each element of fabrication. The present thesis aims to bridge this gap by elaborating on the **`fff_segmenter`** script. This script automates the segmentation of printing lines in an acoustic signal using the direction control signals of the X and Y step motor axes and the signal's sampling frequency. This automation allows for accurate segmentation of contour and raster printing lines, enabling the extraction of relevant information for process monitoring and control. Unlike manual methods, **`fff_segmenter`** is fully automatic and less prone to human error. Operators only need to input the acoustic signal, direction control signals, and sampling frequency, receiving the start and end points in the number of samples for each printing line along with other relevant process information.

Figure 2.4 - Normalized raw signal acquired from a sensor attached to the printer table during a monolayer workpiece FDM fabrication



The segmentation results from **`fff_segmenter`** can be presented graphically for quick visual inspection and are autosaved in predefined data formats for easy import into other MATLAB/Octave analyses. Developed for cartesian RepRap-based FFF printers, which are commonly used in research [6], [35], [113], [135], the segmentation scripts focus on rectangular-shaped monolayer parts, sliced to G-code using standard parameters. The present thesis provides a detailed explanation of the various subfunctions of the **`fff_segmenter`** script, addressing the particularities of these printers and parts while offering a scalable framework for segmenting various shapes and parameters.

The present thesis not only elaborates into the **`fff_segmenter`** script but also demonstrates its development and usage. By integrating these advanced monitoring techniques

and automated segmentation scripts, our primary contributions lie in bridging the knowledge gap through a multifaceted approach. This work methodology involves monitoring the FFF process with an electret microphone attached to the extruder, coupled with extensive signal processing and feature extraction analysis, and applying both SVM and Neural Networks to estimate and classify machine conditions. This comprehensive approach provides significant advancements in effectively monitoring and diagnosing conditions in the FFF process, ensuring accurate segmentation and detailed characterization of the printing process.

- Integration of SVM and Neural Networks with extensive signal processing and feature extraction to evaluate FFF printing conditions using an electret microphone.
- Elaboration on the **`fff_segmenter`** script for fully automated, accurate segmentation of acoustic signals, reducing human error and time consumption.
- Detailed development and usage of the **`fff_segmenter`** script for cartesian RepRap-based FFF printers, offering a scalable framework for various shapes and printing parameters.
- Application of both SVM and Neural Networks to enhance the accuracy and reliability of machine condition classification and estimation in the FFF process.

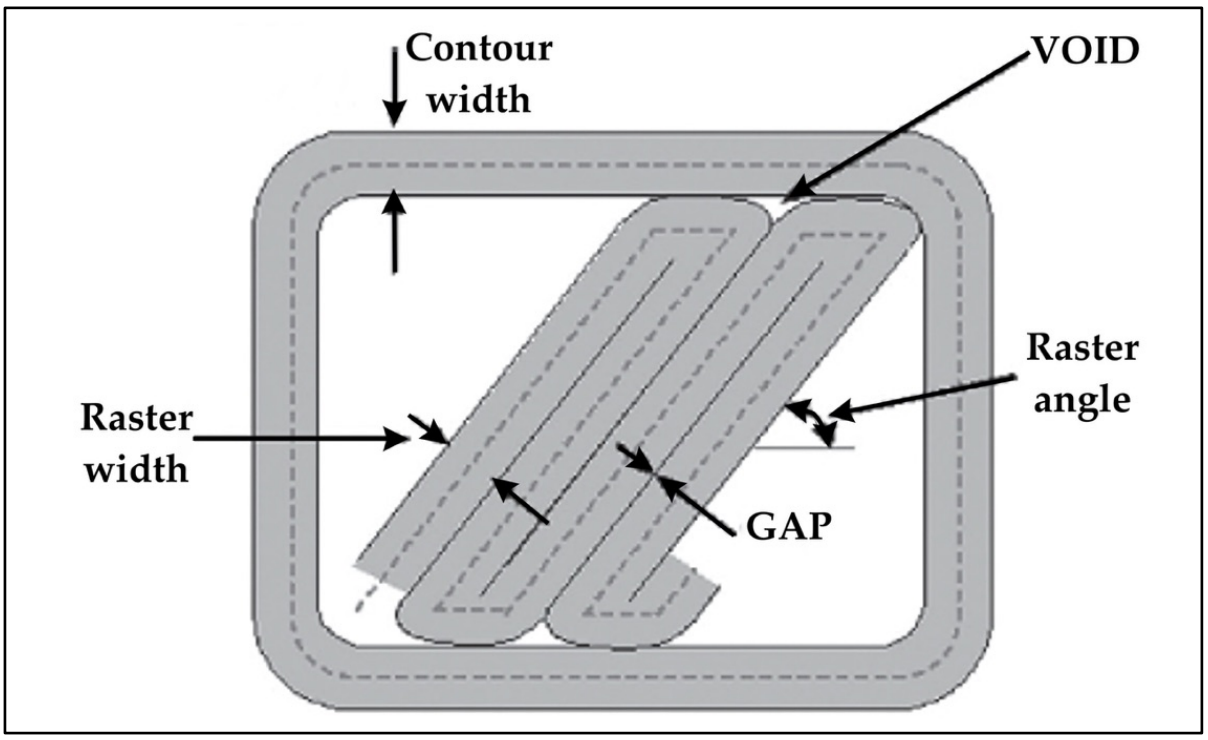
3 – MATERIAL AND METHODS

In this section, the material and methods regarding the development of the **`fff_segmenter`** segmentation script will be presented with extensive details. Furthermore, the material and methods regarding the study about monitoring FFF machine conditions with electret microphones, SVM and neural networks will also be presented.

3.1 STUDY A: MATERIAL AND METHODS REGARDING THE DEVELOPMENT OF THE `FFF_SEGMENTER` SEGMENTATION SCRIPT

The **`fff_segmenter`** script was developed following Free and Open-Source (FOSS) and Open-Source Definition (OSD) guidelines and was made publicly available on GitHub as part of the FFF-Line-Segmentation repository with an Open-Source Initiative (OSI) approved Massachusetts Institute of Technology (MIT) license. This was done in order to allow for the FOSS community to have a framework application that was able to segment an acoustic signal obtained from a first layer FFF 3D print into multiple acoustic blocks related to specific geometrical elements of the printed part, such as contour lines, raster lines, and transition between raster lines, as represented in Figure 3.1, for a specific workpiece geometry and 3D printer model, and to allow for further tracked development to cater to different workpieces geometries and 3D printer models.

Figure 3.1 – Geometrical elements of a FFF printed layer, with representation of the contour width, raster width and angle, the GAP between raster lines, and the VOID between raster and contour type infills.



Source: Altered from Volpato (2017) [8]

In order to adhere to the FOSS and OSD guidelines, the FFF-Line-Segmentation repository was populated with the necessary files for the **`fff_segmenter`** script. These include

instruction on how to use the **`fff_segmenter`** script for both MATLAB and Octave platforms, as well as the necessary signals in .mat format.

The present section will delve into the experimental setup, with explanations in regard to the acquirement of the necessary signals and about accessing and using the **`fff_segmenter`** script. The development of the **`fff_segmenter`** alongside the segmentation results will be discussed in the section 4.1 of the present thesis.

The first version of the **`fff_segmenter`** script was submitted for publication on The Journal of Open Source Software (JOSS) on 05 September 2023. Given the review methodology of The JOSS, the reviewers released public "issues" on the FFF-Line-Segmentation repository, in regard to necessary amendments to the main **`fff_segmenter`** script and other alterations to the FFF-Line-Segmentation repository files. The information displayed on the present section, alongside the information present on section 4.1 of the present thesis are in regard to the version of the **`fff_segmenter`** script published on JOSS on 12 July 2024 [70], and archived in Zenodo on the same date [71]. However, it is important to mention that part of the information displayed in the present thesis is novel and complements what are already available in the Zenodo archive [71].

In order to be usable, the **`fff_segmenter`** requires that three signals, collected synchronously and at the same Frequency of sampling (`Fs`) in the FFF 3D printing of a monolayer workpiece, are provided. The signals are:

1. Sensor signal – A signal collected from a sensor on a specified position of the 3D printer;
2. DirX – The direction control signal for the 3D printer X-axis stepper motors;
3. DirY – The direction control signal for the 3D printer Y-axis stepper motors;

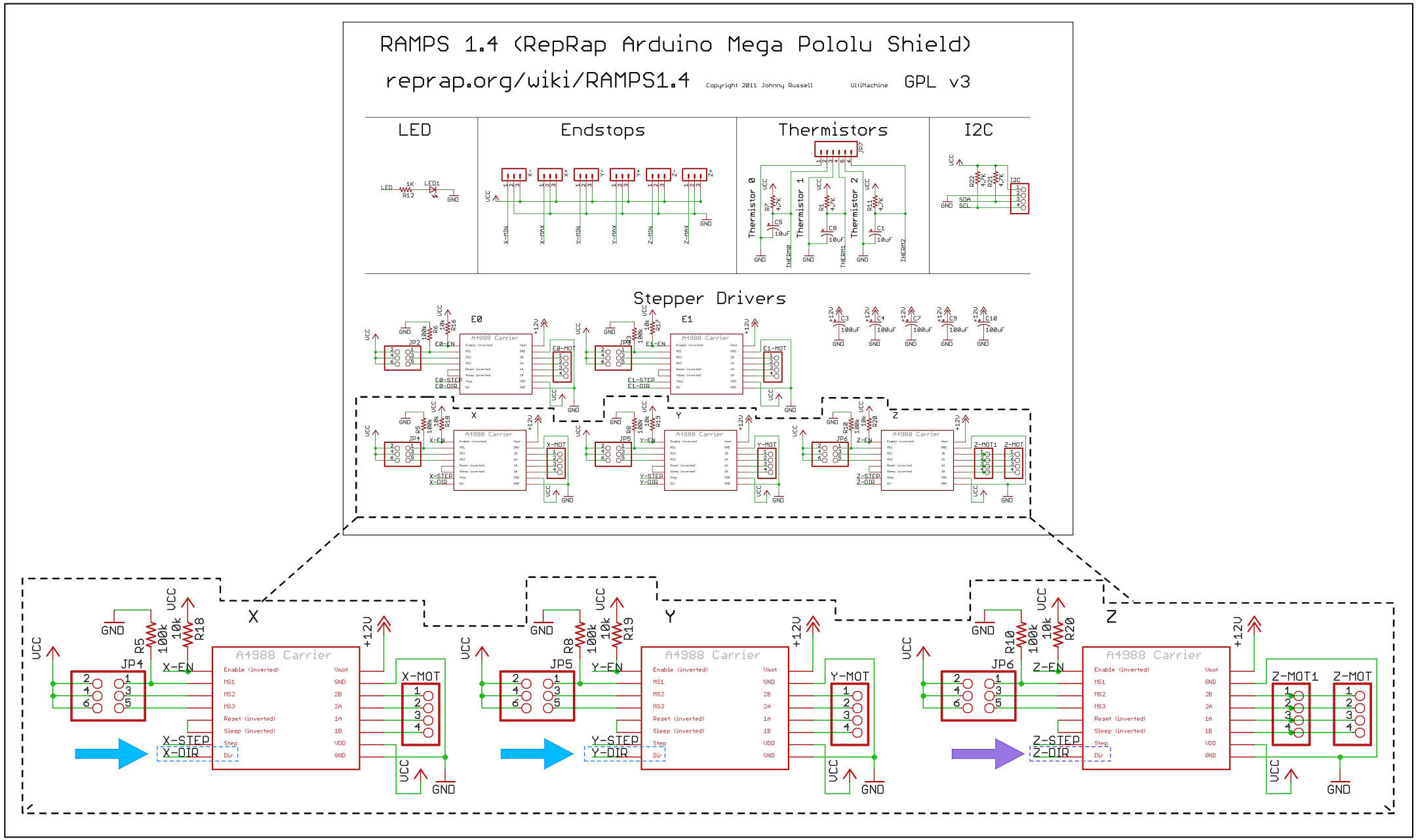
The script was developed for Cartesian RepRap-based FFF printers, which are commonly used in research settings, as represented by the works of Lopes (2021), Lopes and Aguiar (2024), do Carmo *et al.* (2020), Glissoi Lopes et al. (2021), Lopes et al. (2022), Lopes et al. (2022), Glissoi Lopes et al. (2021), Aguiar et al. (2023) and Lopes et al. (2019) [6], [33], [35], [36], [73], [75], [159], [160], [161]. In this type of printers, the direction control signal for both X-axis and Y-axis stepper motors are provided by the RepRap Arduino Mega Pololu Shield (RAMPS) Stepper Drivers (A4988 Carrier) [162], [163], as displayed in Figure 3.2. The 3D printer used in the acquirement of the signals related to the **`fff_segmenter`** segmentation script was the Cartesian RepRap-based FFF Core A1V2 printer from GTMax3D, Americana, Brazil.

In order to allow for the signal acquisition process, the RAMPS pins in regard to the A4988 Carrier boards for the X and Y axis, depicted in Figure 3.2, were connected to a constructed splitter board. The goal of the splitter board, represented in Figure 3.3, is to allow for insertion of splits to the Direction "(Dir)" and "Step" pins. The conjunction of splitter boards and A4988 Carrier boards for the X and Y axis, connected on the A1V2 Printer RAMPS board is represented on Figure 3.4.

The signals were collected *in-situ* during the fabrication of the workpiece. The workpiece's G-code file is available on the FFF-Line-Segmentation GitHub repository (.../gcodes). The slicing process was carried out in the Simplify3D software, by Simplify, with standard printing parameters values, which were provided by the printer manufacturer in the form of a printing profile.

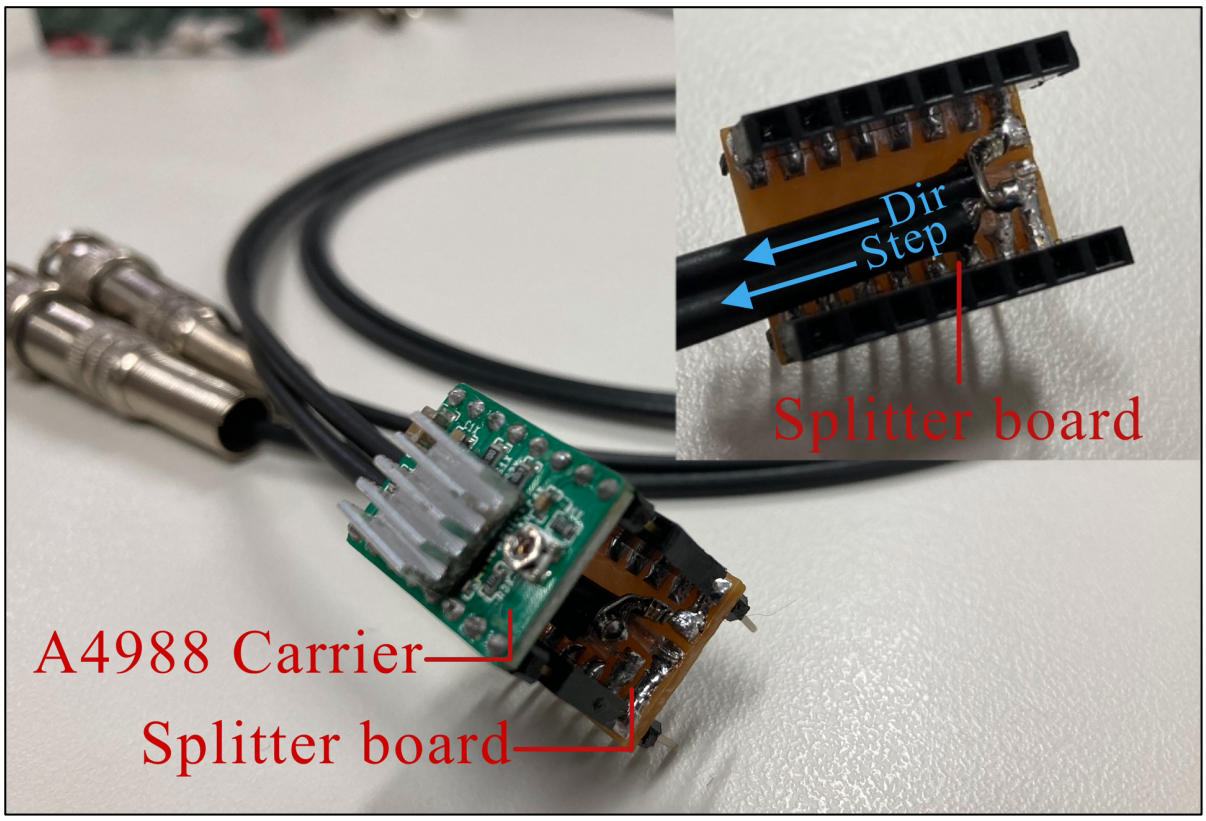
3.1.1 STUDY A: EXPERIMENTAL SETUP

Figure 3.2 - RepRap Arduino Mega Pololu Shield (RAMPS) 1.4 schematic with indications of the stepper motors direction signals



Source: Altered from RepRap team (2024) [164]

Figure 3.3 – Splitter board and connection to the A4988 Carrier, with indications of the cables related to the Dir and Step pins



The printing parameters values utilized are displayed in G-code comments at the beginning of the workpiece's G-code on 'Settings Summary'. The signals were recorded at a specified Fs and temporarily stored on the Data Acquisition device (DAQ) hard drive. Subsequently, they were transferred to a Personal Computer (PC) for further signal processing.

Figure 3.4 – Splitter boards placement on the A1V2 3D priter RAMPS board, with the identification of the which splitter board is related to the X and Y axis

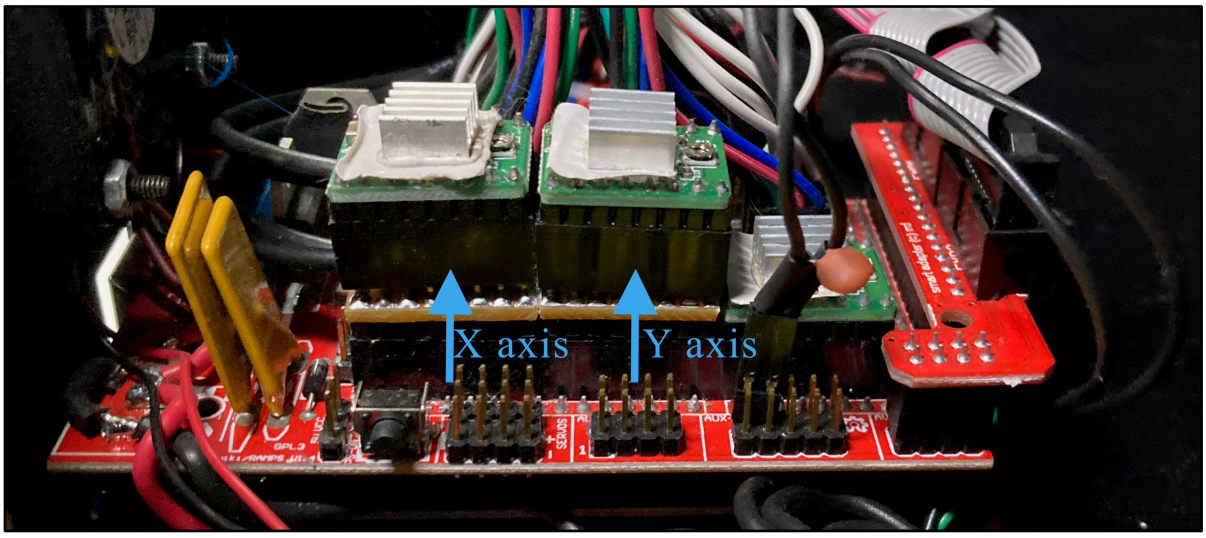
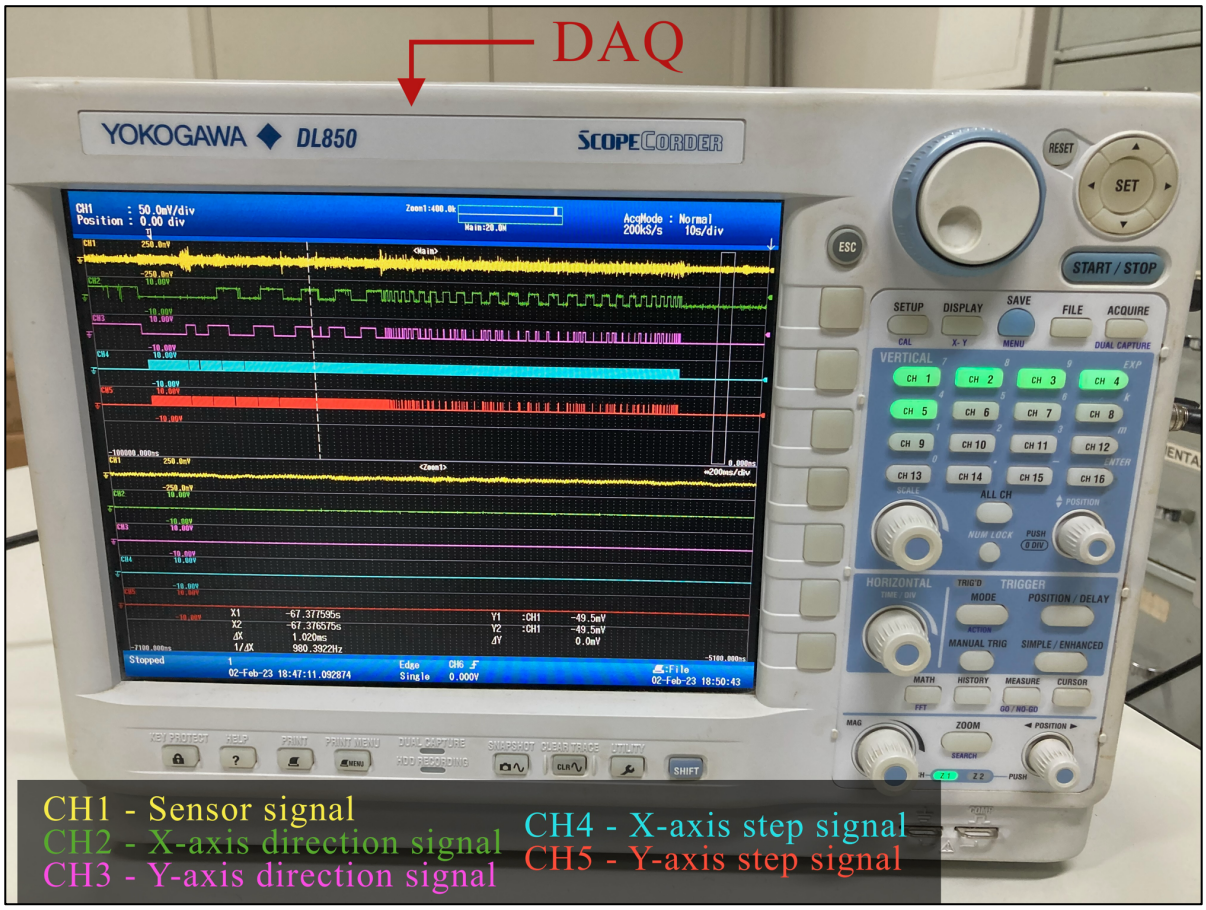


Figure 3.5 – Signal acquisition process visualization on the DAQ, with the representation of the Sensor signal, X-axis and Y-axis direction signals, X-axis and Y-axis step signals



The “Step” signals, obtainable from the pins splits displayed on Figure 3.3, were also acquired in preliminary tests of the **`fff_segmenter`** script development. The Figure 3.5 displays the acquirement of the necessary Sensor and “Dir” signals, alongside the extra “Step” signals. However, the “Step” signals were found to not work for segmentation purposes. Therefore, in subsequent signal acquirements, including in the exemplary datasets, the “Step” signals were not acquired.

In the three exemplary datasets available on the FFF-Line-Segmentation GitHub repository (.../Data), the *`Fs`* used during the signal acquisition process was 200 kS/s. The value of *`Fs`* was defined through preliminary printing tests, which revealed that the frequency content of the signals acquired by the sensors that were related to the printing process was below 30kHz [6], and by the length of the acquired signals. Therefore, 200 kS/s was defined as a *`Fs`* value that is sufficient to attend the Nyquist-Shannon sampling theorem [165], [166], and also that would provide signals that were smaller in size which would facilitate the signal processing and analysis.

The DAQ used was the DL 850 oscilloscope from Yokogawa®, Tokyo, Japan. The three exemplary datasets feature different sensor positions on the 3D printer:

1. *`Test1.mat`* - This dataset includes the *`Acoustic_signal`* monitoring sensor signal, acquired by a PZT attached to the printer table. The placement of the sensor is visible on Figure 3.6. The PZT was a 20mm diameter, model CEB-20D64 by CUI Devices.

2. *Test2.mat* - This dataset includes two monitoring sensor signals. The placement of the sensors is visible on Figure 3.7. The sensor signals are:
   - *Acoustic_signal_table*: Acquired by a PZT placed on the printer bed. The PZT was a 20mm diameter, model CEB-20D64 by CUI Devices;
   - *Acoustic_signal_extruder*: Acquired by a PZT placed on the printer extruder block. The PZT was a 12 mm diameter, model 7BB-12-9 by Murata Electronics.
3. *Test3.mat* - This dataset includes two monitoring sensor signals. The placement of the sensors is visible on Figure 3.8. The sensor signals are:
   - *Signal_extruder*: Acquired by an electret microphone placed on the printer extruder block. The electret microphone was a terminal pin-type with diameter of 9.7 mm, model CMA-4544PF-W by CUI Devices;
   - *Signal_extruder2*: Acquired by a PZT placed in a different position on the printer extruder block. The PZT was a 12 mm diameter, model 7BB-12-9 by Murata Electronics.

Figure 3.6 – *Test1.mat* dataset sensors placement in a glass appendix attached to right side of the printer table

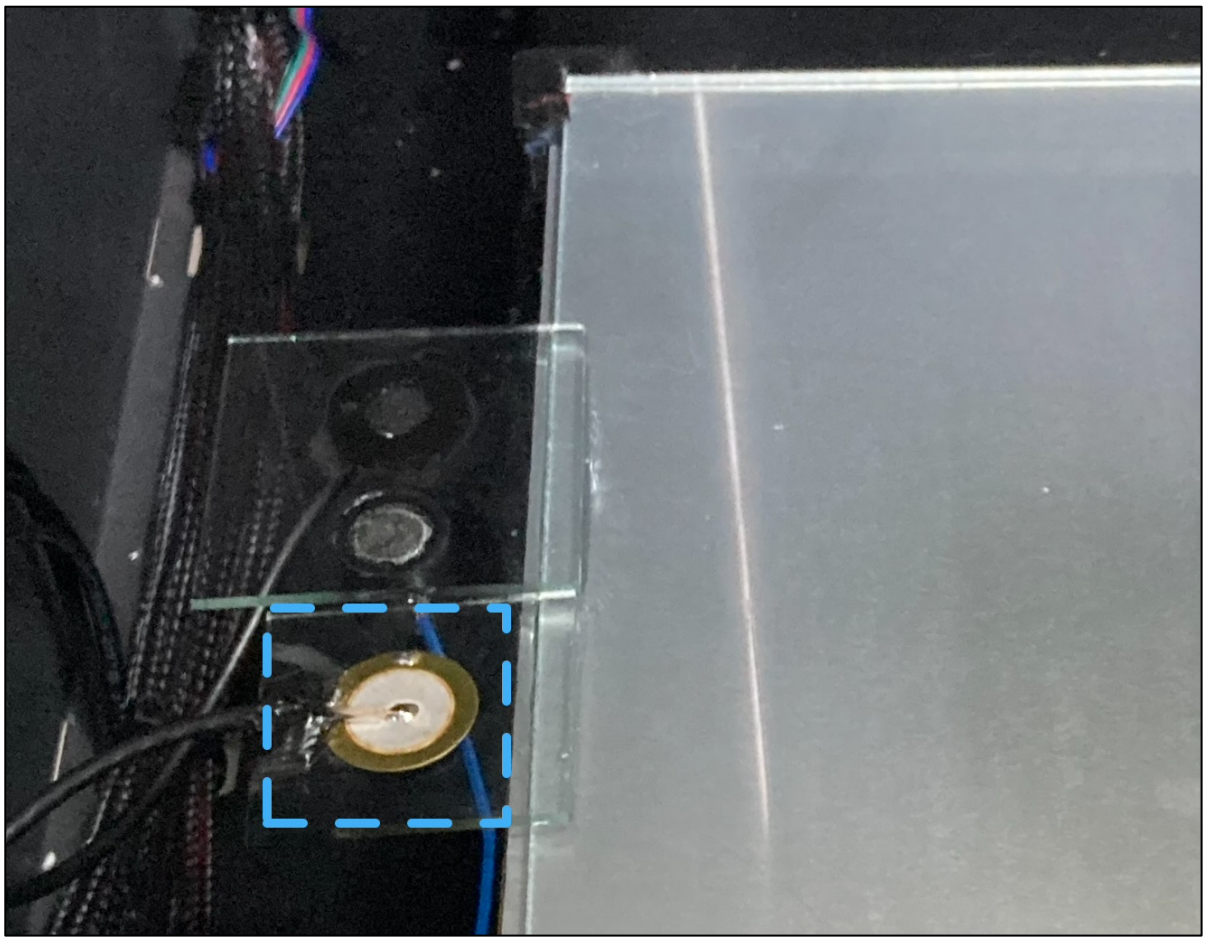


Figure 3.7 – *Test2.mat* dataset sensors placement in a glass appendix attached to the printer table and on the right side of the printer extruder block

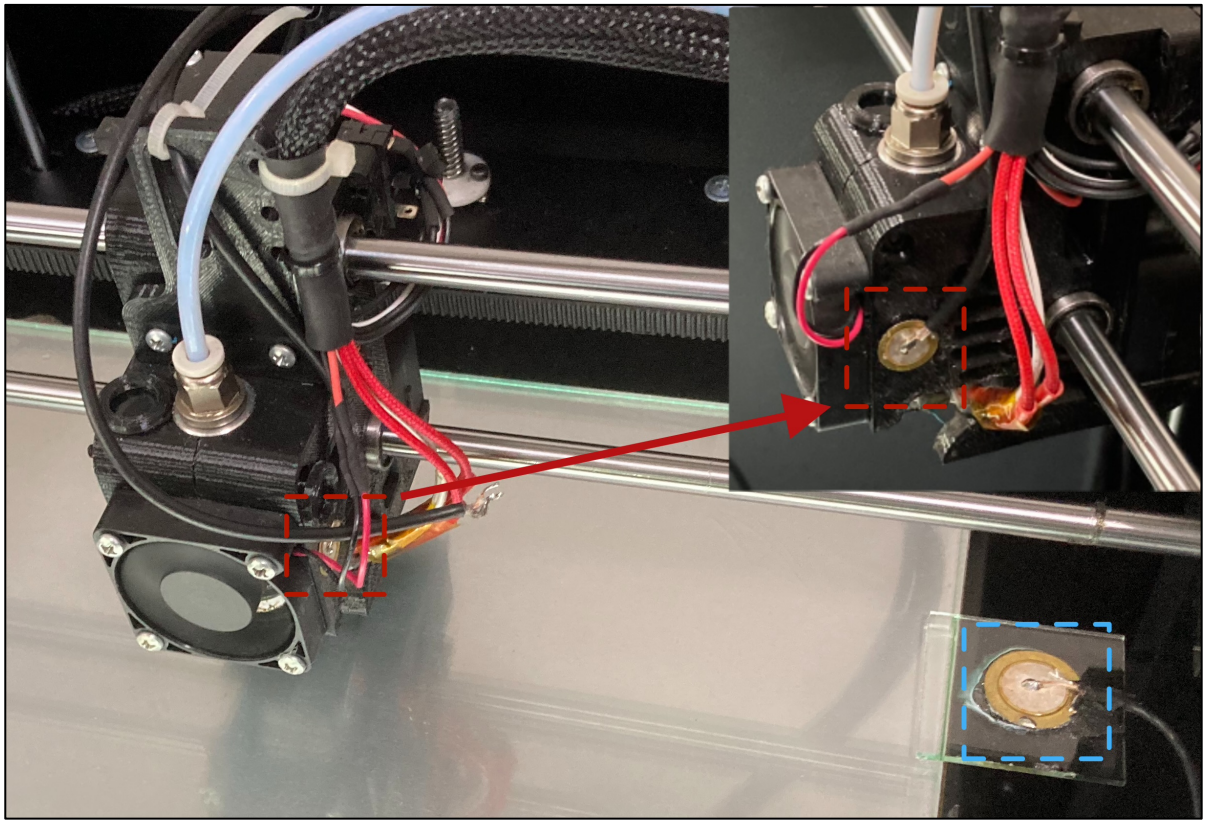
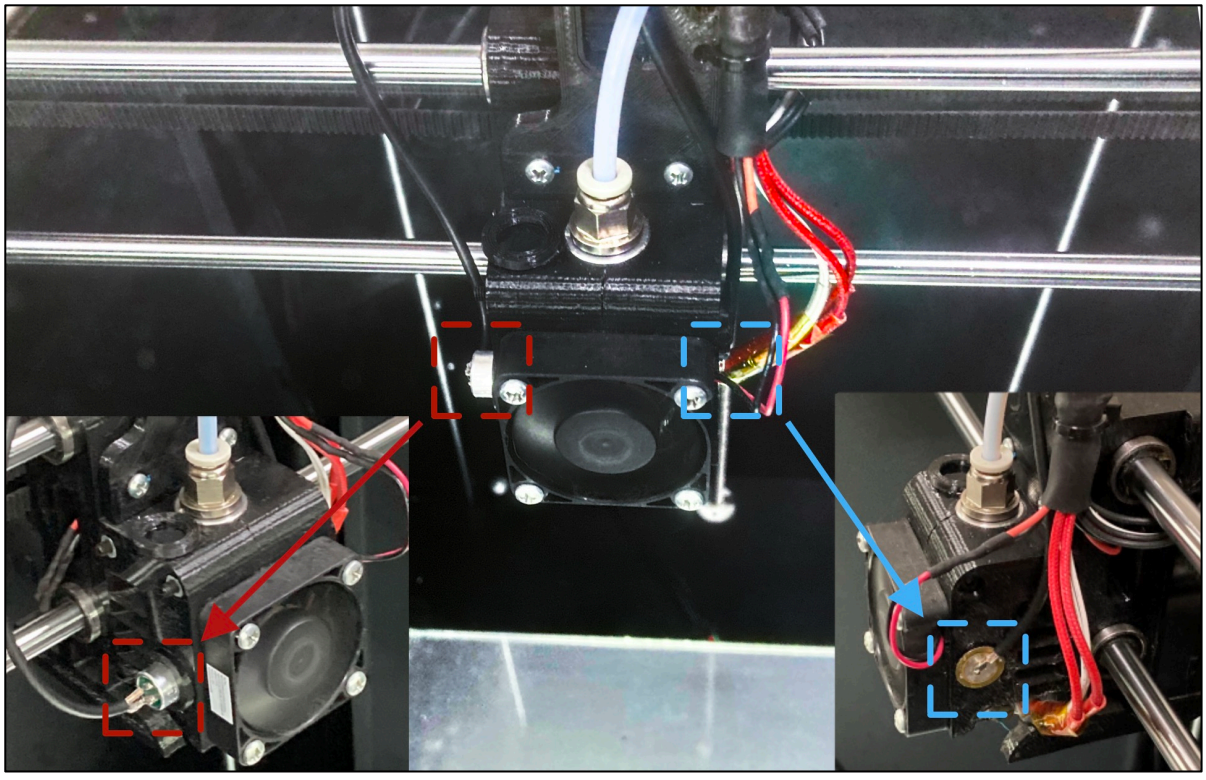


Figure 3.8 – *Test3.mat* dataset sensors placement on the printer extruder block, where an electret microphone was placed on the left side of the block, and a piezoelectric diaphram was placed on the right side of the block.



The three datasets were made available to demonstrate that the **`fff_segmenter`** script can handle monitoring sensor signals from different sources, in terms of positioning and sensor types, and accommodate variations in the start and end indexes of specific geometrical elements of the printed part, which are common in this type of acquisition process.

The choice of different models and sizes for both the sensor types were due to limitations in regard to the available space for positioning, in the case of the sensors attached to the extruder, and due to results obtained in preliminary research which shown that the 20mm diameter PZT was adequate to acquire data from the glass appendix of the printing table.

3.1.2 STUDY A: ACESSING AND USING THE `FFF_SEGMENTER` SCRIPT

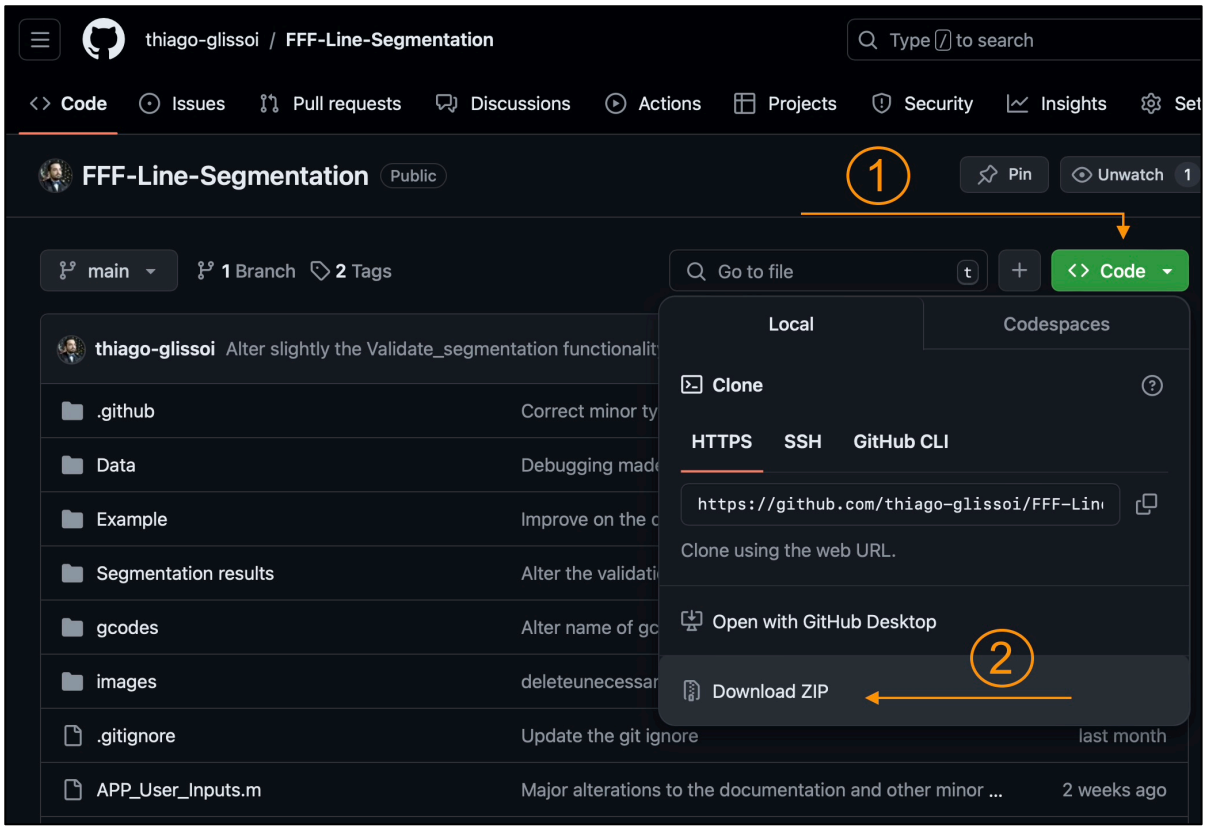
3.1.2.1 STUDY A: OBTAIN THE FFF-LINE-SEGMENTATION GITHUB REPOSITORY FILES

Clone the repository by copying, pasting and running the following git command on a terminal window of a desired folder for the FFF-Line-Segmentation files.

`git clone https://github.com/thiago-glissoi/FFF-Line-Segmentation.git`

Alternatively go to the repository page on GitHub, https://github.com/thiago-glissoi/FFF-Line-Segmentation, and download a ZIP file containing the contents of the FFF-Line-Segmentation repository. Figure 3.9 displays the option to download the FFF-Line-Segmentation repository ZIP file.

Figure 3.9 – Instructional representation on how to perform a manual download of the FFF-Line-Segmentation repository on Github



3.1.2.2 STUDY A: DEPENDENCIES

Before using the **`fff_segmenter`** script, verify if the following dependencies are installed and available in your MATLAB or Octave environment.

For MATLAB, the dependency is:

- Signal Processing Toolbox.

For Octave, the dependencies are:

- Signal Package;
- Control Package.

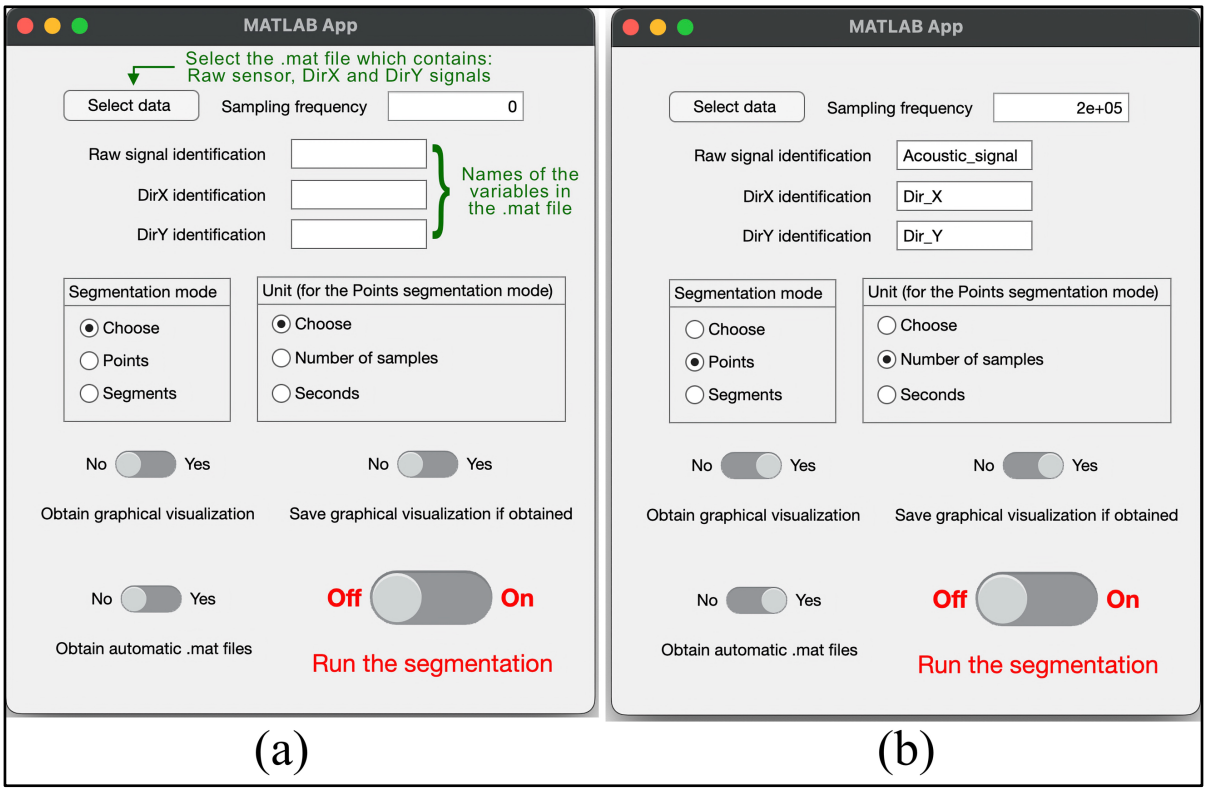
3.1.2.3 STUDY A: MATLAB EXAMPLE

Make sure that the listed dependencies are installed and loaded into MATLAB.

Run the **`fff_segmenter`** by typing the script name directly into the MATLAB command window followed by the press of the Enter/Return key on the keyboard, or by clicking in the run button of the MATLAB text editor within the **`fff_segmenter`** script.

After running the **`fff_segmenter`** script, the user will be presented with the graphical interface displayed on Figure 3.10(a).

Figure 3.10 – MATLAB Input Graphical User Interface (GUI). (a) Unfilled GUI, with comments certain elements of the interface; (b) Filled GUI, with default options and values regarding the *Test1.mat* dataset



Source: Glissoi Lopes *et al.* (2024) [71]

In the graphical interface:

- The user must use the Select data button to select the .mat file which contains the acoustic signal and the X and Y direction control signals.

- The user must insert the Sampling frequency of the signals in Hertz (Hz)/Samples per second (S/s).
- The user must insert the name of the sensor signal that exists in the selected .mat file on the Raw signal identification field.
- The user must insert the name of the direction X axis signal that exists in the selected .mat file on the DirX identification field.
- The user must insert the name of the direction Y axis signal that exists in the selected .mat file on the DirY identification field.
- The user must select the Segmentation mode between `Points` and `Segments`. If the choice is not made, the default `Points` mode will be utilized.
- The user must select the Unit segmentation between `Number of samples` and `Seconds`. If the choice is not made, the default `Number of samples` mode will be utilized.
- The user may select additional Outputs that can be generated by the script. The available outputs are: Obtain graphical visualization, Save graphical visualization if obtained, and Obtain automatic .mat files. If none additional Outputs are selected, the **`fff_segmenter`** function output will only be the segmentation results to the current MATLAB workspace.

About the additional outputs:

- The Obtain graphical visualization option will generate a figure with the segmentation results displayed on top of the Sensor signal.
- The Save graphical visualization if obtained option will save the generated figure in the Segmentation results folder.
- The Obtain automatic .mat files option will save the segmentation results in the Segmentation results folder in .mat format. The output data file name follows a definition that is based on the Segmentation mode choice, and the identification of the sensor signal in the dataset.

For the purpose of this example, the Select data button will be used to load the *`Test1.mat`* file from the FFF-Line-Segmentation's repository Data folder. The Select data button will open a file explorer window, where the user can navigate to the Data folder and select the *`Test1.mat`* file. The rest of the input fields will be filled with the values in regard to the *`Test1.mat`* dataset, with default values for the Segmentation mode and Unit segmentation options, and with all of the available outputs toggled to `Yes`, as displayed on Figure 3.10(b).

When the user toggle to *`On`* the *`Run`* the segmentation button, the GUI closes and the **`fff_segmenter`** script runs with the defined parameters. As a result of running the **`fff_segmenter`** script with default parameters, two new files were generated in the Segmentation results folder, which was created in the MATLAB's current path. The first, named `Points` segmentation results *`Acoustic_signal`*, holds the results of the segmentation in the `Points` segmentation choice, saved in table format. The output data file name follows a definition that is based on the segmentation mode choice, in this case `Points`, and the identification of the sensor signal in the dataset, in this case *`Acoustic_signal`*.

The **`fff_segmenter`** script outputs will be discussed in the segmentation results section.

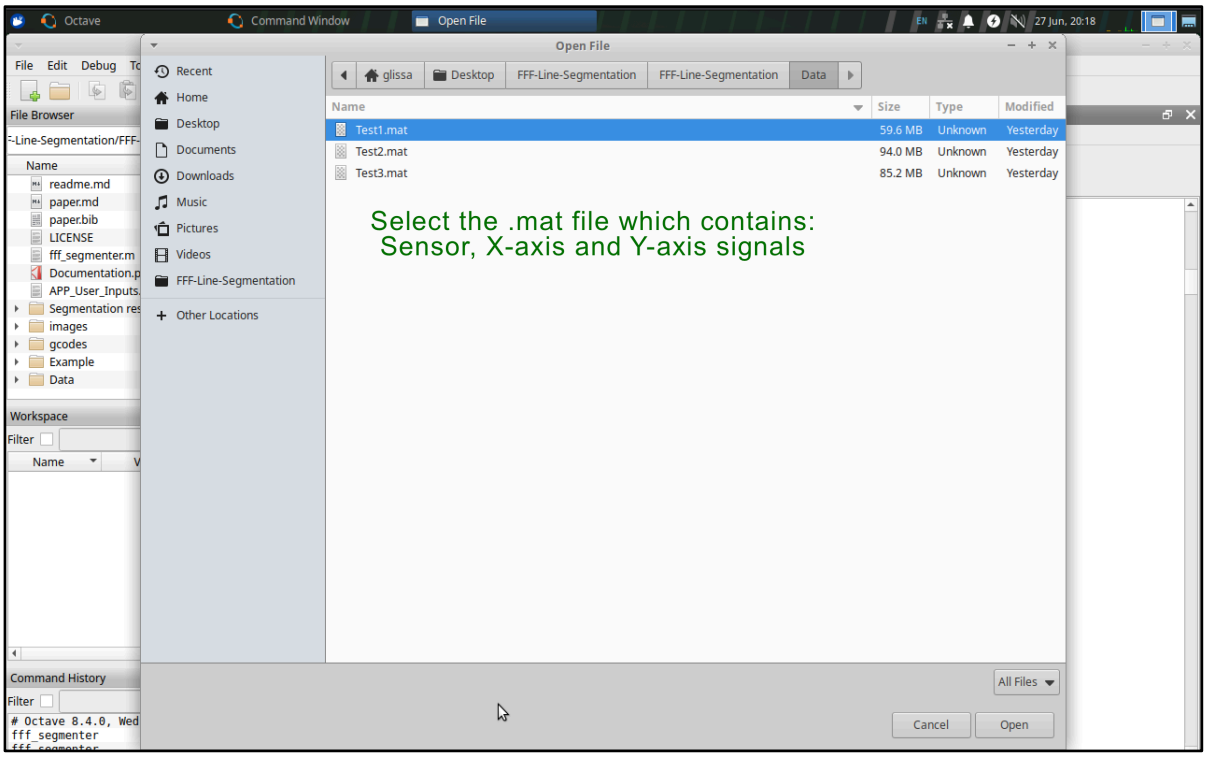
3.1.2.4 STUDY A: OCTAVE EXAMPLE

Make sure that the listed dependencies are installed and loaded into Octave.

Run the **`fff_segmenter`** script by typing directly into the command window followed by the press of the Enter/Return key on the keyboard, or by clicking in the run button of the Octave text editor within the **`fff_segmenter`** script.

After running the **`fff_segmenter`** script, a file explorer window will appear. The user must select the .mat file which contains the acoustic signal and the X and Y direction control signals. For the purpose of this example, the user can navigate to the FFF-Line-Segmentation's repository Data folder and select the *`Test1.mat`* file.

Figure 3.11 – Octave file navigation, running inside an Ubuntu machine, with the Xcfe desktop enviroment and Thunar file manager



Source: Glissoi Lopes *et al.* (2024) [71]

After selecting the data file, the user will be presented with the graphical interface displayed on Figure 3.12(a). The filled values in the input fields are the default values for the Segmentation mode and Unit segmentation options, and with all of the available fields set to N.

In the graphical interface:

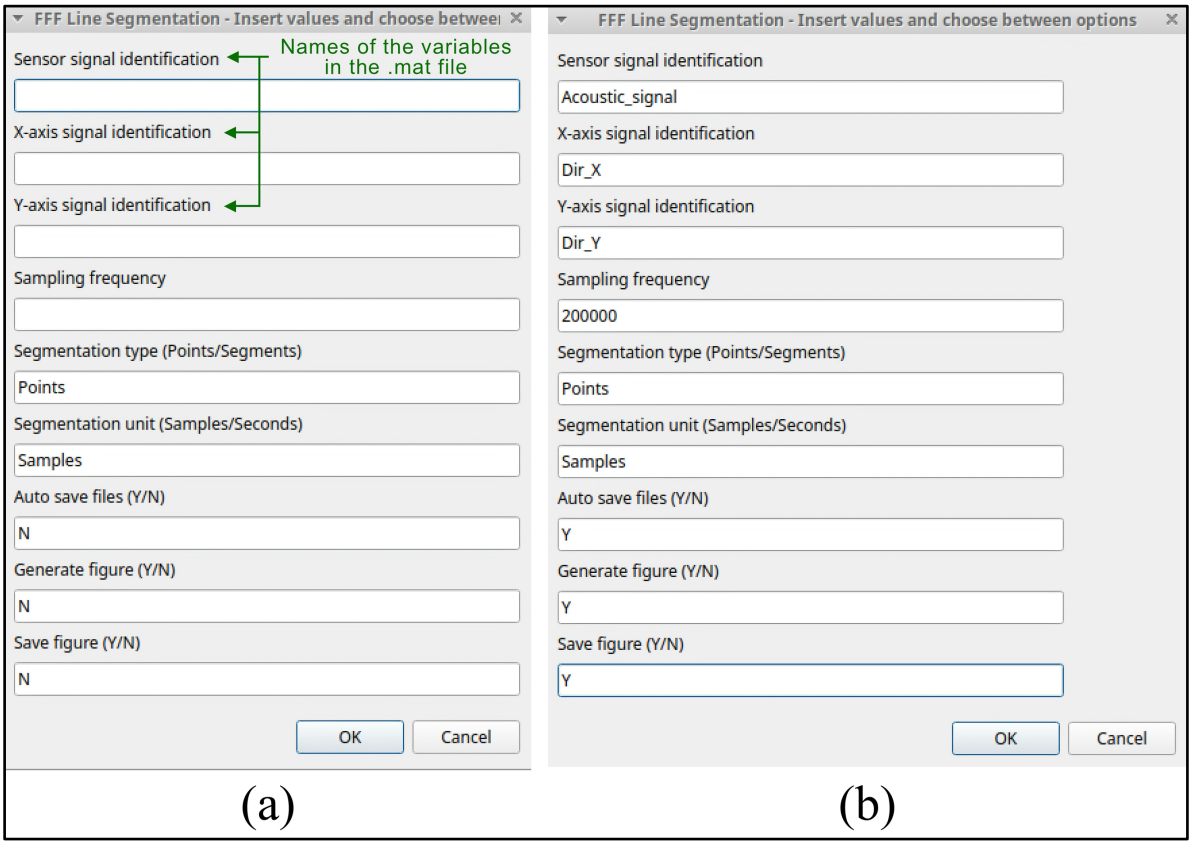
- The user must insert the name of the sensor signal that exists in the selected .mat file on the Sensor signal identification field.
- The user must insert the name of the direction X axis signal that exists in the selected .mat file on the X-axis signal identification field.
- The user must insert the name of the direction Y axis signal that exists in the selected .mat file on the Y-axis signal identification field.

- The user must insert the Sampling frequency of the signals in Hertz (Hz).
- The user must select the Segmentation mode between `Points` and `Segments`. If the choice is not made, the default `Points` mode will be utilized.
- The user must select the Unit segmentation between `Number of samples` and `Seconds`. If the choice is not made, the default `Number of samples` mode will be utilized.
- The user may select additional Outputs that can be generated by the script. The available outputs are: Generate figure, Save figure, and Auto save files. If none additional Outputs are selected, the **`fff_segmenter`** function output will only be the segmentation results to the current Octave workspace.

About the additional outputs:

- The Generate figure option will generate a figure with the segmentation results displayed on top of the Sensor signal.
- The Save figure option will save the generated figure in the Segmentation results folder.
- The Auto save files option will save the segmentation results in the Segmentation results folder in .mat format. The output data file name follows a definition that is based on the Segmentation mode choice, and the identification of the sensor signal in the dataset.

Figure 3.12 – Octave input User Interface (UI). (a) Unfilled UI, with comments certain elements of the interface; (b) Filled UI, with default options and values regarding the *`Test1.mat`* dataset



Source: Glissoi Lopes *et al.* (2024) [71]

The user will fill the fields with the values in regard to the *Test1.mat* dataset, with default values for the Segmentation mode and Unit segmentation options, and with all of the available fields set to `Y` as displayed on Figure 3.12(b).

When the user press Enter/Return key on the keyboard, the UI will be closed and the **fff_segmenter** script will run with the defined parameters. The **fff_segmenter** script outputs will be discussed in the segmentation results section.

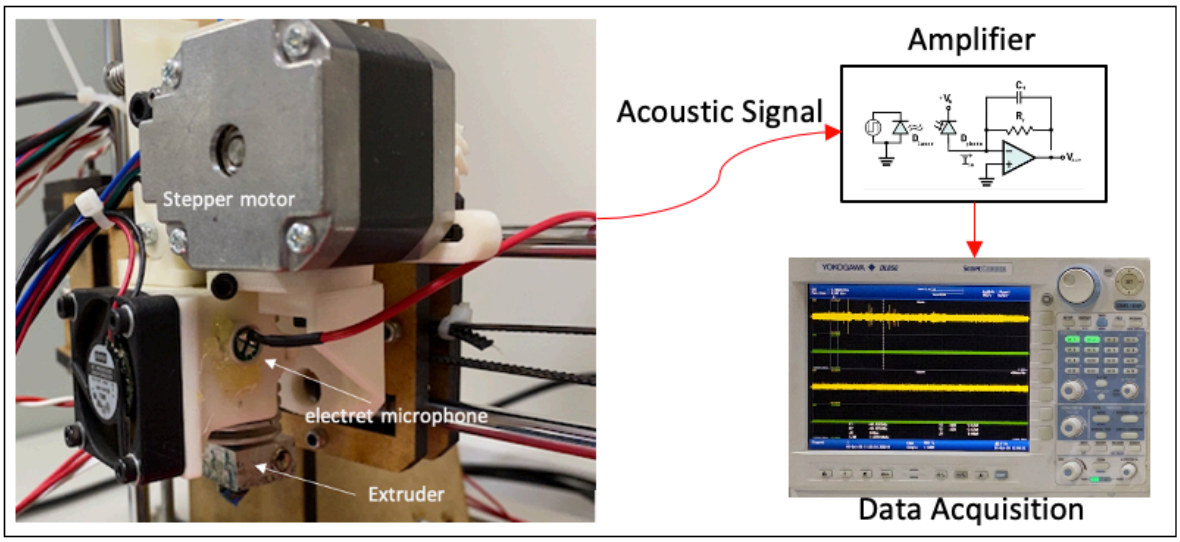
3.2 STUDY B: MATERIAL AND METHODS REGARDING THE STUDY ABOUT MONITORING FFF MACHINE CONDITIONS WITH ELECTRET MICROPHONES, SVM, AND NEURAL NETWORKS

3.2.1 STUDY B: EXPERIMENTAL SETUP

In order to study the feasibility of using the electret microphone along with digital signal processing tools for monitoring the machine conditions in FFF, an experimental setup was developed. The RepRap-based 3D Printer, model Graber i3, of 0.4mm-nozzle diameter was used, in which a terminal pin-type electret microphone of 9.7mm diameter, model CMA-4544PF-W by CUI Devices, and operating frequencies of 20Hz ~ 20kHz, was attached to the direct extruder support through a silicon-based adhesive. The manufacturer of the Graber i3 RepRap-based printer is GTMax3D, Americana, Brazil. The location of the microphone was chosen based on the accessibility, low process intrusion, and low temperature compared to the printer table. It is worth mentioning that in the X and Z axis, only the extruder moves while in the Y axis only the table moves.

The signal from the microphone was processed by a transimpedance amplifier according to Caldwell (2015) [167], and then sent to the ScopeCorder, Model DL 850, for data acquisition at the sampling frequency of 200 kS/s and stored into its data storage device for further downloading and processing. The sampling frequency value was defined through preliminary printing tests, which revealed that the frequency content of the signals acquired by the sensors that were related to the printing process was below 30kHz [6], and by the length of the acquired signals. Therefore, 200 kS/s was defined as a sampling frequency value that is sufficient to attend the Nyquist-Shannon sampling theorem [165], [166], and also that would provide signals that were smaller in size which would facilitate the signal processing and analysis. The manufacturer of the DL 850 model ScopeCorder is Yokogawa®, Tokyo, Japan. Figure 3.13 shows the experimental setup for raw signal acquisition.

Figure 3.13 - Experimental setup regarding the study about monitoring FFF machine conditions with electret microphones, SVM, and neural networks

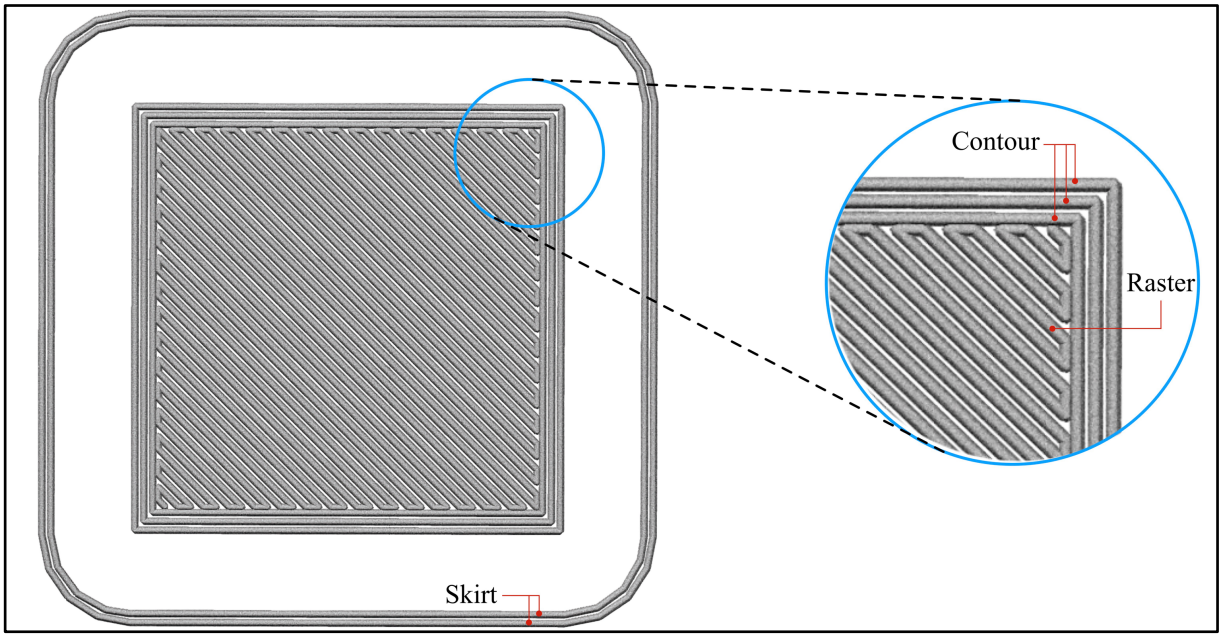


Source: Lopes *et al.* (2023) [51]

3.2.2 STUDY B: 3D PRINTING TESTS OF SINGLE-LAYER PARTS FOR THREE MACHINE CONDITIONS

With the purpose of studying the main machine condition in FFF, that is, normal printing, extruder clogging, and lack of filament, a single-layer part fabrication was designed in SketchUp®, which has a squared geometry with dimensions 25.0x25.0x0.4 mm, with 12 contour lines for the External Infill Pattern (EIP) and 59 raster lines for the Internal Infill Pattern (IIP) with angle of 45 degrees, as shown in Figure 3.14. The PLA filament of 1.75 mm diameter by 3DFila, Belo Horizonte, Brazil, was used.

Figure 3.14 - Single-layer part used in the study B, with a zoom visualization on upper corner of the workpiece with identification of the Raster and Contour lines



The machine conditions were established based on three fabrication conditions of a single-layer part as described previously. The normal machine condition herein defined is regarded as the fabrication of a part without defect, that is, there is no occurrence of any malfunction of the printer during the whole printing process. The main printer parameters for this fabrication condition consisted of the extruder temperature of 190 °C, bed temperature of 60 °C, layer height of 0.4 mm, fill density of 20%-, and first-layer printing speed of 15 mm/s. *On* the other hand, the clogging machine condition was induced during the fabrication of the raster lines by using the command `M104 S100` (set hot end temperature parameter to 100 °C) in the G-code prior to the start of the part's fabrication. Finally, the machine's condition regarding the lack of filament was provoked by cutting manually the filament prior to the part's fabrication. The total length of filament required for a normal part including the skirt was 153.5mm, but it was cut a 100mm filament segment instead, and inserted into the filament feeder, which induced a lack of filament in the region of IIP printing. Three repetitions were conducted in the tests for each machine condition. The ambient temperature was maintained constant at 25 °C. Three repetitions were conducted in the tests for each machine condition. The temperature ambient was maintained constant at 25 °C and the printing bed was set to 60 °C. The tests were conducted at the Data Acquisition and Signal Processing Laboratory (LADAPS), at the São Paulo State University – UNESP, where there was very low background noise.

3.2.3 STUDY B: THE PROPOSED METHOD OF SIGNAL PROCESSING AND FEATURES EXTRACTION – INCLUDING THE SIGNAL SEGMENTATION ALGORITHM;

To obtain a comprehensive understanding of the acoustic signals collected during the tests and extract useful features of the raw signals related to the machine conditions to be applied to the classification models, several procedures were developed based on signal processing in the time and frequency domain. An algorithm was developed for this purpose, which is described as follows and represented on Figure 3.15. These parameters mentioned were chosen empirically.

- Inspecting the raw signals regarding the whole process of manufacturing the part, which comprises the skirt, two infill patterns, and transitions.
- Extracting the segment lines regarding the EIP and the IIP of the printed part, which are the focus of monitoring in this study. A procedure was developed for this purpose, which initially consisted of filtering the raw signals through an equiripple FIR low-pass filter of order 120, passband edge frequency of 1kHz, pass-band ripple equals to 0.01, and stop-band attenuation of 80 decibels. The order of 120 was selected through multiple preliminary tests, which this value allowing for the best results regarding the extraction of the segment lines start and ending indexes.
- Next, a decimation factor of 2500 was applied to the filtered signals and then the normalization was performed.
- Finally, the counts statistic of each five samples with a threshold of 0.18 was computed.

It is natural to investigate the raw signals acquired during the tests in the time domain to understand their behavior, complexity, and the relationship with different patterns of fabrication and failures induced in the printer for the current study, that is, interrupted filament and extruder clogging during the fabrication of a single-layer PLA part.

The frequency content of a signal is of utmost importance in studying any manufacturing process under sensor monitoring, as it provides information and insight about the events occurring in the machine and manufacturing of the part. As the acoustic signals from the 3D printing process are non-stationary and stochastic in nature, the Power Spectral Density (PSD) was used to estimate the distribution of the signal's spectral energy during the fabrication of the part [168]. Thus, The PSD of the raw signals was computed by using the Welch's method, which is also known as the periodogram method, which basically consists of dividing the time signal into successive blocks, creating the periodogram of each block, and averaging. In this work, the PSD was performed in MATLAB using the **`pwelch`** function, with a Hamming window of 65.536, the number of overlapped samples is equal to 32.768, and the number of Discrete Fourier Transform (DFT) points of 65.536.

Based on the analysis of the PSD of the raw signals and the behavior amplitude of the raw signals regarding each machine condition, a band frequency was chosen to apply to the raw signals through a digital filter and extract features thereafter.

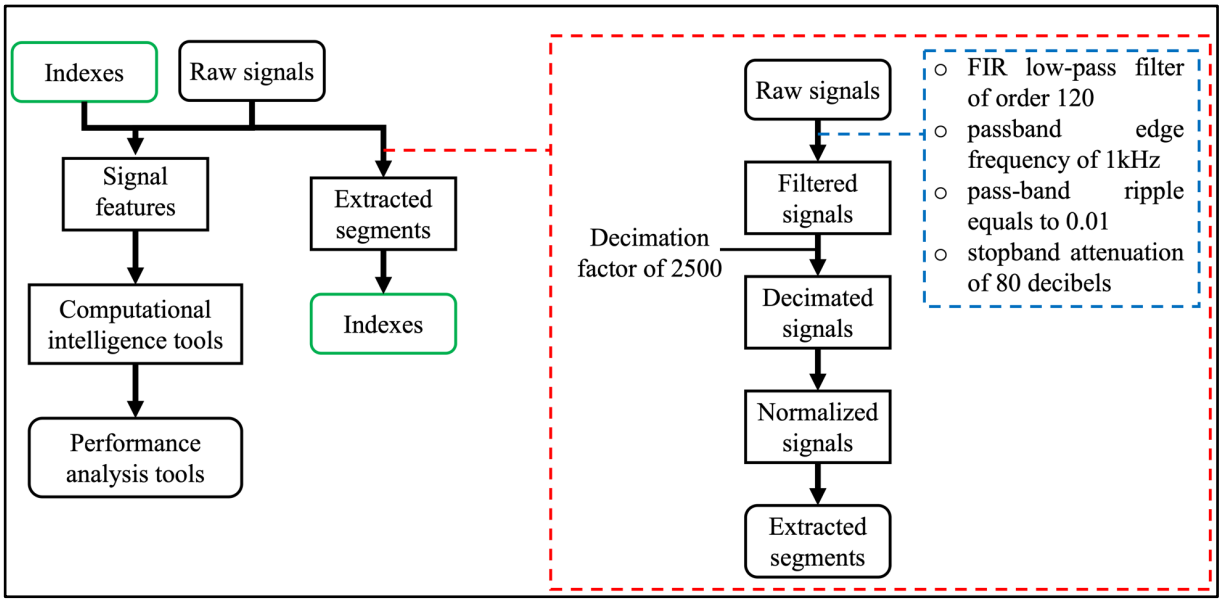
The RMS is the most used statistic applied to signal analysis widespread in industrial applications, and it can be found in a multitude of works on sensor-based monitoring, such as in Alexandre *et al.* (2019), Wu *et al.* (2017), Wu *et al.* (2015) and Liu *et al.* (2018) [57], [63], [113], [135]. As it is a feature used to describe the strength of the signal in the time domain [113], that is, it is related to the power and energy of the signal, the computation of RMS values

is performed in this work. An integration time of 50ms was found suitable for this work. The RMS values were computed from the raw signals with and without a band-pass Infinite Impulse Response (IIR) filter, Butterworth filter of order 5. The RMS values were then filtered by a moving average Finite Impulse Response (FIR) filter of order 20. The analysis is performed just for the time frame regarding the fabrication of the part, that is, for EIP and IIP patterns.

As the acoustic signal from the 3D printing process is random in nature and it is under different machine conditions, a measure of the distortion of the probability distribution may be useful in condition monitoring. This distortion can be calculated by skewness and kurtosis, being the former a measure of asymmetry while the latter a measure of whether the signal is heavy-tailed or light-tailed relative to a normal distribution. The use of skewness and kurtosis can be found in the works of Goyal *et al.* (2017), Nasir *et al.* (2019), Nazir *et al.* (2021) and Talibouya Ba *et al.* (2021) [152], [153], [154], [155]. Thus, the skewness and kurtosis statistics were computed from the raw signals. A sliding window of 1ms was empirically found adequate to compute each statistic value in this work, and then a moving average FIR filter of order 40 was applied. Also, the skewness and kurtosis were computed from the raw acoustic signals with and without an IIR band-pass filter, Butterworth, order 5.

Another important feature of the acoustic signals commonly used to quantify acoustic activity is the counts statistic, which is the number of times a signal crosses a pre-defined threshold per unit of time (ALEXANDRE et al., 2019; LIU et al., 2018; LOPES et al., 2017b). In this work, the counts statistic was computed from a raw signal filtered within a chosen frequency band using an IIR Butterworth band-pass filter of order 5, as well as from the raw signal non-filtered. A sliding time frame of 50ms was used to compute the values of counts along the signal during the fabrication of the part. The threshold of 0.1 V for the raw signal unfiltered and of 0.01 V for the raw signal filtered were found suitable in this work. The counts values were filtered through a moving average FIR filter of order 20.

Figure 3.15 – Schematic representation regarding the steps taken in the study B methodology, with visualization of the general analysis sequence, and detailed sequence in regard to the segment extraction process



The study on the spectra of the raw signals in this work has shown that some frequency bands play an important role in characterizing the printing process, being the frequency band of 350Hz-600Hz chosen as the best to represent the machine conditions. Thus, the ROP statistic was computed from the raw signals, as it is used to analyze a certain frequency band in relation to the whole spectrum content. The use of ROP can be found in several sensor-based works, such as in Thomazella *et al.* (2019), Martins *et al.* (2014) and Alexandre *et al.* (2018) [169], [170], [171]. The sliding window of 50ms was found adequate for computing the ROP along the raw signal for the current study. The values of ROP were then filtered by an FIR moving average filter of order 20.

3.2.4 STUDY B: NEURAL NETWORK MODELS AND SVM FOR CLASSIFYING THE CONDITIONS

After the feature extraction stage, the obtained vectors were used for training classifiers to automate the detection of conditions present in the process. This study evaluated two types of classifiers, SVM and neural networks, to infer machine condition patterns. The classifiers were trained using the default parameters provided by MATLAB's Classification Learner app, including default values for settings such as learning rate, number of epochs, and optimizers.

To ensure the full convergence capacity of the computational models used for damage classification, data preprocessing is crucial for classifier training. The steps adopted in the preprocessing, training, and evaluation of the computational models used in this study are described below and represented on Figure 3.16.

1) Data Normalization

Machine learning algorithms usually require input data to be within a certain range to meet the characteristics of their optimization algorithms. The minimum and maximum values of each feature extracted in the previous stage are calculated. The signals were normalized according to the range of values present in the three repetitions. After normalization, the signals obtained during the experimental test were scaled to the range between 0 and 1.

2) Signal Segmentation

The signals were segmented according to the start of the conditions monitored in this study: normal material deposition after the skirt, filament lack, and clogging. The start times of the different machine conditions were defined through signal analysis and manufactured parts.

3) Signal Windowing

Using the sliding window algorithm with a window size of 100 points, determined empirically, and a displacement of 1 point per iteration, the vector corresponding to each machine condition was transformed into a matrix containing *n* windows of 100 points. Table 3.1 presents the matrices obtained for training, validation, and testing of the classification algorithms.

4) Label Assignment

After constructing the matrices, labels corresponding to each observed condition in the process were assigned, resulting in an m x 1 vector, where m is the number of windows for each condition.

5) Separation of training, validation, and test sets

Construction of the feature matrix, using the windows extracted from the signals and concatenating repetitions 1 and 2, which will be used for training and validating the classification models. The data belonging to the third repetition of the experimental trial will be used exclusively for model testing after training. Using the hold-out validation technique, 80% of the data from the first two repetitions of the trial were used for model training, 20% of the data were segmented for hyperparameter adjustment and validation, and another set containing samples from the third repetition was used to test the predictive performance of the model.

6) Classifier training

The training of classification models was conducted using the Classification Learner toolbox in MATLAB® software version R2022b. SVM algorithms and Artificial Neural Networks (ANN) were used, and all variations of the algorithms present in the toolbox were evaluated.

7) Evaluation of Computational Model Performance

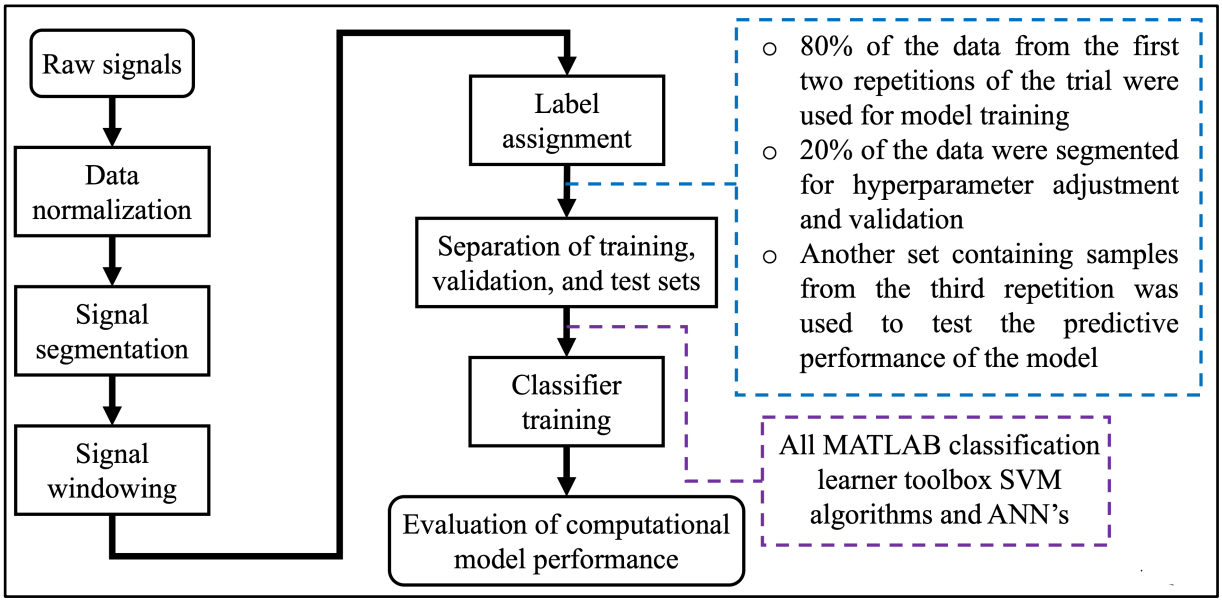
To evaluate the effectiveness of the trained models, classification metrics were used to measure algorithm performance. Confusion matrices were generated for validation and test sets, to analyze the classifier based on the output generated for each machine condition. Receiver Operating Characteristic (ROC) curves were also used to illustrate the model's capacity to classify samples.

Table 3.1 - Training matrix for each test

v	Condition	Signal Length	No. of Windows
#1	Normal	1245	1146
	clogging	1003	904
	Filament Lack	869	770
#2	Normal	1241	1142
	clogging	392	293
	Filament Lack	551	452
#3	Normal	1266	1167
	clogging	998	899
	Filament Lack	730	631

Source: Lopes *et al.* (2023) [51]

Figure 3.16 – Schematic with a deeper representation regarding the steps taken in the study B methodology, with specific visualization of the signal process analysis sequence



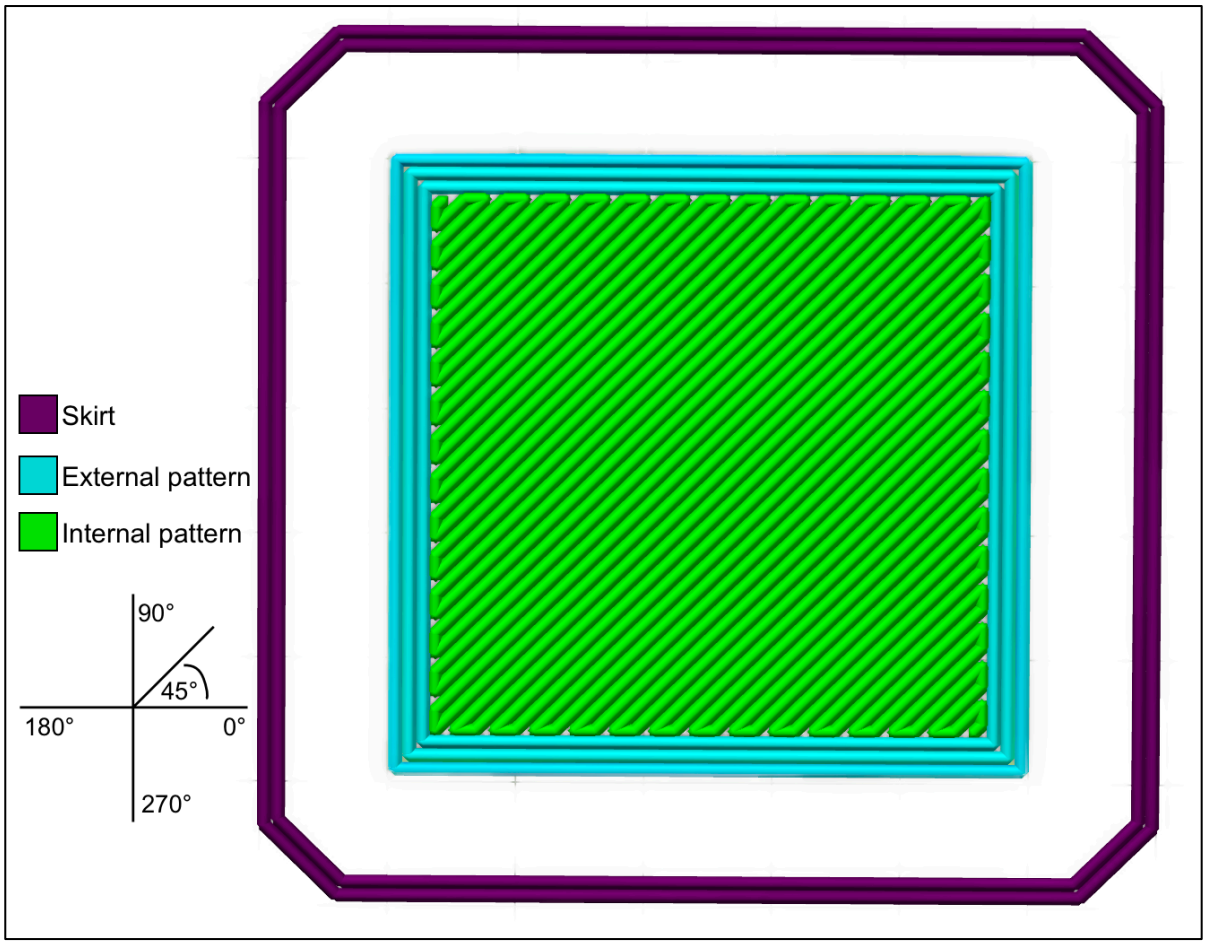
4 – RESULTS AND DISCUSSION

This section shows the results and discussion regarding the development of the **`fff_segmenter`** segmentation script, with the goal of detailing the programming approaches evaluated for the **`fff_segmenter`** segmentation script, as well as to the workpiece and mechanical aspects taken in consideration. Furthermore, it will be presented the results and discussion regarding the study about monitoring FFF machine conditions by a comprehensive signal processing and feature extraction, including spectral analysis, RMS values, ROP, count statistics, kurtosis, and skewness. The results and discussion on the use of machine learning algorithms, particularly SVM and Neural Networks, will also be presented.

4.1 STUDY A: RESULTS AND DISCUSSION REGARDING THE DEVELOPMENT OF THE `FFF_SEGMENTER` SEGMENTATION SCRIPT

4.1.1 STUDY A: CONSIDERATIONS REGARDING THE WORKPIECE

Figure 4.1 – Representation of the elements of fabrication in regard to the monolayer workpiece utilized in the study A

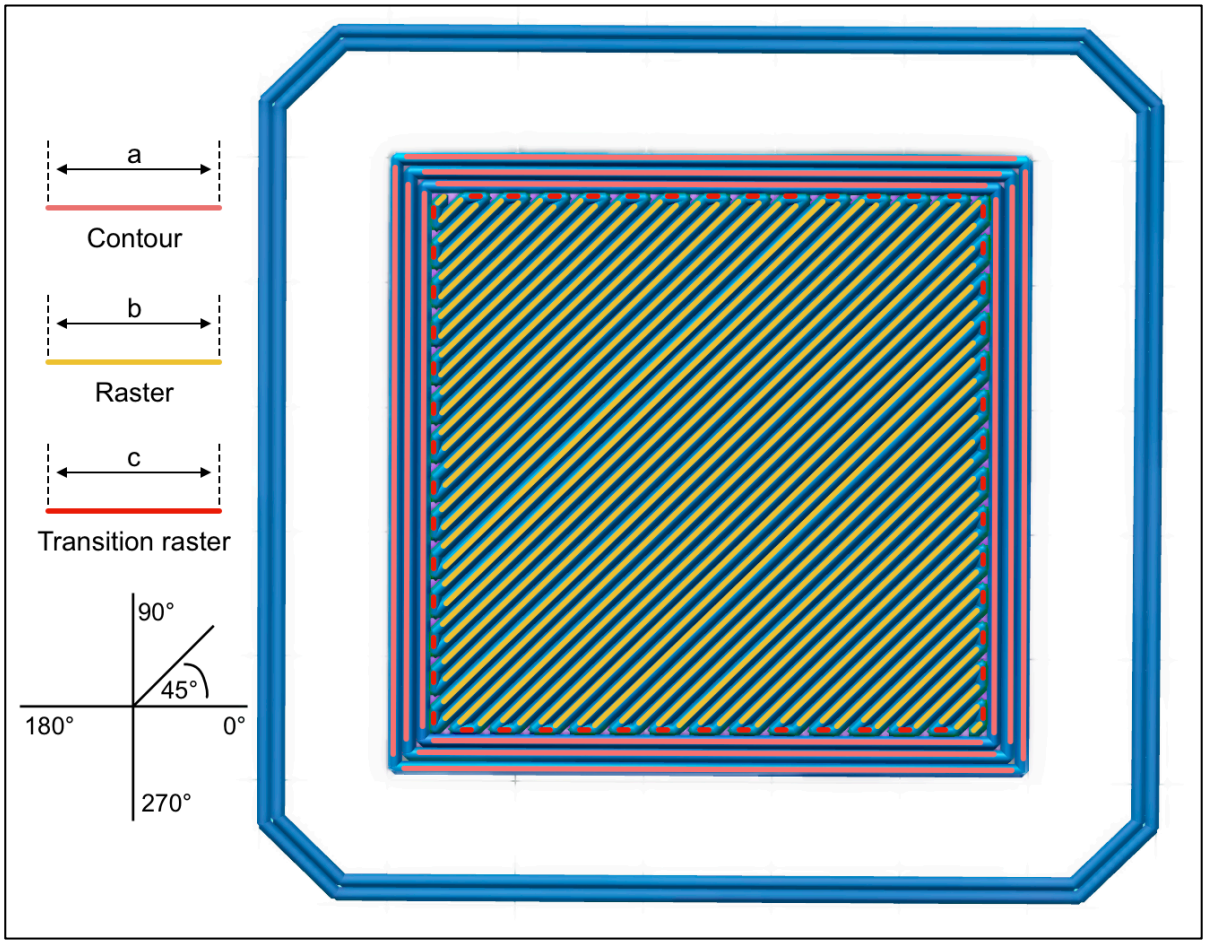


The workpiece used as a reference for the development of the segmentation script consists of the elements mentioned in Figure 4.1. Among them, it is noticeable that the skirt and the external pattern exhibit similarities in terms of their fill behavior. These similarities lie in the fact that both the skirt and the external pattern feature multiple contour lines, some of which are fabricated at orthogonal angles (0°, 90°, 180°, 270°). This complicates the ability of the

segmentation script to utilize this fill behavior (orthogonal fabrications on one of the axes), as the segmentation could confuse the contour lines of the skirt (which are not part of the workpiece itself) with the contour lines of the external pattern.

Because of this, another fill behavior was chosen. The primary criterion for segmentation was defined as the identification of the separation point between the external and internal patterns. This point was found through a fill behavior that considers the lengths of the contour and raster lines. Since the fabrication of the contour lines of the EIP takes significantly longer than the initial raster lines of the IIP, as verified by the displayed length of the contour lines in Figure 4.2 the script seeks to find, by the duration of the fabrication (in number of samples), the signal index where there is a significant drop in perceived duration.

Figure 4.2 – Study A workpiece with identifications of each contour line, raster line, and transition between raster lines (transistion raster)

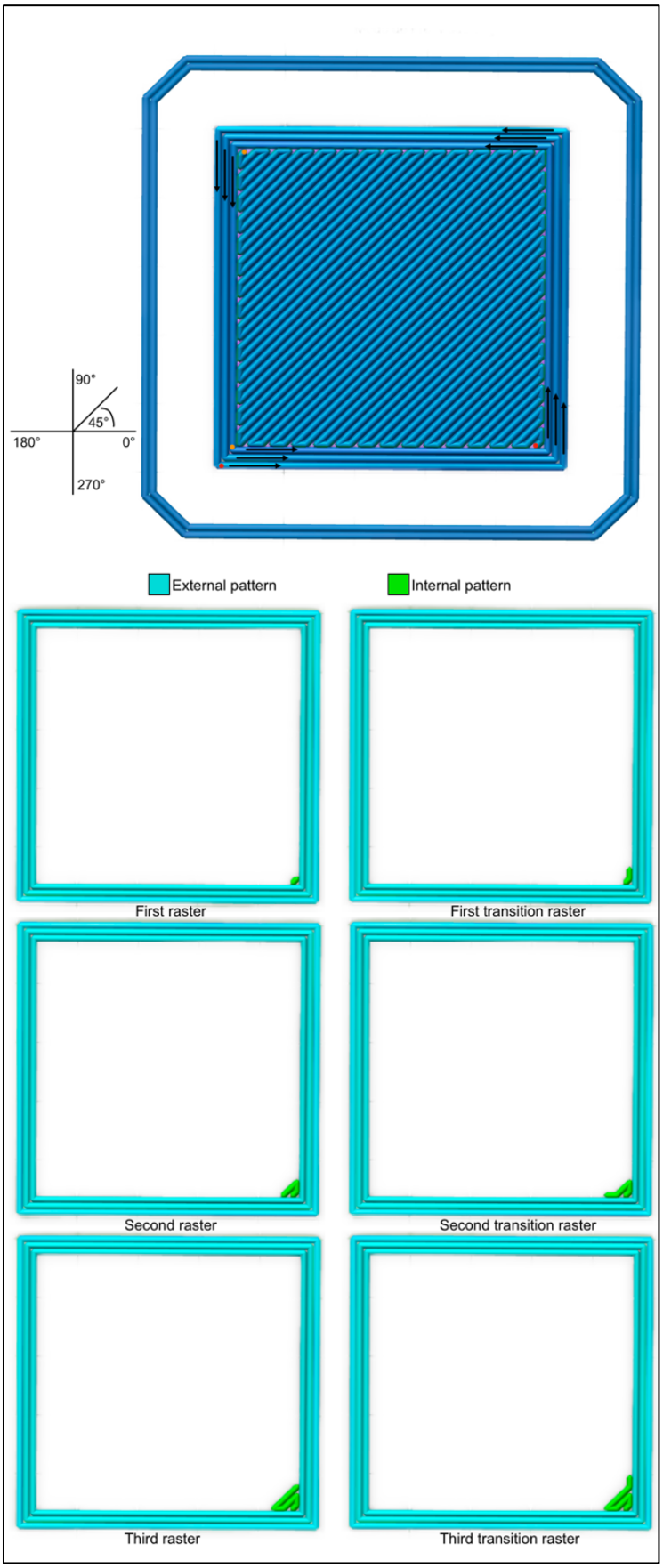


4.1.1.1 STUDY A: SEGMENTATION OF THE EXTERNAL AND INTERNAL PATTERNS

After identifying the separation point between the EIP and IIP, the script aims to segment the external contour lines. For this, the fill behavior of the EIP was used, as verified in Figure 4.2:

- The 4 contour lines furthest from the center are the first to be fabricated, have approximately the same length among themselves, and have the longest length among the lines of the EIP;

Figure 4.3 – Study A workpiece internal pattern fabrication behaviour, with the visualization of the first, second and third raster and transtion raster lines



- The 4 middle contour lines, fabricated after the 4 contour lines furthest from the center, have approximately the same length among themselves and are shorter than the 4 contour lines furthest from the center;
- The 4 contour lines closest to the center, fabricated after the 4 middle contour lines, have approximately the same length among themselves, have the shortest length among the contour lines, and are the last contour lines before the separation point between fill patterns.

After identifying the separation point between the EIP and IIP and completing the segmentation of the external pattern, the script aims to segment the raster lines and transition raster lines. For this, the fill behavior of the IIP was used, as partially verified in Figure 4.3:

- The raster lines are fabricated at angles of 45° and 225° (180° + 45°);
- The raster lines increase in length from the first fabrication to the midpoint of the workpiece, reversing to a behavior of decreasing length from the midpoint to the last fabrication;
- The raster lines increase/decrease in length by an almost constant value;
- The transition raster lines are fabricated at angles of 90° and 180°;
- The transition raster lines have an almost constant length among themselves;
- A raster line fabrication is always preceded and succeeded by transition raster lines, except for the first and last raster lines;
- The first and last raster lines have a shorter length than the length of the transition raster lines.

4.1.2 STUDY A: CONSIDERATIONS BASED ON FABRICATION MOVEMENTS

To carry out the fabrication of the external fill pattern, considering the geometry of the workpiece represented Figure 4.2, some repositioning Movements Without Deposition (MWD) are required.

These MWD, represented in Figure 4.4, are highlighted in Table 4.1, which presents all the movements used for the fabrication of the EIP:

- The first group of MWD, composed of code lines G 247 and G 248, represented in the first row of Figure 4.4, occurs during the repositioning from the final fabrication point of the skirt to the starting fabrication point of the first contour line (code line G 251).
- The second group of MWD, composed of code lines G 255, G 256, and G 258, represented in the second row of Figure 4.4, occurs during the repositioning from the final fabrication point of the contour lines furthest from the center to the starting fabrication point of the middle contour lines (code line G 260).
- The third group of MWD, composed of code lines G 264 and G 265, represented in the third row of Figure 4.4, occurs during the repositioning from the final fabrication point of the middle contour lines to the starting fabrication point of the contour lines closest to the center (code line G 267).
- The fourth group of MWD, composed of code lines G 271 and G 273, represented in the fourth row of Figure 4.4, occurs during the repositioning from the final fabrication point of the contour lines closest to the center to the starting fabrication point of the lines of the IIP (raster and transition raster).

Table 4.1 - External printing pattern movements for *Test1*

Contour printing		Movements Without Deposition (MWD)		Contour Printing sequential to a MWD	
X Coordinate	Y Coordinate	G-code line	Contour line	X direction	Y Direction
215.747	148.508	247	0	0	0
220.297	150.554	248	0	Left	Up
244.747	150.554	251	1	Left	Up
244.747	175.004	252	2	Right	Up
220.297	175.004	253	3	Left	Up
220.297	150.654	254	4	Left	Down
220.297	150.554	255	0	Left	Down
222.297	150.554	256	0	Right	Down
220.847	151.104	258	0	Left	Up
244.197	151.104	260	5	Right	Up
244.197	174.454	261	6	Right	Up
220.847	174.454	262	7	Left	Up
220.847	151.204	263	8	Left	Down
220.847	151.104	264	0	Left	Down
221.397	151.654	265	0	Right	Up
243.647	151.654	267	9	Right	Up
243.647	173.904	268	10	Right	Up
221.397	173.904	269	11	Left	Up
221.397	151.754	270	12	Left	Down
221.397	151.654	271	0	Left	Down
242.865	152.121	273	0	Right	Up

4.1.3 STUDY A: SCRIPT SEGMENTATION OPERATION

The **`fff_segmenter`** script works with both MATLAB and Octave. The segmentation operations work in a similar manner for both software's, with the major distinction being the user input and the script outputs format.

4.1.3.1 STUDY A: USER INPUT

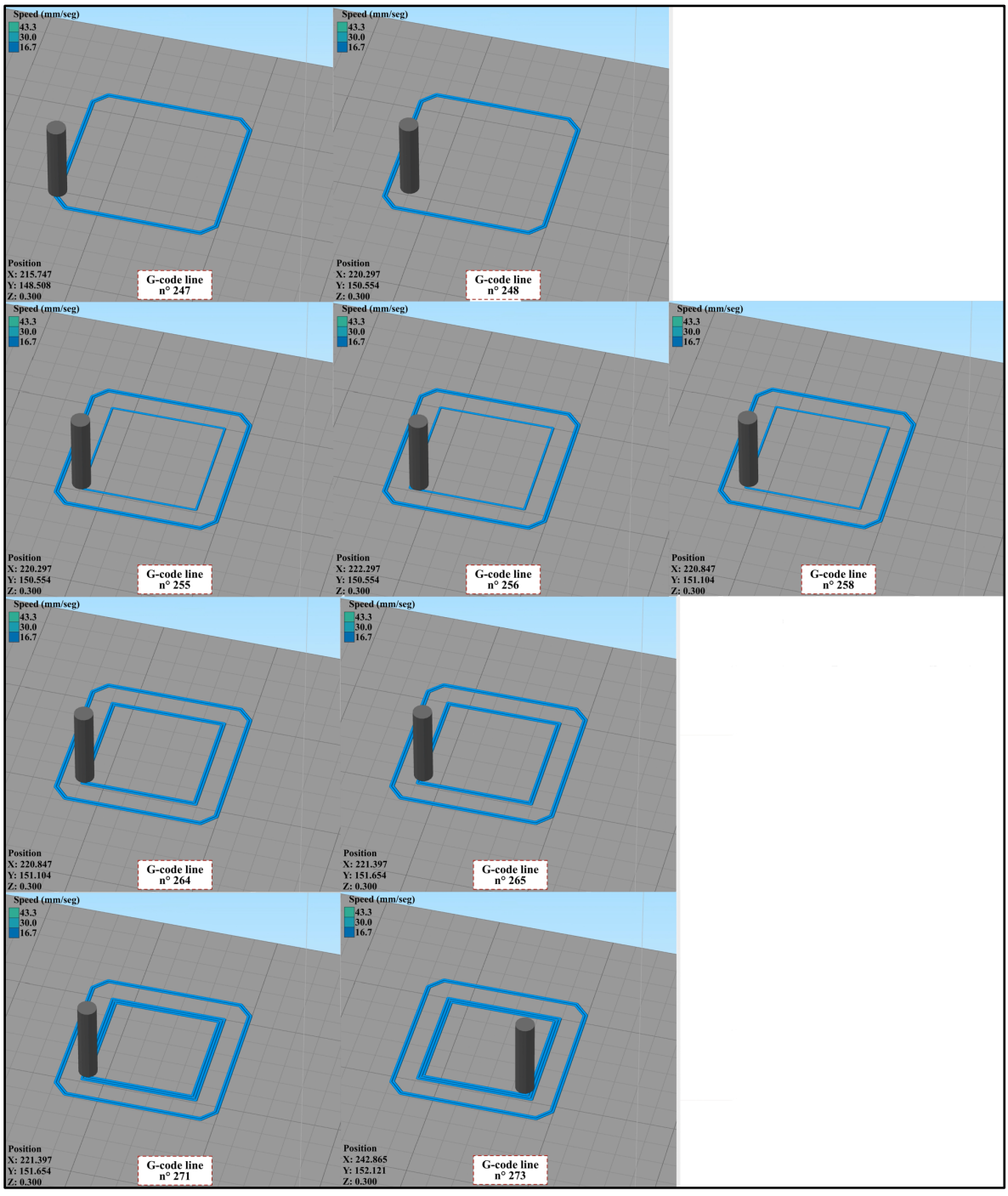
4.1.3.1.1 STUDY A: MATLAB INPUT APP

In order to allow for a facilitated users method for input and selection of options, a simple MATLAB App GUI was designed. As illustrated in Figure 3.10, the app interface comprises several sections and fields to streamline the users input and selection of options for the **`fff_segmenter`** script.

At the top, the "Select data" button allows users to navigate between the folders and choose the dataset, in .mat format, for analysis. Next to this button is a field for specifying the

sampling frequency (*Fs*) used in the data acquisition process of the selected dataset, ensuring that the data is accurately processed according to the correct acquisition rate.

Figure 4.4 – Study A workpiece fabrication Movement Without Deposition (MWD) *Test1* detailing, with visualization of the positions regarding the MWD G-code lines



Below this, there are fields for "Raw signal identification", "DirX identification", and "DirY identification". These fields are intended for users to input the identifiers for the raw monitoring sensor signal and the directional signals (X and Y), respectively, ensuring proper signal identification.

In the middle section, users can select the segmentation mode for the **`fff_segmenter`** script. There are options for choosing either `Points` or `Segments` modes. When

`Points` mode is selected, users must also specify the unit for segmentation, choosing between `Number of samples` and `Seconds`, as indicated by the radio buttons on the right side.

The lower part of the interface includes toggles for additional functionalities in the **`fff_segmenter`** script. Users can enable or disable "Obtain graphical visualization" to obtain a graphical visualization of the segmentation results. If visualization is enabled, there is an option to "Save graphical visualization if obtained", ensuring that the generated graphs can be stored for further analysis. Another toggle allows users to "Obtain automatic .mat files", facilitating the automatic generation of MATLAB files from the segmented data.

Finally, the large switch labeled "*`Run`* the segmentation" at the bottom right is used to initiate the segmentation process. When toggled to "*`On`*", the main **`fff_segmenter`** script resumes execution and also close the app GUI.

4.1.3.1.2 STUDY A: OCTAVE INPUT USER INTERFACE

In order to allow for a facilitated users method for input and selection of options, a simple Octave UI was designed. As illustrated in Figure 3.12, the UI interface comprises several sections and fields to streamline the users input and selection of options for the **`fff_segmenter`** script.

The fields for "Raw signal identification", "DirX identification", and "DirY identification" are intended for users to input the identifiers for the raw monitoring sensor signal and the directional signals (X and Y), respectively, ensuring proper signal identification.

The field for "Sampling frequency" is intended for users to input the numerical value of the sampling frequency (*`Fs`*) used in the data acquisition process of the selected dataset, ensuring that the data is accurately processed according to the correct acquisition rate.

In the same UI, users can select the segmentation mode for the **`fff_segmenter`** script. There are options for choosing either `Points` or `Segments` modes. The default segmentation mode is `Points`.

When `Points` mode is selected, users must also specify the unit for segmentation, choosing between `Number of samples` and `Seconds`. The default segmentation unit is `Number of samples`.

The lower part of the interface includes fields for additional functionalities in the **`fff_segmenter`** script. Another field allows users to opt for "Auto save files (Y/N)", facilitating the automatic generation of MATLAB files from the segmented data. The default save results option is `N` for no.

Users can enable or disable "Generate figure (Y/N)" to obtain a graphical visualization of the segmentation results. The default generate figure option is `N` for no.

If visualization is enabled, there is an option to "Save figure" ensuring that the generated graphs can be stored for further analysis. The default save figure option is `N` for no.

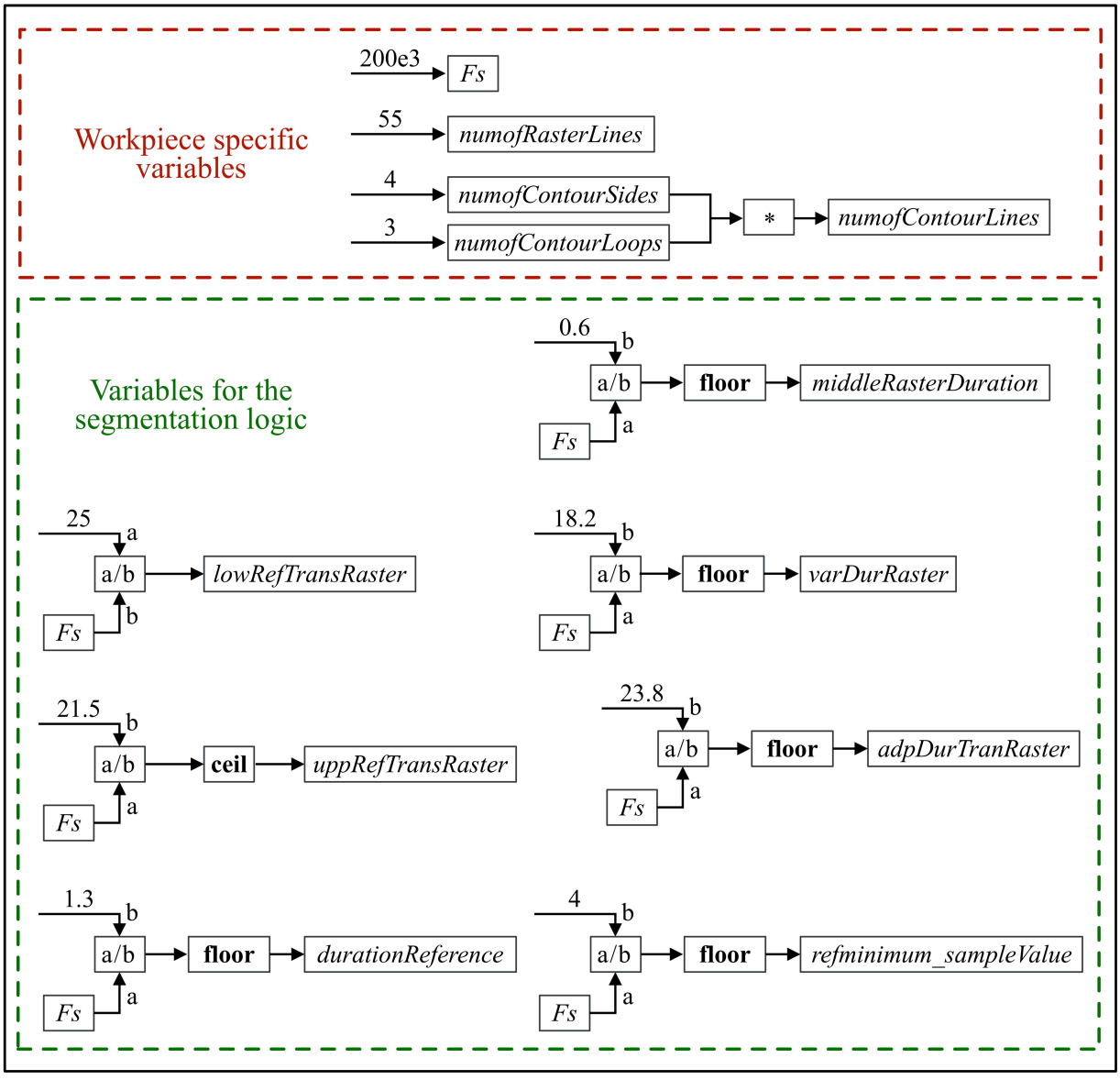
With the press of the Enter button on the keyboard the main **`fff_segmenter`** script resumes execution and also closes the UI.

4.1.3.2 STUDY A: ATRIBUTING SPECIFIC VARIABLES

The schematic displayed on Figure 4.5 shows how specific variables are attributed based on the geometry of the workpiece and are necessary for the present segmentation logic

in the **`fff_segmenter`** script. It is important to point out that these variables are specific to the geometry of the workpiece, as well as to the printing parameters/process settings utilized in the preparation of the workpiece G-code (slicing process). In particular, the speed of the first layer fabrication is the most impactful to the segmentation logic variables displayed below.

Figure 4.5 – Schematic representing the workpiece specific variables values, and the necessary variables values for the segmentation logic utilized in the study A



4.1.3.2.1 STUDY A: WORKPIECE SPECIFIC VARIABLES

The first part of the Figure 4.5 code assigns values to variables that are specific to the geometry of the workpiece. These variables, such as the number of raster lines (`numofRasterLines`), contour sides (`numofContourSides`), and contour loops (`numofContourLoops`), could be obtained by parsing the workpiece's G-code.

In the given code, `numofRasterLines` is set to 55, `numofContourSides` is set to 4, and `numofContourLoops` is set to 3. The total number of contour lines is then calculated as the product of `numofContourSides` and `numofContourLoops`, resulting in 12 contour lines. The value of 3 for the `numofContourLoops` can be found directly in the

workpiece G-code, on line 31 in the comment regarding the `perimeterOutlines` process parameter, as represented in the Appendix I. A script could be designed to parse the G-code and automatically set the value for the *`numofContourLoops`* variable.

To find the *`numofContourSides`* value of 4, a script could be designed to parse the G-code and identify the commands for the outer perimeter involving filament deposition (parameter E) with sufficient displacement. This can be evaluated by calculating the variance in the X and Y parameters along the code lines. In the workpiece, an example of these commands is displayed from line 251 to line 254 in regard to the contour lines furthest from the center, as shown in Appendix I.

Similarly, to determine the *`numofRasterLines`*, a script could be designed to parse the G-code and identify the commands for the `solid layer` that exhibit higher variability in filament deposition (parameter E) with sufficient displacement. This can also be evaluated by calculating the variance in the X and Y parameters along the code lines. An example of these commands is visible Appendix I, from lines 328 to 329 and lines 330 to 331, representing the raster lines and transitions between raster lines on the middle region of the internal printing pattern.

However, it is important to note that this procedure was not implemented in the current version of the **`fff_segmenter`** script due to the lack of necessity. As previously mentioned, the **`fff_segmenter`** script was developed with a specific part geometry and consistent process parameters across the available example datasets, making the workpiece-specific variables constant. In its present version, the **`fff_segmenter`** script fully meets the signal segmentation needs of the Laboratory of Data Acquisition and Signal Processing (LADAPS) research group, which the author of the present thesis, who developed the **`fff_segmenter`** script to its current version, is part of.

Further development of the **`fff_segmenter`** script by the FOSS community could focus on developing and incorporating these automatic scripts that parse the G-code of various workpieces to obtain the appropriate values for the workpiece-specific variables. This would enhance the script's versatility and applicability to different geometries and printing conditions.

4.1.3.2.2 STUDY A: SEGMENTATION LOGIC VARIABLES

The next section of the Figure 4.5 code defines variables essential for the segmentation logic. These variables rely on the *`Fs`*. In the available example datasets, the sampling frequency used for acquiring the signals was constantly 200 kS/s. However, the code uses the *`Fs`* variable instead of the direct numerical value of 200e3 in the mathematical calculations for these variables. This approach allows for flexibility in altering the sampling frequency if the same workpiece and process parameters are used in future signal acquisition processes.

Another major factor for the segmentation logic variables is the speed value for the first layer fabrication. The numerical values utilized in the mathematical calculations below were obtained considering a fixed value of the first layer printing speed for the fabrications from which the three available datasets originated. The used default printing speed is 20 mm/s, and the first layer speed percentage regarding the default printing speed is 100. Therefore, the printing speed was 20 mm/s throughout the fabrication of the workpiece.

The variables for the segmentation logic include:

- *lowRefTransRaster*: Lower number of samples reference value for the transition raster, calculated as *Fs*/25.
    - This variable is used to define the low range reference value for the transition between raster lines duration. Considering the *Fs* of 200e3, the value calculated by 200e3/25 with the **round** command is 8,000 samples, which was found to be adequate as a lower range reference for the transition between raster lines with the used printing speed of 20 mm/s.
- *uppRefTransRaster*: Upper number of samples reference value for the transition raster, calculated as **round**(*Fs*/22.2222,0).
    - This variable is used to define the upper range reference value for the transition between raster lines duration. Considering the *Fs* of 200e3, the value calculated by 200e3/22.2222 with the **round** command is 9,000 samples, which was found to be adequate as an upper range reference for the transition between raster lines with the used printing speed of 20 mm/s.
- *varDurRaster*: Variation of the duration between raster lines, calculated as **round**(*Fs*/18.1818,0).
    - This variable is used to define the default value for the variation between raster lines durations. Considering the *Fs* of 200e3, the value calculated by 200e3/18.1818 with the **round** command is 11,000 samples, which was found to be adequate as a default value for the variation between raster lines durations with the used printing speed of 20 mm/s.
- *adpDurTranRaster*: Adopted duration for the transition raster, calculated as **round**(*Fs*/23.8095,0).
    - This variable is used to define the default reference value for the transition between raster lines duration. Considering the *Fs* of 200e3, the value calculated by 200e3/23.8095 with the **round** command is 8,300 samples, which was found to be adequate as a default reference value for the transition between raster lines with the used printing speed of 20 mm/s.
- *DurationReference*: Known duration for the last contour printing, calculated as **round**(*Fs*/1.33333,0).
    - This variable provides a reference duration for the final contour line, assisting in determining the end of the external printing pattern. Considering the *Fs* of 200e3, the value calculated by 200e3/1.33333 with the **round** command is 150,000 samples, which was found to be adequate as a duration reference for the last contour printing with the used printing speed of 20 mm/s.
- *refminimum_sampleValue*: Minimum number of samples reference for the **test_Minvariations** subfunction, calculated as **round**(*Fs*/4,0).
    - This variable sets the minimum number of samples required for the **test_Minvariations** subfunction to validate specific signal variations. Considering the *Fs* of 200e3, the value calculated by 200e3/4 with the **round** command is 50,000

samples, which was found to be adequate as a minimum number of samples required for the **`test_Minvariations`** subfunction with the used printing speed of 20 mm/s.

- *`middleRasterDuration`*: Middle raster duration value, calculated as **`round`**(*`Fs`*/0.645161290322581,0).
    - This variable defines a middle duration for the raster lines, used as a reference in the segmentation process. Considering the *`Fs`* of 200e3, the value calculated by 200e3/0.645161290322581 with the **`round`** command is 310,000 samples, which was found to be adequate as a middle duration for the raster lines with the used printing speed of 20 mm/s.

Further development of the **`fff_segmenter`** script could focus on creating and incorporating automatic scripts to parse the G-code of various workpieces. As an example, one of these scripts could dynamically extract the printing speed, identify key durations for the segmentation logic, calculate the duration for all raster lines printing, and determine the maximum duration to set the *`middleRasterDuration`*, which corresponds to the longest raster line due to the part geometry. This is only one of the calculations that could be made with information extracted from the G-code. The FOSS community could enhance the script versatility and applicability to different printing speeds, geometries, and printing conditions by developing and incorporating these automatic scripts to obtain the appropriate values for the segmentation logic variables.

4.1.3.3 STUDY A: PRE-PROCESSING

One of the necessary pre-processing steps for the segmentation script is the correction of amplitude fluctuations in the control signals for the stepper motors' direction. Such fluctuations were observed in all control signals for direction, in both the *`Test1`* dataset (Figure 4.6) and the *`Test2`* dataset (Figure 4.7). However, it is important to note that more significant amplitude fluctuations were observed in the directional signal for the X stepper motor in the *`Test1`* dataset. This may have occurred due to issues with the data acquisition process for this dataset. To correct these incorrect fluctuations between 0V and 5V, the code shown in Appendix I was applied, which uses a 2V threshold to define values of 0V or 5V.

As a result, directional signals were obtained that displayed values of either 0V or 5V, as shown in Figure 4.8 (*`Test1`* dataset) and Figure 4.9 (*`Test2`* dataset).

To facilitate the representation of acoustic sensor signals alongside the control signals for direction, the code shown in Appendix I was applied. This code employs a sub-function called **`Normaliz3r`** that normalizes data vectors between binary values (0 and 1) or between -1 and 1.

Figure 4.6 - DEBUG Point of Interest 1 (POI-1) for `Test1`, where the raw direction signals of both X and Y axis are visible, and an aproximation on the timeframe between 50s and 55s is displayed for each signal

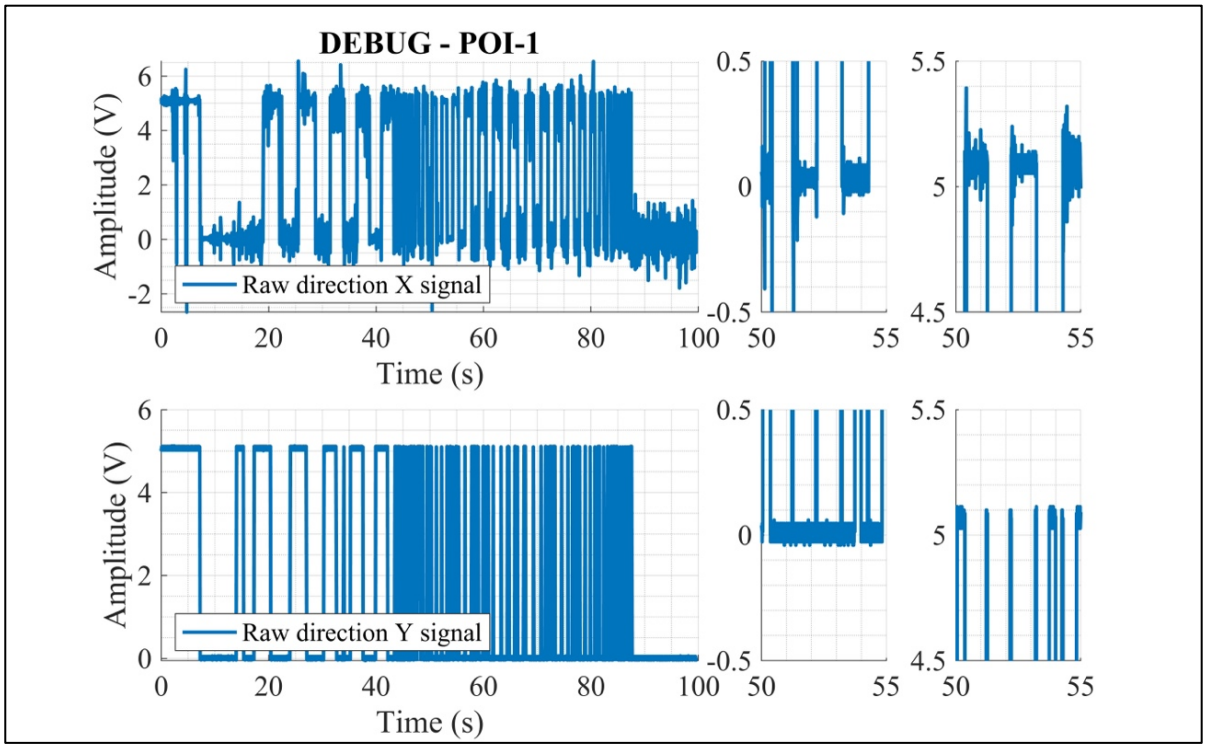


Figure 4.7 - DEBUG Point of Interest 1 (POI-1) for `Test2`, where the raw direction signals of both X and Y axis are visible, and an aproximation on the timeframe between 50s and 55s is displayed for each signal

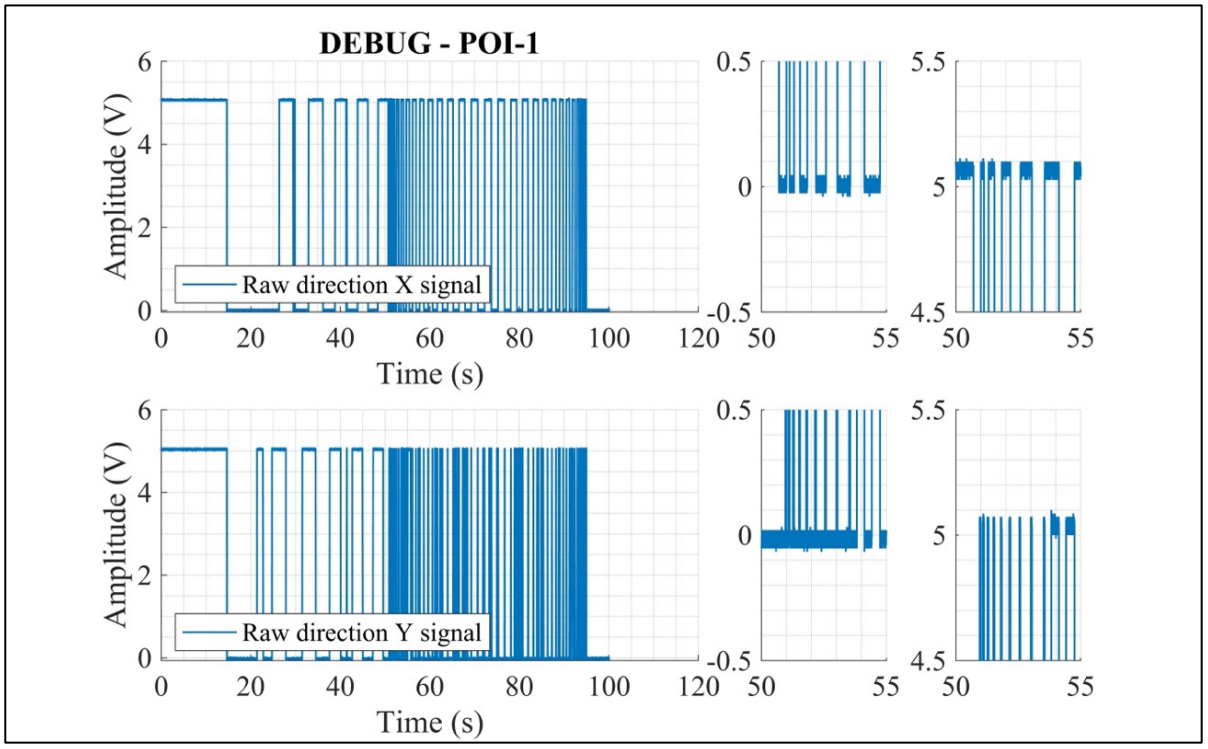


Figure 4.8 - DEBUG Point of Interest 2 (POI-2) for *Test1*, where the raw adjusted direction signals of both X and Y axis are visible, and an aproximation on the timeframe between 50s and 55s is displayed for each signal

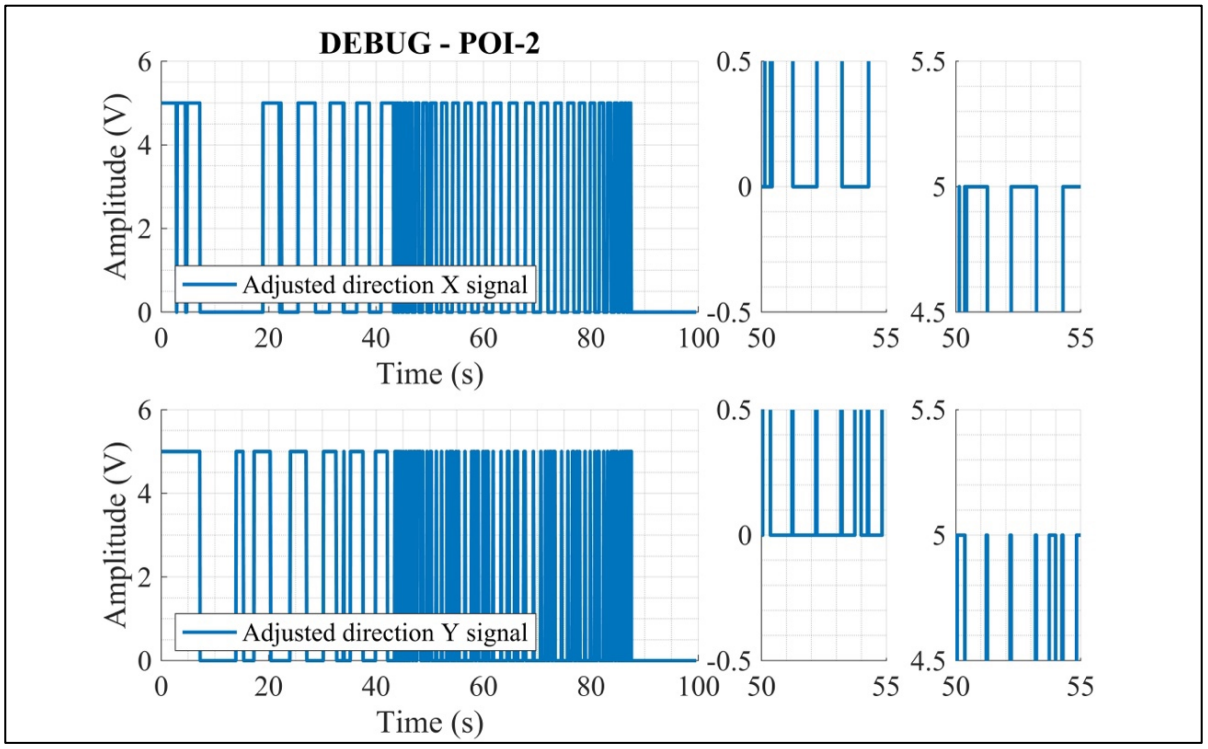
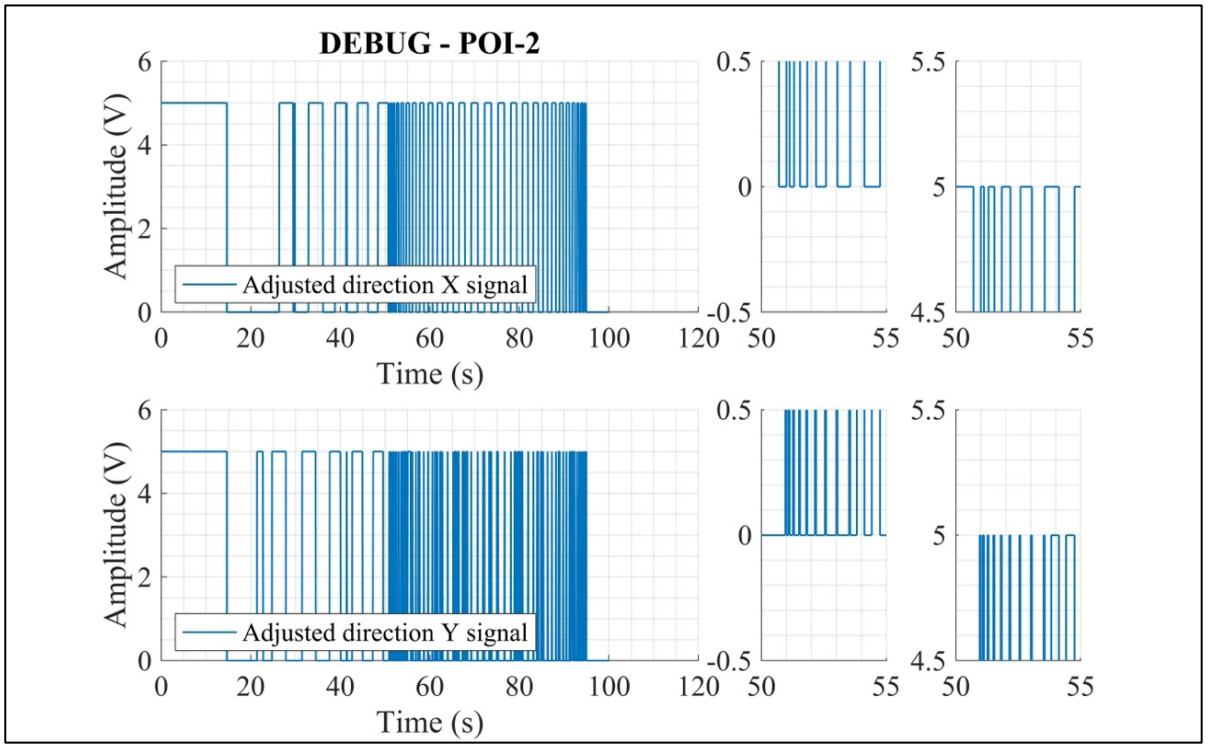


Figure 4.9 - DEBUG Point of Interest 2 (POI-2) for *Test2*, where the raw adjusted direction signals of both X and Y axis are visible, and an aproximation on the timeframe between 50s and 55s is displayed for each signal



As a result, directional signals were obtained that displayed values of either 0 or 1, as shown in Figure 4.10 (*Test1* dataset) and Figure 4.11 (*Test2* dataset).

Figure 4.10 - DEBUG POI-3 for *Test1*

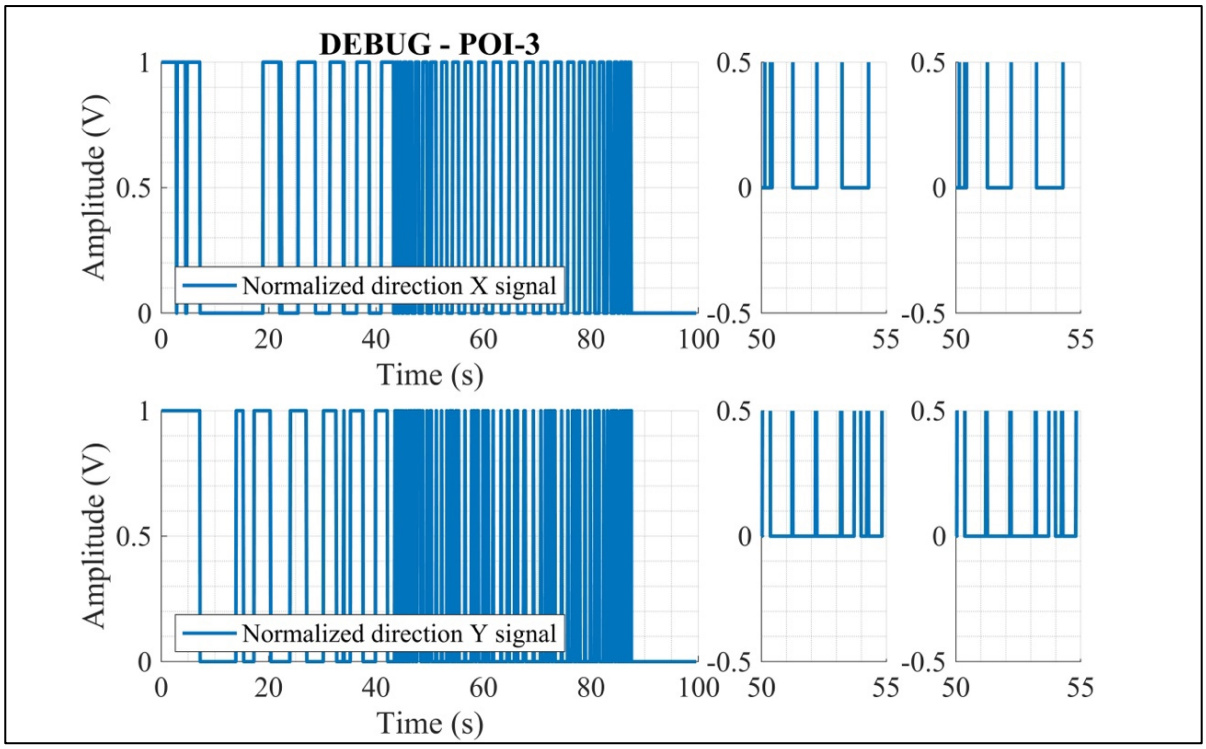
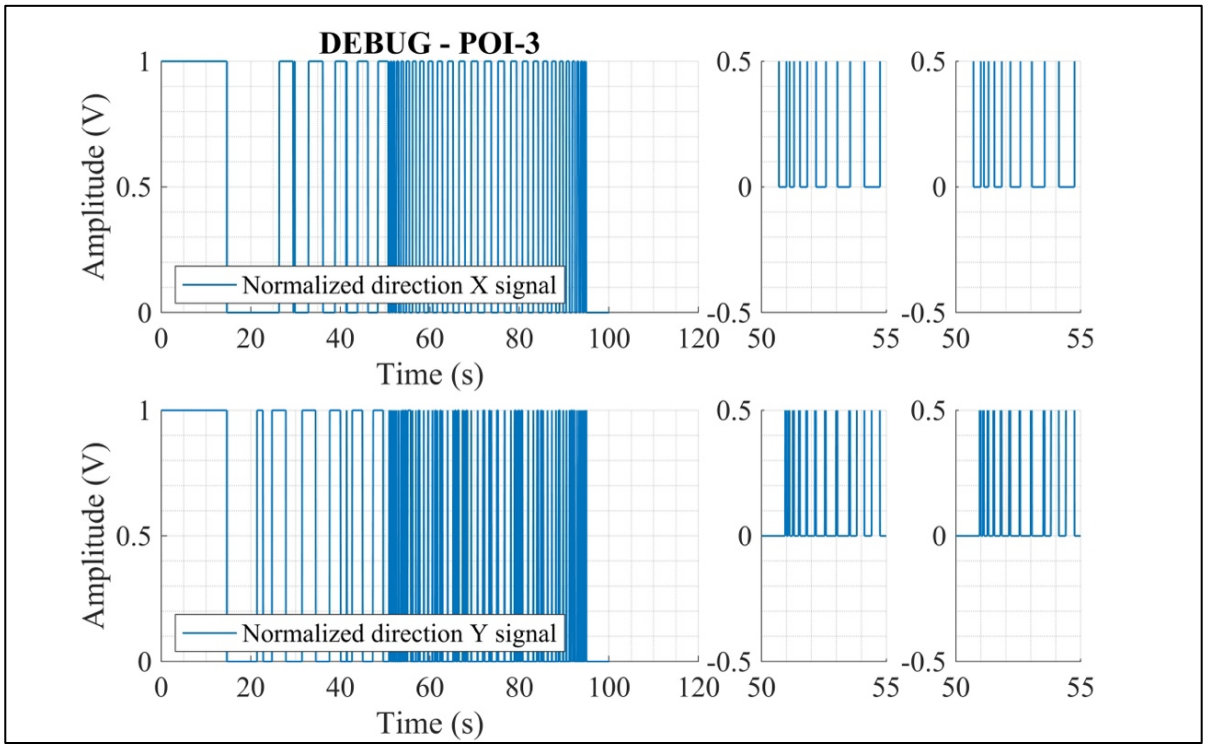


Figure 4.11 - DEBUG Point of Interest 3 (POI-3) for *Test1*, where the normalized direction signals of both X and Y axis are visible, and an aproximation on the timeframe between 50s and 55s is displayed for each signal



Another necessary pre-processing step is the verification of the occurrence of an issue concerning the number of variations (directional changes) in the stepper motor signals. As can be seen in Figure 4.12, specific periods of the directional change signals display a number of variations incompatible with the geometry of the workpiece.

Figure 4.12 - DEBUG Point of Interest 4 (POI-4) for `Test1`, where the normalized direction X signal is visible, alongside an aproximation of the signal on the timeframe between 50.11s and 50.16s, and on the timeframe between 50.133s and 50.135s.

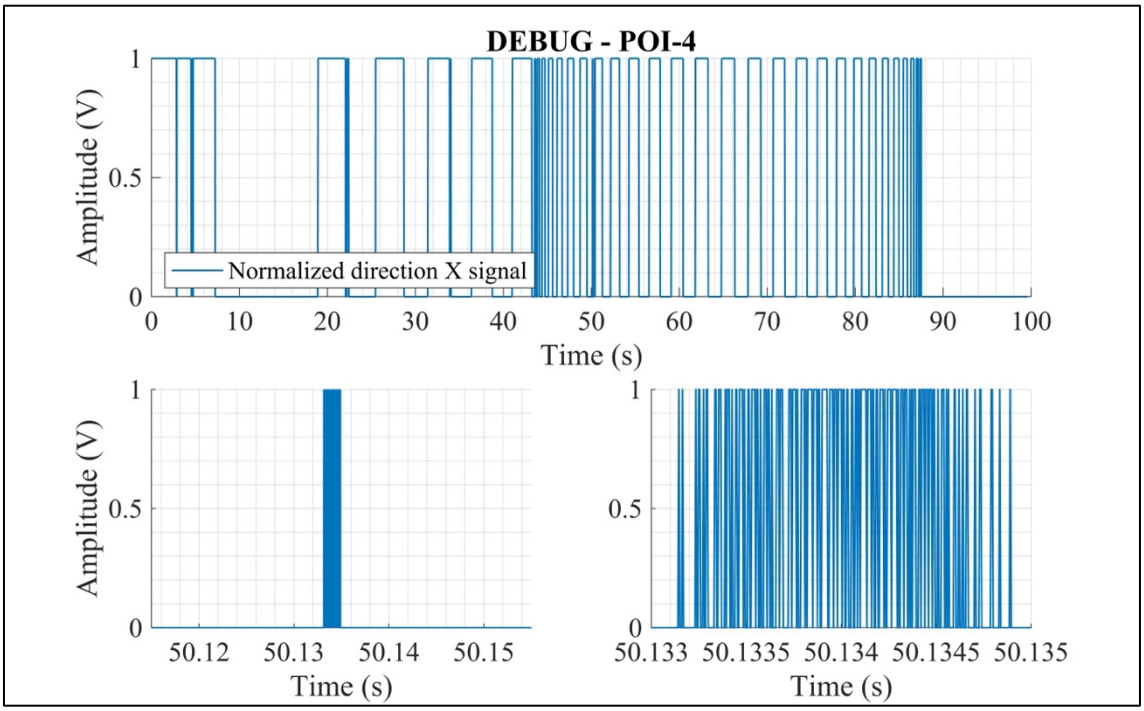
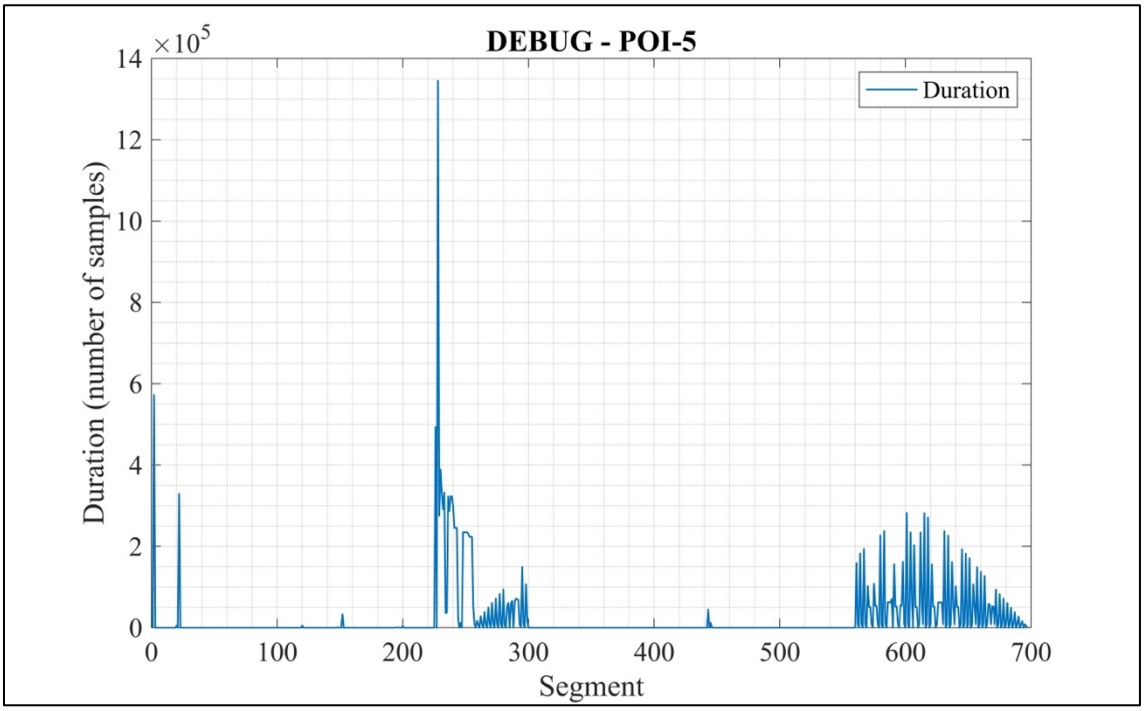


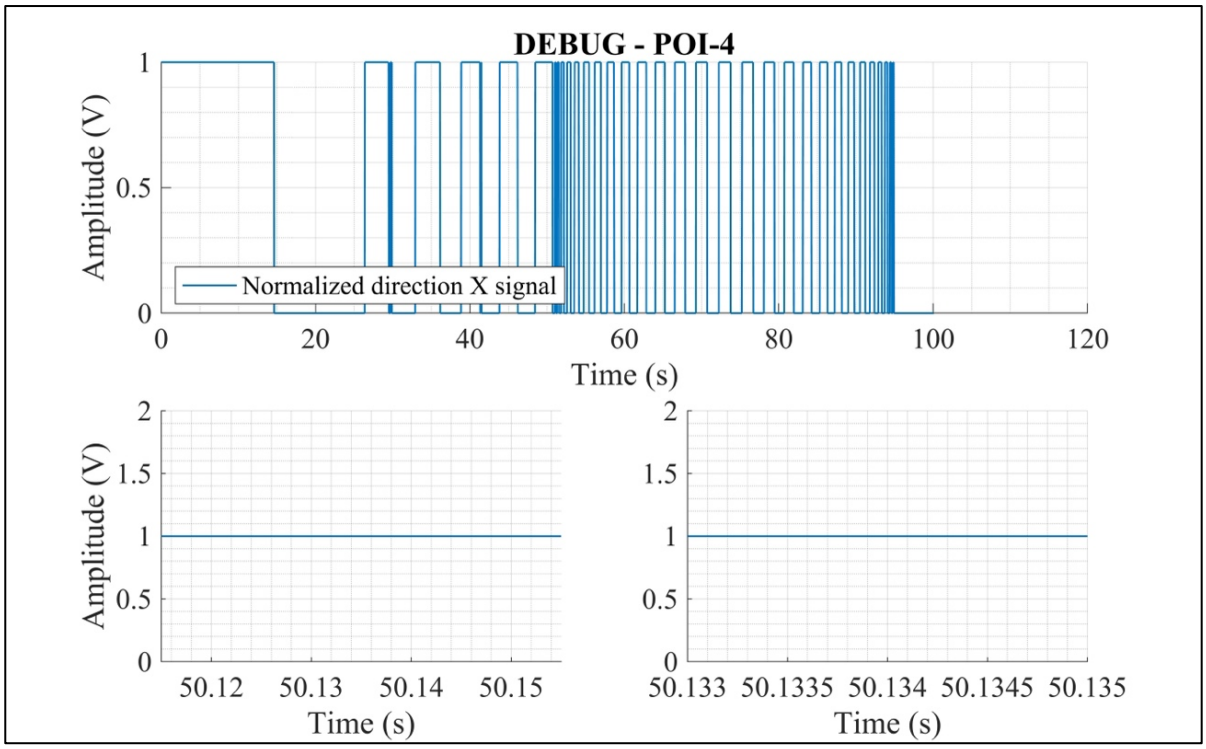
Figure 4.13 - DEBUG Point of Interest 5 (POI-5) for `Test1`, where the duration value for each obtained segment is displayed



This is reflected in the calculation of the `Duration`, which uses the start and end points of the workpiece's manufacturing to calculate the `Duration` of each line, in number of samples, as shown in Figure 4.13. It is believed that this issue occurs only in the directional

signal of the *Test1* dataset, given that the directional signal of the *Test2* dataset, shown in Figure 4.14, does not exhibit this phenomenon.

Figure 4.14 - DEBUG Point of Interest 5 (POI-5) for *Test2*, where the normalized direction X signal is visible, alongside an aproximation of the signal on the timeframe between 50.11s and 50.16s, and on the timeframe between 50.133s and 50.135s.



To verify this occurrence, the code shown in Appendix I was inserted. This code calls the sub-function **test_Minvariations** and returns a *resultProblem* variable as either true or false.

4.1.3.4 STUDY A: EXTERNAL PATTERN SEGMENTATION

The first step for external pattern segmentation is to obtain the *Duration* vector. This is done because, as the printing speed was constant throughout the fabrication of the part, various analyses can be conducted. These analyses relate the length of the fabrication lines (contour, raster, and raster transition) shown in Figure 4.2, with the duration of these fabrication lines in terms of sample numbers.

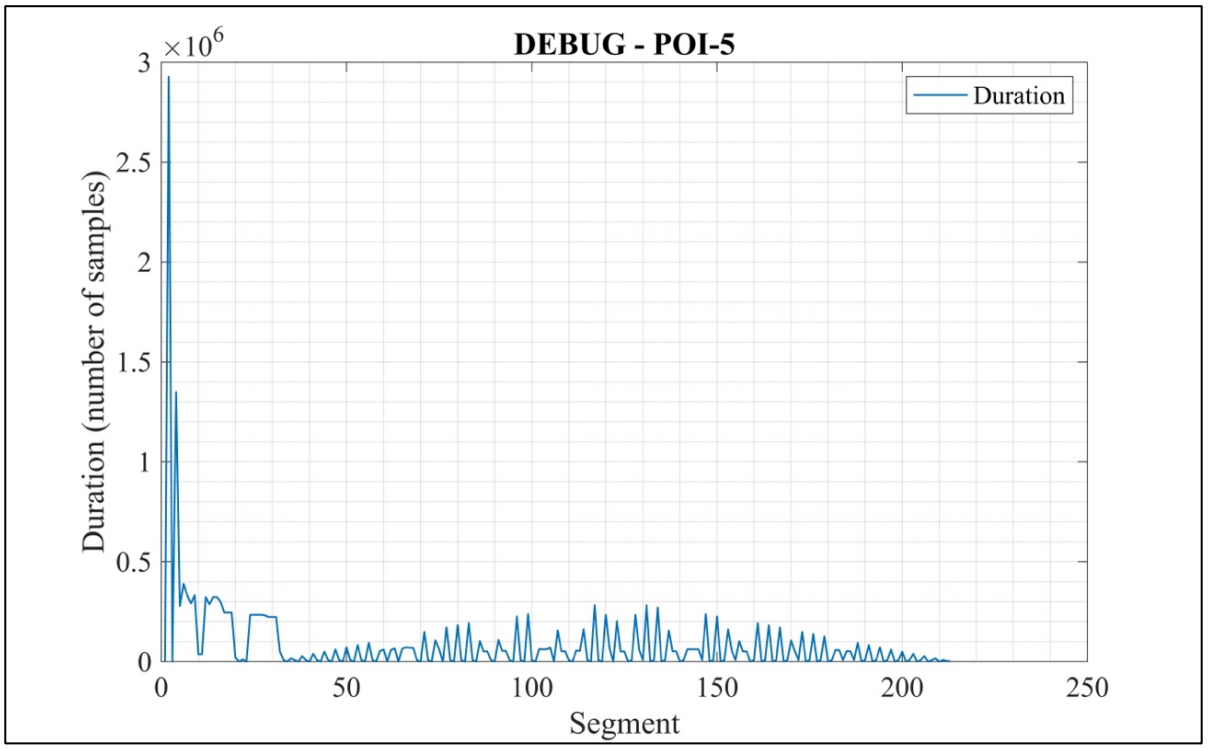
The *Duration* is obtained from the code represented in Appendix I. This code calls the sub-function **obtainDuration** and returns the matrix *Duration*. The first column pertains to the value of the duration itself, the second column is the index related to the endpoint of the fabrication line, and the third column is the index related to the starting point of the fabrication line.

The first column of the *Duration* is represented in Figure 4.13 (*Test1* dataset) and in Figure 4.15 (*Test2* dataset).

Based on these duration values, the separation point between the external and internal fabrication patterns will be identified. To find this separation point, the entire first column of *Duration* is traversed until a known duration value is found (*DurationReference*,

which is the duration of line 12 fabrication). Then, the positions related to the start of the fabrication for lines 10, 11, and 12 are stored. It is known that these three should be very similar, so a test is run on lines 10 and 11. If they are within the same interval, the end of the external pattern is identified. Otherwise, the search for this pattern in the duration values continues.

Figure 4.15 - DEBUG Point of Interest 5 (POI-5) for *Test2*, where the duration value for each obtained segment is displayed



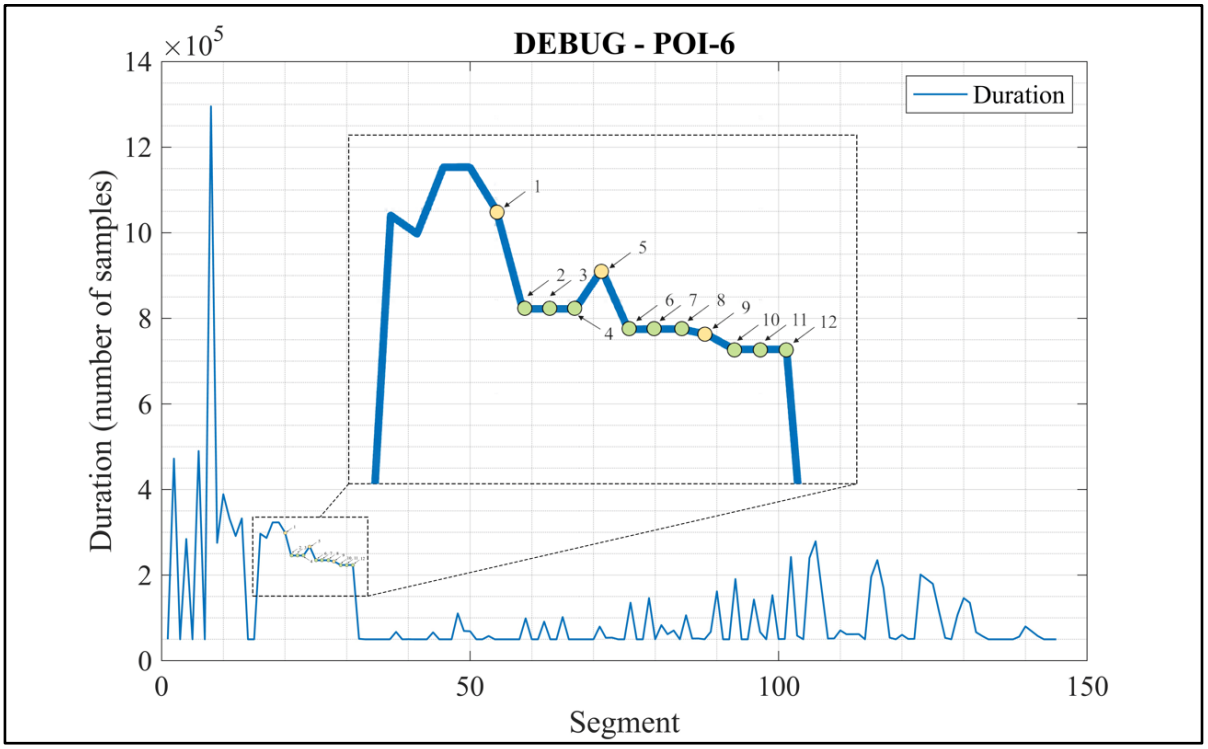
Having identified the separation point, the indices related to the start of the contour lines are found. These indices are stored in the variable *externalLines*. With these starting indices, a temporary matrix related to the contour lines, named *indexContourTemp*, is obtained. The first column pertains to the duration value of the contour line, the second column is the index related to the endpoint of the contour line, and the third column is the index related to the starting point of the contour line.

Obtaining this temporary matrix is necessary because, at a later stage, it will be crucial to identify and separate the periods related to MWD from the external pattern.

Having obtained the temporary matrix for the contour lines, the next step is to obtain the periods related to the MWD and, with these, get the correct contour lines matrix. To find the periods related to the MWD, the information presented in Figure 4.4 and Table 4.1, as discussed earlier, should be referred to.

After analyses correlating the external pattern fabrication phenomena with the obtained duration graph, it was observed that the periods related to the MWD are added to the duration of the subsequent contour lines following an MWD occurrence.

Figure 4.16 - *Test1* Debug Point of Interest 6 (POI-6) MWD's detailing, where the duration value for each obtained segment is displayed alongside an approximation on the segments related to the external pattern



This phenomenon was observed for the *Test1* and *Test2* datasets. However, for the *Test3* dataset, an inverse behavior occurred, where the MWD decreased the duration value of the directly subsequent contour line. This can be observed in Figure 60, between segments 18 and 19. The exact reason for this is undetermined, but it is suspected that there was some type of interference in the data acquisition system during the test for the *Test3* dataset, which led to the absence of some change in either the X or Y direction. The code displayed in Figure 20 represents the obtaining of the MWD periods and subsequently, the correct contour lines matrix.

To obtain the period related to the first group of MWD, the average between the duration values of contour lines 2, 3, and 4 is calculated. This average is stored in the variable *meanContourGroup1*. Afterward, for the cases observed for the *Test1* and *Test2* datasets, the value of contour line 1 is subtracted by the obtained average. The result of this operation represents the correct duration of contour line 1, stored in column 3 of the matrix *adjustedContourLine1*. This duration is then related to the starting index of contour line 2, to find the appropriate index for the start of contour line 1. The remainder represents the duration of the first group of MWD, and this duration is related to the appropriate index for the start of contour line 1, to obtain the index indicating the start of this MWD group. For the case observed in the *Test3* dataset, the only difference in the code (the **`else`** situation on line 16 of Figure 20) is in how the average of contour lines 2, 3, and 4 is related to the duration of contour line 1.

Concerning the second and third groups of MWD, for all three datasets observed, the duration was obtained using the same procedure described as functional for the first MWD

group in the *Test1* and *Test2* datasets, with differences regarding which lines were employed for obtaining the average.

As a result, the matrices *indexContour* and *contourRepositions* were obtained. In these matrices, the first column pertains to the duration value of the contour line or MWD period, the second column is the index related to the endpoint of the contour line or MWD period, and the third column is the index related to the starting point of the contour line or MWD period. It's important to note that the *contourRepositions* matrix is not complete. As verified in Figure 4 and Table 1, there would be a fourth group of MWD, related to the transition period between the fabrication of the last contour line and the first raster line. To determine this fourth MWD group, and consequently complete the *contourRepositions* matrix, it is necessary to proceed to the segmentation of the internal pattern, which will allow determining the index related to the start of the first raster line's fabrication.

4.1.3.5 STUDY A: INTERNAL PATTERN SEGMENTATION

The first step in segmenting the internal pattern is to obtain the duration vector. This is done because, as the printing speed was constant throughout the entire fabrication of the part, various analyses can be performed relating the length of the fabrication lines (contour, raster, and raster transition), as shown in Figure 4.2 and Figure 4.3, to the duration of these fabrication lines in the number of samples.

It's worth noting that, unlike what was done for the external pattern, the issue depicted in Figure 4.13 will not be checked. This is because the internal pattern has very small raster fill lines, as seen in Figure 4.3 for the first raster line.

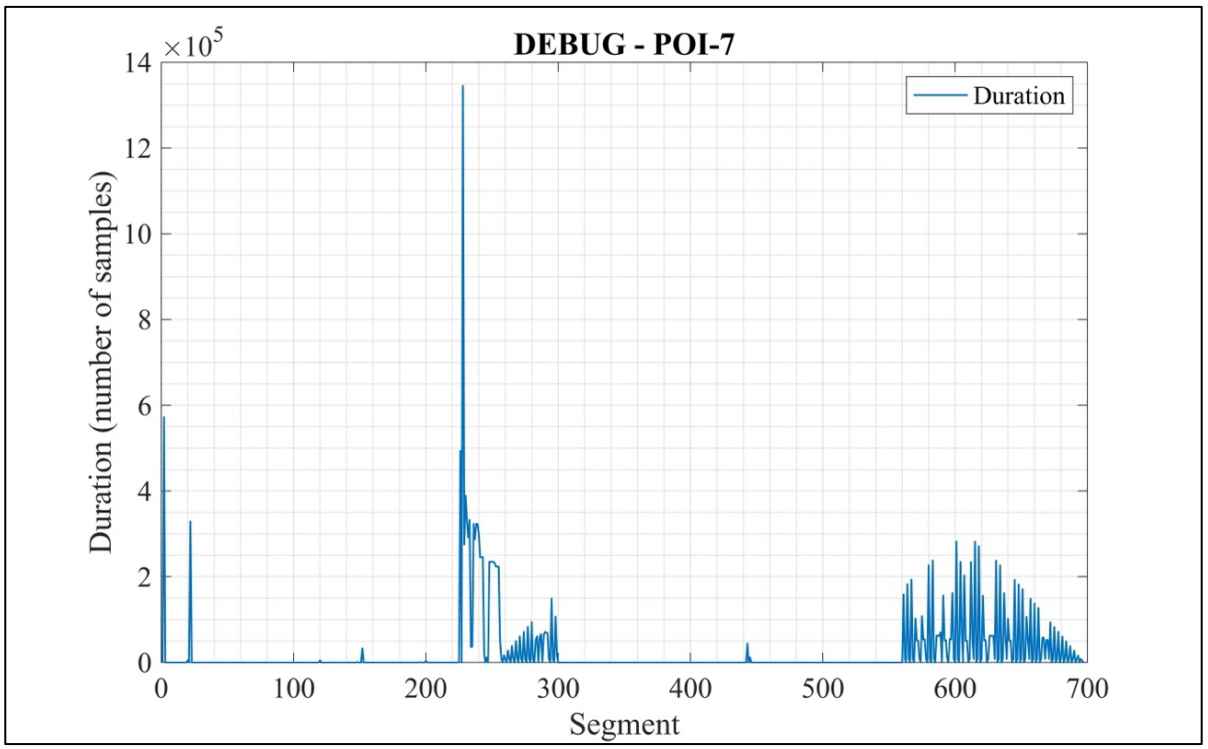
Thus, when calling the sub-function **obtainDuration**, the code shown in Figure 7.10 uses the variable *resultProblem* with a predefined value as `false` and returns the *Duration* matrix. The first column is related to the duration value itself, the second column is the index corresponding to the end point of the fabrication line, and the third column is the index corresponding to the starting point of the fabrication line.

Upon analyzing the duration values obtained from the *Duration* matrix, as shown in Figure 4.17, it was observed that there are significantly more fabrication segments than expected raster lines and raster transitions, as per the geometry of the part represented in Figure 4.2. Analysis in Figure 4.17 reveals that there are many segments with very short duration values. Therefore, it is necessary to apply a threshold filter so that only internal pattern fabrication lines exceeding the shortest expected duration for the internal geometry of the part are represented.

The chosen threshold was 8,000 samples, given that it is known that the raster transition lines have approximately the same length, as depicted in Figure 4.2, and this length, in a signal acquired at a sampling frequency of 200kS/s, represents a duration between 8,100 and 9,000 samples.

Nevertheless, it's important to highlight that there are two lines in the internal pattern with a duration less than 8,000 samples—the first and the last raster lines. However, at this point, the threshold filter will be applied even though segments related to the first and last raster lines will be eliminated. These lines will be obtained later in this analysis, following a manufacturing logic between raster lines and transitions between raster lines.

Figure 4.17 – Debug Point of Interest 7 (POI-7) for `Test1`, where the duration value for each obtained segment is displayed



The code displayed in Figure 7.11 shows how to obtain the `Duration2` matrix with the application of the predetermined threshold. The first column relates to the duration value itself, the second column is the index corresponding to the end point of the fabrication line, and the third column is the index corresponding to the starting point of the fabrication line.

After obtaining the `Duration2` matrix, the segmentation of raster lines and raster transition lines can begin. The segmentation logic will be based on the previously mentioned internal pattern fabrication behavior (Internal Pattern Segmentation). The discussed fabrication behavior is partially verified in Figure 4.18, with the exception of regions with atypical behavior (abnormal).

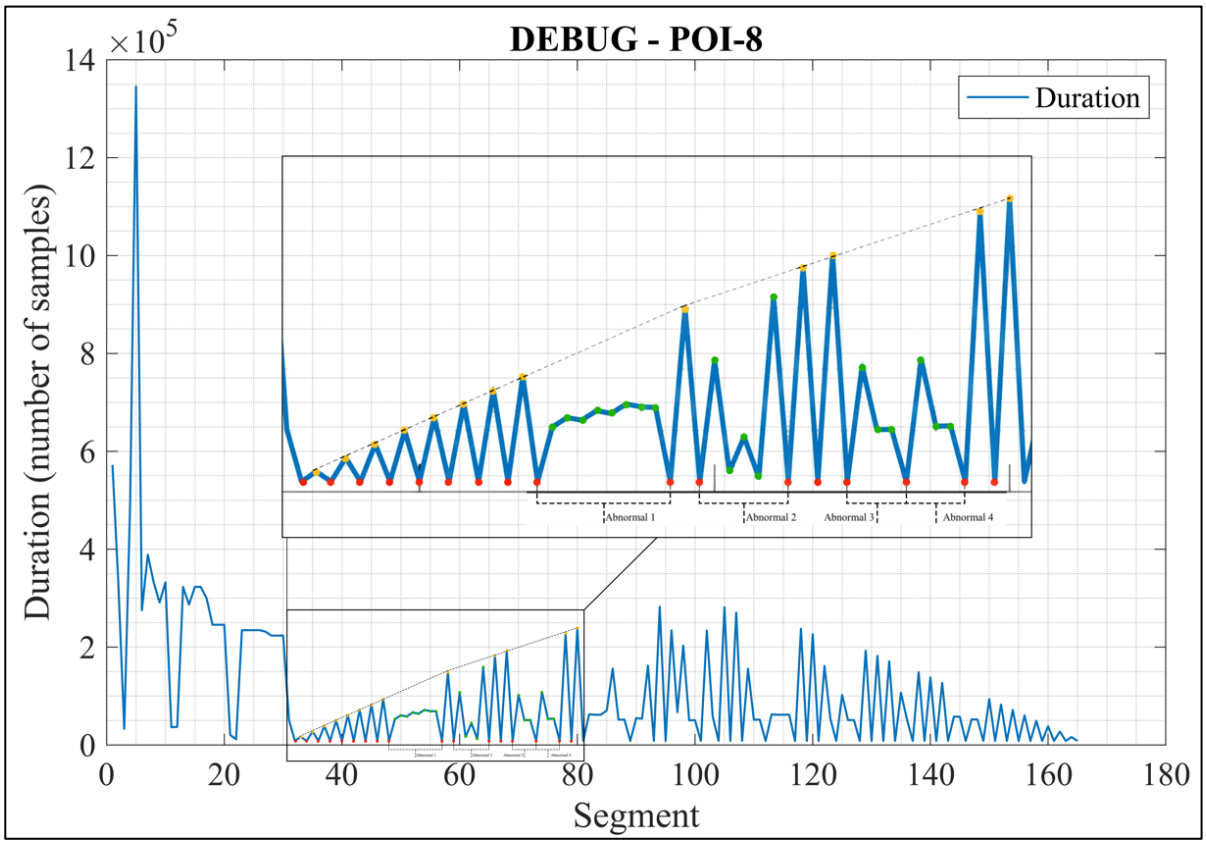
In the abnormal regions identified in Figure 4.18, the following fabrication behaviors are observed:

- Abnormal 1 - There are eight fabrication segments (identified by green circles) between raster transition lines (identified by red circles), where `transitionRaster` -> `rasterLineCount` sets should be observed, with the `rasterLineCount` adding a value of approximately 11,000 samples in duration compared to the directly preceding `rasterLineCount`. This abnormal region is preceded and followed by normal regions;
- Abnormal 2 - There are five fabrication segments (identified by green circles) between raster transition lines (identified by red circles), where `transitionRaster` -> `rasterLineCount` sets should be observed, with the `rasterLineCount` adding a value of approximately 11,000 samples in duration compared to the directly preceding `rasterLineCount`. This abnormal region is preceded and followed by normal regions;

- Abnormal 3 - There are three fabrication segments (identified by green circles) between raster transition lines (identified by red circles), where `transitionRaster -> rasterLineCount` sets should be observed, with the `rasterLineCount` adding a value of approximately 11,000 samples in duration compared to the directly preceding `rasterLineCount`. This abnormal region is preceded by a normal region and followed by abnormal region 4;
- Abnormal 4 - There are three fabrication segments (identified by green circles) between raster transition lines (identified by red circles), where `transitionRaster -> rasterLineCount` sets should be observed, with the `rasterLineCount` adding a value of approximately 11,000 samples in duration compared to the directly preceding `rasterLineCount`. This abnormal region is preceded by abnormal region 3 and followed by a normal region.

It should be noted that such abnormal behavior regions also appear in the `Test2` and `Test3` datasets. However, they relate to different segments than those observed for the `Test1` dataset. Thus, it becomes evident that such abnormal regions occur in the internal pattern fabrication in all evaluated datasets. This characteristic could originate from the data acquisition system or the extruder's control system itself. To determine the source more accurately, more specific tests are required.

Figure 4.18 – Debug Point of Interest 8 (POI-8) for `Test1`, where the duration value for each obtained segment is displayed alongside an approximation on the first third of the internal printing pattern, where multiple abnormal behaviour regions are present



With this understanding, the code shown in Figure 7.12 represents the acquisition of the *Duration3* matrix. Initially, the code locates in the *Duration2* matrix the indices corresponding to rows that have fewer than 9,000 samples and saves them in the vector *linesUdrUppVal*. This vector will serve as a guide for the iteration of the main **for** loop in the script and as a basis for identifying regions of normal and abnormal behavior. Moreover, the code uses the variable *middleRasterDuration* with the value of 310,000 samples, equivalent to the duration of manufacturing the central raster line with a sampling frequency of 200kS/s.

In each iteration of the **for** loop, sequential indices corresponding to the transition raster lines are initially stored. This is done to allow the diagnosis of a normal situation (*transitionRaster -> rasterLineCount -> transitionRaster*), or an abnormal situation (such as those observed in Figure 4.18). This diagnosis is carried out through the subfunction **detectAnom**.

Subsequently, the raster duration values directly preceding and sequentially preceding the current point in the *Duration3* matrix are stored. This allows identification of whether the manufacturing of the internal pattern has reached the raster line immediately subsequent to the middle of the filled area (at which point the **for** loop will end) and provides a reference relative to the duration of the last suitable raster line, necessary for correcting behavior observed in abnormal situations.

Next, the script will proceed to acquire a temporary matrix, named *tempDuration*, following the result of the normal or abnormal situation test. If the test result is `true`, it indicates a normal situation in which the script will proceed to obtain the *tempDuration* matrix by calling the subfunction **isNormal**. On the other hand, if the test result is `false`, it indicates an abnormal situation, in which the script will proceed to obtain the *tempDuration* matrix by calling the subfunction **isAnormal**.

The result obtained from the *tempDuration* matrix is then added to the *Duration3* matrix. The **for** loop continues until one of the two termination situations occurs:

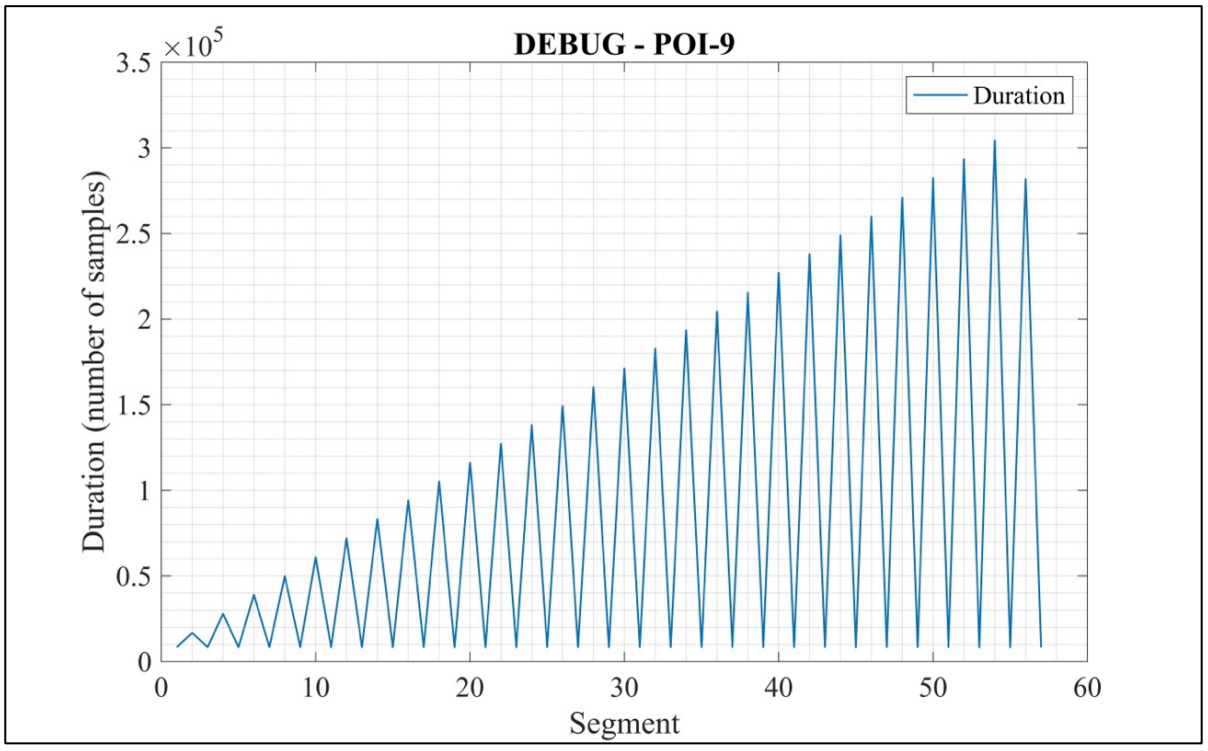
- If the raster duration value directly preceding the current point in the *Duration3* matrix is less than the sequentially preceding raster duration value. This indicates that internal manufacturing has transitioned from increasing to decreasing behavior;
- If the raster duration value directly preceding the current point in the *Duration3* matrix is greater than the duration value contained in the variable *middleRasterDuration*.

For both termination situations, the **for** loop is interrupted upon reaching the midpoint of the IIP manufacturing. The termination conditions may seem redundant, but they allow the segmentation script to handle and correct any deviations should an abnormal situation occur in the region related to the manufacturing of the middle of the internal pattern.

In the obtained *Duration3* matrix, the first column relates to the duration value itself, the second column is the index relative to the end point of the manufacturing line, and the third column is the index relative to the starting point of the manufacturing line. Figure 4.19 represents the duration values corresponding to raster lines and transition raster lines. It is possible to observe that segment 55 represents the manufacturing of the middle raster line, and

segment 57 represents the manufacturing of the first raster line where the behavior changes from increasing to decreasing.

Figure 4.19 - Debug Point of Interest 9 (POI-9) for *Test1*, where the duration value for each obtained segment in regard to the first half of the internal printing pattern is displayed, alongside one raster and two transition rasters segments in regard to the second half of the internal printing pattern



After this, the code shown in Figure 7.13 represents the adjustment of the *Duration3* matrix, leading to the creation of the *Duration3*_v2 matrix. The new matrix was obtained to eliminate the segments with indices higher than the segment representing the fabrication of the middle raster line. This is done to have an internal fill matrix up to the fabrication of the middle line, so as to enable the mirroring of durations in index retrieval. Figure 4.20 displays the duration values related to raster lines and transition raster lines of the part, providing an opportune moment for applying the duration mirroring procedure in index retrieval.

The code shown in Appendix I describes the procedure for duration mirroring in index retrieval. This procedure is based on the internal pattern filling characteristics represented in Figure 4.2 and discussed earlier. In summary, the procedure allows for the automatic retrieval of indices related to raster lines and transition raster lines that make up the fabrication from the midpoint to the end of the internal fill (characterized by a reduction in duration between the raster lines). These duration values are stored in the *Duration4* matrix.

In the obtained *Duration4* matrix, the first column relates to the duration value itself, the second column is the index related to the endpoint of the fabrication line, and the third column is the index related to the starting point of the fabrication line. Figure 4.21 displays the duration values for the IIP fabrications, excluding the first and last raster lines. This can be observed by analyzing Figure 4.21, with a magnification at the start of the IIP where an identification of the second raster lines duration visible in red, and first and second transition between

raster lines durations in green. This allows the observation that the first and last durations represent transition raster segments. Therefore, it is necessary to obtain a sixth matrix with the missing first and last raster lines.

Figure 4.20 - Debug Point of Interest 10 (POI-10) for `Test1` where the duration value for each obtained segment in regard to the first half of the internal printing pattern is displayed

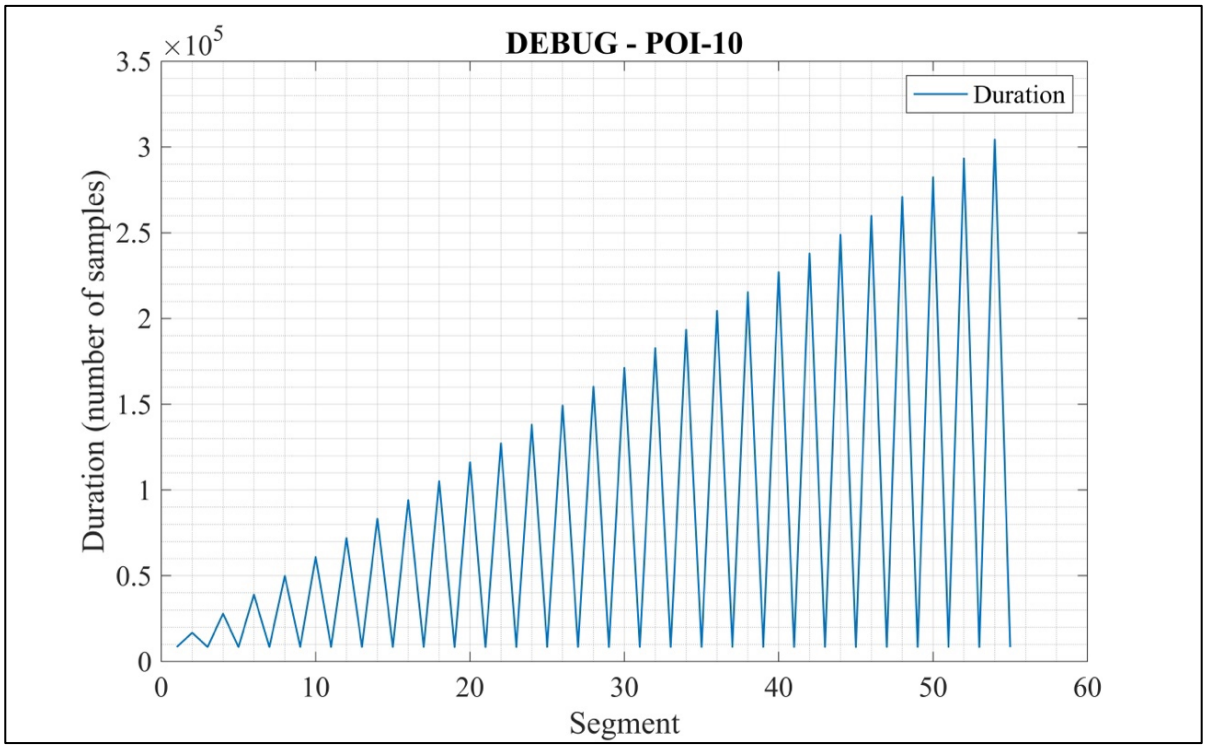
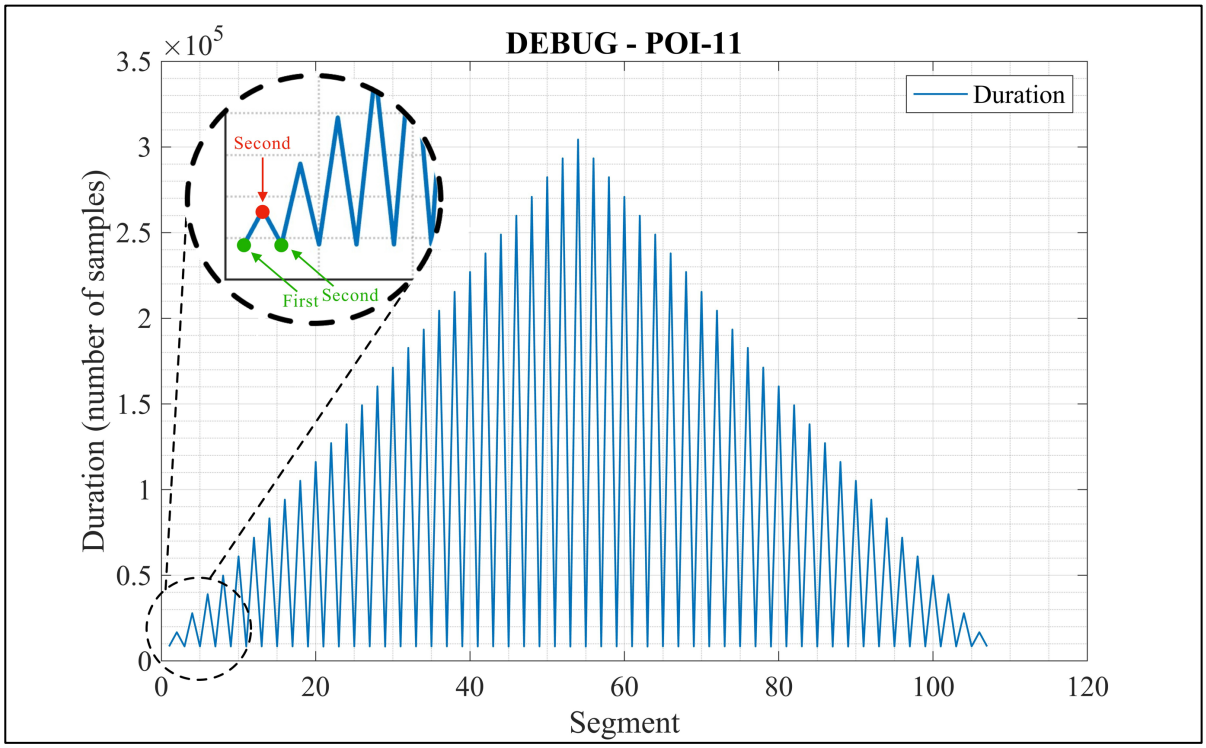


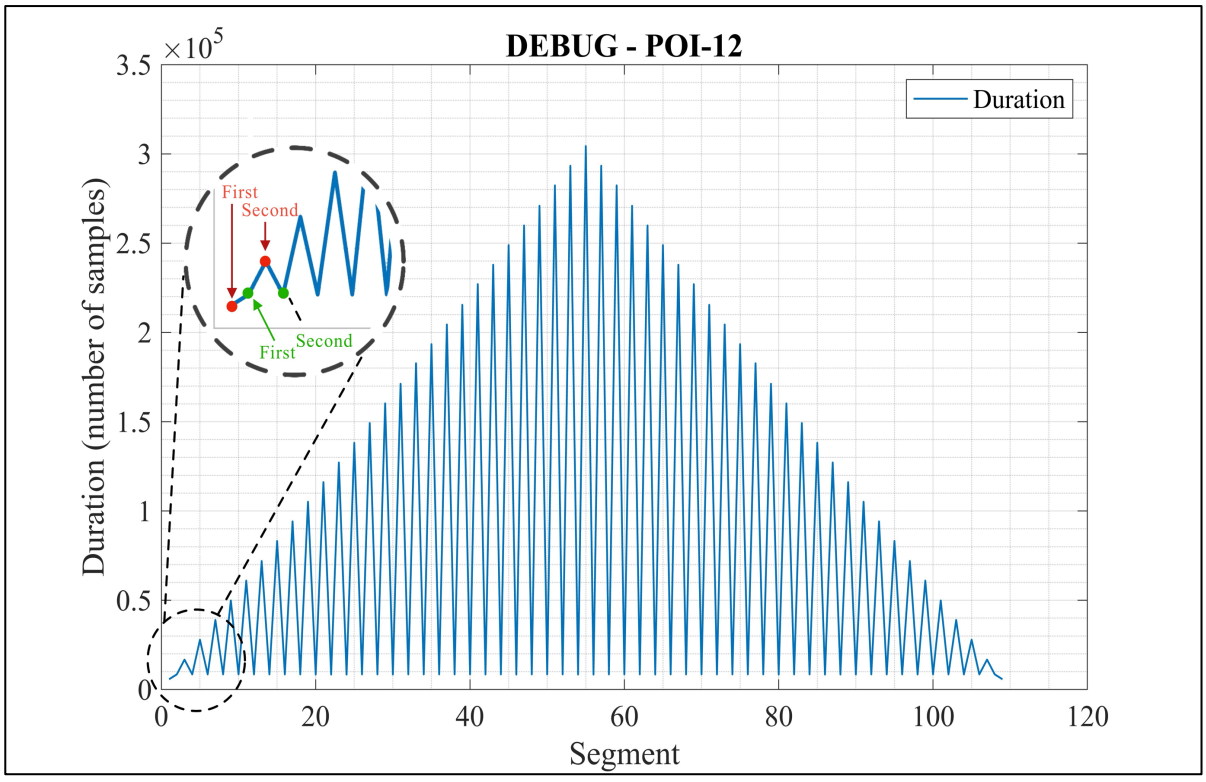
Figure 4.21 - DEBUG Point of Interest 11 (POI-11) for `Test1`, where the duration value for each obtained segment in regard to the almost complete internal printing pattern is displayed, alongside an approximation on the first segments of the internal printing pattern



The code shown in Figure 7.15 outlines the procedure for defining the first and last raster lines of the IIP. To obtain the first raster line, the duration of the second raster line is taken as a starting point, and 11,000 samples are subtracted, which is the increment factor between raster lines. Almost the same procedure is applied to obtain the last raster line, where the duration of the penultimate raster line is taken and 11,000 samples are added, which is the decrement factor between raster lines. This procedure is based on the internal pattern filling characteristics represented in Figure 4.2 and discussed earlier.

As a result, the `Duration4_v2` matrix is obtained. In the `Duration4_v2` matrix, the first column relates to the duration value itself, the second column is the index related to the endpoint of the fabrication line, and the third column is the index related to the starting point of the fabrication line. From `Duration4_v2`, it is only necessary to separate the indices related to the raster lines and between the transition raster lines, and to obtain the fourth and final MWD group. Figure 4.22 presents the duration of the lines of the IIP, with a magnification at the start of the IIP where an identification of the first and second raster lines durations visible in red, and first and second transition between raster lines durations in green.

Figure 4.22 - DEBUG Point of Interest 12 (POI-12) for `Test1`, where the duration value for each obtained segment in regard to the complete internal printing pattern is displayed, alongside an approximation on the first segments of the internal printing pattern



The code shown in Figure 7.16 outlines the procedure for separating the indices related to raster lines and between transition raster lines, and for obtaining the fourth MWD group.

The matrix `index_raster` contains only the values related to raster lines, while the matrix `index_trans_raster` contains only the values related to transition raster lines. In both cases, the first column relates to the duration value itself, the second column is the index

related to the endpoint of the fabrication line, and the third column is the index related to the starting point of the fabrication line.

Next, the fourth group of MWD is obtained by calculating the difference between the index for the start of the fabrication of the first raster line and the index for the end of the fabrication of the last contour line. The result is stored in the variable *contourToRasterReposition*. After this, an adjustment is made to the contour indices, storing the altered values in the matrix *indexContourAlt*, to allow for a decimation procedure when generating the figures.

The code shown in Figure 7.17 outlines the procedure for obtaining the segmentation script results based on the user's choice (`Points` or `Segments`). The code shown in Figure 7.18 outlines the procedure for storing variables and generating figures according to the user's choices.

4.1.4 STUDY A: SEGMENTATION RESULTS

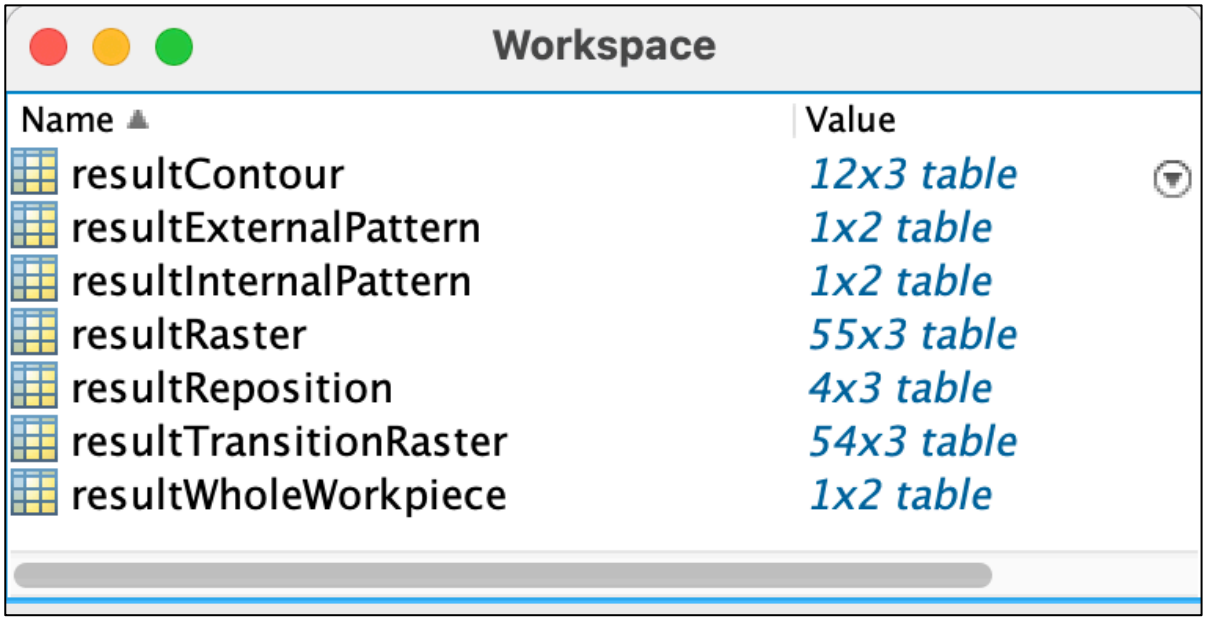
Upon executing the **`fff_segmenter`** script with default parameters, two new files were created in the Segmentation results folder for both MATLAB and Octave, located in their respective current paths. The first file, named `Points` segmentation results *Acoustic_signal*, contains segmentation results for the `Points` segmentation choice. This file is saved in table format in MATLAB and in struct format in Octave. The naming convention for the output data file follows the segmentation mode choice, `Points` in this case, and the sensor signal identifier in the dataset, *Acoustic_signal*.

In MATLAB, opening the generated table reveals that the `Points` segmentation mode produces three columns for each geometric feature and two columns for pattern separation. Specifically, the first column indicates the *Duration* of the feature fabrication, the second column marks the first instant index, identified as StartPoint, and the third column shows the EndPoint of the feature fabrication using the default number of samples mode. This is illustrated in the MATLAB workspace (Figure 4.23) and the segmentation results (Figure 4.24).

Similarly, in Octave, opening the struct file shows that the `Points` segmentation mode generates similar columns for geometric features and pattern separation, with identical data arrangements. This is demonstrated in the Octave workspace (Figure 4.25) and the segmentation results (Figure 4.26).

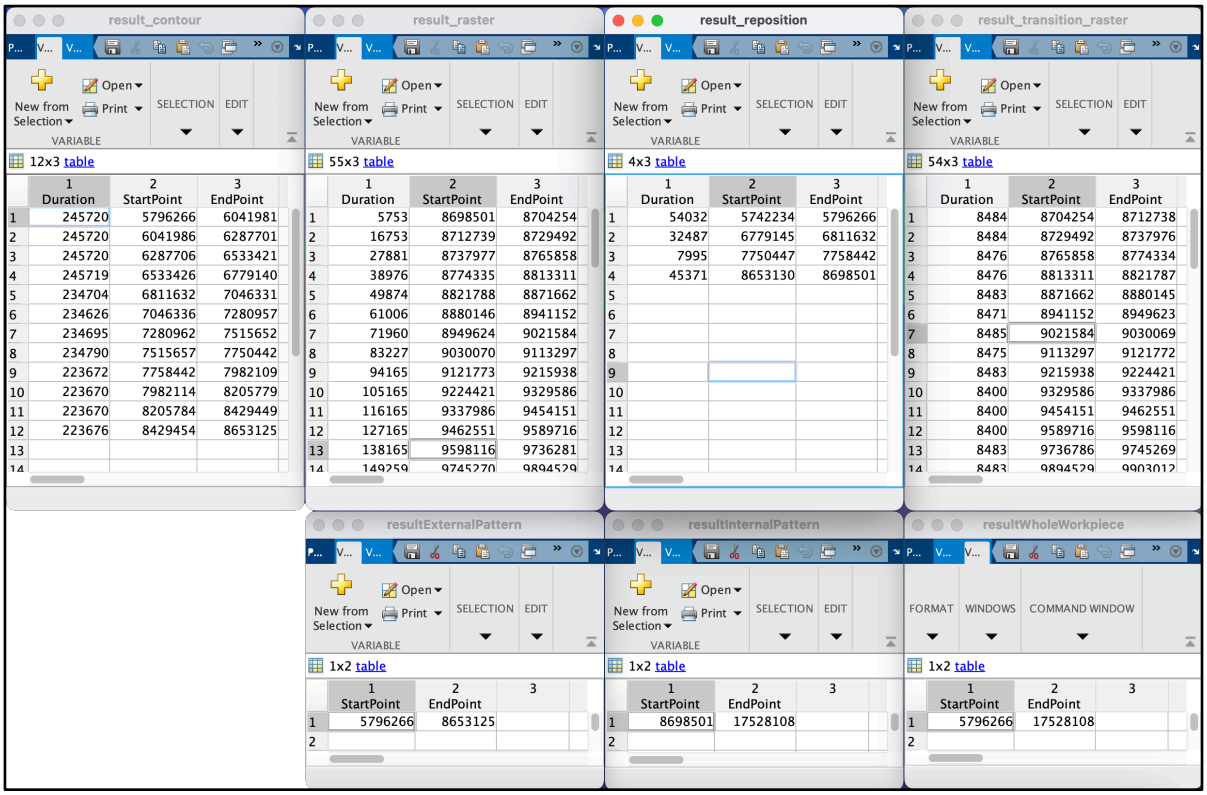
The second file, named Segmentation results *Acoustic_signal*, is an automatically saved figure representing the segmentation results with predetermined resolution and formatting. The image for both MATLAB and Octave is represented in Figure 4.27.

Figure 4.23 – MATLAB workspace with the segmentation results tables



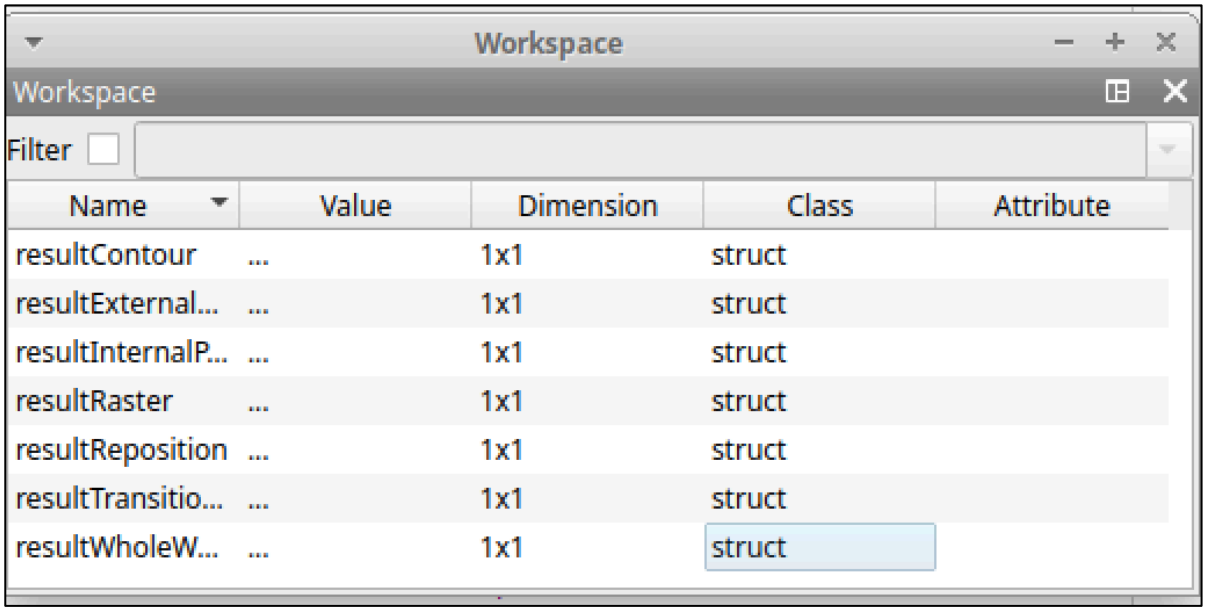
Source: Glissoi Lopes *et al.* (2024) [71]

Figure 4.24 – MATLAB segmentation results tables, with a representation of each result table content



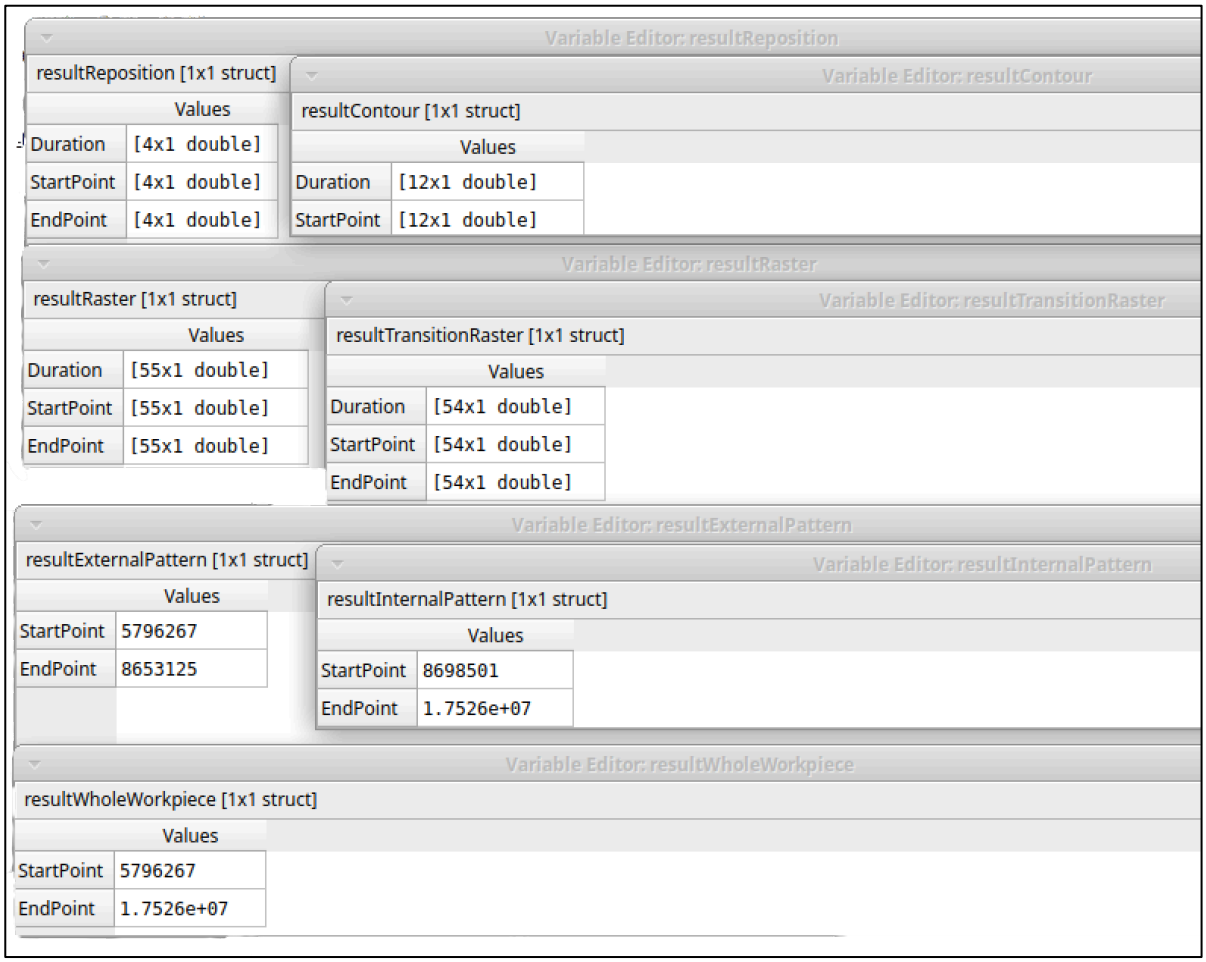
Source: Glissoi Lopes *et al.* (2024) [71]

Figure 4.25 – Octave workspace with the segmentation results structs



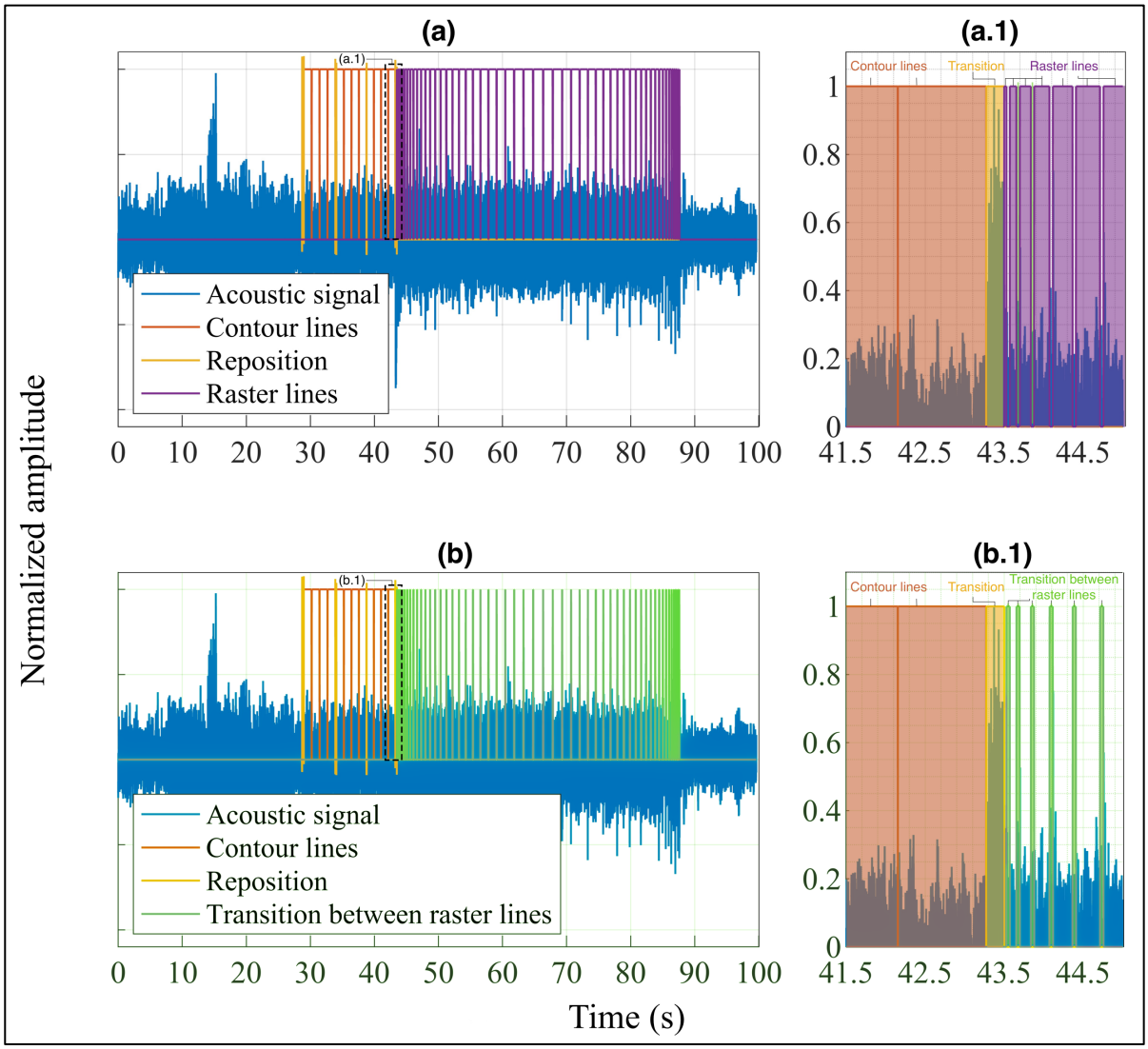
Source: Glissoi Lopes *et al.* (2024) [71]

Figure 4.26 – Octave segmentation results structs, with a representation of each result struct content



Source: Glissoi Lopes *et al.* (2024) [71]

Figure 4.27 – Graphical representation of the segmentation results upon the `Test1.mat` dataset acoustic signal, with specific visualization of the segmentation results in the transition period between external and internal infill patterns



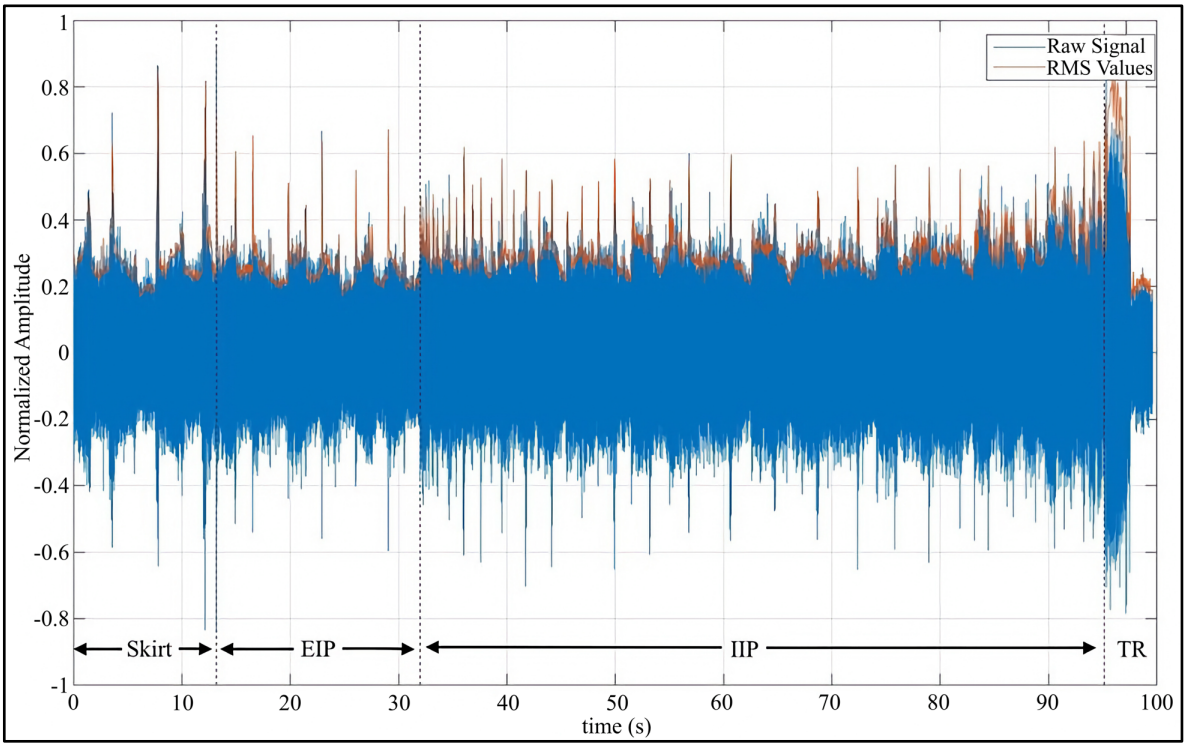
Source: Lopes *et al.* (2024) [70]

4.2 STUDY B: RESULTS AND DISCUSSION REGARDING THE STUDY ABOUT MONITORING FFF MACHINE CONDITIONS WITH ELECTRET MICROPHONES, SVM, AND NEURAL NETWORKS

4.2.1 STUDY B: EVALUATION AND EXTRACTION OF THE RAW SIGNALS

Figure 4.28 illustrates the raw signal (blue) and RMS values (red) throughout the entire printing operation under normal conditions, repetition 1. The inherently stochastic nature of the raw signal is evident, encompassing four distinct stages of fabrication: 1) the skirt; 2) the contour lines related to the EIP; 3) the raster lines related to the IIP; and 4) the transition phase from the conclusion of the IIP to the extruder's home position (TR). Identifying the start and finish of the single-layer part printing and the transition between EIP and IIP from the raw signal alone is challenging. To aid in pinpointing these moments, a video recording was made during fabrication, with key moments indicated by dashed lines in Figure 4.28. The RMS values in the figure further clarify the stages of fabrication.

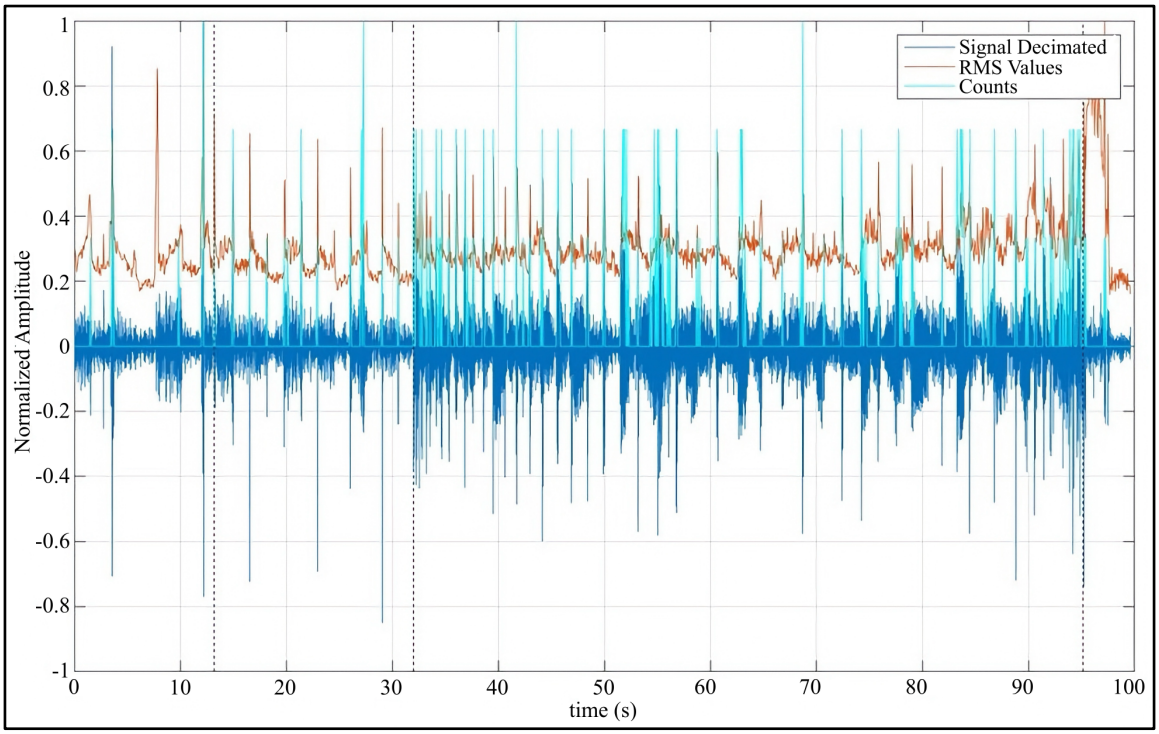
Figure 4.28 - Raw Signal and RMS Values for Normal Printing Condition



Source: Lopes *et al.* (2023) [51]

Figure 4.29 presents the results from the algorithm for delineating the segment lines of the fabricated part. The counts statistic applied to the filtered and decimated raw signal successfully identified most of the contour and raster lines for EIP and IIP, respectively, though some fabricated lines were missed. Despite this, the algorithm effectively separated the EIP and IIP regions of the part, which is the focus of this study. Future improvements could include enhancements to the algorithm and incorporating control signals from the printer's stepper motor to accurately define each moment of fabrication.

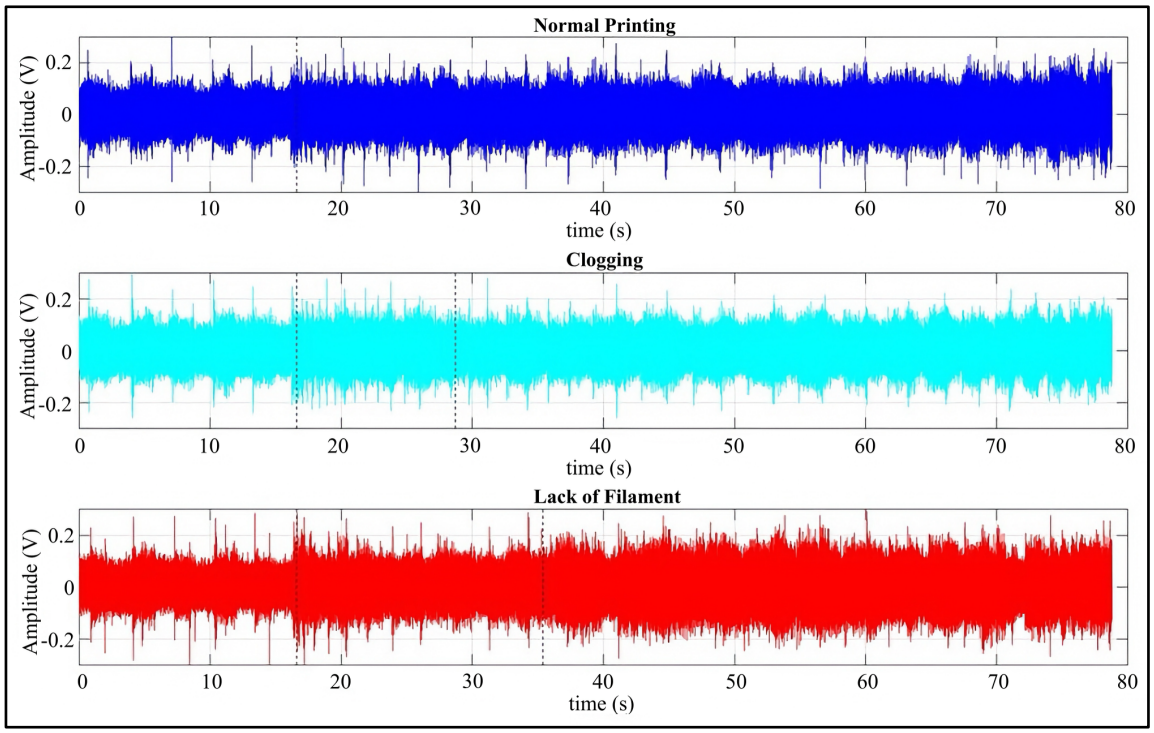
Figure 4.29 - Decimated Raw Signal, RMS Values, and Counts Statistic



Source: Lopes *et al.* (2023) [51]

4.2.2 STUDY B: RAW SIGNALS FOR THE EXTERNAL AND INTERNAL IN-FILL PATTERNS

Figure 4.30 - Raw Signals for the Normal Printing, Clogging and Lack of Filament machine conditions



Source: Lopes *et al.* (2023) [51]

Figure 4.30 illustrates the extracted raw signals for EIP and IIP under all machine conditions from repetition 1 of each test: standard condition, extruder clogging, and filament shortage. The variation in amplitude for each machine condition is evident. The dashed lines at 16.6s indicate the transition between EIP and IIP, at 28.7s the extruder clogging event, and at 35.4s the filament shortage occurrence.

To better analyze and understand these signals in relation to the machine conditions, a magnified view is provided in Figure 4.32. The amplitude differences for each machine condition are clearly visible. During clogging, the raw signal amplitude decreases, attributed to the attenuation of the sound pressure level caused by the melted filament in the extruder. The sound absorption is significant due to the larger volume of PLA filament inside the extruder [172], [173], [174], [175]. Conversely, there is an increase in sound level pressure when the filament is missing, caused by sound wave reflections within the extruder walls, leading to constructive interferences and increased amplitude. These different machine conditions produce distinct sound characteristics influenced by factors like material shape, type, and physical impact [173].

Figure 4.31 – Obtained workpieces. (a), (b), and (c): Under clogging condition; (d), (e), and (f): Under filament lack condition

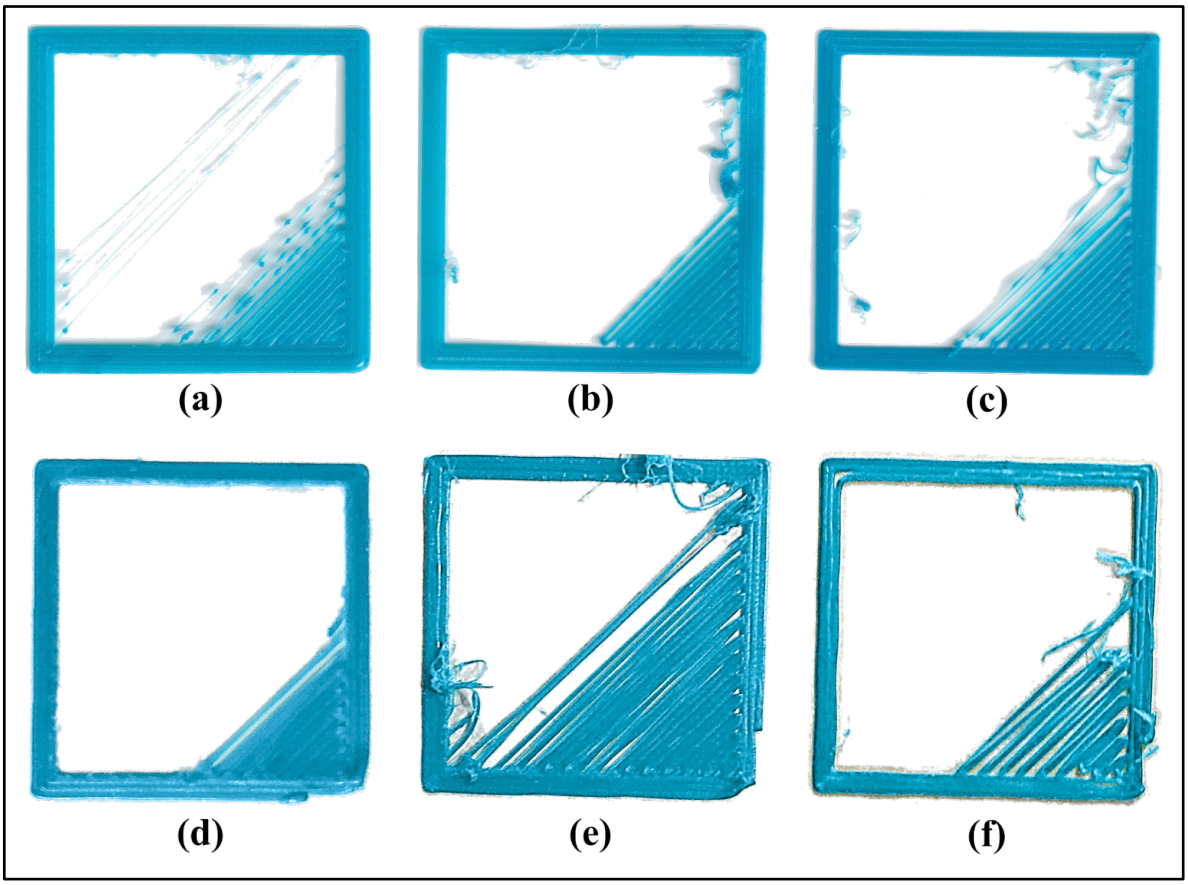
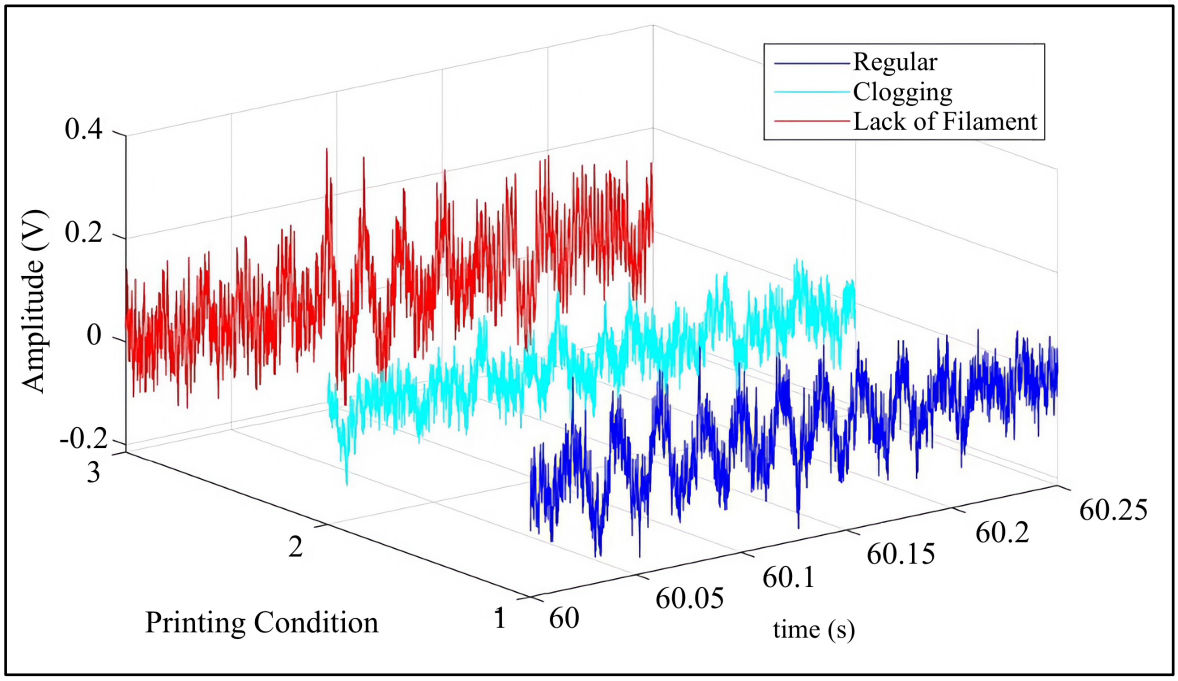


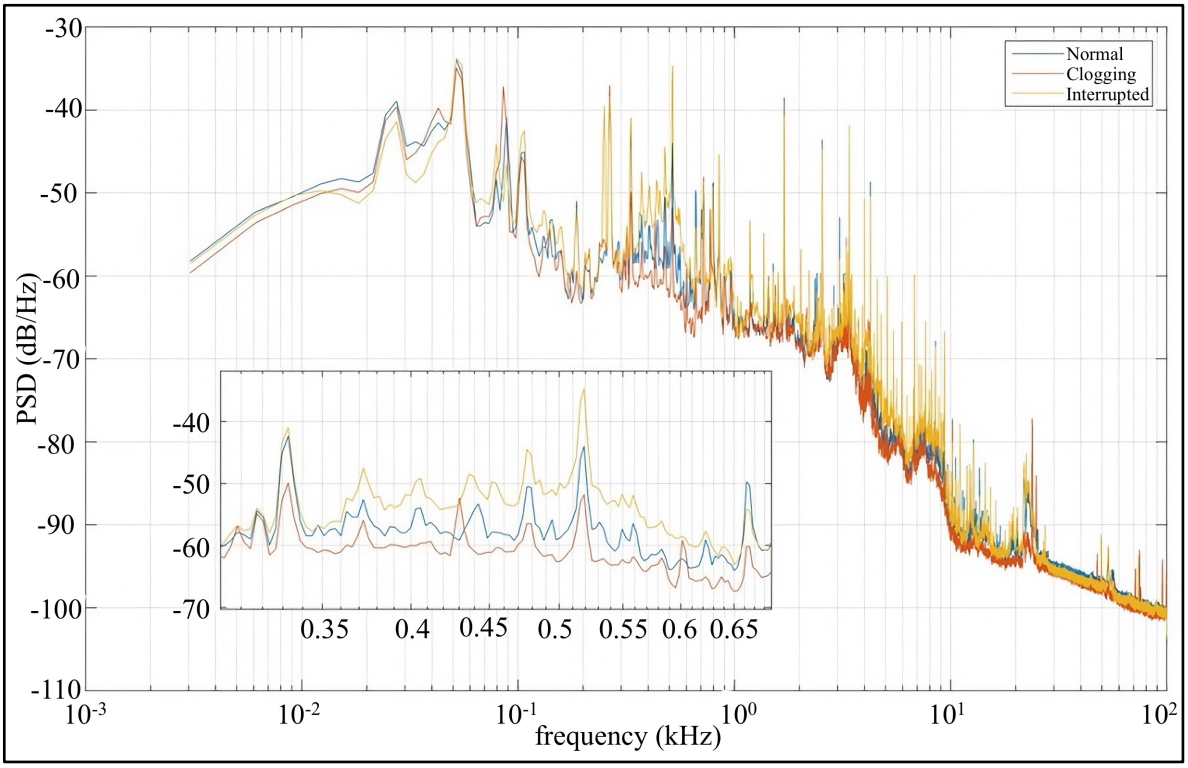
Figure 4.32 - Magnified Raw Signals for Normal Printing, Clogging and Lack of Filament machine conditions



Source: adapted from Lopes *et al.* (2023) [51]

4.2.3 STUDY B: SPECTRAL ANALYSIS AND FREQUENCY BAND DETERMINATION

Figure 4.33 - Spectral Analysis of Raw Signals for Normal Printing, Clogging and Interrupted (Lack of Filament) machine conditions and Selected Frequency Band



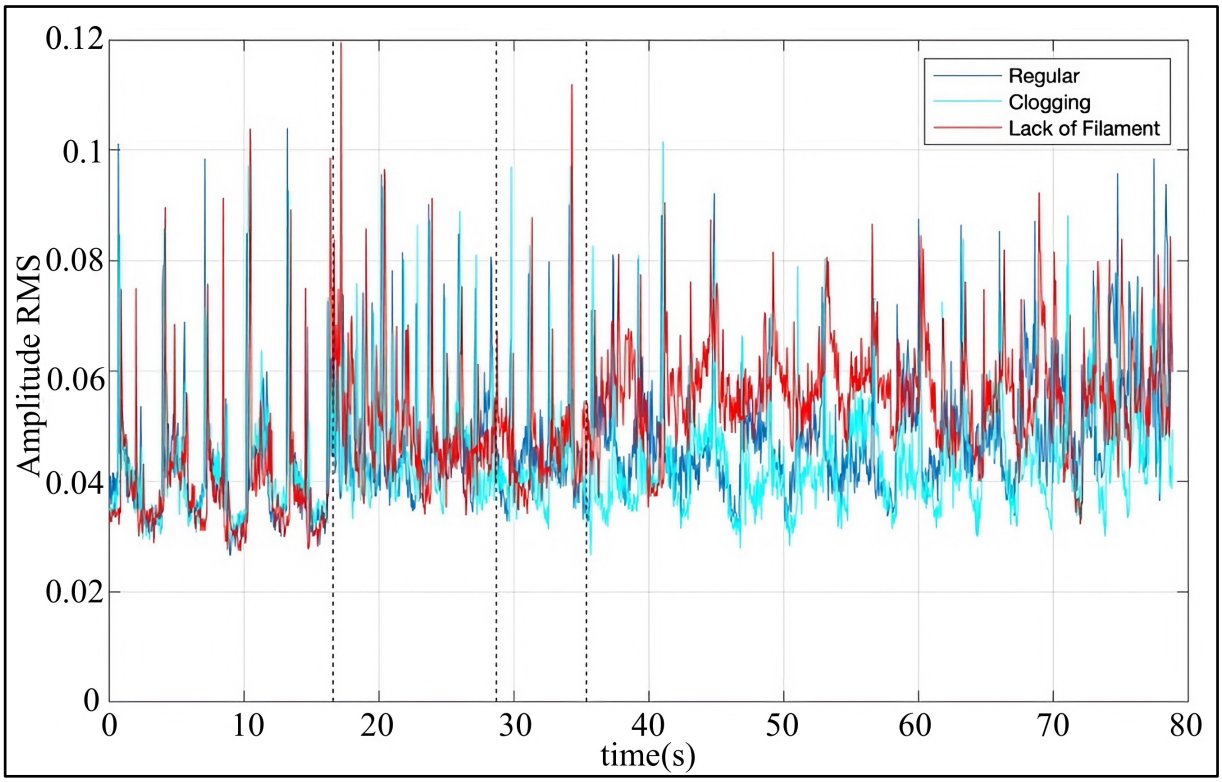
Source: Lopes *et al.* (2023) [51]

The PSD of the raw signals for each machine condition and the magnified view of the selected frequency band are presented in Figure 4.33. The spectra exhibit similar behavior within the electret microphone's frequency response range (20Hz to 20kHz), with higher power levels between 10Hz and 4kHz, decreasing significantly thereafter. Resonance frequencies and spikes are present for all conditions at approximately 30Hz, 55Hz, 85Hz, 105Hz, 265Hz, 330Hz, 520Hz, and 660Hz. Failure conditions show these resonance frequencies with altered power levels. A frequency band of 350Hz to 600Hz, which best represents the studied machine conditions, was selected. The multitude of spikes is mainly due to the stepper motors' movements and other printer mechanisms [176], [177], [178].

4.2.4 STUDY B: ROOT MEAN SQUARE VALUE ANALYSIS

Figure 4.34 shows the RMS values computed from the unfiltered raw signals of repetition 1. The amplitude differences for each machine condition are evident, with a decrease in amplitude for the clogging condition and an increase for filament shortage. The dashed lines indicate the change of printing pattern (EIP to IIP), clogging, and filament shortage, respectively. RMS values are directly related to the signal's energy and power [179], and a similar analysis to that of the raw signals can be applied here. The sound wave attenuation during clogging and the increased sound reflections during filament shortage are evident. The spikes are mainly due to changes in segment lines and the printer's stepper motors and mechanisms [176], [177], [180]. Despite the visible amplitude changes, the high noise and spikes result in a high standard deviation of RMS values, limiting their classification utility.

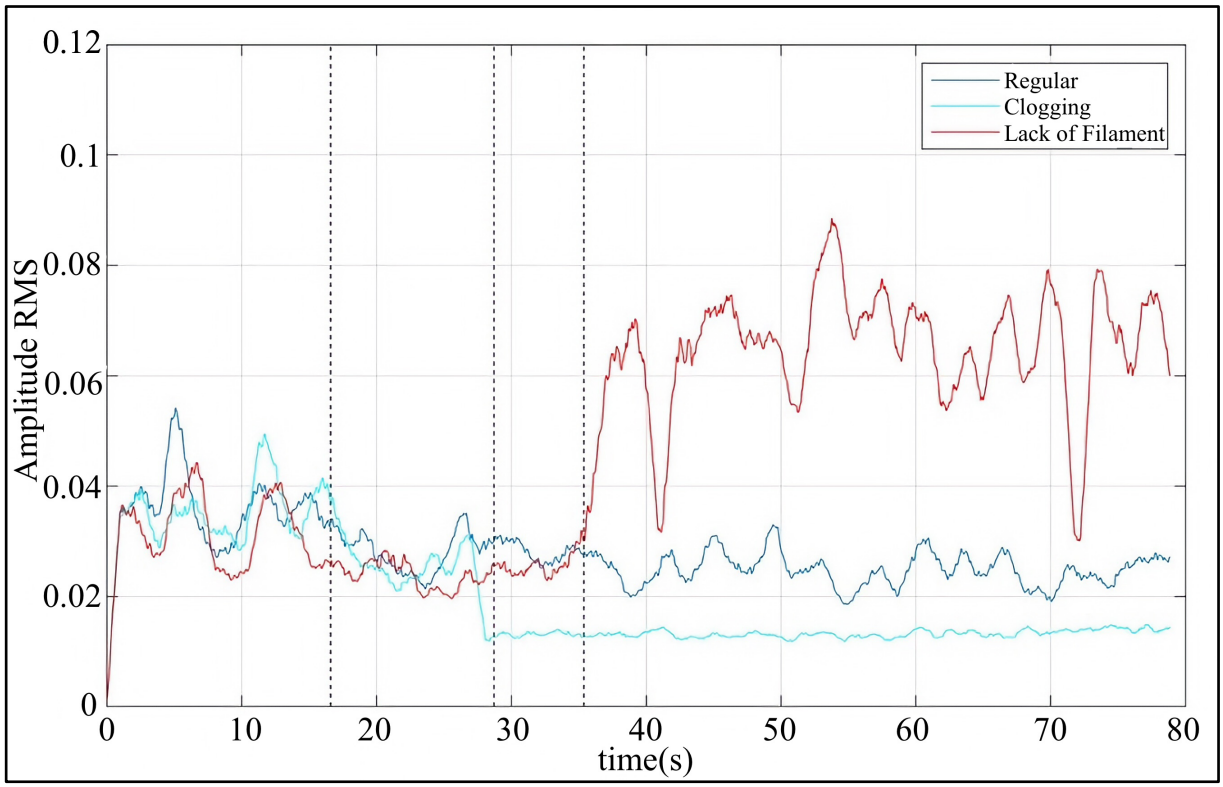
Figure 4.34 - RMS Values from Unfiltered Raw Signals for Normal Printing, Clogging and Interrupted (Lack of Filament) machine conditions



Source: Lopes *et al.* (2023) [51]

Figure 4.35 displays the RMS values computed from the raw signals filtered in the 350Hz to 600Hz frequency band. The machine conditions are more distinguishable, with the filtered raw signals containing information relevant to the phenomena studied. The lower standard deviation makes this statistic more suitable for classification purposes. RMS values indicate the onset of clogging and filament shortage conditions.

Figure 4.35 - RMS Values from Filtered Raw Signals for Normal Printing, Clogging and Lack of Filament machine conditions

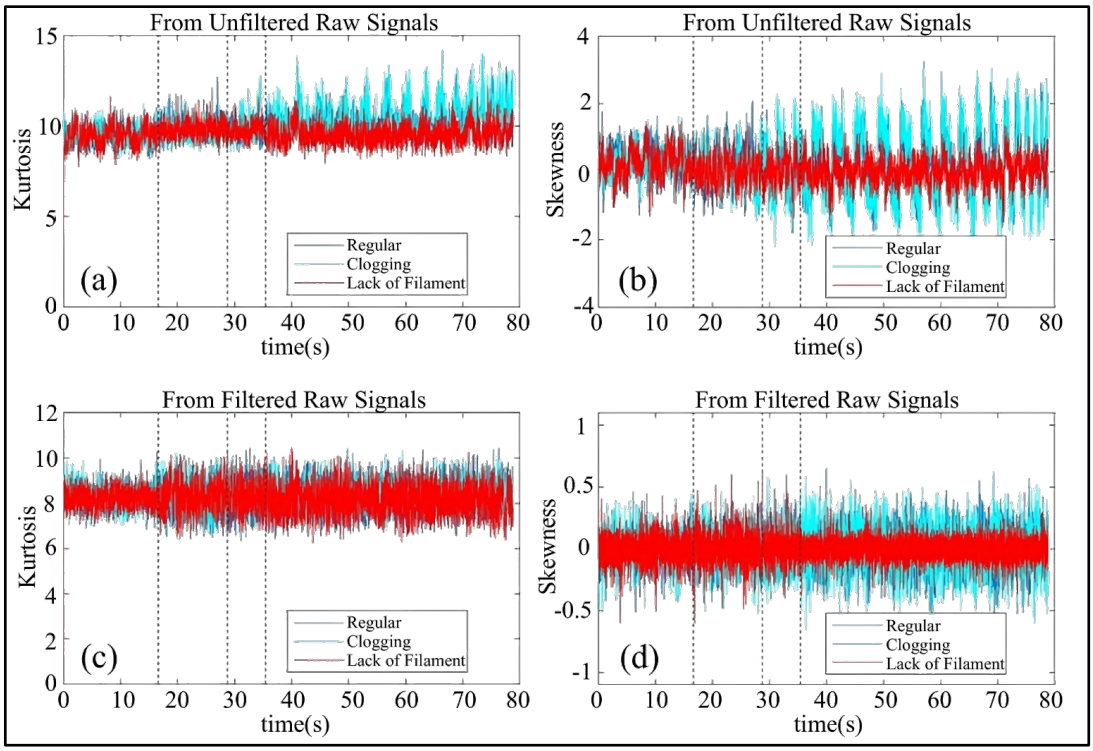


Source: Lopes *et al.* (2023) [51]

4.2.5 STUDY B: ANALYSIS OF KURTOSIS AND SKEWNESS

Kurtosis and Skewness statistics were computed for both unfiltered and filtered raw signals within the selected frequency band, as shown in Figure 4.36. The dashed lines indicate the moments of printing pattern change, clogging, and filament lack conditions, respectively. Kurtosis values from the unfiltered raw signal can effectively distinguish clogging conditions from others (Figure 4.36(a)), whereas they fail to differentiate conditions when computed from the filtered raw signal (Figure 4.36(c)). Conversely, skewness values can classify between clogging and other machine conditions in both scenarios (Figure 4.36(b) and Figure 4.36(d)), with higher efficacy in the unfiltered signal. Thus, applying the passband filter worsens the results of these statistics for classifying the machine conditions. Nevertheless, Figure 4.36(a) and Figure 4.36(b) clearly demonstrate that kurtosis and skewness are useful indicators of clogging conditions. Kurtosis measures the tail size and peaks of a signal [155], [181], while skewness measures the asymmetry of the distribution [154]. Moreover, the large amplitude oscillation in skewness during clogging (Figure 4.36(b)) makes it appealing for monitoring and classification.

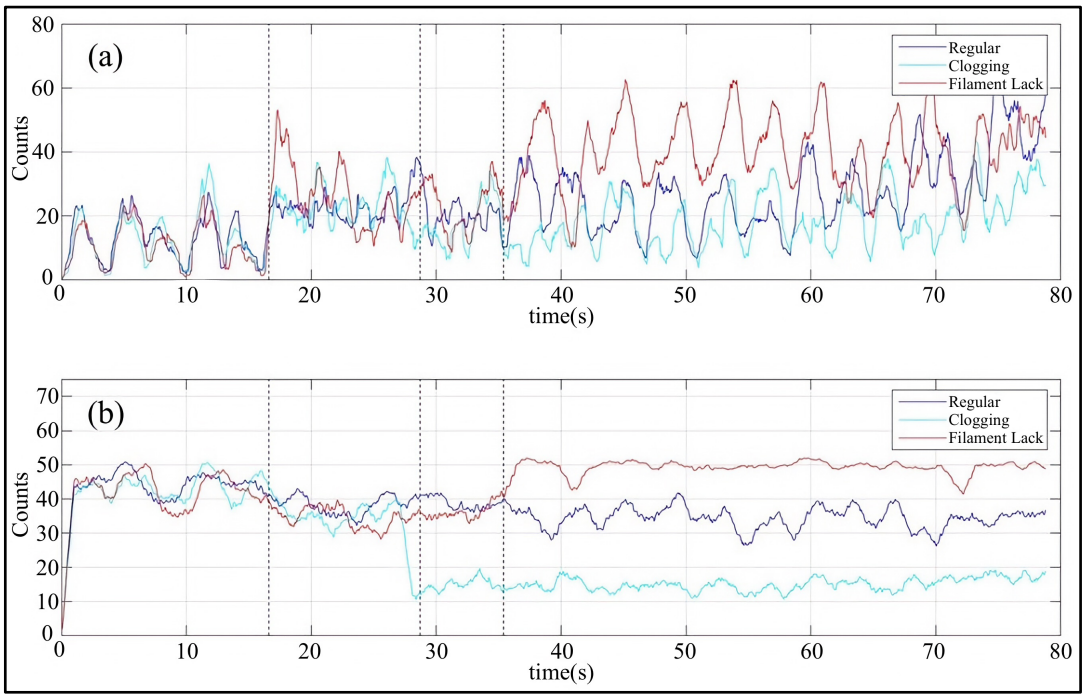
Figure 4.36 - Kurtosis (a) and Skewness (b) from Unfiltered Raw Signals, and Kurtosis (c) and Skewness (d) from Filtered Raw Signals for Normal Printing, Clogging and Lack of Filament machine conditions



Source: Lopes *et al.* (2023) [51]

4.2.6 STUDY B: COUNTS STATISTIC RESULTS AND DISCUSSION

Figure 4.37 - Counts from Unfiltered (a) and Filtered (b) Raw Signals for Normal Printing, Clogging and Filament Lack machine conditions



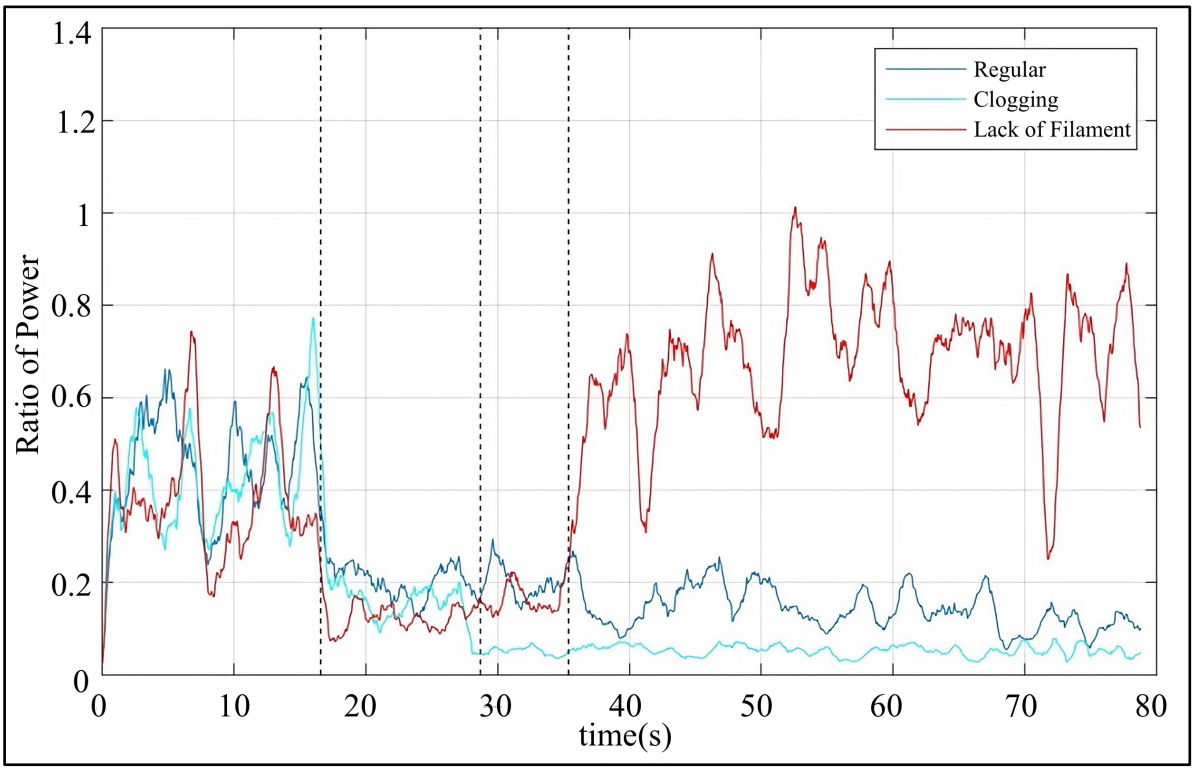
Source: Lopes *et al.* (2023) [51]

Figure 4.37 presents the counts statistic results computed from unfiltered (a) and filtered (b) raw signals within the selected frequency band for repetition 1 of each machine condition. The dashed lines indicate the times of printing pattern change from EIP to IIP, clogging, and filament lack, respectively. This statistical parameter, widely used in the AE community, counts the number of times a signal crosses a predefined threshold within a time frame, thus measuring acoustic activity [134], [135]. Figure 4.37(a) shows a visible difference between machine conditions, with increased acoustic activity during filament lack and a slight decrease during clogging. This behavior is more pronounced when the counts statistic is computed from filtered raw signals (Figure 4.37(b)), making it appealing for machine condition monitoring and classification models. The Counts statistic also indicates the occurrence of clogging and filament lack events.

4.2.7 STUDY B: ANALYSIS OF THE RATIO OF POWER

Figure 4.38 shows the ROP between the signal power within the selected frequency band (350Hz–600Hz) and the total signal power for each 50ms time frame during the printing process. The dashed lines represent the moments of pattern change (EIP to IIP), clogging, and filament lack for repetition 1. The results clearly show ROP's ability to distinguish between machine conditions. Its behavior is similar to RMS values computed from the filtered raw signal, which is reasonable since RMS is related to signal power. However, ROP considers the total power within the frequency band of interest, making it promising for monitoring machine conditions or classification models. The ROP statistic also indicates the occurrence times of pattern changes, clogging, and filament lack.

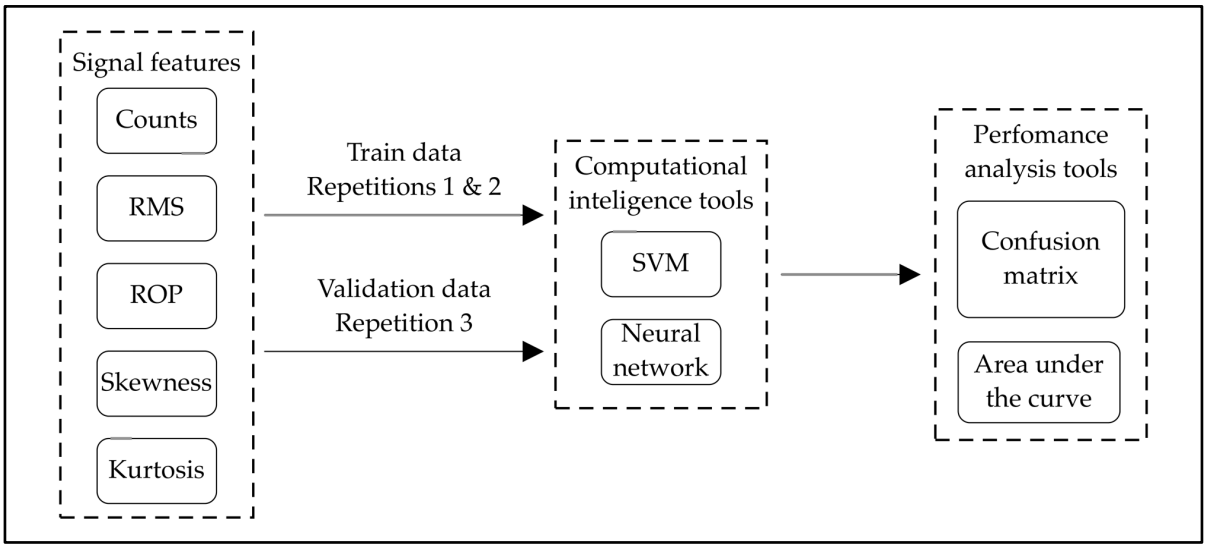
Figure 4.38 - Ratio of Power for Normal Printing, Clogging and Filament Lack machine conditions



Source: Lopes *et al.* (2023) [51]

The workflow for neural network and SVM analysis is shown in Figure 4.39. Signal features were derived from both unfiltered and filtered raw signals. This section discusses both types of signal features. The Counts feature is highlighted first as its results are similar to other features, which are summarized in a table on section 4.2.10.

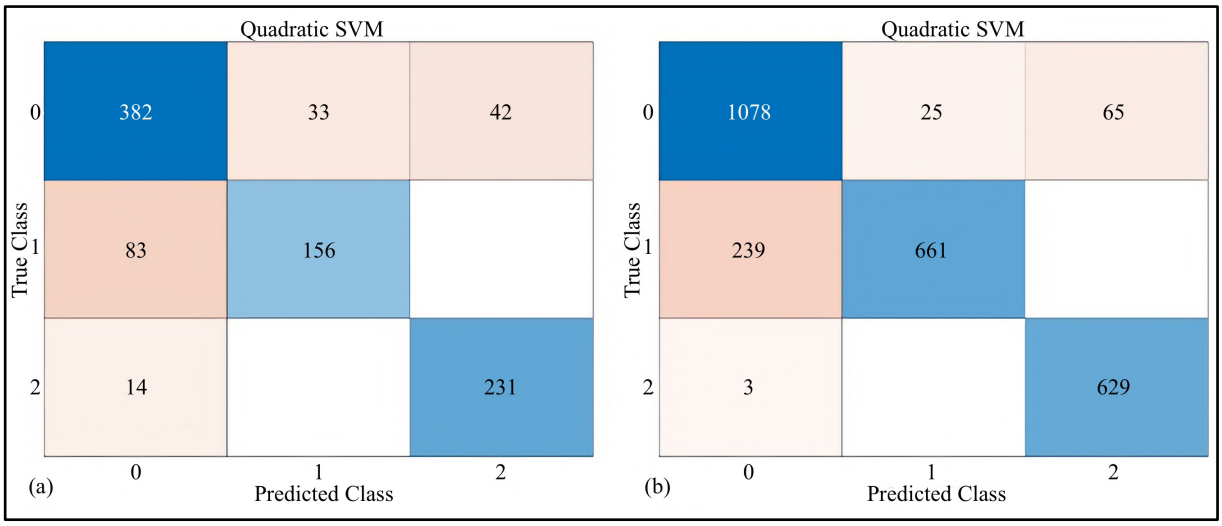
Figure 4.39 - Neural network and SVM analysis workflow



Source: Lopes *et al.* (2023) [51]

4.2.8 STUDY B: PERFORMANCE ANALYSIS FOR THE COUNTS FEATURE OBTAINED FROM THE RAW SIGNAL

Figure 4.40 - Confusion matrix for (a) validation and (b) Test data



Source: Lopes *et al.* (2023) [51]

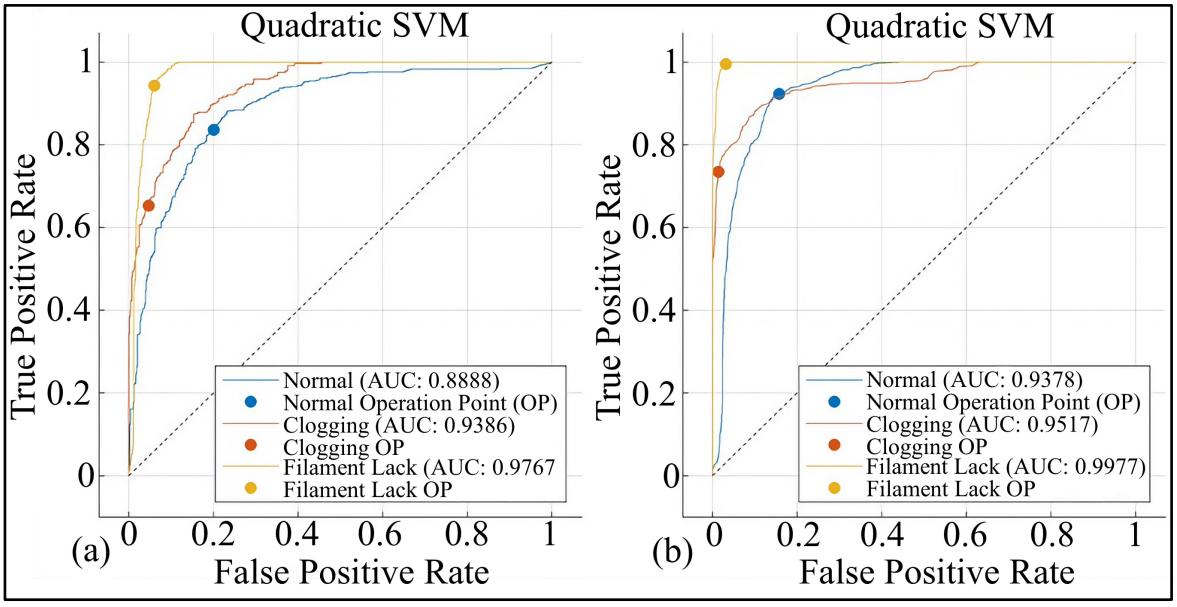
The training of computational models in this study used data from tests #1 and #2, with classification performance tested using data from test #3 to ensure the classifier had no prior exposure to the test data during training and validation. After training, the accuracy of the classifiers using the unfiltered Counts statistic data was calculated. Detailed performance graphs, such as ROC curves and confusion matrices for all tests and computational intelligence tools, are not included in this thesis as they are reserved for future publications. Confusion matrices

for validation and test sets are shown in Figure 4.40 for the Quadratic SVM algorithm. Classifiers achieved accuracy between 48.57% and 83.42% for the validation set, and between 43.26% and 87.7% for the test set. The SVM algorithm with a quadratic kernel function and automatic scaling achieved the best result.

To analyze performance by class, the Area Under the Curve (AUC) graphic is shown in Figure 4.41. The clogging condition had the worst performance, with a 34.7% error rate, due to difficulty in separating clogging from normal machine operation conditions. This overlap can be seen in Figure 4.41(a), showing signal overlap between machine conditions.

To analyze the performance obtained in each class, the AUC graphic is displayed in Figure 4.41. It is noted that the clogging condition had the worst performance in this classifier, showing an error rate of 34.7%. This is due to the difficulty in separability between clogging and normal machine operation conditions, as can be seen in Figure 4.41(a) in which it is possible to observe the signal overlap between machine conditions.

Figure 4.41 - Area Under the Curve for (a) Validation and (b) Test Data



Source: Lopes *et al.* (2023) [51]

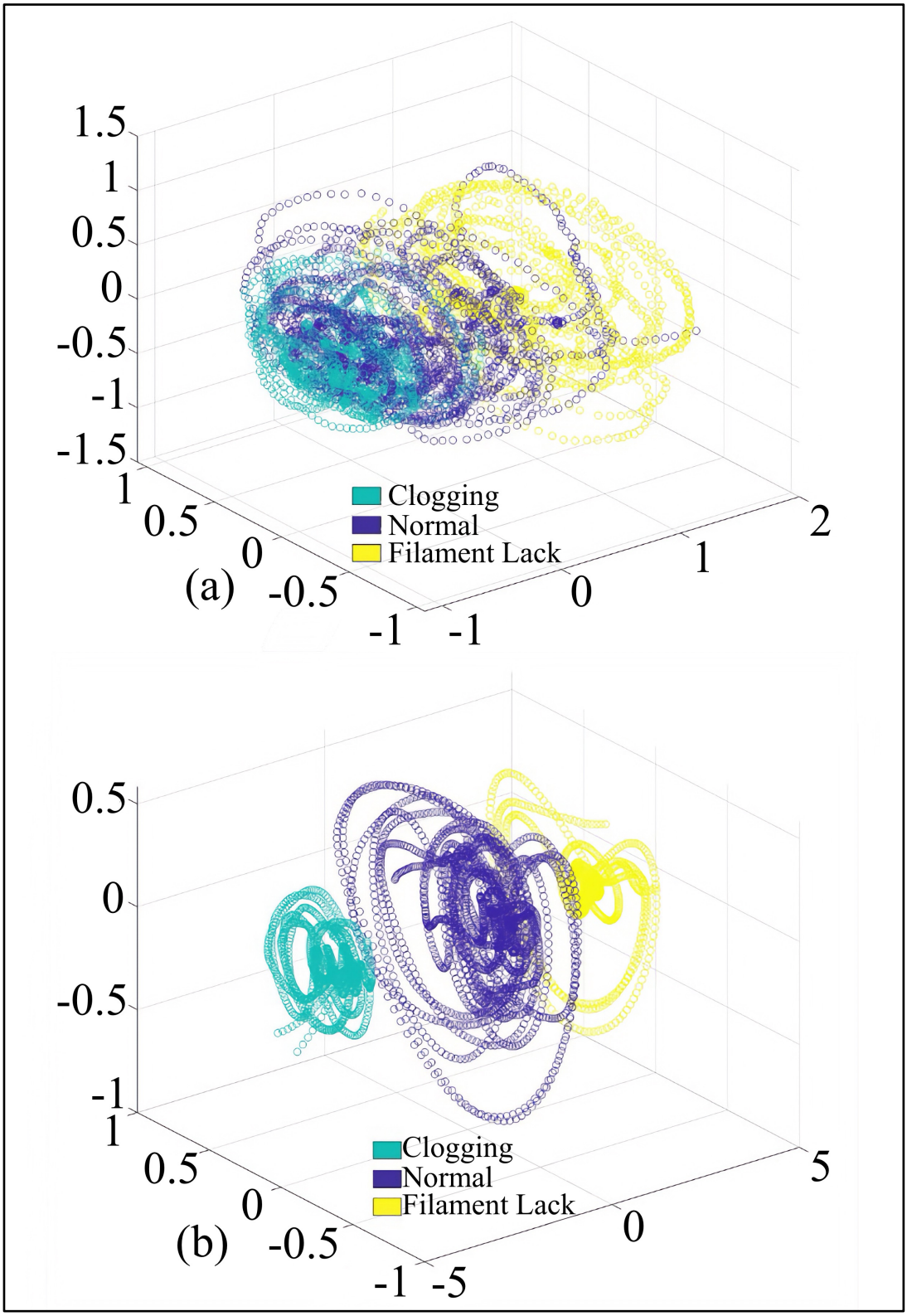
4.2.9 STUDY B: PERFORMANCE ANALYSIS FOR THE COUNTS FEATURE OBTAINED FROM THE FILTERED RAW SIGNAL

Classifiers trained using filtered data achieved high accuracy, with most cases reaching 100%. This performance prompted an investigation into the impact of signal filtering to assess the feasibility and check for potential overfitting of the computational model. The Principal Component Analysis (PCA) algorithm with three principal components was used to visualize the feature space of the training samples (Repetition 1 and 2), generated with the Counts statistic with and without filtering. Filtering allowed for better class separability, as demonstrated by the PCA analysis using the three main components to illustrate the feature space of the conditions studied. The impact of using the filter is shown in Figure 4.42.

The classifiers trained with filtered data achieved high accuracy due to the degree of separability achieved by filtering the signals. This result demonstrates the effectiveness of the

adopted methodology, serving as a foundation for training models with other features extracted from the signal in this study.

Figure 4.42 - Feature space for Counts statistic for (a) raw unfiltered signal and (b) filtered signal for Normal Printing, Clogging and Filament Lack machine conditions



Source: Lopes *et al.* (2023) [51]

4.2.10 STUDY B: PERFORMANCE ANALYSIS FOR THE RMS, ROP, SKEWNESS AND KURTOSIS

Machine learning algorithms were used to train models on other features investigated in this study. After training, the algorithms showed high performance on the test set for all features except Kurtosis, which did not prove suitable for classifying the conditions in this study, even after signal filtering. Thus, results for this feature were not presented. The results for each feature are shown in Table 4.2.

SVM models use different types of kernels, which influence how data is transformed to find the optimal separating hyperplane [182]. The Linear SVM is simple and straightforward, being suitable for linearly separable data. However, its performance in skewness is low, with 56.82% in validation and 57.25% in testing, indicating that it is not effective at capturing more complex and asymmetric patterns in the data.

On the other hand, both Quadratic SVM and Cubic SVM show better capabilities for capturing nonlinear patterns. Quadratic SVM achieved 91.07% skewness in validation and 85.50% in testing, while Cubic SVM reported 88.34% and 86.49%, respectively. Both models outperform the Linear SVM, with the Quadratic showing a slight improvement over the Cubic in terms of skewness, though the difference between them is small.

The Gaussian SVMs use radial basis kernels, allowing them to capture more complex separation patterns. Among the different granularities, the Fine Gaussian SVM shows skewness of 77.92% in validation and 75.18% in testing. The Medium Gaussian SVM strikes the best balance between the three metrics, with 94.29% skewness in validation and 92.14% in testing, showing that it captures data asymmetry well and generalizes efficiently. Finally, the Coarse Gaussian SVM achieves 83.37% skewness in validation and 82.31% in testing, indicating an intermediate performance that, while solid, may miss some finer details in data separation.

Table 4.2 - Results for RMS, ROP, and Skewness

Model	Accuracy % (Validation)			Accuracy % (Test)		
	RMS	ROP	Skewness	RMS	ROP	Skewness
Linear SVM	100	100	56,82	100	100	57,25
Quadratic SVM	100	100	91,07	100	100	85,50
Cubic SVM	100	100	88,34	100	100	86,49
Fine Gaussian SVM	100	100	77,92	99,78	99,78	75,18
Medium Gaussian SVM	100	100	94,29	100	100	92,14
Coarse Gaussian SVM	100	100	83,37	100	100	82,31
Narrow Neural Network	100	100	69,98	100	100	74,69
Medium Neural Network	100	100	79,90	100	100	74,94
Wide Neural Network	100	100	82,88	100	100	84,52
Bilayered Neural Network	100	100	87,10	100	100	86,00
Trilayered Neural Network	100	100	83,62	99,37	100	87,47

Source: Lopes *et al.* (2023) [51]

Neural Network models vary in complexity based on the number of layers and neurons per layer. The deeper the model, the more capable it is of capturing complex relationships in the data, but it also becomes more susceptible to overfitting [183].

The Narrow Neural Network is a simpler model with fewer layers and neurons, which limits its ability to capture complex patterns. This is reflected in the lower skewness of 69.98% during validation and 74.69% in testing, making it less effective compared to deeper models.

The Medium Neural Network offers a slight improvement over the narrow model, with a skewness of 79.90% in validation and 74.94% in testing. While it performs better in modeling the asymmetry of the data, the drop in performance from validation to testing suggests that its generalization ability is still somewhat limited.

The Wide Neural Network, which contains more neurons, has a greater ability to capture complex patterns in the data. This is shown by the increase in skewness, with 82.88% in validation and 84.52% in testing. The model performs well in both phases, showing improved capability in capturing data asymmetry.

The Bilayered Neural Network, with an additional layer, further improves its ability to model complex and asymmetric patterns. It achieves a skewness of 87.10% in validation and 86.00% in testing. The consistency between validation and testing shows that the model maintains a good balance between complexity and generalization.

Finally, the Trilayered Neural Network, with yet another layer, seems to strike the best balance for generalization. With 83.62% skewness in validation and 87.47% in testing, this model not only adjusts well to the data during training but also performs even better in real-world testing scenarios, indicating strong generalization capabilities.

Therefore, the classifiers' ability to distinguish samples for each condition in this study highlights the effectiveness of the signal processing and feature extraction steps in determining the machine condition under analysis.

5 – CONCLUSION

In conclusion, this thesis has significantly advanced the monitoring and diagnostic capabilities of the Fused Filament Fabrication (FFF) process through the integration of advanced signal processing techniques and computational intelligence tools. By employing an electret microphone attached to the extruder for data acquisition, extensive signal processing and feature extraction analyses were conducted. These analyses revealed distinguishable patterns associated with various machine conditions such as normal operation, extruder clogging, and filament absence.

Spectral analysis played a crucial role in characterizing the printing process, identifying frequency values associated with defects, and extracting features such as Root Mean Square (RMS) values, Counts statistics, and Ratio of Power (ROP), which effectively differentiated between conditions when signals were filtered within selected frequency bands. Implementing machine learning algorithms, notably Neural Networks (NN) and Support Vector Machine (SVM), demonstrated high efficacy in classifying machine conditions based on the extracted features, with SVM achieving an impressive 100% accuracy.

Moreover, the thesis elaborates on the **`fff_segmenter`** script, developed following Free and Open-Source (FOSS) and Open-Source Definition (OSD) guidelines and made publicly available on GitHub with an MIT license. This script automates the segmentation of acoustic signals using the direction control signals of the X and Y step motor axes and the signal's sampling frequency, with data collected via an electret microphone. This automation significantly reduces errors and time consumption associated with manual segmentation methods, providing accurate segmentation of contour and raster printing lines. The script's segmentation results can be visually inspected and autosaved in predefined formats, facilitating further analysis and integration into other MATLAB or Octave applications.

The **`fff_segmenter`** script is designed to be scalable and result-oriented, particularly for Cartesian RepRap-based FFF printers. The script was tested using three exemplary datasets available on the FFF-Line-Segmentation GitHub repository, featuring different low-cost sensors positioned on the 3D printer. These datasets included signals from PZT sensors placed on the printer table and extruder block, as well as an electret microphone on the extruder block. This approach ensures the script's adaptability to sensors and sensors positioning, enhancing the reliability and applicability of the monitoring methodology across different FFF monitoring approaches.

Thus, this thesis has provided a robust framework for enhancing the monitoring, control, and diagnostic capabilities of the FFF process. The integration of low-cost sensory device (electret microphone), signal processing, machine learning, and open-source tools offers a scalable and reliable method for real-time process monitoring, paving the way for future advancements in the field of AM.

5.1 SUGGESTIONS FOR FUTURE WORKS.

- Explore the integration of additional low-cost sensors beyond electret microphones, such as accelerometers or other vibroacoustic sensors, and evaluate their positioning on the 3D printer to further enhance the monitoring and diagnostic capabilities of the FFF process;

- Investigating more advanced machine learning models, such as deep learning algorithms, could potentially improve the accuracy and robustness of the classification and prediction of machine conditions, addressing more complex scenarios in the FFF process;
- Improve the **`fff_segmenter`** script for different parts geometries, as well as incorporating direct G-Code information extraction capabilities can significantly improve the automation and efficiency of the **`fff_segmenter`** segmentation script, promoting broader adoption of the technology in AM.

6 – REFERENCES

[1] B. Elhazmiri, N. Naveed, M. N. Anwar, e M. I. U. Haq, “The role of additive manufacturing in industry 4.0: An exploration of different business models”, *Sustainable Operations and Computers*, vol. 3, p. 317–329, jan. 2022, doi: 10.1016/j.susoc.2022.07.001.

[2] I. J. Solomon, P. Sevvel, e J. Gunasekaran, “A review on the various processing parameters in FDM”, *Mater Today Proc*, nº xxxx, p. 10–15, 2020, doi: 10.1016/j.matpr.2020.05.484.

[3] T. G. Lopes, A. Senna De Oliveira Candido, e I. B. G. Puzipe, “A MANUFATURA ADITIVA EM PROJETOS DE PESQUISA - PROGRESSO E DESENVOLVIMENTOS NOS ÚLTIMOS CINCO ANOS”, em *Avanços Tecnológicos, Gestão da Qualidade e Linguagem*, Dialética., vol. 1, A. Bezerra, S. da S. Pinto, e V. R. P. De Souza, Orgs., Dialética, 2024, 7, p. 147–171. Acessado: 2 de abril de 2024. [Online]. Disponível em: https://www.researchgate.net/publication/376713793_A_Manufatura_Aditiva_em_Projetos_de_Pesquisa_-_Progresso_e_Desenvolvimentos_nos_Ultimos_Cinco_Anos

[4] T. G. Lopes, I. B. G. Puzipe, Z. R. F. Antonio, L. E. P. Gimenes, G. P. M. Junior, e A. S. de O. Candido, “A Utilização de Manufatura Aditiva em Projetos de Pesquisa”, em *Anais do II Congresso de Inovação e Tecnologia – FATEC Lins*, A. Pazin e F. L. Meira, Orgs., Lins-SP: Centro Paula Souza, 2018, p. 104–112. [Online]. Disponível em: http://revista.fateclins.edu.br/congresso/edicoes.xhtml

[5] S. S. Crump, “Apparatus and method for creating three-dimensional objects”, 5,121,329, 1992

[6] T. G. LOPES, “Detecção e classificação de anomalias durante o processo de manufatura aditiva por fusão e deposição por meio de transdutores piezelétricos e processamento de sinais”, Dissertação, Universidade Estadual Paulista “Júlio de Mesquita Filho” - UNESP, Bauru, 2021. Acessado: 5 de setembro de 2022. [Online]. Disponível em: https://repositorio.unesp.br/handle/11449/204399

[7] B. Shaqour *et al.*, “Gaining a better understanding of the extrusion process in fused filament fabrication 3D printing: a review”, *International Journal of Advanced Manufacturing Technology*, vol. 114, nº 5–6, p. 1279–1291, 2021, doi: 10.1007/s00170-021-06918-6.

[8] N. Volpato, *Manufatura Aditiva: Tecnologias e Aplicações da Impressão 3D*, 1º ed, vol. 1. São Paulo: Blutcher, 2017.

[9] S. Singh, G. Singh, C. Prakash, e S. Ramakrishna, “Current status and future directions of fused filament fabrication”, *J Manuf Process*, vol. 55, nº April, p. 288–306, 2020, doi: 10.1016/j.jmapro.2020.04.049.

[10] D. G. Schniederjans, “Adoption of 3D-printing technologies in manufacturing: A survey analysis”, *Int J Prod Econ*, vol. 183, nº November 2016, p. 287–298, 2017, doi: 10.1016/j.ijpe.2016.11.008.

[11] P. K. Lim *et al.*, “Use of 3D Printed Models in Resident Education for the Classification of Acetabulum Fractures”, *J Surg Educ*, vol. 75, nº 6, p. 1679–1684, 2018, doi: 10.1016/j.jsurg.2018.04.019.

[12] A. Tahayeri *et al.*, “3D printed versus conventionally cured provisional crown and bridge dental materials”, *Dental Materials*, vol. 34, nº 2, p. 192–200, 2018, doi: 10.1016/j.dental.2017.10.003.

[13] C. V. Ferreira, J. R. L. dos Santos, e J. V. L. da Silva, “Exemplos de aplicações da prototipagem rápida”, em *Prototipagem Rápida - Tecnologias e Aplicações*, 1º ed, N. Volpato, Org., São Paulo: Blucher, 2007, 6, p. 29.

[14] R. Jiang, R. Kleer, e F. T. Piller, “Predicting the future of additive manufacturing: A Delphi study on economic and societal implications of 3D printing for 2030”, *Technol Forecast Soc Change*, vol. 117, p. 84–97, 2017, doi: 10.1016/j.techfore.2017.01.006.

[15] M. Attaran, “The rise of 3-D printing: The advantages of additive manufacturing over traditional manufacturing”, *Bus Horiz*, vol. 60, nº 5, p. 677–688, 2017, doi: 10.1016/j.bushor.2017.05.011.

[16] C. H. Ahrens *et al.*, *Prototipagem Rápida - Tecnologias e Aplicações*, 1º ed. São Paulo: Blucher, 2007.

[17] E. Peed e N. Lee, “Open Source 3D Printing, History of”, em *Encyclopedia of Computer Graphics and Games*, Cham: Springer International Publishing, 2024, p. 1298–1302. doi: 10.1007/978-3-031-23161-2_280.

[18] T. G. Lopes, V. D. Kennerly, P. R. Aguiar, C. S. Junior, P. M. De Carvalho Monson, e D. M. Daddona, “Detection and Classification of Defects in 3D Printing using a Novel Skewness and Kurtosis-based Parameter of Sound Signals and Machine Learning”, em *2024 International Conference on Control, Automation and Diagnosis (ICCAD)*, IEEE, maio 2024, p. 1–5. doi: 10.1109/ICCAD60883.2024.10553900.

[19] S. Bechtold, “3D Printing, Intellectual Property and Innovation Policy”, *IIC International Review of Intellectual Property and Competition Law*, vol. 47, nº 5, 2016, doi: 10.1007/s40319-016-0487-4.

[20] H. Hasdiansah, R. I. Yaqin, P. Pristiansyah, M. L. Umar, e B. H. Priyambodo, “FDM-3D printing parameter optimization using taguchi approach on surface roughness of thermoplastic polyurethane parts”, *International Journal on Interactive Design and Manufacturing (IJIDeM)*, vol. 17, nº 6, p. 3011–3024, dez. 2023, doi: 10.1007/s12008-023-01304-w.

[21] A. Rodríguez-Panes, J. Claver, e A. M. Camacho, “The influence of manufacturing parameters on the mechanical behaviour of PLA and ABS pieces manufactured by FDM: A comparative analysis”, *Materials*, vol. 11, nº 8, 2018, doi: 10.3390/ma11081333.

[22] L. Di Angelo, P. Di Stefano, e A. Marzola, “Surface quality prediction in FDM additive manufacturing”, *The International Journal of Advanced Manufacturing Technology*, vol. 93, nº 9–12, p. 3655–3662, dez. 2017, doi: 10.1007/s00170-017-0763-6.

[23] C. Ursini e L. Collini, “FDM Layering Deposition Effects on Mechanical Response of TPU Lattice Structures”, *Materials*, vol. 14, nº 19, p. 5645, set. 2021, doi: 10.3390/ma14195645.

[24] L. Rodríguez-Parada, P. F. Mayuet, e A. J. Gámez, “Industrial product design: Study of FDM technology for the manufacture of thermoformed prototypes”, *Procedia Manuf*, vol. 41, p. 587–593, 2019, doi: 10.1016/j.promfg.2019.09.046.

[25] F. Napolitano, E. Cozzolino, I. Papa, A. Astarita, e A. Squillace, “Experimental integrated approach for mechanical characteristic optimization of FDM-printed PLA in an

energy-saving perspective", *The International Journal of Advanced Manufacturing Technology*, vol. 121, nº 5–6, p. 3551–3565, jul. 2022, doi: 10.1007/s00170-022-09535-z.

[26] E. Cozzolino, F. Napolitano, I. Papa, A. Squillace, e A. Astarita, "Influence of the Heated-Bed Material on PLA Mechanical Properties and Energy Consumption in the FDM Process", *Arab J Sci Eng*, maio 2024, doi: 10.1007/s13369-024-09170-8.

[27] E. Cozzolino, F. Napolitano, A. Astarita, V. Lopresto, I. Papa, e A. Squillace, "Sustainability of Fused Deposition Modeling: The Role of the Plate Material", 2023, p. 99–105. doi: 10.1007/978-3-031-28547-9_12.

[28] V. Kostakis e M. Papachristou, "Commons-based peer production and digital fabrication: The case of a RepRap-based, Lego-built 3D printing-milling machine", *Telematics and Informatics*, vol. 31, nº 3, p. 434–443, ago. 2014, doi: 10.1016/j.tele.2013.09.006.

[29] J. Horvath, "Open Source", em *Mastering 3D Printing*, Berkeley, CA: Apress, 2014, p. 21–29. doi: 10.1007/978-1-4842-0025-4_3.

[30] S. Mellor, L. Hao, e D. Zhang, "Additive manufacturing: A framework for implementation", *Int J Prod Econ*, vol. 149, p. 194–201, mar. 2014, doi: 10.1016/j.ijpe.2013.07.008.

[31] T. G. Lopes, "O PROCESSO DE MANUFATURA ADITIVA POR IMPRESSÃO 3D COMO INSTRUMENTO EDUCACIONAL ATIVO", em *Avanços Tecnológicos, Gestão da Qualidade e Linguagem*, Dialética., vol. 1, A. Bezerra, S. da S. Pinto, e V. R. P. De Souza, Orgs., Dialética, 2024, 8, p. 173–204. Acessado: 2 de abril de 2024. [Online]. Disponível em: https://www.researchgate.net/publication/376713862_O_Processo_de_Manufatura_Aditiva_por_Impressao_3D_como_Instrumento_Educacional_Ativo

[32] A. B. Damasceno, T. N. Paneque, V. C. F. Teles, M. A. A. T. F. Moraes, e T. G. Lopes, "O Efeito do Parâmetro Densidade de Preenchimento na Obtenção de Peças pelo Processo FFF", em *V Congresso de Inovação e Tecnologia | VII Workshop de Iniciação Científica e Tecnológica*, Lins: Fatec Lins, nov. 2022.

[33] T. G. Lopes e P. Roberto De Aguiar, "IMPACTO DA VARIAÇÃO TÉRMICA NA EFICIÊNCIA DE MICROFONES DE BAIXO CUSTO PARA MONITORAMENTO DO PROCESSO DE IMPRESSÃO 3D", em *Avanços Tecnológicos, Gestão da Qualidade e Linguagem*, Dialética., vol. 1, A. P. Bezerra, S. da S. Pinto, e V. R. P. De Souza, Orgs., Dialética, 2024, 13, p. 329–351. Acessado: 2 de abril de 2024. [Online]. Disponível em: https://www.researchgate.net/publication/376713595_Impacto_da_Variacao_Termica_na_Eficiencia_de_Microfones_de_Baixo_Custo_para_Monitoramento_do_Processo_de_Impressao_3D

[34] M. Kocisko, M. Teliskova, J. Torok, e J. Petrus, "Postprocess Options for Home 3D Printers", *Procedia Eng*, vol. 196, nº June, p. 1065–1071, 2017, doi: 10.1016/j.proeng.2017.08.063.

[35] M. G. F. do Carmo, T. G. Lopes, V. S. Bombonatti, P. R. Aguiar, e T. V. França, "Studying the Defects and Geometric Anomalies on Monolayer Parts Obtained via the Fused Deposition Modeling Process", em *The First International Conference on "Green" Polymer Materials 2020*, Basel Switzerland: MDPI, nov. 2020, p. 40. doi: 10.3390/CGPM2020-07159.

[36] T. Glissoi Lopes, L. Marques Queiroz, V. Bombonatti, M. Carmo, P. Aguiar, e T. França, “THE INFLUENCE OF PRINTING PARAMETERS ON MONOLAYER PART FEATURES IN FUSED FILAMENT FABRICATION”, em *Proceedings of the 26th International Congress of Mechanical Engineering*, Florianópolis/SC: ABCM, 2021. doi: 10.26678/ABCM.COBEM2021.COB2021-0745.

[37] D. R. Pereira, E. Andreoti, G. S. Marin, L. G. da R. Silva, e T. G. Lopes, “A impressão 3D como ferramenta na obtenção de peças para projeto de cidade inteligente”, em *VI Congresso de Inovação e Tecnologia | VIII Workshop de Iniciação Científica e Tecnológica*, Lins: Fatec Lins, nov. 2023.

[38] Y. Fu, A. Downey, L. Yuan, A. Pratt, e Y. Balogun, “In situ monitoring for fused filament fabrication process: A review”, *Addit Manuf*, vol. 38, nº July 2020, p. 101749, fev. 2021, doi: 10.1016/j.addma.2020.101749.

[39] J. V. L. da Silva, “Planejamento de processo para prototipagem rápida”, em *Prototipagem Rápida - Tecnologias e Aplicações*, 1º ed, N. Volpato, Org., São Paulo: Blucher, 2007, 4, p. 37.

[40] P. Nath, J. D. Olson, S. Mahadevan, e Y. T. T. Lee, “Optimization of fused filament fabrication process parameters under uncertainty to maximize part geometry accuracy”, *Addit Manuf*, vol. 35, nº March, p. 101331, 2020, doi: 10.1016/j.addma.2020.101331.

[41] J. Hartcher-O’Brien, J. Evers, e E. Tempelman, “Surface roughness of 3D printed materials: Comparing physical measurements and human perception”, *Mater Today Commun*, vol. 19, nº February, p. 300–305, 2019, doi: 10.1016/j.mtcomm.2019.01.008.

[42] T. G. Lopes, Z. R. F. Antonio, C. S. Junior, E. L. V. Ruas, e P. R. Aguiar, “A PRIMEIRA CAMADA COMO INDICADOR DE QUALIDADE DO PLANEJAMENTO DO PROCESSO DE IMPRESSÃO 3D”, em *Anais do XXVII Simpósio de Engenharia de Produção (SIMPEP)*, Bauru, 2020, p. 1–12. [Online]. Disponível em: http://www.simpep.feb.unesp.br/anais_simpep.php?e=13

[43] H. Wu, Z. Yu, e Y. Wang, “Experimental study of the process failure diagnosis in additive manufacturing based on acoustic emission”, *Measurement*, vol. 136, p. 445–453, mar. 2019, doi: 10.1016/j.measurement.2018.12.067.

[44] Y. Li, W. Zhao, Q. Li, T. Wang, e G. Wang, “In-Situ Monitoring and Diagnosing for Fused Filament Fabrication Process Based on Vibration Sensors”, *Sensors*, vol. 19, nº 11, p. 2589, jun. 2019, doi: 10.3390/s19112589.

[45] Y. Tlegenov, G. S. Hong, e W. F. Lu, “Nozzle condition monitoring in 3D printing”, *Robot Comput Integr Manuf*, vol. 54, nº December 2017, p. 45–55, 2018, doi: 10.1016/j.rcim.2018.05.010.

[46] N. Volpato, “Os principais processos de prototipagem rápida”, em *Prototipagem Rápida - Tecnologias e Aplicações*, 1º ed, N. Volpato, Org., São Paulo: Blucher, 2007, 3, p. 45.

[47] C. Wendt, S. R. Fernández-Vidal, Á. Gómez-Parra, M. Batista, e M. Marcos, “Processing and Quality Evaluation of Additive Manufacturing Monolayer Specimens”, *Advances in Materials Science and Engineering*, vol. 2016, p. 1–8, 2016, doi: 10.1155/2016/5780693.

[48] P. Bhavsar, B. Sharma, W. Moscoso-Kingsley, e V. Madhavan, “Detecting first layer bond quality during FDM 3D printing using a discrete wavelet energy approach”, *Procedia Manuf*, vol. 48, p. 718–724, 2020, doi: 10.1016/j.promfg.2020.05.104.

[49] H. Wu, Z. Yu, e Y. Wang, “A New Approach for Online Monitoring of Additive Manufacturing Based on Acoustic Emission”, em *Proceedings of the ASME 2016 International Manufacturing Science and Engineering Conference (MSEC2016)*, Blacksburg: ASME, jun. 2016, p. 8. doi: 10.1115/MSEC2016-8551.

[50] T. G. Lopes, P. R. Aguiar, T. V. França, P. de O. Conceição Júnior, C. Soares Junior, e Z. R. F. Antonio, “Time-Domain Analysis of Acoustic Emission Signals during the First Layer Manufacturing in FFF Process”, *Engineering Proceedings*, vol. 27, nº 1, p. 83, nov. 2022, doi: 10.3390/ecsa-9-13285.

[51] T. G. Lopes, P. R. Aguiar, P. M. de C. Monson, D. M. D’Addona, P. de O. Conceição Júnior, e R. G. de Oliveira Junior, “Machine condition monitoring in FDM based on electret microphone, SVM, and neural networks”, *The International Journal of Advanced Manufacturing Technology*, out. 2023, doi: 10.1007/s00170-023-12375-0.

[52] M. A. A. Viera *et al.*, “Low-Cost Piezoelectric Transducer for Ceramic Grinding Monitoring”, *IEEE Sens J*, vol. 19, nº 17, p. 7605–7612, set. 2019, doi: 10.1109/JSEN.2019.2917119.

[53] M. A. A. Viera, R. Gotz, P. R. de Aguiar, F. A. Alexandre, B. O. Fernandez, e P. Oliveira Junior, “A Low-Cost Acoustic Emission Sensor based on Piezoelectric Diaphragm”, *IEEE Sens J*, p. 1–1, 2020, doi: 10.1109/JSEN.2020.2988478.

[54] D. M. S. Ribeiro, P. O. Conceição JR, R. D. Sodário, M. Marchi, P. R. Aguiar, e E. C. Bianchi, “Low-Cost Piezoelectric Transducer Applied To Workpiece Surface Monitoring in Grinding Process”, *ABCM International Congress of Mechanical Engineering - COBEM*, vol. 23, nº 1–10, 2015.

[55] T. G. Lopes *et al.*, “Study of the Influence of Temperature on Low-Cost Piezoelectric Transducer Response for 3D Printing Process Monitoring”, em *2019 7th International Engineering, Sciences and Technology Conference (IESTEC)*, IEEE, out. 2019, p. 544–549. doi: 10.1109/IESTEC46403.2019.00103.

[56] D. M. S. S. Ribeiro, P. R. Aguiar, L. F. G. G. Fabiano, D. M. D’Addona, F. G. Baptista, e E. C. Bianchi, “Spectra Measurements Using Piezoelectric Diaphragms to Detect Burn in Grinding Process”, *IEEE Trans Instrum Meas*, vol. 66, nº 11, p. 3052–3063, nov. 2017, doi: 10.1109/TIM.2017.2731038.

[57] F. A. Alexandre, P. R. Aguiar, R. Götz, M. A. Aulestia Viera, T. G. Lopes, e E. C. Bianchi, “A Novel Ultrasound Technique Based on Piezoelectric Diaphragms Applied to Material Removal Monitoring in the Grinding Process”, *Sensors*, vol. 19, nº 18, p. 3932, set. 2019, doi: 10.3390/s19183932.

[58] L. Barbosa, T. G. Lopes, P. R. Aguiar, R. G. de Oliveira Junior, e T. V. França, “Evaluating Temperature Influence on Low-Cost Microphone Response for 3D Printing Process Monitoring”, *Engineering Proceedings*, vol. 10, nº 1, p. 67, nov. 2021, doi: 10.3390/ecsa-8-11251.

[59] G. M. Sessler e J. E. West, “Self-Biased Condenser Microphones with High Capacitance”, *J Acoust Soc Am*, vol. 34, nº 12, p. 1981–1982, dez. 1962, doi: 10.1121/1.1937012.

[60] G. M. Sessler e J. E. West, “The electret microphone”, *IEEE Transactions on Broadcast and Television Receivers*, vol. BTR-10, nº 1, p. 73–76, maio 1964, doi: 10.1109/TBTR1.1964.6312040.

[61] E. Nogueira, J. S. Gil, e J. L. S. Bote, “Lifetime of electret microphones by thermal degradation analysis via electroacoustic measurements”, *Microelectronics Reliability*, vol. 81, nº December 2017, p. 95–100, 2018, doi: 10.1016/j.microrel.2017.12.018.

[62] O. AlShorman *et al.*, “Sounds and acoustic emission-based early fault diagnosis of induction motor: A review study”, 2021, *SAGE Publications Inc.* doi: 10.1177/1687814021996915.

[63] H. Wu, Z. Yu, e Y. Wang, “Real-time FDM machine condition monitoring and diagnosis based on acoustic emission and hidden semi-Markov model”, *The International Journal of Advanced Manufacturing Technology*, vol. 90, nº 5–8, p. 2027–2036, maio 2017, doi: 10.1007/s00170-016-9548-6.

[64] M. C. Gomes, L. C. Brito, M. Bacci da Silva, e M. A. Viana Duarte, “Tool wear monitoring in micromilling using Support Vector Machine with vibration and sound sensors”, *Precis Eng*, vol. 67, p. 137–151, jan. 2021, doi: 10.1016/j.precisioneng.2020.09.025.

[65] J. Lyu e S. Manoochehri, “Dimensional Prediction for FDM Machines Using Artificial Neural Network and Support Vector Regression”, em *Volume 1: 39th Computers and Information in Engineering Conference*, American Society of Mechanical Engineers, ago. 2019. doi: 10.1115/DETC2019-97963.

[66] J. S. Kim, C. S. Lee, S.-M. Kim, e S. W. Lee, “Development of Data-Driven In-Situ Monitoring and Diagnosis System of Fused Deposition Modeling (FDM) Process Based on Support Vector Machine Algorithm”, *International Journal of Precision Engineering and Manufacturing-Green Technology*, vol. 5, nº 4, p. 479–486, ago. 2018, doi: 10.1007/s40684-018-0051-4.

[67] R. Yamashita, M. Nishio, R. K. G. Do, e K. Togashi, “Convolutional neural networks: an overview and application in radiology”, *Insights Imaging*, vol. 9, nº 4, p. 611–629, ago. 2018, doi: 10.1007/s13244-018-0639-9.

[68] H. Li, Z. Yu, F. Li, Q. Kong, e J. Tang, “Real-time polymer flow state monitoring during fused filament fabrication based on acoustic emission”, *J Manuf Syst*, vol. 62, p. 628–635, jan. 2022, doi: 10.1016/j.jmsy.2022.01.007.

[69] P. R. Aguiar, T. G. Lopes, D. D’Addona, R. Gotz, e T. V França, “A Study on Acoustic Signals from an Electret Microphone in 3D Printing”, *Procedia CIRP*, vol. 126, p. 651–655, 2024, doi: 10.1016/j.procir.2024.08.282.

[70] T. G. Lopes, P. M. de Carvalho Monson, P. R. de Aguiar, R. G. de Oliveira Junior, e P. O. C. Junior, “fff_segmenter: A signal segmentation script for acoustic FFF fabrication data in MATLAB”, *J Open Source Softw*, vol. 9, nº 99, p. 6620, jul. 2024, doi: 10.21105/joss.06620.

[71] T. Glissoi Lopes, P. M. de Carvalho Monson, P. R. Aguiar, R. Götz de Oliveira Junior, e P. O. Conceição Junior, “fff_segmenter: A signal segmentation script for acoustic FFF fabrication data in MATLAB”, 12 de julho de 2024, *Zenodo, Online*: v3.0.1. doi: 10.5281/zenodo.12733091.

[72] L. Barbosa, T. G. Lopes, P. R. Aguiar, P. M. De Carvalho Monson, R. G. De Oliveira, e P. De Oliveira Conceição, “Electret Microphone and Counts Statistic in Monitoring 3D Printing”, em *2023 15th IEEE International Conference on Industry Applications (INDUSCON)*, IEEE, nov. 2023, p. 802–806. doi: 10.1109/INDUSCON58041.2023.10374939.

[73] T. G. Lopes, I. M. M. Rocha, P. R. Aguiar, e T. V. França, “Influence of Vibroacoustic Phenomena from FFF Process on Surface Characteristics of Printed Parts”, *Engineering Proceedings*, vol. 19, nº 1, p. 44, maio 2022, doi: 10.3390/ECP2022-12615.

[74] E. L. V. Ruas, P. R. de Aguiar, W. N. Lopes, T. G. Lopes, e C. S. Junior, “Monitoramento da operação de dressagem por meio de emissão acústica e índice de dano”, em *Proceedings of the 11º Congresso Brasileiro de Engenharia de Fabricação*, Curitiba: ABCM, 2021, p. 7. doi: 10.26678/ABCM.COBEF2021.COB21-0229.

[75] T. G. Lopes, L. D. Freire, P. A. da Cunha, P. R. Aguiar, e T. V. França, “Evaluating Liquid Influence on Low-Cost Piezoelectric Transducer Response for Elastic Emission Machining Monitoring”, *Engineering Proceedings*, vol. 24, nº 1, p. 7, set. 2022, doi: 10.3390/IECMA2022-12910.

[76] E. L. V. Ruas, W. N. Lopes, P. R. de Aguiar, T. G. Lopes, e P. O. C. Junior, “Monitoring the dressing operation of conventional aluminum oxide grinding wheels through damage index, power spectral density, and piezoelectric sensors”, *The International Journal of Advanced Manufacturing Technology*, jun. 2023, doi: 10.1007/s00170-023-11682-w.

[77] A. BEZERRA, S. S. PINTO, e V. R. P. SOUZA, *Avanços Tecnológicos, Gestão da Qualidade e Linguagem*, Dialética., vol. 1. Dialética, 2024. doi: 10.48021/978-65-270-1474-4.

[78] V. C. F. Teles, A. B. Damasceno, T. N. Paneque, M. A. A. T. F. Moraes, e T. G. Lopes, “O efeito do Posicionamento do Modelo Tridimensional para o Fatiamento na Obtenção de Peças pelo Processo FFF”, em *V Congresso de Inovação e Tecnologia | VII Workshop de Iniciação Científica e Tecnológica*, Lins: Fatec Lins, nov. 2022.

[79] M. A. A. T. F. Moraes, A. B. Damasceno, T. N. Paneque, V. C. F. Teles, e T. G. Lopes, “UM ESTUDO DE CASO COMPARATIVO ENTRE VEÍCULOS A COMBUSTÍVEL FOSSIL E ELÉTRICOS NA CIDADE DE LINS-SP”, em *V Congresso de Inovação e Tecnologia | VII Workshop de Iniciação Científica e Tecnológica*, Lins: FATEC Lins, nov. 2022. Acessado: 17 de julho de 2024. [Online]. Disponível em: https://www.researchgate.net/publication/365791866_UM_ESTUDO_DE_CASO_COMPARATIVO_ENTRE_VEICULOS_A_COMBUSTIVEL_FOSSIL_E_ELETRICOS_NA_CIDADE_DE_LINS-SP

[80] M. Hirsch *et al.*, “Assessing the capability of in-situ nondestructive analysis during layer based additive manufacture”, *Addit Manuf*, vol. 13, p. 135–142, jan. 2017, doi: 10.1016/J.ADDMA.2016.10.004.

[81] G. MATTERA, “Defect monitoring in wire arc additive manufacturing using frequency domain analysis”, maio 2024, p. 50–59. doi: 10.21741/9781644903131-6.

[82] M. Giulio, P. Joseph, e N. Luigi, “A Time-Frequency Domain Feature Extraction Approach Enhanced by Computer Vision for Wire Arc Additive Manufacturing Monitoring Using Fourier and Wavelet Transform”, *Journal of Advanced Manufacturing Systems*, maio 2024, doi: 10.1142/S021968672450032X.

[83] B. Yuan *et al.*, “Machine-Learning-Based Monitoring of Laser Powder Bed Fusion”, *Adv Mater Technol*, vol. 1800136, p. 1–6, 2018, doi: 10.1002/admt.201800136.

[84] G. Mattera, A. Caggiano, e L. Nele, “Optimal data-driven control of manufacturing processes using reinforcement learning: an application to wire arc additive manufacturing”, *J Intell Manuf*, jan. 2024, doi: 10.1007/s10845-023-02307-w.

[85] G. Mattera, A. Caggiano, e L. Nele, “Correction: Optimal data-driven control of manufacturing processes using reinforcement learning: an application to wire arc additive manufacturing”, *J Intell Manuf*, jul. 2024, doi: 10.1007/s10845-024-02450-y.

[86] G. Mattera, Z. Pan, A. Caggiano, J. Polden, P. A. Commins, e L. Nele, “Anomaly detection of Wire Arc Additively Manufactured parts via Surface Tension Transfer through unsupervised machine learning techniques”, em *17th CIRP Conference on Intelligent Computation in Manufacturing Industry*, Naples, jul. 2023.

[87] C. Wang, X. P. Tan, S. B. Tor, e C. S. Lim, “Machine learning in additive manufacturing: State-of-the-art and perspectives”, *Addit Manuf*, vol. 36, nº January, p. 101538, 2020, doi: 10.1016/j.addma.2020.101538.

[88] E. Cozzolino, A. J. Tiley, A. J. Ramirez, A. Astarita, e E. D. Herderick, “Energy efficiency of Gaussian and ring profiles for LPBF of nickel alloy 718”, *The International Journal of Advanced Manufacturing Technology*, vol. 132, nº 5–6, p. 3093–3104, maio 2024, doi: 10.1007/s00170-024-13511-0.

[89] E. Cozzolino, V. Lopresto, D. Borrelli, A. Caraviello, e A. Astarita, “An integrated approach to investigate the energy consumption for manufacturing and surface finishing 3D printed Inconel 718 parts”, *J Manuf Process*, vol. 79, p. 193–205, jul. 2022, doi: 10.1016/j.jmapro.2022.04.045.

[90] E. Manco, E. Cozzolino, e A. Astarita, “Laser polishing of additively manufactured metal parts: a review”, *Surface Engineering*, vol. 38, nº 3, p. 217–233, mar. 2022, doi: 10.1080/02670844.2022.2072080.

[91] L. W. Koester, H. Taheri, T. A. Bigelow, L. J. Bond, e E. J. Faierson, “In-situ acoustic signature monitoring in additive manufacturing processes”, em *AIP Conference Proceedings*, AIP Publishing LLC, abr. 2018, p. 020006. doi: 10.1063/1.5031503.

[92] M. Strantza, D. Van Hemelrijck, P. Guillaume, e D. G. Aggelis, “Acoustic emission monitoring of crack propagation in additively manufactured and conventional titanium components”, *Mech Res Commun*, vol. 84, p. 8–13, set. 2017, doi: 10.1016/j.mechrescom.2017.05.009.

[93] K. Wasmer, C. Kenel, C. Leinenbach, e S. A. Shevchik, “In Situ and Real-Time Monitoring of Powder-Bed AM by Combining Acoustic Emission and Artificial Intelligence”, em *International Conference on Additive Manufacturing in Products and Applications*, Cham: Springer International Publishing, 2017, p. 200–209. doi: 10.1007/978-3-319-66866-6_20.

[94] F. Baumann, M. Schön, J. Eichhoff, e D. Roller, “Concept Development of a Sensor Array for 3D Printer”, *Procedia CIRP*, vol. 51, p. 24–31, 2016, doi: 10.1016/j.procir.2016.05.041.

[95] G. P. Greeff e M. Schilling, “Closed loop control of slippage during filament transport in molten material extrusion”, *Addit Manuf*, vol. 14, p. 31–38, 2017, doi: 10.1016/j.addma.2016.12.005.

[96] B. P. Heller, D. E. Smith, e D. A. Jack, “Effects of extrudate swell and nozzle geometry on fiber orientation in Fused Filament Fabrication nozzle flow”, *Addit Manuf*, vol. 12, p. 252–264, out. 2016, doi: 10.1016/j.addma.2016.06.005.

[97] C. Luo, X. Wang, K. B. Migler, e J. E. Seppala, “Effects of feed rates on temperature profiles and feed forces in material extrusion additive manufacturing”, *Addit Manuf*, vol. 35, nº January, p. 101361, 2020, doi: 10.1016/j.addma.2020.101361.

[98] J. R. C. Dizon, A. H. Espera, Q. Chen, e R. C. Advincula, “Mechanical characterization of 3D-printed polymers”, *Addit Manuf*, vol. 20, p. 44–67, mar. 2018, doi: 10.1016/j.addma.2017.12.002.

[99] A. R. Torrado, C. M. Shemelya, J. D. English, Y. Lin, R. B. Wicker, e D. A. Roberson, “Characterizing the effect of additives to ABS on the mechanical property anisotropy of specimens fabricated by material extrusion 3D printing”, *Addit Manuf*, vol. 6, p. 16–29, 2015, doi: 10.1016/j.addma.2015.02.001.

[100] L. Santana, J. L. Alves, A. da C. Sabino Netto, e C. Merlini, “A comparative study between PETG and PLA for 3D printing through thermal, chemical and mechanical characterization”, *Revista Materia*, vol. 23, nº 4, 2018, doi: 10.1590/s1517-707620180004.0601.

[101] Md. H. Ali, S. Kurokawa, E. Shehab, e M. Mukhtarkhanov, “Development of a Large-scale multi-extrusion FDM printer, and its challenges”, *International Journal of Lightweight Materials and Manufacture*, jun. 2022, doi: 10.1016/j.ijlmm.2022.10.001.

[102] C. Wendt, A. P. Valerga, O. Droste, M. Batista, e M. Marcos, “FEM based evaluation of Fused Layer Modelling monolayers in tensile testing”, *Procedia Manuf*, vol. 13, p. 916–923, 2017, doi: 10.1016/j.promfg.2017.09.160.

[103] Q. Zhu, H. Li, K. Yu, H. Zhang, e Q. Zhang, “In-process ultrasonic inspection of first layer detachment during additive manufacturing”, *The International Journal of Advanced Manufacturing Technology*, vol. 121, nº 11–12, p. 8341–8356, ago. 2022, doi: 10.1007/s00170-022-09910-w.

[104] M. Enoki, H. Inaba, Y. Mizutani, M. Nakano, e M. Ohtsu, *The Japanese Society for Non-Destructive Inspection. Practical Acoustic Emission Testing*. 2016. doi: 10.1007/978-4-431-55072-3.

[105] P. E. Mix, *Introduction to nondestructive testing : a training guide*. Wiley, 2005.

[106] W. N. Lopes, P. R. Aguiar, P. O. Conceicao Junior, F. R. L. Dotto, B. O. Fernandez, e E. C. Bianchi, “Study of the Use of Piezoelectric Diaphragm as a Low-Cost Alternative to the Acoustic Emission Sensor in Dressing Operation of Aluminum Oxide Wheels”, *IEEE Sens J*, vol. 21, nº 16, p. 18055–18062, 2021, doi: 10.1109/JSEN.2021.3085246.

[107] N. Ullah, Z. Ahmed, e J.-M. Kim, “Pipeline Leakage Detection Using Acoustic Emission and Machine Learning Algorithms”, *Sensors*, vol. 23, nº 6, p. 3226, mar. 2023, doi: 10.3390/s23063226.

[108] C. Ennaceur, A. Laksimi, C. Hervé, e M. Cherfaoui, “Monitoring crack growth in pressure vessel steels by the acoustic emission technique and the method of potential difference”, *International Journal of Pressure Vessels and Piping*, vol. 83, nº 3, p. 197–204, mar. 2006, doi: 10.1016/j.ijpvp.2005.12.004.

[109] A. Olszewska, “Using the acoustic emission method for testing aboveground vertical storage tank bottoms”, *Applied Acoustics*, vol. 188, jan. 2022, doi: 10.1016/j.apacoust.2021.108564.

[110] S. M. Pirskawetz e S. Schmidt, “Detection of wire breaks in prestressed concrete bridges by Acoustic Emission analysis”, *Developments in the Built Environment*, vol. 14, abr. 2023, doi: 10.1016/j.dibe.2023.100151.

[111] S. Grigg, R. Pullin, e C. A. Featherston, “Acoustic emission source location in complex aircraft structures using three closely spaced sensors”, *Mech Syst Signal Process*, vol. 164, fev. 2022, doi: 10.1016/j.ymssp.2021.108256.

[112] S. A. Shevchik, C. Kenel, C. Leinenbach, e K. Wasmer, “Acoustic emission for in situ quality monitoring in additive manufacturing using spectral convolutional neural networks”, *Addit Manuf*, vol. 21, p. 598–604, maio 2018, doi: 10.1016/j.addma.2017.11.012.

[113] H. Wu, Y. Wang, e Z. Yu, “In situ monitoring of FDM machine condition via acoustic emission”, *The International Journal of Advanced Manufacturing Technology*, vol. 84, nº 5–8, p. 1483–1495, set. 2015, doi: 10.1007/s00170-015-7809-4.

[114] Z. Yang, L. Jin, Y. Yan, e Y. Mei, “Filament breakage monitoring in fused deposition modeling using acoustic emission technique”, *Sensors (Switzerland)*, vol. 18, nº 3, p. 1–16, 2018, doi: 10.3390/s18030749.

[115] F. Li, Z. Yu, Z. Yang, e X. Shen, “Real-time distortion monitoring during fused deposition modeling via acoustic emission”, *Struct Health Monit*, vol. 19, nº 2, p. 412–423, mar. 2020, doi: 10.1177/1475921719849700.

[116] E. G. Bakhoum e M. H. M. Cheng, “Novel electret microphone”, *IEEE Sens J*, vol. 11, nº 4, p. 988–994, 2011, doi: 10.1109/JSEN.2010.2077276.

[117] S. S. Kraman, G. R. Wodicka, Y. Oh, e H. Pasterkamp, “Measurement of Respiratory Acoustic Signals”, *Chest*, vol. 108, nº 4, p. 1004–1008, 1995, doi: 10.1378/chest.108.4.1004.

[118] F. C. Souza, S. D. Franco, R. V. Arencibia, J. E. S. Leal, E. B. Teodoro, e F. F. Ramos Neto, “Acoustic emission assessment of measurement errors caused by gaps in chemical composition analyzes carried out using a portable spark spectrometer”, *Measurement*, vol. 151, p. 107105, fev. 2020, doi: 10.1016/j.measurement.2019.107105.

[119] J. Li, X. Gao, L. Fang, W. Zhang, e H. Cha, “Resonant photoacoustic detection of trace gas with DFB diode laser”, *Opt Laser Technol*, vol. 39, nº 6, p. 1144–1149, 2007, doi: 10.1016/j.optlastec.2006.09.007.

[120] M. W. Sigrist, “Trace gas monitoring by laser-photoacoustic spectroscopy”, *Infrared Phys Technol*, vol. 36, nº 1, p. 415–425, 1995, doi: 10.1016/1350-4495(94)00093-Z.

[121] K. Albion, L. Briens, C. Briens, e F. Berruti, “Detection of the breakage of pharmaceutical tablets in pneumatic transport”, *Int J Pharm*, vol. 322, nº 1–2, p. 119–129, 2006, doi: 10.1016/j.ijpharm.2006.05.039.

[122] K. Albion, L. Briens, C. Briens, F. Berruti, e G. Book, “Flow regime determination in upward inclined pneumatic transport of particulates using non-intrusive acoustic probes”, *Chemical Engineering and Processing: Process Intensification*, vol. 46, nº 6, p. 520–531, 2007, doi: 10.1016/j.cep.2006.06.012.

[123] K. Albion, L. Briens, C. Briens, e F. Berruti, “Flow regime determination in horizontal pneumatic transport of fine powders using non-intrusive acoustic probes”, *Powder Technol*, vol. 172, nº 3, p. 157–166, 2007, doi: 10.1016/j.powtec.2006.10.040.

[124] C. Sosna, T. Walter, e W. Lang, “Response time of thermal flow sensors with air as fluid”, *Sens Actuators A Phys*, vol. 172, nº 1, p. 15–20, 2011, doi: 10.1016/j.sna.2011.02.023.

[125] K. Albion, L. Briens, C. Briens, F. Berruti, e S. McDougall, “Detection of oversized material in a hydrotransport slurry pipe using a non-invasive acoustic method”, *Powder Technol*, vol. 190, nº 3, p. 361–371, 2009, doi: 10.1016/j.powtec.2008.08.020.

[126] K. Albion, L. Briens, C. Briens, e F. Berruti, “Modelling of oversized material flow through a horizontal hydrotransport slurry pipe to optimize its acoustic detection”, *Powder Technol*, vol. 194, nº 1–2, p. 18–32, 2009, doi: 10.1016/j.powtec.2009.03.017.

[127] L. Briens, R. Smith, e C. Briens, “Monitoring of a rotary dryer using acoustic emissions”, *Powder Technol*, vol. 181, nº 2, p. 115–120, 2008, doi: 10.1016/j.powtec.2006.12.004.

[128] N. G. Iyer e S. R. Norman, “Analysis of acoustic signals from rotating machines for wear detection”, em *2014 International Conference on Recent Trends in Information Technology*, IEEE, abr. 2014, p. 1–6. doi: 10.1109/ICRTIT.2014.6996206.

[129] D. J. Hill, G. Heins, e M. Thiele, “Reduction of torque ripple induced acoustic emissions in permanent magnet synchronous motors”, *2017 IEEE International Electric Machines and Drives Conference, IEMDC 2017*, 2017, doi: 10.1109/IEMDC.2017.8002353.

[130] V. Nguyen e A. Dugenske, “An I2C based architecture for monitoring legacy manufacturing equipment”, *Manuf Lett*, vol. 15, p. 67–70, 2018, doi: 10.1016/j.mfglet.2017.12.018.

[131] N. Lambos, G. C. Vosniakos, e G. Papazetis, “Low-cost automatic identification of nozzle clogging in material extrusion 3D printers”, em *Procedia Manufacturing*, Elsevier B.V., 2020, p. 274–279. doi: 10.1016/j.promfg.2020.10.039.

[132] H. A. Kishawy, H. Hegab, U. Umer, e A. Mohany, “Application of acoustic emissions in machining processes: analysis and critical review”, *International Journal of Advanced Manufacturing Technology*, vol. 98, nº 5–8, p. 1391–1407, set. 2018, doi: 10.1007/s00170-018-2341-y.

[133] Z. Nazarchuk, V. Skalskyi, e O. Serhiyenko, *Foundations of Engineering Mechanics Acoustic Emission Methodology and Application*, 1st ed. Cham, Switzerland: Springer International Publishing AG, 2017. doi: 10.1007/978-3-319-49350-3.

[134] W. N. Lopes *et al.*, “Digital signal processing of acoustic emission signals using power spectral density and counts statistic applied to single-point dressing operation”, *IET Science, Measurement and Technology*, vol. 11, nº 5, p. 631–636, ago. 2017, doi: 10.1049/iet-smt.2016.0317.

[135] J. Liu, Y. Hu, B. Wu, e Y. Wang, “An improved fault diagnosis approach for FDM process with acoustic emission”, *J Manuf Process*, vol. 35, nº August, p. 570–579, out. 2018, doi: 10.1016/j.jmapro.2018.08.038.

[136] D. M. Daddona, S. Conte, W. N. Lopes, P. R. De Aguiar, E. C. Bianchi, e R. Teti, “Tool Condition Monitoring of Single-point Dressing Operation by Digital Signal Processing of AE and AI”, *Procedia CIRP*, vol. 67, p. 307–312, 2018, doi: 10.1016/j.procir.2017.12.218.

[137] P. R. Aguiar, P. J. A. Serni, F. R. L. Dotto, e E. C. Bianchi, “In-process grinding monitoring through acoustic emission”, *Journal of the Brazilian Society of Mechanical Sciences and Engineering*, vol. 28, nº 1, p. 118–124, mar. 2006, doi: 10.1590/S1678-58782006000100014.

[138] G. B. Lucas, B. A. de Castro, M. A. Rocha, e A. L. Andreoli, “Study of a Low-Cost Piezoelectric Sensor for Three Phase Induction Motor Load Estimation”, *Proc West Mark Ed Assoc Conf*, vol. 4, nº 1, p. 46, fev. 2019, doi: 10.3390/ecsa-5-05723.

[139] D. Giridhar, L. Vijayaraghavan, e R. Krishnamurthy, “Acoustic emission response of sintered alumina zirconia composite during grooving process”, *NDT and E International*, vol. 46, nº 1, p. 55–62, 2012, doi: 10.1016/j.ndteint.2011.11.002.

[140] J. Webster, W. P. Dong, e R. Lindsay, “Raw Acoustic Emission Signal Analysis of Grinding Process”, *CIRP Ann Manuf Technol*, vol. 45, nº 1, p. 335–340, 1996, doi: 10.1016/S0007-8506(07)63075-3.

[141] K. Jemielniak, “Some aspects of acoustic emission signal pre-processing”, *J Mater Process Technol*, vol. 109, nº 3, p. 242–247, fev. 2001, doi: 10.1016/S0924-0136(00)00805-0.

[142] H. Y. Kim, S. R. Kim, J. H. Ahn, e S. H. Kim, “Process monitoring of centerless grinding using acoustic emission”, *J Mater Process Technol*, vol. 111, nº 1–3, p. 273–278, abr. 2001, doi: 10.1016/S0924-0136(01)00533-7.

[143] M. A. Aulestia Viera *et al.*, “A Time–Frequency Acoustic Emission-Based Technique to Assess Workpiece Surface Quality in Ceramic Grinding with PZT Transducer”, *Sensors*, vol. 19, nº 18, p. 3913, 2019, doi: 10.3390/s19183913.

[144] B. Wang e Z. Liu, “Acoustic emission signal analysis during chip formation process in high speed machining of 7050-T7451 aluminum alloy and Inconel 718 superalloy”, *J Manuf Process*, vol. 27, p. 114–125, 2017, doi: 10.1016/j.jmapro.2017.04.003.

[145] L. Pilný, G. Bissacco, L. De Chiffre, e J. Ramsing, “Acoustic emission-based in-process monitoring of surface generation in robot-assisted polishing”, *Int J Comput Integr Manuf*, vol. 29, nº 11, p. 1218–1226, nov. 2016, doi: 10.1080/0951192X.2015.1034180.

[146] X. Xie, Q. Huang, J. Long, Q. Ren, W. Hu, e S. Liu, “A new monitoring method for metal rust removal states in pulsed laser derusting via acoustic emission techniques”, *J Mater Process Technol*, vol. 275, nº July 2019, p. 116321, 2020, doi: 10.1016/j.jmatprotec.2019.116321.

[147] P. R. Aguiar, P. J. A. Serni, E. C. Bianchi, e F. R. L. Dotto, “In-process grinding monitoring by acoustic emission”, *2004 IEEE International Conference on Acoustics, Speech, and Signal Processing*, vol. 5, p. V-405–8, 2004, doi: 10.1109/icassp.2004.1327133.

[148] C. H. R. Martins, P. R. Aguiar, A. Frech, e E. C. Bianchi, “Tool condition monitoring of single-point dresser using acoustic emission and neural networks models”, *IEEE Trans Instrum Meas*, vol. 63, nº 3, p. 667–679, 2014, doi: 10.1109/TIM.2013.2281576.

[149] F. A. Alexandre, W. N. Lopes, F. I. Ferreira, F. R. L. Dotto, P. R. de Aguiar, e E. C. Bianchi, “Chatter Vibration Monitoring in the Surface Grinding Process through Digital Signal Processing of Acceleration Signal”, *Proc West Mark Ed Assoc Conf*, vol. 2, nº 3, p. 126, 2017, doi: 10.3390/ecsa-4-04927.

[150] C. H. R. Martins, P. R. Aguiar, A. Frech, e E. C. Bianchi, “Neural Networks Models for Wear Patterns Recognition of Single-point Dresser”, *IFAC Proceedings Volumes*, vol. 46, nº 9, p. 1524–1529, 2013, doi: 10.3182/20130619-3-RU-3018.00222.

[151] E. C. T. Ba, M. R. Dumont, P. S. Martins, R. M. Drumond, M. P. Martins da Cruz, e V. F. Vieira, “Investigation of the effects of skewness Rsk and kurtosis Rku on tribological behavior in a pin-on-disc test of surfaces machined by conventional milling and turning processes”, *Materials Research*, vol. 24, nº 2, 2021, doi: 10.1590/1980-5373-mr-2020-0435.

[152] V. Nasir, J. Cool, e F. Sassani, “Acoustic emission monitoring of sawing process: artificial intelligence approach for optimal sensory feature selection”, *International Journal of Advanced Manufacturing Technology*, vol. 102, nº 9–12, p. 4179–4197, jun. 2019, doi: 10.1007/s00170-019-03526-3.

[153] Q. Nazir e C. Shao, “Online tool condition monitoring for ultrasonic metal welding via sensor fusion and machine learning”, *J Manuf Process*, vol. 62, nº August 2020, p. 806–816, 2021, doi: 10.1016/j.jmapro.2020.12.050.

[154] E. C. Talibouya Ba, M. R. Dumont, P. S. Martins, R. M. Drumond, M. P. M. da Cruz, e V. F. Vieira, “Investigation of the effects of skewness Rsk and kurtosis Rku on tribological behavior in a pin-on-disc test of surfaces machined by conventional milling and turning processes”, *Materials Research*, vol. 24, nº 2, p. 1–14, 2021, doi: 10.1590/1980-5373-MR-2020-0435.

[155] D. Goyal, Vanraj, B. S. Pabla, e S. S. Dhami, “Condition Monitoring Parameters for Fault Diagnosis of Fixed Axis Gearbox: A Review”, *Archives of Computational Methods in Engineering*, vol. 24, nº 3, p. 543–556, jul. 2017, doi: 10.1007/s11831-016-9176-1.

[156] G. Mattera, J. Polden, A. Caggiano, L. Nele, Z. Pan, e J. Norrish, “Semi-supervised learning for real-time anomaly detection in pulsed transfer wire arc additive manufacturing”, *J Manuf Process*, vol. 128, p. 84–97, out. 2024, doi: 10.1016/j.jmapro.2024.07.142.

[157] G. Mattera, J. Polden, A. Caggiano, P. Commins, L. Nele, e Z. Pan, “Anomaly Detection of Wire Arc Additively Manufactured Parts via Surface Tension Transfer through Unsupervised Machine Learning Techniques”, *Procedia CIRP*, vol. 126, p. 686–691, 2024, doi: 10.1016/j.procir.2024.08.288.

[158] M. Lebold, K. Mcclintic, R. Campbell, C. Byington, e K. Maynard, “Review of vibration analysis methods for gearbox diagnostics and prognostics”, *54th Meeting of the Society for Machinery Failure Prevention Technology*, 2000.

[159] T. Glissoi Lopes, M. Carmo, L. Marques Queiroz, P. Aguiar, e T. França, “FEASIBILITY OF OPTICAL PROFILOMETRY FOR QUALITY CHARACTERIZATION OF MONOLAYER PARTS OBTAINED BY FUSED FILAMENT FABRICATION”, em *Proceedings of the 26th International Congress of Mechanical Engineering*, Florianópolis/SC: ABCM, 2021. doi: 10.26678/ABCM.COBEM2021.COB2021-0751.

[160] P. R. Aguiar, T. G. Lopes, D. M. D’Addona, R. Gotz, e T. V. França, “A Study on Acoustic Signals from an Electret Microphone in 3D Printing (under publishing)”, em *17th CIRP Conference on Intelligent Computation in Manufacturing Engineering*, Naples, Italy: ELSEVIER B.V., jul. 2023.

[161] T. G. Lopes, R. M. Rocha, P. R. Aguiar, F. A. Alexandre, e T. V. França, “Evaluating Temperature Influence on Low-Cost Piezoelectric Transducer Response for 3D Printing

Process Monitoring", *Proc West Mark Ed Assoc Conf*, vol. 42, nº 1, p. 26, nov. 2019, doi: 10.3390/ecsa-6-06571.

[162] GTMax3D, "CONJUNTO 4 DRIVER A4988 - POLOLU REPRAP RAMPS STEP-STICK", https://www.gtmax3d.com.br/componentes/4-driver-a4988-pololu-reprap-ramps-stepstick.

[163] GTMax3D, "RAMPS REPRAP1.4 - IMPRESSORA 3D - PARA ARDUINO", https://www.gtmax3d.com.br/componentes/ramps-reprap-1-4.

[164] RepRap team, "Arduino Mega Pololu Shield", RepRap Org Wiki. Acessado: 6 de julho de 2024. [Online]. Disponível em: https://reprap.org/wiki/Arduino_Mega_Pololu_Shield

[165] A. Yadav, "Nyquist-Shannon Sampling Theorem", em *Digital Communication*, 2009.

[166] E. J. Candes e M. B. Wakin, "An Introduction To Compressive Sampling", *IEEE Signal Process Mag*, vol. 25, nº 2, 2008, doi: 10.1109/msp.2007.914731.

[167] J. Caldwell, "Single-Supply, Electret Microphone Pre-Amplifier Reference Design", *Texas Instruments, Technical document, Reference Guide.*, nº TIDU765-January 2015, p. 1–23, 2015.

[168] Y. Hioka e K. Niwa, "Estimating power spectral density for spatial audio signal separation: An effective approach for practical applications", *Acoust Sci Technol*, vol. 38, nº 4, p. 175–184, 2017, doi: 10.1250/ast.38.175.

[169] R. Thomazella, W. N. Lopes, P. R. Aguiar, F. A. Alexandre, A. A. Fiocchi, e E. C. Bianchi, "Digital signal processing for self-vibration monitoring in grinding: A new approach based on the time-frequency analysis of vibration signals", *Measurement (Lond)*, vol. 145, 2019, doi: 10.1016/j.measurement.2019.05.079.

[170] C. H. R. Martins, P. R. Aguiar, A. Frech, e E. C. Bianchi, "Tool Condition Monitoring of Single-Point Dresser Using Acoustic Emission and Neural Networks Models", *IEEE Trans Instrum Meas*, vol. 63, nº 3, p. 667–679, mar. 2014, doi: 10.1109/TIM.2013.2281576.

[171] F. A. Alexandre *et al.*, "Tool condition monitoring of aluminum oxide grinding wheel using AE and fuzzy model", *International Journal of Advanced Manufacturing Technology*, vol. 96, p. 67–79, janeiro de 2018. doi: 10.1007/s00170-018-1582-0.

[172] L. Beranek e T. Mellow, *Acoustics: Sound Fields, Transducers and Vibration*, 2sd ed. Academic Press, 2019.

[173] M. K. Korucu, Ö. Kaplan, O. Büyük, e M. K. Güllü, "An investigation of the usability of sound recognition for source separation of packaging wastes in reverse vending machines", *Waste Management*, vol. 56, p. 46–52, 2016, doi: 10.1016/j.wasman.2016.06.030.

[174] W. R. Hendee e E. R. Ritenour, *Medical imaging physics*. Wiley-Liss, 2002.

[175] P. A. Tipler e G. Mosca, *Physics for Scientists and Engineers*, 6º ed. New York, NY: W. H. Freeman and Company, 2008.

[176] I. Kubiak, A. Przybysz, e A. Stańczak, "Usefulness of acoustic sounds from 3D printers in an eavesdropping process and reconstruction of printed shapes", *Electronics (Switzerland)*, vol. 9, nº 2, 2020, doi: 10.3390/electronics9020297.

[177] C. Song, F. Lin, Z. Ba, K. Ren, C. Zhou, e W. Xu, “My smartphone knows what you print: Exploring smartphone-based side-channel attacks against 3D printers”, *Proceedings of the ACM Conference on Computer and Communications Security*, vol. 24-28-October-2016, p. 895–907, 2016, doi: 10.1145/2976749.2978300.

[178] S. Y. Yu, A. V. Malawade, S. R. Chhetri, e M. A. Al Faruque, “Sabotage Attack Detection for Additive Manufacturing Systems”, *IEEE Access*, vol. 8, p. 27218–27231, 2020, doi: 10.1109/ACCESS.2020.2971947.

[179] J. O. Smith, *Mathematics of the Discrete Fourier Transform (DFT) with Audio Applications*, 2sd. W3K Publishing, 2007.

[180] M. A. Al Faruque, S. R. Chhetri, A. Canedo, e J. Wan, “Acoustic Side-Channel Attacks on Additive Manufacturing Systems”, *2016 ACM/IEEE 7th International Conference on Cyber-Physical Systems, ICCPS 2016 - Proceedings*, 2016, doi: 10.1109/ICCPS.2016.7479068.

[181] A. S. Sait e Y. I. Sharaf-Eldeen, “A review of gearbox condition monitoring based on vibration analysis techniques diagnostics and prognostics”, *Conference Proceedings of the Society for Experimental Mechanics Series*, vol. 5, nº March 2011, p. 307–324, 2011, doi: 10.1007/978-1-4419-9428-8_25.

[182] R. Guido, S. Ferrisi, D. Lofaro, e D. Conforti, “An Overview on the Advancements of Support Vector Machine Models in Healthcare Applications: A Review”, *Information*, vol. 15, nº 4, p. 235, abr. 2024, doi: 10.3390/info15040235.

[183] A. Dorbane, F. Harrou, e Y. Sun, “Exploring Deep Learning Methods to Forecast Mechanical Behavior of FSW Aluminum Sheets”, *J Mater Eng Perform*, vol. 32, nº 9, p. 4047–4063, maio 2023, doi: 10.1007/s11665-022-07376-1.

7– APPENDIX I

Figure 7.1 - *numofContourLoops* value found in the workpiece G-code



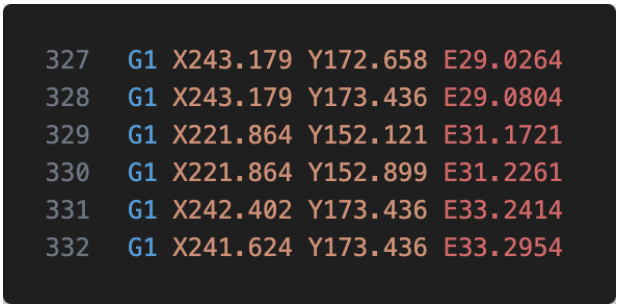
```
31  ;  perimeterOutlines,3
```

Figure 7.2 - Outer perimeter G-code in regard to contour lines furthest from the center



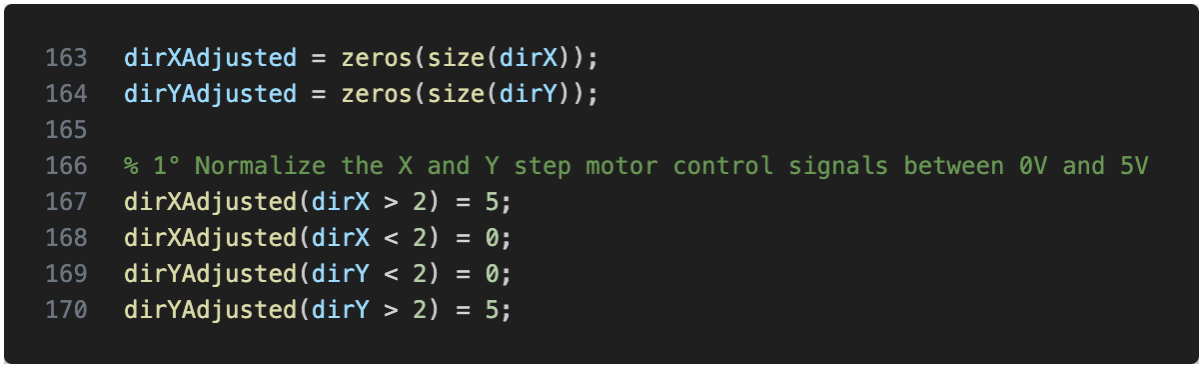
```
247  ; feature outer perimeter
248  G1 X220.297 Y150.554 F9000
249  G1 E0.0000 F3600
250  G92 E0.0000
251  G1 X244.747 Y150.554 E1.6966 F1200
252  G1 X244.747 Y175.004 E3.3932
253  G1 X220.297 Y175.004 E5.0897
254  G1 X220.297 Y150.654 E6.7794
255  G1 X220.297 Y150.554 F1200
256  G1 X222.297 Y150.554 F1200
```

Figure 7.3 - Internal printing pattern G-code in regard to the middle raster lines and transition between raster lines



```
327  G1 X243.179 Y172.658 E29.0264
328  G1 X243.179 Y173.436 E29.0804
329  G1 X221.864 Y152.121 E31.1721
330  G1 X221.864 Y152.899 E31.2261
331  G1 X242.402 Y173.436 E33.2414
332  G1 X241.624 Y173.436 E33.2954
```

Figure 7.4 - Code for normalize the X and Y step motor control signals between 0V and 5V



```
163  dirXAdjusted = zeros(size(dirX));
164  dirYAdjusted = zeros(size(dirY));
165
166  % 1° Normalize the X and Y step motor control signals between 0V and 5V
167  dirXAdjusted(dirX > 2) = 5;
168  dirXAdjusted(dirX < 2) = 0;
169  dirYAdjusted(dirY < 2) = 0;
170  dirYAdjusted(dirY > 2) = 5;
```

Figure 7.5 - Code to test for the occurrence of the variation problem

```
% 2° Normalize the acoustic signal, and the X and Y step motor control
% signals between -1 and 1 (acoustic signal) and 0 & 1 (step motor signals)

sensorSignalNormalized = Normaliz3r(sensorSignal);
dirYAdjustedNormalized = Normaliz3r(dirYAdjusted);
dirXAdjustedNormalized = Normaliz3r(dirXAdjusted);
```

Figure 7.6 - Code to obtain the *Duration* matrix

```
% 4° Obtain the duration vector
Duration = obtainDuration(sensorSignalNormalized, dirXAdjustedNormalized,...
    dirYAdjustedNormalized, resultProblem, refminimum_sampleValue);
```

Figure 7.7 - Code to find the separation point

```
% 5° Find the separation point

for i = 1:length(Duration(:,1))

    resultSep = determin_separation_point(Duration, i, durationReference);

    if resultSep == true
        patternVariationPoint = Duration(i,2);
        break;
    else
        clear resultSep
    end
end
% \ 5°
```

Figure 7.8 - Code to obtain the temporary contour lines matrix

```
% 6° Contour lines obtaining
separationIndex = find(Duration(:,3) == patternVariationPoint);
externalLines = zeros(1,13);
duration3Length = 1;

for i = 1:13
    externalLines(1,i) = Duration(separationIndex-13+i,3);
end
for i = 1:length(externalLines)-1
    indexCountourTemp(duration3Length,1) = externalLines(i+1) - externalLines(i);
    indexCountourTemp(duration3Length,2) = externalLines(i);
    indexCountourTemp(duration3Length,3) = externalLines(i+1);
    duration3Length = duration3Length+1;
end
% \ 6 °
```

Figure 7.9 - Code to obtain the correct contour lines matrix and MWD matrix

```
% 7° Repositioning evaluation and contour lines correction

% reposition 1
meanCountourGroup1 = round(mean([indexCountourTemp(numofContourSides-2,1) indexCountourTemp(numofContourSides-1,1)...
    indexCountourTemp(numofContourSides,1)]),0);

adjustedContourLine1(1,1) = meanCountourGroup1;
adjustedContourLine1(1,3) = indexCountourTemp(1,3);
adjustedContourLine1(1,2) = indexCountourTemp(1,3) - meanCountourGroup1;

if indexCountourTemp(1,1) - meanCountourGroup1 < 1
    repoToContour1(1,1) = abs(indexCountourTemp(1,1) - meanCountourGroup1);
    repoToContour1(1,3) = adjustedContourLine1(1,2);
    repoToContour1(1,2) = repoToContour1(1,3)...
        - repoToContour1(1,1);
else
    repoToContour1(1,1) = indexCountourTemp(1,1) - meanCountourGroup1;
    repoToContour1(1,3) = adjustedContourLine1(1,2);
    repoToContour1(1,2) = indexCountourTemp(1,2);
end

% reposition 2
meanContourGroup2 = round(mean([indexCountourTemp(6,1) indexCountourTemp(7,1)...
    indexCountourTemp(8,1)]),0);

adjustedContourLine2(1,1) = meanContourGroup2;
adjustedContourLine2(1,3) = indexCountourTemp(5,3);
adjustedContourLine2(1,2) = indexCountourTemp(5,3) - meanContourGroup2;

repoToContour2(1,1) = indexCountourTemp(5,1) - meanContourGroup2;
repoToContour2(1,3) = adjustedContourLine2(1,2);
repoToContour2(1,2) = indexCountourTemp(5,2);

% reposition 3
meanContourGroup3 = round(mean([indexCountourTemp(10,1) indexCountourTemp(11,1)...
    indexCountourTemp(numofContourLines,1)]),0);

adjustedContourLine3(1,1) = meanContourGroup3;
adjustedContourLine3(1,3) = indexCountourTemp(9,3);
adjustedContourLine3(1,2) = indexCountourTemp(9,3) - meanContourGroup3;

repoToContour3(1,1) = indexCountourTemp(9,1) - meanContourGroup3;
repoToContour3(1,3) = adjustedContourLine3(1,2);
repoToContour3(1,2) = indexCountourTemp(9,2);

indexContour = indexCountourTemp;
indexContour(1,:) = adjustedContourLine1;
indexContour(5,:) = adjustedContourLine2;
indexContour(9,:) = adjustedContourLine3;

contourRepositions = [repoToContour1; repoToContour2; repoToContour3];
% \ 7°
```

Figure 7.10 - Code to obtain the first duration matrix for the internal pattern

```
% 8° Obtaining first duration matrix for the internal pattern
% There is no need to check for the problem of too many consecutive transition lines here
% since there are very small line segments in the internal pattern. On the contrary,
% this could cause some issues. So the result_problem value is set to false.
resultProblem = false;

% Obtaining duration matrix
Duration = obtainDuration(sensorSignalNormalized, ...
    dirXAdjustedNormalized,...
    dirYAdjustedNormalized, ...
    resultProblem, refminimum_sampleValue);
    % \ 8°
```

Figure 7.11 - Code to obtain the second duration matrix for the internal pattern

```
295  % 9° Obtaining second duration matrix for the internal pattern
296
297  % Filtering the duration matrix to remove the small line segments
298  indexValuesAbvRef = 1;
299  Duration2 = zeros(3);
300  alterationDuration = lowRefTransRaster;
301  for i = 1:length(Duration(:,1))
302      if Duration(i,1) > alterationDuration
303          Duration2(indexValuesAbvRef,:) = Duration(i,:);
304          indexValuesAbvRef = indexValuesAbvRef + 1;
305      end
306  end
307
308  clear Duration
309      % \ 9°
```

Figure 7.12 - Code to obtain the third duration matrix for the internal pattern

```
% 10° Obtaining third duration matrix for the internal pattern

linesUdrUppVal = find(Duration2(:,1) < uppRefTransRaster);
Duration3 = zeros(3);
previousPeak = 0;
previousPeak2 = 0;

for i = 1:length (linesUdrUppVal)
    if i == length (linesUdrUppVal)
        break;
    end
    initialIndex = linesUdrUppVal(i);
    finalIndex = linesUdrUppVal(i+1);
    result = detectAnom(initialIndex, finalIndex);
    previousPeak2 = previousPeak;
    previousPeak = Duration3(end-1,1);
    if  previousPeak < previousPeak2 % Change of behaviour from increasing to decreasing
        break;
    end
    if  previousPeak > middleRasterDuration % Is larger than the middle raster duration,
        % found the end of the increasing behaviour
        break;
    end
    if result == true % normal situation
        tempDuration= isNormal( ...
            Duration2, ...
            initialIndex, ...
            finalIndex, ...
            1);
        if Duration3(1,1) == 0
            Duration3 = tempDuration;
        else
            Duration3 = [Duration3(1:end-1,:); tempDuration];
        end
        clear tempDuration
    else % abnormal situation
        tempDuration = isAbnormal( ...
            Duration2, ...
            initialIndex, ...
            finalIndex, ...
            previousPeak, varDurRaster, adpDurTranRaster);
        Duration3 = [Duration3(1:end-1,:); tempDuration];
        clear tempDuration
    end
end

clear Duration2
% \ 10°
```

Figure 7.13 - Code to obtain the fourth duration matrix for the internal pattern

```
% 11° Obtaining fourth duration matrix for the internal pattern
indexPreviousPeak2 = find (Duration3(:,1) == previousPeak2);
Duration3_v2 = Duration3(1:end-(end-indexPreviousPeak2)+1,:);
% \ 11°
```

Figure 7.14 - Code to obtain the fifth duration matrix for the internal pattern

```
% 12° Obtaining fifth duration matrix for the internal pattern
% Raster area mirroring

duration3Length = length(Duration3_v2(:,1));
Duration4 = Duration3_v2;

for i = 1:length(Duration3_v2(:,1))-2
    if i == 1
        Duration4(duration3Length,1) = Duration3_v2(length(Duration3_v2(:,1))-i-1,1);
        Duration4(duration3Length,3) = Duration3_v2(length(Duration3_v2(:,1))-i,2);
        Duration4(duration3Length,2) = Duration4(duration3Length,3) + Duration4(duration3Length,1);
        duration3Length = duration3Length + 1;
    end
    if i ~= 1
        Duration4(duration3Length,1) = Duration3_v2(length(Duration3_v2(:,1))-i-1,1);
        Duration4(duration3Length,3) = Duration4(duration3Length-1,2);
        Duration4(duration3Length,2) = Duration4(duration3Length,3) + Duration4(duration3Length,1);
        duration3Length = duration3Length + 1;
    end
end

clear Duration3_v2

% \ 12°
```

Figure 7.15 - Code to obtain the sixth duration matrix for the internal pattern

```
% 13° Obtaining sixth duration matrix for the internal pattern
% Obtain the first raster line and add to the beggining of the duraction matrix
Duration4_v2(1,2) = Duration4(1,3);
Duration4_v2(1,1) = Duration4(2,1)-varDurRaster;
Duration4_v2(1,3) = Duration4_v2(1,2) - Duration4_v2(1,1);
Duration4_v2(2:length(Duration4(:,1))+1,:) = Duration4;

% Obtain the last raster line and add to the end of the duraction matrix
Duration4_v2(length(Duration4(:,1))+2,3) = Duration4_v2(length(Duration4(:,1))+1,2);
Duration4_v2(length(Duration4(:,1))+2,1) = Duration4_v2(length(Duration4(:,1)),1)-varDurRaster;
Duration4_v2(length(Duration4(:,1))+2,2) = Duration4_v2(length(Duration4(:,1))+2,1) + Duration4_v2(length(Duration4(:,1))+2,3);

clear Duration4
% \ 13°
```

Figure 7.16 - Code to obtain the index values from the last duration matrix

```
% 14° Obtaining the index values from the last duration matrix
rasterLineCount = 1;
transitionLineCount = 1;

for j = 1:length(Duration4_v2(:,1))
    if Duration4_v2(j,1) < lowRefTransRaster || Duration4_v2(j,1) > uppRefTransRaster
        index_raster(rasterLineCount,:) = Duration4_v2(j,:);
        rasterLineCount = rasterLineCount + 1;
    else
        index_trans_raster(transitionLineCount,:) = Duration4_v2(j,:);
        transitionLineCount = transitionLineCount + 1;
    end
end

contourToRasterReposition(1,3) = indexContour(numofContourLines,3);
contourToRasterReposition(1,2) = Duration4_v2(1,3);
contourToRasterReposition(1,1) = contourToRasterReposition(1,2) -...
    contourToRasterReposition(1,3);

contourToRasterRepositionAux = contourToRasterReposition;

contourToRasterReposition(1,2) = contourToRasterRepositionAux(1,3);
contourToRasterReposition(1,3) = contourToRasterRepositionAux(1,2);

indexContourAlt = indexContour;

for i = 1:1:numofContourLines
    indexContourAlt(i,2) = indexContour(i,2);
    indexContourAlt(i,3) = indexContour(i,3)-5;
end

if length(index_raster) < numofRasterLines
    [index_raster,index_trans_raster] =...
        adjust_internal(index_raster,index_trans_raster);

end

% Verify external pattern integrity

square1ExternalPattern = mean (indexContourAlt(1:numofContourSides,1));
square2ExternalPattern = mean (indexContourAlt((numofContourSides+1):(numofContourSides*2),1));

if abs(square2ExternalPattern - square1ExternalPattern) > (varDurRaster+4e3)
    [contourRepositions, indexContourAlt] = adjustExternalPattern(contourRepositions, indexContourAlt);
end

%

% Verify internal pattern integrity
rasterAuxMatrix = index_raster;
rasterAuxMatrix(1,numofContourSides) = 0;

for i = 2:length(index_raster(:,1))
    rasterAuxMatrix(i,numofContourSides) = abs(index_raster(i,(numofContourSides-1)) - index_raster(i-1,2));
end

maxRasterAux = max(rasterAuxMatrix(:,numofContourSides));

indexAdjust = find (rasterAuxMatrix(:,numofContourSides) > (varDurRaster-1e3));

if maxRasterAux > uppRefTransRaster
    [index_raster, index_trans_raster] = adjustInternalPattern(index_raster, index_trans_raster, indexAdjust);
end

%

signalReposition = Compos3r(sensorSignalNormalized,contourToRasterReposition(:,2:3))+...
    Compos3r(sensorSignalNormalized,contourRepositions(:,2:3));
signalRaster = Compos3r(sensorSignalNormalized, index_raster(:,2:3));
signalTransRaster = Compos3r(sensorSignalNormalized, index_trans_raster(:,2:3));
signalContour = Compos3r(sensorSignalNormalized, indexContourAlt(:,2:3));

% \ 14°
```

Figure 7.17 - Code to obtain the segmentation results

```
% 15° Obtain the segmentation results

testSegmentChoice = strcmp(segmentationChoice,'Points');

testxticksChoice = strcmp(xticksChoice,'Seconds');

if testSegmentChoice == true
    resultReposition = [contourRepositions; contourToRasterReposition];
    resultContour = indexContourAlt;
    resultRaster = index_raster;
    resultTransitionRaster = index_trans_raster;
    resultWholeWorkpiece = [resultContour(1,2) resultRaster(numofRasterLines,2)];
    resultExternalPattern = [resultContour(1,2) resultContour(numofContourLines,3)];
    resultInternalPattern = [resultRaster(1,3) resultRaster(numofRasterLines,2)];

    if testxticksChoice == true
        resultReposition = convUni(sensorSignalNormalized, resultReposition, Fs);
        resultContour = convUni(sensorSignalNormalized, resultContour, Fs);
        resultRaster = convUni(sensorSignalNormalized, resultRaster, Fs);
        resultTransitionRaster = convUni(sensorSignalNormalized, resultTransitionRaster, Fs);
        resultWholeWorkpiece = convUni(sensorSignalNormalized, resultWholeWorkpiece, Fs);
        resultExternalPattern = convUni(sensorSignalNormalized, resultExternalPattern, Fs);
        resultInternalPattern = convUni(sensorSignalNormalized, resultInternalPattern, Fs);
    end

    resultReposition = obtainTable(resultReposition(:,1),...
        resultReposition(:,2), resultReposition(:,3));
    resultContour = obtainTable(resultContour(:,1),...
        resultContour(:,2), resultContour(:,3));
    resultRaster = obtainTable(resultRaster(:,1),...
        resultRaster(:,3), resultRaster(:,2));
    resultTransitionRaster = obtainTable(resultTransitionRaster(:,1),...
        resultTransitionRaster(:,3), resultTransitionRaster(:,2));

    StartPoint = resultWholeWorkpiece(1);
    EndPoint = resultWholeWorkpiece(2);
    resultWholeWorkpiece = table(StartPoint,EndPoint);

    StartPoint = resultExternalPattern(1);
    EndPoint = resultExternalPattern(2);
    resultExternalPattern = table(StartPoint,EndPoint);

    StartPoint = resultInternalPattern(1);
    EndPoint = resultInternalPattern(2);
    resultInternalPattern = table(StartPoint,EndPoint);

end

testSegmentChoice = strcmp(segmentationChoice,'segments');

if testSegmentChoice == true
    resultReposition = gen_signal_segments(sensorSignalNormalized,...
        contourRepositions);
    resultReposition(1,numofContourSides) = gen_signal_segments(sensorSignalNormalized,...
        contourToRasterReposition);
    resultContour = gen_signal_segments(sensorSignalNormalized, indexContour);
    resultRaster = gen_signal_segments(sensorSignalNormalized, index_raster);
    resultTransitionRaster = gen_signal_segments(sensorSignalNormalized, index_trans_raster);
    resultWholeWorkpiece = gen_signal_segments(sensorSignalNormalized, [resultContour(1,2) resultRaster(numofRasterLines,2)]);
    resultExternalPattern = gen_signal_segments(sensorSignalNormalized, [resultContour(1,2) resultContour(numofContourLines,3)]);
    resultInternalPattern = gen_signal_segments(sensorSignalNormalized, [resultRaster(1,3) resultRaster(numofRasterLines,2)]);
end

% \ 15°
```

Figure 7.18 - Code to save the results and generate the graphs

```
% 16° Save the results and generate the graphs

if saveChoice == 'Y'
    save_files(resultReposition, resultContour, resultRaster,...
        resultTransitionRaster, resultWholeWorkpiece, resultExternalPattern,...
        resultInternalPattern, segmentationChoice, signalIdentifier);
end

if graphical == 'Y'
    gen_graph(signalReposition, sensorSignalNormalized, Fs,...
        signalIdentifier, signalContour, signalRaster,...
        signalTransRaster, index_raster, figureChoice);
end

% \ 16°
```